

https://dspace.org/

Acid mine drainage treatment by coagulation process using a synthesized sulphate-based coal fly ash coagulant

Apua, Momboyo Clotilde

2021

https://hdl.handle.net/10539/32162

Downloaded from a DSpace repository. https://dspace.org/

ACID MINE DRAINAGE TREATMENT BY COAGULATION PROCESS USING A SYNTHESIZED SULPHATE-BASED COAL FLY ASH COAGULANT

Momboyo Clotilde Apua

A thesis submitted to the Faculty of Engineering and the Built Environment, University of the Witwatersrand, Johannesburg, in fulfillment of the requirements for the degree of Doctor of Philosophy.

Johannesburg, 2020

DECLARATION

I declare that this thesis is my own unaided work. It is being submitted for the degree of Doctor of Philosophy to the University of the Witwatersrand, Johannesburg. It has not been submitted before for any degree or examination to any other University.

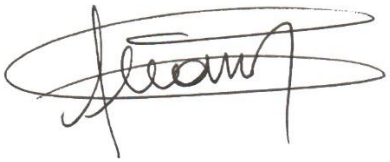

_____

Momboyo Clotilde Apua

11th day of February 2020

ABSTRACT

The study focused on the synthesis of a composite coagulant containing polymeric sulphates of Fe, Al, Si, Mg, and Ca from coal fly ash (CFA). Thereafter, the study assessed the performance of the produced composite coagulant in the treatment of acid mine drainage (AMD).

The CFA, a by-product of coal combustion rich in Fe, Al, Si, Mg, and Ca oxides was used in this investigation to synthesize a composite coagulant. This was performed using direct pressure H_2SO_4 leaching process. The results of the study found that the recoveries of Fe, Al, Si, Mg, and Ca from CFA were influenced by the concentration of H_2SO_4, temperature, solid to liquid ratio, and time. Subsequently, the extraction process of metals and silicon were optimized using the concentration of H_2SO_4, temperature, solid to liquid ratio, and time process variables.

The raw and processed CFA samples were analysed. The results showed that particle size distribution of the leach residues compared to raw changed during the leaching process. The SEM analysis revealed that new phases were present in the treated CFA sample compared to raw CFA. The morphology of CFA residues revealed that porous and stem-like structures were formed after leaching.

Investigations of kinetic mechanism, based on the shrinking core model, showed that the rate of the dissolution of CFA is controlled by mixed controlled mechanism (diffusion and chemical reaction). Investigation of the Arrhenius expression for Fe, Al, and Si revealed that Fe required more activation energy (59769.35 J/mole) for its acid dissolution, followed by Al (7248.228 J/mole) and silicon (5751.126 J/mole). The kinetic model study showed that zero-order kinetic model fitted mainly the investigated elements.

Before treatment by coagulation process, the quality of the raw AMD sample was determined in terms of elemental composition, total dissolved solids (TDS), and turbidity. The synthesized complex coagulant performed better in the removal of Al, Fe, Mn, Mg, Ca, Si, Zn, Ni, TDS, and turbidity in AMD treatment. The removal of these impurities was affected strongly by coagulant dosage, pH, and time.

The optical microscopy and SEM/EDS investigations of the floc formation revealed that pollutants adsorption onto hydroxide precipitates occurred during the coagulation process.

A comparison of the conventional iron and aluminium sulphate coagulants showed that the produced composite coagulant performed better than conventional coagulants in terms of removal of Mg, Ca, Si, Zn, and TDS. However, the performance of the conventional iron and aluminium sulphate coagulants was quite similar for the removal of Al, Fe, Mn and Ni.

In general, little information is available about the equilibrium capacities and adsorption kinetics of CFA-based coagulant for Al, Fe, Mn, Mg, Ca, Si, Zn, and Ni in aqueous solution. Furthermore, very limited information is available on the thermodynamic and kinetics aspects of adsorption of other element compounds onto other hydroxide precipitate-based adsorbents. Therefore, in order to better understand the adsorption process equilibrium and kinetics, a comprehensive study was conducted. The adsorption isotherm study showed that Temkin and BET equations best fitted the coagulation process. Both, Temkin and BET equations revealed that the adsorption energy was less than zero (i.e., exothermic behaviour). The chemical reaction kinetic model study suggested the applicability of the pseudo-second-order kinetic model. The molecule diffusion kinetic model investigation showed that multi adsorption stage occurred during the process. The intraparticle diffusion coefficients for the different pollutants were calculated from Weber–Morris and Boyd's models; and the results showed that the intraparticle diffusion coefficients, of the specific pollutants are in the range of 1.8 10^{-11} to 0.57 10^{-13} cm^2/sec and 1.05 10^{-12} to 1.87 10^{-12} cm^2/sec, respectively, (except for Ni and Ca for the Weber–Morris model).

The development of models for both processes, coagulant synthesis by leaching of CFA and AMD treatment by the synthesized coagulant, was performed with a new approach that fits the behaviour of the coagulant production and AMD treatment based on the software called "Eureqa Newtonian". The results showed that the model equations (y is the concentration and *t* the time) to predict the dissolution of Fe, Al, Si, Mg, and Ca from CFA in acidic medium are, respectively: $y = 57.3 - \frac{9.4\,t}{1.2-(0.3\,t)^{52.7}}$ (R^2 value of 0.95); $y = -79.9 + 52.7\,t - 9.1\,t^2 + 0.5\,t^3 + 62.6\,t^{-1}$ (R^2 value of 0.99); $y = 1.01\,t + 5.9$ (R^2 value of 1); $y = 58.7 + 4.1\,t - 0.2\,t^2$ (R^2 value of 0.91); and $y = 5.6\,t - 0.04\,t^3$ (R^2 value of 0.98).

However, for the prediction of AMD coagulation behaviour, results showed a polynomial equation form as $Ax^n + Bx^{n-1} + \cdots + Fx + G = 0$. The model equations can be summarized as follows where the input and output variables are time and concentration, respectively: the equation obtained for Al was $y = 0.01x^2 - 0.59x + 10.61$ with $R^2 = 0.87$, for Fe as $y = 0.0001x^4 - 0.01x^3 + 0.41x^2 - 8.13x + 63.44$ with $R^2 = 0.99$, for Zn as $y = 0.054x^2 - 2.56x + 47.44$ with $R^2 = 0.78$, for Si as $y = -0.0011x^3 + 0.12x^2 - 3.53x + 86.09$ with $R^2 = 0.96$, for Mn as $y = -0.0003x^3 + 0.028x^2 - 0.66x + 57.69$ with $R^2 = 0.98$, for Mg as $y = 0.0055x^2 - 0.22x + 66.66$ with $R^2 = 0.90$, for Ca as $y = 0.017x^2 - 1.14x + 92.44$ with $R^2 = 0.88$, and for Ni as $y = -0.0002x^4 + 0.022x^3 - 0.62x^2 + 3.9x + 96.19$ with $R^2 = 0.98$.

In addition, a mathematical model was developed based on the first principle of material balance to predict the dissolution of CFA with time. The dissolution model of a partial differential equation was applied to describe the mass transfer of element as it moves through the CFA particle towards the solution. The results showed that mathematical model for the CFA dissolution as function of time is as follows:

$$y(z) = 6.98 \text{ x } 10^{-11}\, e^{42.10 \text{ x } 10^{6} z} + \ 3.09 \text{ x } 10^{4} z\, e^{42.10 \text{ x } 10^{6} z}$$

DEDICATION

This thesis is dedicated to my wonderful son Rudy Mandio Ipoma, for his inestimable support and being my source of strength.

ACKNOWLEDGEMENTS

I would like to thank God and father of my lord and saviour Jesus Christ, who has blessed me in Christ with every spiritual blessing in the heavenly places. Thanks to him for being my sufficiency.

To my son Rudy Mandio Ipoma for always trusting in me, your continued encouragement, your financial support, and for always keeping me in your prayers. I did everything to make you proud of me.

I would like to express my sincere gratitude and appreciation to the following people and / or Institutions for their assistance and contributions in the completion of this thesis:

- My Supervisor Prof. Geoffrey S. Simate for his supervision, opinions, comments and suggestions on this research.
- Mrs Nomsa Baloyi and Mr Edouard Malenga (Extraction metallurgy laboratory/University of Johannesburg) for their technical help with XRF, XRD, SEM/EDS, FTIR, and PSD analyses. Their incredible assistance in the research laboratory is greatly appreciated. I am grateful for their help, experience and enthusiasm about work.

LIST OF REFERRED PUBLICATIONS

M. Clotilde Apua, Geoffrey S. Simate. Characterization of coal fly ash for the production of coagulant for usage in wastewater treatment - Conference paper. *Materials Science and Technology* 2018, DOI 10.7449, 9 pages.

M. Clotilde Apua, Geoffrey S. Simate. Production of a coal fly ash-based coagulant using sulphuric acid solutions. *Journal of Chemical and Metallurgy* Submitted. 2019.

TABLE OF CONTENTS

Section ***Page***

Declaration....ii

Abstract....iii

Dedication....vi

Acknowledgements....vii

List of referred publications....viii

Table of contents....ix

List of figures....xiv

List of tables....xxiv

List of abbreviations....xxxi

CHAPTER 1: INTRODUCTION....1

1.1 Research Background and Motivation....1

1.2 Hypothesis....3

1.3 Justification of the study....3

1.4 Reseach Aims and Objectives....4

1.5 Thesis outline....5

References....7

CHAPTER 2: LITERATURE REVIEW....11

2.1 Introduction....11

2.2 Coal fly ash....11

2.2.1 Occurrence and genesis of minerals in coal fly ash....11

2.2.2 Characteristics of coal fly ash....15

2.2.3 World coal fly ash production 18
2.2.4 Waste and disposal challenges 19
2.2.5 Uses of coal fly ash 20
2.3 Water and wastewater treatment coagulants 23
2.3.1 Ferrous sulphate 24
2.3.2 Ferric sulphate 24
2.3.3 Aluminium sulphate 24
2.3.4 Advantages and disadvantages of ferric and aluminium sulphates 25
2.4 Synthesis of coal fly ash-based coagulant 27
2.5 Chemistry of leaching reactions 27
2.6 Kinetics of dissolution reactions 28
2.7 Thermodynamics of complex formation 30
2.8 Typical required concentration of coagulant for water and wastewater treatment 33
2.9 Acid mine drainage 36
2.10 Coagulation of wastewater 37
2.10.1 Coagulation description 37
2.10.2 Colloidal suspensions 40
2.10.3 Water and wastewater impurities 42
2.10.4 Colloid stability and destabilization 43
2.10.5 Chemical aspects of metal cation (Fe^{3+}, Al^{3+}, Si^{x+}, Mg^{2+}, and Ca^{2+}) salts as coagulants 44
2.10.6 Mechanisms of wastewater coagulation 47
2.11 Adsorption isotherms and mechanism 50
2.12 Kinetic modelling of adsorption in a batch system 55
2.13 Process modelling 59
2.14 Anterior works 59
2.15 Summary 62
References 64

CHAPTER 3: EXPERIMENTAL METHODOLOGY 84
3.1 Introduction 84

3.2 Materials and methods 84
3.3 Analytical techniques 86
3.3.1 Coal fly ash sample preparation 86
3.3.2 Particle size distribution 87
3.3.3 X-ray diffraction spectroscopy 87
3.3.4 X-ray fluorescence spectroscopy 88
3.3.5 Fourier-transform infrared spectroscopy 90
3.3.6 Scanning electron microscopy coupled with energy dispersive spectroscopy 91
3.3.7 Inductively coupled plasma optical emission spectroscopy 91
3.3.8 Optical microscopy 92
3.4 Chemical equilibrium diagrams 92
3.4.1 Eh-pH diagram for the Fe–SO_4^{2-}–H_2O system 92
3.4.2 Eh–pH diagram for the Al–SO_4^{2-}–H_2O system 93
3.5 Coagulant synthesis 93
3.6 Leaching kinetic study 95
3.7 Fitting model analysis and mathematical modelling of the leaching process 96
3.8 Coagulation study 96
3.9 Adsorption study 99
3.10 Coagulation kinetics study 99
3.11 Comparison of the performance of the produced composite coagulant with the conventional coagulants 100
3.12 Fitting models analysis and mathematical modeling 100
3.13 Summary 100
References 102

CHAPTER 4: PRODUCTION OF A COMPLEX COAGULANT FROM COAL FLY ASH 104
4.1 Introduction 104
4.2 Results and discussion 104
4.2.1 Coal fly ash characterization 104

4.2.2 Leaching of iron, aluminium, and other elements from coal fly ash 111
4.3 Leaching kinetics of coal fly ash 128
4.3.1 Kinetic mechanism 128
4.3.2 Kinetic models 136
4.4 Conclusion 146
References 148

CHAPTER 5: PERFORMANCE OF THE PRODUCED COMPLEX COAGULANT 153
5.1 Introduction 153
5.2 Results and discussion 153
5.2.1 Coal mine wastewater characterization 153
5.2.2 Coagulation of toxic elements and turbidity from acid coal mine drainage 154
5.3 Characteristics of the treated coal mine wastewater after optimisation 177
5.4 Coagulation mechanism of the produced complex coagulant 178
5.5 Flocs formation analysis using optical microscopy 180
5.6 Scanning electron microscopy coupled with Energy Dispersive Spectroscopy (SEM/EDS) of the dry sludge 186
5.7 Comparative study of the performance of synthesized composite coagulant with conventional ferric sulphate and aluminium sulphate coagulants 189
5.8 Adsorption isotherm study 191
5.8.1 Langmuir model 192
5.8.2 Freundlich model 196
5.8.3 Temkin model 198
5.8.4 BET model 201
5.8.5 Coefficients of determination 204
5.9 Coagulation kinetics of the synthesized composite coagulant 206
5.9.1 Adsorption reaction models 207
5.9.2 Adsorption diffusion models 229
5.9.3 Coefficient of determination 240

5.10 Conclusion 242
References 244

CHAPTER 6: MODELLING BEHAVIOURS OF THE PROCESSES OF SYNTHESIS OF COMPLEX COAGULANT AND ACID MINE DRAINAGE TREATMENT USING THE PRODUCED COAGULANT 252
6.1 Introduction 252
6.2 Synthesis of the complex coagulant by leaching process 252
6.2.1 Fitting models analysis 252
6.2.2 Mathematical modelling development of leaching of coal fly ash 258
6.3 Acid mine drainage treatment by coagulation process 264
6.3.1 Fitting model analysis 264
6.4. Conclusion 271
References 273

CHAPTER 7: CONCLUSION AND RECOMMENDATIONS 274
7.1 Conclusion 274
7.1.1. Introduction 274
7.1.2. Production of coagulant by leaching process 274
7.1.3. Acid mine drainage treatment by coagulation process 276
7.1.4. Modelling behaviours of the processes of synthesis of complex coagulant and acid mine drainage treatment using the produced coagulant 278
7.1.5. Potential application in industry 278
7.2 Recommendations 279
7.2.1. Production of coagulant by leaching process 279
7.2.2. Acid mine drainage treatment by coagulation process 279

APPENDIX A 281
APPENDIX B 296
APPENDIX C 330
APPENDIX D 337
REFERRED PUBLICATION 339

LIST OF FIGURES

Figure	***Description***	***Page***
Figure 1.1:	Total Primary Energy Supply in South Africa, 2014….....	4
Figure 2.1:	Mechanism of CFA formation during coal combustion…	14
Figure 2.2:	Schematic diagram of the coal fly ash production from coal-fired power plant ….....	14
Figure 2.3:	Typical colours of coal fly ash…	15
Figure 2.4:	Illustration of negatively charged colloidal particles surrounded in solution by positively charged counter-ions, forming an electrical double layer (colloidal particles suspended in water may hold either a negative or a positive charge)	39
Figure 2.5:	Schematic illustration of the various ways followed by cation hydroxide species in solution or at a surface in contact with the solution …	49
Figure 3.1:	Flow diagram depicting the experimental and analytical methods….....	85
Figure 3.2:	(a) Schematic and (b) pictorial set-up of batch sulphuric acid leaching of Fe and Al from CFA in the Chemical Engineering laboratory of the University of Johannesburg….....	95
Figure 3.3:	(a) Schematic and (b) pictorial set-up of coagulation process of coagulant from CFA …	97
Figure 4.1:	Curve of particle size distribution (PSD) of CFA sample shows that the sample has a P80 particle diameter of 49 µm …	105
Figure 4.2:	XRD pattern of CFA. Q, M, and H indicate quartz (SiO_2), mullite ($Al_{5.65}Si_{0.35}O_{9.175}$), and hematite ($Fe_2O_3$), respectively.....	106
Figure 4.3:	FTIR spectrum for CFA …	107
Figure 4.4:	Scanning electron micrograph (SEM) of the CFA showing smooth spheres	109

Figure 4.5: SE images with elemental spectra of the CFA spheres (spots A, B, C, and D). These CFA particles have small variations in proportions of Al, Fe, and Si..... 110

Figure 4.6: Eh–pH diagram for the Fe–SO_4^{2-}–H_2O system at 25 °C; Total SO_4^{2-} concentration = 1.5 M. This diagram has been drawn using the Hydra/Medusa software 112

Figure 4.7: Eh–pH diagram for the Al–SO_4^{2-}–H_2O system at 25 °C; Total SO_4^{2-} concentration = 1.5 M. This diagram has been drawn using the Hydra/Medusa software 113

Figure 4.8: Effect of time on the leaching of elements from CFA sample (particle size: −49 µm, RT (23±2 °C), 1 M H_2SO_4, 300 rpm, S/L = 0.33) …..... 115

Figure 4.9: Effect of H_2SO_4 concentration on the leaching of elements from CFA sample (particle size: −49 µm, RT (23±2 °C), 300 rpm, S/L= 0.33, 1 hour) … 116

Figure 4.10: Effect of temperature on the leaching of elements from CFA sample (particle size: −49 µm, 1.5 M H_2SO_4, 300 rpm, S/L= 0.33, 1 hour) … 117

Figure 4.11: Effect of S/L on the leaching of elements from CFA sample (particle size: −49 µm, 1.5 M H_2SO_4, 150 °C, 300 rpm, 1 hour) … 119

Figure 4.12: Effect of time on optimal experimental conditions (particle size: −49 µm, 1.5 M H_2SO_4, 150 °C, S/L, 0.20, 300 rpm) …..... 120

Figure 4.13: Complex coagulant. (Conditions: particle size: −49 µm, 1.5 M H_2SO_4, 150 °C, S/L= 0.20, 300 rpm, and 6 hours). 121

Figure 4.14: Particle size distribution of the treated CFA with H_2SO_4 under optimal experimental conditions at different leaching stages: (a) 1 hour leaching, (b) 3 hours leaching, and (c) 6 hours leaching … 123

Figure 4.15: Comparison of XRD pattern of the raw to the treated CFA with H_2SO_4 leaching under optimal experimental conditions in different times..... 124

Figure 4.16: Comparison of FTIR spectrum of the raw to the treated CFA with H_2SO_4 leaching under optimal experimental conditions in different times …. 126

Figure 4.17: SEM micrographs of CFA particles at different leaching stages. (a) raw CFA; (b) CFA after 1 hour leaching (c) CFA after 3 hours leaching, and (d) CFA after 6 hours leaching …..... 127

Figure 4.18: Determination of the rate controlling factor of leaching of iron …..... 129

Figure 4.19: Determination of the rate controlling factor of leaching of aluminium… 130

Figure 4.20: Determination of the rate controlling factor of leaching of silicon… ..... ….131

Figure 4.21: Determination of the rate controlling factor of leaching of calcium … ..... ….132

Figure 4.22: Determination of the rate controlling factor of leaching of magnesium … 133

Figure 4.23: Determination of E_a …..... 134

Figure 4.24: E_a for aluminium extraction…..... 135

Figure 4.25: Zero-order kinetic model for the leaching of Fe, Al, Si, Ca, and Mg from coal fly ash. (Particle size: −49 μm, 1.5 M H_2SO_4, 150 °C, S/L= 0.20, 300 rpm, and 6 hours) … 137

Figure 4.26: Half-order kinetic model for the leaching of Fe, Al, Si, Ca, and Mg from coal fly ash. (Particle size: −49 μm, 1.5 M H_2SO_4, 150 °C, S/L= 0.20, 300 rpm, and 6 hours) … 139

Figure 4.27: First-order kinetic model for the leaching of Fe, Al, Si, Ca, and Mg from coal fly ash. (Particle size: −49 μm, 1.5 M H_2SO_4, 150 °C, S/L= 0.20, 300 rpm, and 6 hours) … 140

Figure 4.28: Second-order kinetic model for the leaching of Fe, Al, Si, Ca, and Mg from coal fly ash. (Particle size: −49 μm, 1.5 M H_2SO_4, 150 °C, S/L= 0.20, 300 rpm, and 6 hours). … 142

Figure 4.29: Hixson-Crowell kinetic model for the leaching of Fe, Al, Si, Ca, and Mg from coal fly ash. (Particle size: −49 μm, 1.5 M H_2SO_4, 150 °C, S/L= 0.20, 300 rpm, and 6 hours) … 143

Figure 4.30: Gompertz model for the leaching of Fe, Al, Si, Ca, and Mg from coal fly ash. (Particle size: −49 μm, 1.5 M H_2SO_4, 150 °C, S/L= 0.20, 300 rpm, and 6 hours) …. 145

Figure 5.1: Hydroxide precipitation diagram, 25 ^oC … 155

Figure 5.2: Evaluation of the effect of the amount of the synthesized coagulant in reducing TDS from acidic coal mine drainage sample (AMD/coagulant ratio: 2,5; initial TDS: 5276 mg/L; pH: 7; RT (20±1 °C); coagulant dosage as $C_{Fe+Al+Si+Mg+Ca}$: 24594,48 mg/L; 5 minutes rapid mixing at 300 rpm; 20 minutes slow mixing at 30 rpm) 158

Figure 5.3: Evaluation of the effect of the feed concentration in reducing TDS from acidic coal mine drainage sample (AMD/coagulant ratio: 2,5; pH: 7; RT (20±1 °C); 5 minutes rapid mixing at 300 rpm; 20 minutes slow mixing at 30 rpm) … 160

Figure 5.4: Effect of coagulant dosage (mg/L) and pH on removal of TDS from acidic coal mine drainage (initial TDS concentration was 720.2 mg/L, initial pH: 4–10; AMD/coagulant ratio: 2.5; RT (23±2 °C); 5 minutes rapid mixing at 300 rpm; 20 minutes slow mixing at 30 rpm) …. 162

Figure 5.5: Effect of coagulant dosage (mg/L) and pH on removal of Fe from acidic coal mine drainage (initial Fe concentration was 1.64 mg/L; initial pH: 4–10; AMD/coagulant ratio: 2.5; RT (23±2 °C); 5 minutes rapid mixing at 300 rpm; 20 minutes slow mixing at 30 rpm) … 163

Figure 5.6: Effect of coagulant dosage (mg/L) and pH on removal of Al from acidic coal mine drainage (initial Al concentration was 13.86 mg/L; initial pH: 4–10; AMD/coagulant ratio: 2.5; RT (23±2 °C); 5 minutes rapid mixing at 300 rpm; 20 minutes slow mixing at 30 rpm) … 164

Figure 5.7: Effect of coagulant dosage (mg/L) and pH on removal of Mn from acidic coal mine drainage (initial Mn concentration was 13.52 mg/L; initial pH: 4–10; AMD/coagulant ratio: 2.5; RT (23±2 °C); 5 minutes rapid mixing at 300 rpm; 20 minutes slow mixing at 30 rpm)…. 165

Figure 5.8: Effect of coagulant dosage (mg/L) and pH on removal of Si from acidic coal mine drainage: (initial Si concentration was 0.91 mg/L; initial pH:

4–10; AMD/coagulant ratio: 2.5; RT (23±2 °C); 5 minutes rapid mixing at 300 rpm; 20 minutes slow mixing at 30 rpm) … 166

Figure 5.9: Effect of coagulant dosage (mg/L) and pH on removal of Mg from acidic coal mine drainage (initial Mg concentration was 30.18 mg/L; initial pH: 4–10; AMD/coagulant ratio: 2.5; RT (23±2 °C); 5 minutes rapid mixing at 300 rpm; 20 minutes slow mixing at 30 rpm).… 167

Figure 5.10: Effect of coagulant dosage (mg/L) and pH on removal of Ca from acidic coal mine drainage (initial Ca concentration was 31.13 mg/L; initial pH: 4–10; AMD/coagulant ratio: 2.5; RT (23±2 °C); 5 minutes rapid mixing at 300 rpm; 20 minutes slow mixing at 30 rpm) … 168

Figure 5.11: Effect of coagulant dosage (mg/L) and pH on removal of Zn from acidic coal mine drainage (initial Zn concentration was 0.93 mg/L; initial pH: 4–10; AMD/coagulant ratio: 2.5; RT (23±2 °C); 5 minutes rapid mixing at 300 rpm; 20 minutes slow mixing at 30 rpm).… 169

Figure 5.12: Effect of coagulant dosage (mg/L) and pH on removal of Ni from acidic coal mine drainage (initial Ni concentration was 13.86 (initial pH: 4–10; AMD/coagulant ratio: 2.5; RT (23±2 °C); 5 minutes rapid mixing at 300 rpm; 20 minutes slow mixing at 30 rpm).… 170

Figure 5.13: Turbidity reduction at different pH and coagulant dosage (mg/L) (initial turbidity 87.7 NTU; initial pH: 4–10; AMD/coagulant ratio: 2.5; RT (23±2 °C); 5 minutes rapid mixing at 300 rpm; 20 minutes slow mixing at 30 rpm).… 172

Figure 5.14: Change of pH after adding different doses of the composite coagulant in acid coal mine drainage sample … 173

Figure 5.15: Change of total dissolved solids and toxic elements concentrations at different temperatures of coagulation process. Conditions: 20 mg/L coagulant dosage, pH 7, coagulant time = 20 minutes, temperature = 20–50 °C …..... 174

Figure 5.16: Change of toxic elements and total dissolved solids concentrations after different times of coagulation process. Conditions: 20 mg/L coagulant dosage, pH 7, RT (20±1 °C), coagulant time = 1–50 minutes … 176

Figure 5.17: Coal mine drainage. (a) Before and (b) after treatment (1 hour settling). Conditions: 50mL wastewater, adjusted the initial pH 7 by NaOH and H_2SO_4, produced coagulant dosage 20 mg/L, 20 minutes' treatment … 177

Figure 5.18: The optical microscope images showing flocs formation during coagulation using the composite coagulant under optimal experimental conditions at (a) 10, (b) 20, (c) 30, and (d) 40 minutes …..... 182

Figure 5.19: The optical microscope images showing flocs formation during coagulation using the composite coagulant under optimal experimental conditions at (a) 50, (b) 60, (c) 70, and (d) 80 minutes …..... 183

Figure 5.20: The optical microscope images showing flocs formation during coagulation using the composite coagulant under optimal experimental conditions at (a) 90, (b) 100, (c) 110, and (d) 120 minutes…..... 184

Figure 5.21: The optical microscope images showing flocs formation during coagulation using the composite coagulant under optimal experimental conditions at (a) 130, (b) 140, and (c) 150 minutes… 185

Figure 5.22: SEM images with elemental spectra of the sludge (a) pH 4 and (b) pH 7. Conditions: 20mg/L coagulant dosage, RT (23±2 °C); 5 minutes rapid mixing at 300 rpm; 20 minutes slow mixing at 30 rpm) … 187

Figure 5.23: SEM images with elemental spectra of the sludge (a) pH 11 and (b) pH 12. Conditions: 20mg/L coagulant dosage, RT (23±2 °C); 5 minutes rapid mixing at 300 rpm; 20 minutes slow mixing at 30 rpm) … 188

Figure 5.24: Langmuir adsorption isotherm model for the removal of (a) Al, Fe, Zn, (b) Mn, (c) Mg, Ca, and (d) Si, Ni onto hydroxide precipitates (pH: 7; coagulant dosage:20 mg/L; flash mixing time: 5 minutes; coagulation time (slow mixing time): 1–50 minutes) … 194

Figure 5.25: Freundlich equilibrium isotherms model for the sorption of (a) Ca, Mg, Mn, (b) Ni, Si, (c) Al, Fe, and (d) Zn on hydroxide precipitates (pH: 7; coagulant dosage:20 mg/L; flash mixing time: 5 minutes; coagulation time (slow mixing time): 1–50 minutes) … 197

Figure 5.26: Temkin equilibrium isoterm model for the adsorption of (a) Si, Zn, Ni, Fe, and (b) Al, Mn, Ca, Mg onto hydroxide precipitates (pH: 7; coagulant dosage:20

mg/L; flash mixing time: 5 minutes; coagulation time (slow mixing time): 1–50 minutes) 200

Figure 5.27: BET equilibrium isoterm model for the adsorption of (a) Al, Fe, Zn, (b) Ca, Si, and (c) Mn, Mg, Ni onto hydroxide precipitates (pH: 7; coagulant dosage:20 mg/L; flash mixing time: 5 minutes; coagulation time (slow mixing time): 1–50 minutes) 203

Figure 5.28: (a) Adsorption rate curves of Al and (b) Pseudo-first-order reaction kinetics for the adsorption of Al onto hydroxide precipitate. (pH: 7, coagulant dosage 20 mg/L, and RT 23 ±2 ^{o}C) … 209

Figure 5.29: (a) Adsorption rate curves of Fe and (b) Pseudo-first-order reaction kinetics for the adsorption of Fe onto hydroxide precipitate. (pH: 7, coagulant dosage 20 mg/L, and RT 23 ±2 ^{o}C) … 210

Figure 5.30: (a) Adsorption rate curves of Mn and (b) Pseudo-first-order reaction kinetics for the adsorption of Mn onto hydroxide precipitate. (pH: 7, coagulant dosage 20 mg/L, and RT 23 ±2 ^{o}C) … 211

Figure 5.31: (a) Adsorption rate curves of Ca and (b) Pseudo-first-order reaction kinetics for the adsorption of Ca onto hydroxide precipitate. (pH: 7, coagulant dosage 20 mg/L, and RT 23 ±2 ^{o}C) … 212

Figure 5.32: (a) Adsorption rate curves of Mg and (b) Pseudo-first-order reaction kinetics for the adsorption of Mg onto hydroxide precipitate. (pH: 7, coagulant dosage 20 mg/L, and RT 23 ±2 ^{o}C) … 213

Figure 5.33: (a) Adsorption rate curves of Si and (b) Pseudo-first-order reaction kinetics for the adsorption of Si onto hydroxide precipitate. (pH: 7, coagulant dosage 20 mg/L, and RT 23 ±2 ^{o}C) … 214

Figure 5.34: (a) Adsorption rate curves of Zn and (b) Pseudo-first-order reaction kinetics for the adsorption of Zn onto hydroxide precipitate. (pH: 7, coagulant dosage 20 mg/L, and RT 23 ±2 ^{o}C) … 215

Figure 5.35: (a) Adsorption rate curves of Ni and (b) Pseudo-first-order reaction kinetics for the adsorption of Ni onto hydroxide precipitate. (pH: 7, coagulant dosage 20 mg/L, and RT 23 ±2 ^{o}C) … 216

Figure 5.36: Pseudo-second-order reaction kinetics for the adsorption of Fe, Al, and Zn onto hydroxide precipitate. (pH: 7, coagulant dosage 20 mg/L, and RT 23 ±2 ^{o}C) … 219

Figure 5.37: Pseudo-second-order reaction kinetics for the adsorption of Mn, Ca, and Mg onto hydroxide precipitate. (pH: 7, coagulant dosage 20 mg/L, and RT 23 ±2 ^{o}C) … 220

Figure 5.38: Pseudo-second-order reaction kinetics for the adsorption of Si onto hydroxide precipitate. (pH: 7, coagulant dosage 20 mg/L, and RT 23 ±2 ^{o}C) … 220

Figure 5.39: Pseudo-second-order reaction kinetics for the adsorption of Ni onto hydroxide precipitate. (pH: 7, coagulant dosage 20 mg/L, and RT 23 ±2 ^{o}C) 221

Figure 5.40: Elovich reaction kinetics for the adsorption of Al, Mn, Ca, and Mg onto hydroxide precipitate (pH: 7, coagulant dosage 20 mg/L, and RT 23 ±2 ^{o}C). 223

Figure 5.41: Elovich reaction kinetics for the adsorption of Si, Ni, Zn, and Fe onto hydroxide precipitate (pH: 7, coagulant dosage 20 mg/L, and RT 23 ±2 ^{o}C). 224

Figure 5.42: Second-order reaction kinetics for the adsorption of Al, Si, and Ni onto hydroxide precipitate (pH: 7, coagulant dosage 20 mg/L, and RT 23 ±2 ^{o}C). 227

Figure 5.43: Second-order reaction kinetics for the adsorption of Mn, Ca, and Mg onto hydroxide precipitate (pH: 7, coagulant dosage 20 mg/L, and RT 23 ±2 ^{o}C). 228

Figure 5.44: Second-order reaction kinetics for the adsorption of Fe and Zn onto hydroxide precipitate (pH: 7, coagulant dosage 20 mg/L, and RT 23 ±2 ^{o}C). 228

Figure 5.45: Weber-Morris diffusion kinetics for the adsorption of Al, Mn, Mg, and Ca onto hydroxide precipitate (pH: 7, coagulant dosage 20 mg/L, and RT 23 ±2 ^{o}C). 231

Figure 5.46: Weber-Morris diffusion kinetics for the adsorption of Fe, Si, Zn, and Ni onto hydroxide precipitate (pH: 7, coagulant dosage 20 mg/L, and RT 23 ±2 ^{o}C). 232

Figure 5.47: Boyd's diffusion kinetics for the adsorption of Al, Fe, Mn, and Ca onto hydroxide precipitate (pH: 7, coagulant dosage 20 mg/L, and RT 23 ±2 ^{o}C). 235

Figure 5.48: Boyd's diffusion kinetics for the adsorption of Mg, Si, Zn, and Ni onto hydroxide precipitate (pH: 7, coagulant dosage 20 mg/L, and RT 23 ±2 ^{o}C). … 236

Figure 5.49: Bangham's diffusion kinetics for the adsorption of Al, Fe, Mn, Mg, and Ca onto hydroxide precipitate (pH: 7, coagulant dosage 20 mg/L, and RT 23 ±2 ^{o}C) … 238

Figure 5.50: Bangham's diffusion kinetics for the adsorption of Ni, Si, and Zn onto hydroxide precipitate (pH: 7, coagulant dosage 20 mg/L, and RT 23 ±2 ^{o}C) … 239

Figure 6.1: Iron recovery from CFA with time … 252

Figure 6.2: Aluminium recovery from CFA with time …..... 254

Figure 6.3: Silicon recovery from CFA with time …..... 255

Figure 6.4: Magnesium recovery from CFA with time … 256

Figure 6.5: Calcium recovery from CFA with time … 257

Figure 6.6: Convection and diffusion flux during dissolution process of coal fly ash …..... 259

Figure 6.7: Aluminium concentration with position during the leaching process … 263

Figure 6.8: Residual aluminium in coal mine wastewater with time … 264

Figure 6.9: Residual iron in coal mine wastewater with time … 265

Figure 6.10: Residual zinc in coal mine wastewater with time … 266

Figure 6.11: Residual silicon in coal mine wastewater with time … 267

Figure 6.12: Residual manganese in coal mine wastewater with time …..... 268

Figure 6.13: Residual magnesium in coal mine wastewater with time … 269

Figure 6.14: Residual calcium in coal mine wastewater with time … 270

Figure 6.15: Residual nickel in coal mine wastewater with time … 271

Figure A.1: Determination of Ea using chemical reaction kinetic model…… 291

Figure A.2: Determination of Ea using chemical reaction kinetic model for Al before 150 ^{0}C ……..... 291

Figure A.3: Determination of Ea using chemical reaction kinetic model for Al after 150 ^{0}C ……..... 292

Figure B.1: Pseudo-second-order for the adsorption of silicon after 1 min coagulation's time … 323

Figure D.1: Basic optical system of a laser diffraction particle size analyser ….... 337

Figure D.2: Basic system of an x-ray diffraction spectrometer ….... 337

Figure D.3: Basic system of an x-ray fluorescence spectrometer … 338

LIST OF TABLES

Table	***Description***	***Page***
Table 2.1:	Typical percent range of chemical composition of coal fly ash by coal type	18
Table 2.2:	Estimated CFA annual production by country 2010	19
Table 2.3:	Advantages and disadvantages of iron and aluminium coagulants	26
Table 2.4:	Summary of the rate equations	29
Table 2.5:	Maximum allowable concentrations of certain constituents in industrial effluent discharge (mg/l, except where otherwise stated) and health effects of various toxic heavy metals	34
Table 2.6:	Classification of particle sizes	40
Table 2.7:	Some polynuclear hydrolysis species	46
Table 2.8:	Single-component adsorption isotherm models used	52
Table 2.9:	Reaction kinetic models used for the adsorption reactions	57
Table 2.10:	Diffusion kinetic models used for the adsorption reactions	58
Table 4.1:	Chemical composition of CFA sample. Only important elements from important phases are presented	106
Table 4.2:	Band assignment for coal fly ash compounds related to the band positions in cm^{-1}	108
Table 4.3:	Energy dispersive spectrometry (EDS) w% of elements in CFA	111
Table 4.4:	Chemical composition of the coagulant produced by H_2SO_4 leaching of the CFA sample	122
Table 4.5:	Chemical composition of the raw and treated CFA samples	125
Table 4.6:	Calculated E_a for the dissolution of elements	135
Table 4.7:	Linear kinetic coefficients of determination (R^2)	146
Table 4.8:	Kinetic model parameters	146

Table 5.1: Chemical analysis of the coal mine wastewater sample 154

Table 5.2: Chemical analysis of the treated coal mine wastewater obtained from treatment of the acid coal mine drainage sample by the complex coagulant 178

Table 5.3: Energy dispersive spectrometry (EDS) w% of elements in the sludge. 189

Table 5.4: Results of treating coal mine wastewater with different coagulants. Residual TDS and toxic elements (%) and turbidity (NTU). 190

Table 5.5: adsorption capacity (q_e) of pollutant at time *t* 191

Table 5.6: Langmuir isotherm parameters calculated for metals, silicon, and TDS removal by the produced complex coagulant. 195

Table 5.7: Freundlich isotherm parameters 198

Table 5.8: Temkin isotherm parameters 201

Table 5.9: BET isotherm parameters 204

Table 5.10: Linear isotherm coefficients of determination ($\boldsymbol{R^2}$) 206

Table 5.11: kinetic parameters of the pseudo-first-order kinetic model for Al, Fe, Mn, Mg, Ca, Si, Zn, and Ni. 217

Table 5.12: kinetic parameters of the pseudo-second-order kinetic model for Al, Fe, Mn, Mg, Ca, Si, Zn, and Ni 221

Table 5.13: kinetic parameters of the Elovich kinetic model for Al, Fe, Mn, Mg, Ca, Si, Zn, and Ni 225

Table 5.14: kinetic parameters of the second order kinetic model for Al, Fe, Mn, Mg, Ca, Si, Zn, and Ni 229

Table 5.15: kinetic parameters of the Weber-Morris kinetic model for Al, Fe, Mn, Mg, Ca, Si, Zn, and Ni 233

Table 5.16: Rate parameters of the Boyd's kinetic model for Al, Fe, Mn, Mg, Ca, Si, Zn, and Ni 236

Table 5.17: kinetic parameters of the Bangham's kinetic model for Al, Fe, Mn, Mg, Ca, Si, Zn, and Ni 239

Table 5.18: Linear kinetic coefficients of determination (R^2) 241

Table A.1: Data from the effect of time on the dissolution experiments of iron, aluminium, silicon, magnesium, and calcium 281

Table A.2: Data from the effect of sulphuric acid concentration on the dissolution experiments of iron, aluminium, silicon, magnesium, and calcium..... 282

Table A.3: Data from the effect of temperature on the dissolution experiments of iron, aluminium, silicon, magnesium, and calcium 283

Table A.4: Data from the effect of solid-liquid ratio on the dissolution experiments of iron, aluminium, silicon, magnesium, and calcium 284

Table A.5: Data from the effect of time on optimal experimental conditions on the dissolution experiments of iron, aluminium, silicon, magnesium, and calcium 285

Table A.6: Data from the Kinetic of dissolution of iron 286

Table A.7: Data from the Kinetic dissolution of aluminium..... 287

Table A.8: Data from the Kinetic of dissolution of silicon 288

Table A.9: Data from the Kinetic dissolution of calcium 289

Table A.10: Data from the Kinetic dissolution of magnesium 290

Table A.11: Data from the zero-order kinetic model 293

Table A.12: Data from the half-order kinetic model..... 293

Table A.13: Data from the first-order kinetic model 294

Table A.14: Data from the second-order kinetic model..... 294

Table A.15: Data from the Hixson-Crowell kinetic model 295

Table A.16: Data from the Gompertz kinetic model..... 295

Table B.1: Data from the effect of the volume of the composite coagulant on the coagulation experiments of TDS..... 296

Table B.2: Data from the effect of the initial concentration of wastewater on the coagulation experiments of TDS..... 296

Table B.3: Data from the effect of composite coagulant dosage and pH on the coagulation experiments of TDS 297

Table B.4: Data from the effect of composite coagulant dosage and pH on the coagulation experiments of iron 298

Table B.5: Data from the effect of composite coagulant dosage and pH on the coagulation experiments of aluminium 299

Table B.6: Data from the effect of composite coagulant dosage and pH on the coagulation experiments of manganese 300

Table B.7: Data from the effect of composite coagulant dosage and pH on the coagulation experiments of silicon 301

Table B.8: Data from the effect of composite coagulant dosage and pH on the coagulation experiments of magnesium 302

Table B.9: Data from the effect of composite coagulant dosage and pH on the coagulation experiments of calcium 303

Table B.10: Data from the effect of composite coagulant dosage and pH on the coagulation experiments of zinc 304

Table B.11: Data from the effect of composite coagulant dosage and pH on the coagulation experiments of nickel 305

Table B.12: Data from the effect of composite coagulant dosage and pH on the coagulation experiments of turbidity 306

Table B.13: Data from the effect of composite coagulant dosage on the final pH of wastewater experiments 307

Table B.14: Data from the effect of temperature on the coagulation experiments ... 308

Table B.15: Data from the effect of time on the coagulation experiments 309

Table B.16: Data from the Langmiur adsorption isotherm model for the removal of Al, Fe, Zn, and Mn 310

Table B.17: Data from the Langmiur adsorption isotherm model for the removal of Mg, Ca, Si, and Ni 311

Table B.18: Data from the Freundlich adsorption isotherm model for the removal of Mn, Ca, Mg, Si, and Ni 312

Table B.19: Data from the Freundlich adsorption isotherm model for the removal of Al, Fe, and Zn..... 313

Table B.20: Data from the Temkin adsorption isotherm model for the removal of Si, Zn, Ni, and Fe..... 314

Table B.21: Data from the Temkin adsorption isotherm model for the removal of Al, Mn, Ca, and Mg 315

Table B.22: Data from the BET adsorption isotherm model for the removal of Al, Fe, Zn, Ca, and Si..... 316

Table B.23: Data from the BET adsorption isotherm model for the removal of Mn, Mg, and Ni 317

Table B.24: Data from the adsorption rate and the pseudo-first-order reaction kinetics for the adsorption of Al 318

Table B25: Data from the adsorption rate and the pseudo-first-order reaction kinetics for the adsorption of Fe 318

Table B.26: Data from the adsorption rate and the pseudo-first-order reaction kinetics for the adsorption of Mn 319

Table B.27: Data from the adsorption rate and the pseudo-first-order reaction kinetics for the adsorption of Ca..... 319

Table B.28: Data from the adsorption rate and the pseudo-first-order reaction kinetics for the adsorption of Mg 320

Table B.29: Data from the adsorption rate and the pseudo-first-order reaction kinetics for the adsorption of Si..... 320

Table B.30: Data from the adsorption rate and the pseudo-first-order reaction kinetics for the adsorption of Zn..... 321

Table B.31: Data from the adsorption rate and the pseudo-first-order reaction kinetics for the adsorption of Ni 321

Table B.32: Data from pseudo-second-order reaction kinetics for the adsorption of Fe, Al, and Zn..... 322

Table B.33: Data from pseudo-second-order reaction kinetics for the adsorption of Mn, Ca, and Mg 322

Table B.34: Data from pseudo-second-order reaction kinetics for the adsorption of Si 323

Table B.35: Data from pseudo-second-order reaction kinetics for the adsorption of Ni 324

Table B.36: Data from the Elovich reaction kinetics for the adsorption of Al, Mn, Ca, and Mg 324

Table B.37: Data from the Elovich reaction kinetics for the adsorption of Si, Ni, Zn, and Fe 325

Table B.38: Data from the second-order reaction kinetics for the adsorption of Al, Si, and Ni 325

Table B.39: Data from the second-order reaction kinetics for the adsorption of Mn, Ca, and Mg 326

Table B.40: Data from the second-order reaction kinetics for the adsorption of Fe and Zn 326

Table B.41: Data from the Weber-Morris diffusion kinetics for the adsorption of Al, Mn, Mg, and Ca 327

Table B.42: Data from the Weber-Morris diffusion kinetics for the adsorption of Fe, Si, Zn, and Ni 327

Table B.43: Data from the Boyd's diffusion kinetics for the adsorption of Al, Fe, Mn, and Ca 328

Table B.44: Data from the Boyd's diffusion kinetics for the adsorption of Mg, Si, Zn, and Ni 328

Table B.45: Data from the Banbham's diffusion kinetics for the adsorption of Al, Fe, Mn, Ca, and Mg 329

Table B.46: Data from the Banbham's diffusion kinetics for the adsorption of Ni, Si, and Zn 329

Table C.1: Data from the dissolution of iron 330

Table C.2: Data from the dissolution of aluminium 330
Table C.3: Data from the dissolution of silicon 331
Table C.4: Data from the dissolution of magnesium 331
Table C.5: Data from the dissolution of calcium 332
Table C.6: Data from the coagulation of aluminium 333
Table C.7: Data from the coagulation of iron 333
Table C.8: Data from the coagulation of manganese 334
Table C.9: Data from the coagulation of magnesium 334
Table C.10: Data from the coagulation of calcium 335
Table C.11: Data from the coagulation of silicon 335
Table C.12: Data from the coagulation of zinc 336
Table C.13: Data from the coagulation of nickel 336

LIST OF ABBREVIATIONS

AMD	Acid mine drainage
BET	Brunauer–Emmett–Teller
CFA	Coal fly ash
FAA	Flame atomic absorption spectrometry
FTIR	Fourier transform infrared spectroscopy
EDS	Energy dispersive spectroscopy
EU	Europe
ICP-OES	Inductively coupled plasma optical emission spectroscopy
MW	Megawatt
NTU	Nephelometric turbidity units
PSD	Particle size distribution
RT	Room temperature
S/L	Solid to liquid ratio
SEM	Scanning Electron Microscopy
TDS	Total dissolved solids
XRD	X-ray Diffraction
XRF	X-ray Fluorescence

CHAPTER 1
INTRODUCTION

1.1 Research Background and Motivation

Energy production by combustion of coal at 1200–1700 °C generates significant by-products that pose serious management issues of storage and/or disposal (Blisset and Rowson, 2012). These by-products include bottom ash, fly ash, and slag (Viraraghavan, 1982). Normally, these by-products are stockpiled and/or discarded, but they, consequently, pollute the environment. As a result of the limited commercial uses of coal fly ash (CFA), in particular, considerable research has been undertaken to find some alternative applications (Iyer and Scott, 2001; Ahmaruzzaman, 2010; Blisset and Rowson, 2012).

The CFA is an abundant waste residue produced from coal combustion in coal-fired power plants (Yao et al., 2014). Most of this waste is dumped into landfills, which could have destructive effects on the use of land. Furthermore, CFA particles are small (diameter from 0.5 to 100 μm) and are easily blown into the atmosphere by the wind. Therefore, unprocessed CFA may also be a source of serious environmental issues because it pollutes the atmosphere (Bian et al., 2009).

Research has shown that only a small fraction of the total CFA produced (20–30%) is used in the following applications: (1) substitute material for cement (Rafieizonooz et al., 2016), (2) asphalt filler (Blisset and Rowson, 2012; Dot. Gov, 2015), (3) flowable fill (Siriwardane et al., 2003; Mishra and Karanam, 2006), (4) soil stabilization (Pandey and Singh, 2010; Manoharan et al., 2010; Yao et al., 2015), (5) adsorbent of individual pollutants in flue gases (Rubel et al., 2005; Lissianski et al., 2009), (6) extraction of metals (Matjie et al., 2005), (7) manufacture of glass and ceramics (Peng et al., 2005; Erol et al., 2008), (8) production of zeolites (Inada et al., 2005), (9) catalysts and catalyst supports (Muhammad et al., 2012; Yao et al. 20015), (10) wastewater treatments as a low-cost adsorbent for organic removal (Itskos et al., 2010; Ali et al., 2012), and (11) synthesis of geopolymers (Blissett and Rowson, 2012). However, despite various applications stated previously, there is still a need to find other alternative ways of utilizing CFA productively so as to protect the environment and to diminish its disposal on land (Vadapalli et al.,

2008). At the moment, CFA has promising applications in the treatment of wastewater because of its physical properties such as porosity and surface area, and the presence of chemical components such as iron oxide and alumina (Apua and Simate, 2018).

Basically, the main chemical components of CFA are iron, aluminium, silicon, magnesium, and calcium oxides. Iron and aluminium oxides are essential raw materials for the production of coagulants for water and wastewater treatment through the coagulation process. The technique is environmentally friendly (Li et al., 2009; Ahmaruzzaman, 2010; Fan et al., 2005). It must be noted that over the years, ores or chemical salts of aluminium and iron have been used as raw materials by most coagulant manufacturers. Nevertheless, aluminium and iron minerals (or chemicals) are expensive. Moreover, their use in the manufacture of coagulants consumes large quantities of limited mineral resources, thus increasing their scarcity (Fan et al., 2003). More, the weight proportion of iron and aluminium oxides in CFA is suitable for producing complex coagulants (Yan et al., 2012).

Also, several researchers have studied the role of other important elements, such as magnesium, calcium, and silicon ions, as potential coagulants for the treatment of wastewater (Bidhendi et al., 2007; Semerjian and Ayoub, 2003; Li et al., 2016). Then, CFA can be used to produce high polymeric composite. In wastewater treatment, a composite coagulant is effective due to its multivalence which attracts strongly to colloidal particles and assures a high degree of removal. Therefore, CFA has become a significant resource for the production of coagulants and researchers are more interested in this study nowadays (Ahmaruzzaman, 2010). Use of CFA to manufacture complex coagulants can, therefore, result in significant savings, since CFA cost much less than industrial-grade iron or aluminium ores. In addition, such a concept to using these by-products would help to conserve precious land resources used as landfills and lessen the environmental degradation resulting from storage and disposal techniques presently used in several countries (Fan et al., 2003). In wastewater treatment, a composite coagulant is effective due to its multivalence which strongly attracts colloidal particles and ensures a high degree of removal.

Although coagulation of wastewater using CFA-based coagulant has been reported in literature as already alluded to, there is a need to explore other means of improving the yield of the coagulant from CFA and the quality of the treated wastewater by coagulation using CFA-based coagulant. Therefore, the main focus of this research was to use CFA, a known source of increasing solid waste currently in the world which is available in South

Africa, as a feed material for the production of complex coagulants and to utilize the produced coagulants for treating acid mine drainage (AMD) through the coagulation process. To produce wastewater treatment coagulant from CFA, direct pressure leaching was used. Evaluation of the coagulant on AMD treatment was performed so as to ascertain its suitability as a coagulant for AMD.

1.2 Hypothesis

The CFA is made up of oxides such as Fe_2O_3, Al_2O_3, and MgO which can be dissolved in acidic solution to produce Fe^{3+}, Al^{3+}, and Mg^{2+} ions under controlled conditions using leaching process. The leach solution containing Fe^{3+}, Al^{3+}, and Mg^{2+} ions can be used to treat wastewater under controlled conditions using coagulation process. It is, therefore, hypothesised that leaching of CFA will produce higher yield of coagulant for treatment of wastewater.

1.3 Justification of the study

In recent years, several coagulants have been used for treating water and wastewater in laboratory and pilot-scale experiments (Menezes et al., 2010). Nevertheless, CFA minerals dissolution is an area that still needs to be explored and developed. From available reports, around 70% of energy needs in South Africa are directly derived from coal (Figure 1.1) (South Africa-International Energy Agency, 2017). Almost 25 million tons of CFA are produced per annum by Eskom, the country's largest electrical utility. Only 5% is used for cement and brick making while the rest is disposed of in ash dams or stacked on land as ash dumps (Hunter, 2018).

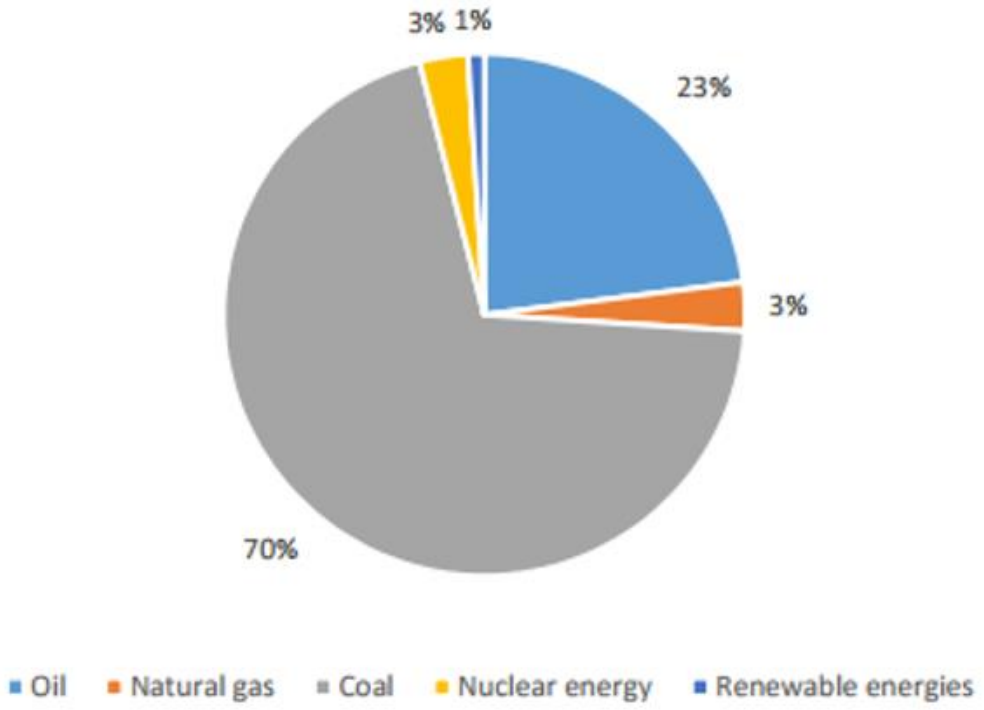

Figure 1.1: Total Primary Energy Supply in South Africa, 2014 (Fisher and Downes, 2015).

Furthermore, the rapid industrial development that causes an increase of the amount of produced wastewater which pollutes the environment (Bingtao and Li, 2011; Golob et al.; 2005). Specifically, mining wastewater effluent which can damage human health and ecosystems is becoming a serious worldwide problem (Schwarzenbach et al., 2010). The use of CFA in the synthesis of coagulant for AMD treatment is very useful in addressing the problem of CFA disposal into landfills and will also help to address the water pollution issue (Fan et al., 2003). Thus, this project using South African CFA to produce complex coagulant for AMD treatment is of interest in managing such both solid waste and wastewater effluent while sustaining the environment.

1.4 Research aims and objectives

The main aim of this project was to produce a complex coagulant from CFA and subsequently use it to treat AMD via the coagulation process. The main aim was achieved by the means of the following objectives:

- To characterize the CFA.
- To produce a complex coagulant by sulphuric acid leaching of iron, aluminium, silicon, magnesium, and calcium from CFA.

- To characterize and upgrade the complex coagulant to reach commercial standard as chemicals and substitute source of AMD treatment coagulant.
- To optimize the coagulant production process parameters.
- To determine the quality of AMD.
- To study the coagulation performance of the produced coagulant in treating AMD.
- To optimize the coagulation process parameters.

1.5 Thesis outline

The thesis outline shown below gives a brief description of what will be discussed in the chapters.

Chapter 1

This chapter presents a general introduction to the study and contains: research background and motivation, hypothesis, justification of the study, research aims and objectives and the thesis outline.

Chapter 2

This chapter provides the literature survey of the overall study. Extensive literature on CFA, characteristics, classification, genesis, production and disposal challenges of CFA, water and wastewater treatment coagulants, CFA-based coagulant synthesis process description, and mechanism of CFA-based coagulant synthesis are discussed. Moreover, coagulation process description and mechanism of waste water coagulation are reported.

Chapter 3

The methodology used, the design of the research, all the analytical methods and experimental procedures used in this work are described in this chapter. It also explains the operating conditions of the equipment used in the synthesis of CFA-based coagulant and in the waste water coagulation process, characterization of the material sample, the analyses of the produced coagulant and the treated waste water.

Chapter 4

This chapter presents the findings from the complex coagulant production process. Results from the characterization of the raw CFA, process optimization, characterization of the produced coagulant solution, comparative study of the raw with the treated CFA, and kinetics analysis are presented and discussed.

Chapter 5

Chapter 5 provides the findings from the coagulation process. Results from the characterization of the raw AMD, process optimization, comparative study of the synthesized coagulant with conventional ferric sulphate coagulant, and mechanisms of coagulation are presented and discussed.

Chapter 6

Results from the modelling behaviours of the processes of synthesis of complex coagulant by leaching of CFA and AMD treatment using the produced coagulant are presented and discussed in chapter 6.

Chapter 7

Summary of main findings of the research work is provided in chapter 7. Shortcomings and challenges encountered are presented while recommendations for future work are made.

Appendices

This section gives selected analysis and pertinent data.

References

Ahmaruzzaman, M., 2010. A review on the utilization of fly ash. *Progress in Energy and Combustion Science* 36, 327–363.

Ali, I., Asim, M. and Khan, T.A., 2012. Low cost adsorbents for the removal of organic pollutants from wastewater. *Journal of environmental management*, *113*, 170–183.

Apua, M.C., Simate, G.S., 2018. Characterization of coal fly ash for the production of coagulant for usage in wastewater treatment. *Materials Science and Technology (MS&T)*, 1512–1521.

Bian, Z., Dong, J., Lei, S., Leng, H., Mu, S., Wang, H., 2009. The impact of disposal and treatment of coal mining wastes on environment and farmland. *Environmental Geology* 58, 625–634.

Bidhendi, N.G.R., Torabian, A., Ehsani, H., Razmkhah, H., 2007. Evaluation of industrial dyeing wastewater treatment with coagulants and polyelectrolyte as coagulant aid. *Iranian Journal of Environmental Health Science & Engineering* 4 (1), 29–36.

Bingtao, L., Li, Z., 2011. Experimental Study on Wastewater Treatment by Fly ash Coagulant. *Environmental sciences*, 1363–1366.

Blissett, R.S., Rowson, N.A., 2012. A review of the multi-component utilisation of coal fly ash. *Fuel* 97, 1–23.

Dot.gov., 2015. Fly Ash Facts for Highway Engineers. Available at https://www.fhwa.dot.gov/pavement/recycling/fach01.cfm. Accessed March 2018.

Erol, M., Kucukbayrak, S., Ersoy-Mericboyu, A., 2008. Comparison of the properties of glass, glass–ceramic and ceramic materials produced from coal fly ash. *Journal of Hazardous Materials* 153, 418–425.

Fan, M., Brown, R.C., Leeuwen, J.H.V., Nomura, M., Zhuang, Y., 2003. The kinetics of producing sulfate-based complex coagulant from fly ash. *Chemical Engineering and Processing* 42, 1019–1025.

Fan, M., Brown, R.C., Wheelock, T.D., Cooper, A.T., Nomura, M., Zhuang, Y., 2005. Production of a complex coagulant from fly ash. *Chemical Engineering Journal* 106, 269–277.

Fisher, N. and Downes, G. 2015. South Africa Role Coal Energy Security. Available at http://www.iea.org/ciab/South_Africa_Role_Coal_Energy_Security.pdf. Accessed March 2018.

Golob, V., Vinder, A., Simonic, M., 2005. Efficiency of the coagulation/flocculation method for the treatment of dye bath effluents. *Dyes Pigments* 67, 93–97.

Hunter, M., 2018. South African Fly Ash Used to Help Build the Continent's Longest Suspension Bridge. *Applications, Science, and Sustainability of Coal Ash*, 1, 18–19.

Inada, M., Tsujimoto, H., Eguchi, Y., Enomoto, N. and Hojo, J., 2005. Microwave-assisted zeolite synthesis from coal fly ash in hydrothermal process. *Fuel*, 84 (12-13), 1482–1486.

Itskos, G, Koukouzas, N, Vasilatos, C, Megremi, I, Moutsatsou, A., 2010. Comparative uptake study of toxic elements from aqueous media by the different particle size-fractions of fly ash. *Journal of Hazardous Materials* 183, 787–792.

Iyer, R.S., Scott, J.A., 2001. Power station fly ash—a review of value-added utilization outside of the construction industry. *Resources, Conservation and Recycling* 31, 217–228.

Li, L., Fan, M., Brown, R.C., Koziel, J.A., Leeuwen, J. H., 2009. Production of a new wastewater treatment coagulant from fly ash with concomitant flue gas scrubbing. *Journal of harzardous Materials* 162, 1430–1437.

Li, H., Liu, S., Zhao, J. and Feng, N., 2016. Removal of reactive dyes from wastewater assisted with kaolin clay by magnesium hydroxide coagulation process. *Colloids and Surfaces A: Physicochemical and Engineering Aspects*, 494, 222–227.

Lissianski, V.V., Maly, P.M., Seeker, W.R. and Zamansky, V.M., General Electric Co, 2009. *Method for removal of mercury emissions from coal combustion*. U.S. Patent 7,514,052.

Manoharan, V., Yunusa, I.A.M., Loganathan, P., Lawrie, R., Skilbeck, C.G., Burchett, M.D., Murray, B.R., Eamus, D., 2010. Assessments of Class F fly ashes for amelioration

of soil acidity and their influence on growth and uptake of Mo and Se by canola. *Fuel* 89, 3498–3504.

Matjie, R.H., Bunt, J.R., van Heerden, J.H.P., 2005. Extraction of alumina from coal fly ash generated from a selected low rank bituminous South African coal. *Minerals Engineering* 18(3), 299–310.

Menezes, J.C.S.S., Silva, R.A., Arce, I.S., Schneider, I.A.H., 2010. Production of a polyalumino-iron sulphate coagulant by chemical precipitation of a coal mining acid drainage. *Minerals Engineering* 23, 249–251.

Mishra, M.K., Karanam, U.M.R., 2006. Geotechnical characterisation of fly ash composites for backfilling mine voids. *Geotechnical and Geological Engineering* 24, 1749–1765.

Muhammad, S., Saputra, E., Sun, H., Izidoro, J.D.C., Fungaro, D.A., Ang, H.M., Tadé, M.O. and Wang, S., 2012. Coal fly ash supported Co 3 O 4 catalysts for phenol degradation using peroxymonosulfate. *Rsc Advances*, 2 (13), 5645–5650.

Pandey, V.C., Singh, N., 2010. Impact of fly ash incorporation in soil systems. *Agriculture, Ecosystems and Environment* 136, 16–27.

Peng, F., Liang, K.M., Hu, A.M., 2005. Nano-crystal glass–ceramics obtained from high alumina coal fly ash. *Fuel* 84, 341–346.

Rafieizonooz, M., Mirza, J., Salim, M.R., Hussin, M.W. and Khankhaje, E., 2016. Investigation of coal bottom ash and fly ash in concrete as replacement for sand and cement. *Construction and Building Materials*, *116*, 15–24.

Rubel, A., Andrews, R., Gonzalez, R., Groppo, J., Robl, T., 2005. Adsorption of Hg and NOx on coal by-products. *Fuel* 84, 911–916.

Schwarzenbach, R.P., Egli, T., Hofstetter, T.B., Von Gunten, U. and Wehrli, B., 2010. Global water pollution and human health. *Annual Review of Environment and Resources*, *35*, 109–136.

Semerjian, L., Ayoub, G.M., 2003. High-pH–magnesium coagulation–flocculation in wastewater treatment. *Advances in Environmental Research*, 7(2), 389–403.

Siriwardane, H.J., Kannan, R.S.S., Ziemkiewicz, P.F., 2003. Use of Waste Materials for Control of Acid Mine Drainage and Subsidence. *Journal of Environmental Engineering* 129 (10), 910–915.

South Africa-International Energy Agency, 2017. South Africa. Available at http://www.iea.org/ciab/South_Africa_Role_Coal_Energy_Security.pdf. Accessed 08 August 2017.

Vadapalli, V.R.K., Klink, M.J., Etchebers, O., Petrik, L.F, Gitari, W., White, R.A., Key, D., Iwuoha, E., 2008. Neutralization of acid mine drainage using fly ash, and strength development of the resulting solid residues. *South African Journal of Science* 104, 317–322.

Viraraghavan, T., 1982. Ash Utilization in Water Quality Management. Available at https://web.anl.gov/PCS/acsfuel/preprint%20archive/Files/38_3_CHICAGO_08-93_0939.pdf. Accessed March 2018.

Yan, L., Wang, Y., Ma, H., Han, Z., Zhang, Q. and Chen, Y., 2012. Feasibility of fly ash-based composite coagulant for coal washing wastewater treatment. *Journal of hazardous materials*, 203, 221–228.

Yao, Z.T., Xia, M.S., Sarker, P.K., Chen, T., 2014. A review of the alumina recovery from coal fly ash, with a focus in China. *Fuel* 120, 74–85.

Yao, Z.T., Ji, X.S., Sarker, P.K., Tang, J.H., Ge, L.Q., Xia, M.S. and Xi, Y.Q., 2015. A comprehensive review on the applications of coal fly ash. *Earth-Science Reviews, 141*, 105–121.

CHAPTER 2

LITERATURE REVIEW

2.1 Introduction

This chapter provides the literature survey, an overview upon coal fly ash (CFA), CFA coagulant production and its use in water and wastewater treatment, acid mine drainage (AMD) and its treatment, AMD treatment using CFA coagulant, equilibrium approach, kinetics of reactions, information from anterior works on CFA coagulant preparation and wastewater treatment using CFA coagulant.

2.2 Coal fly ash

Combustion of bituminous and sub-bituminous coal and lignite for electricity production in thermal power plants produces solid wastes such as fly ash, bottom ash, boiler slag and flue gas desulphurization materials, which are generally known as coal combustion by-products (Jala and Goyal, 2006). Ash that falls into the bottom combustion chamber is called bottom ash, while fly ash is the fine particle (with diameter from 0.5 to 100 μm) that is transported from the combustion chamber with flue gas. Generally, fly ash is taken by electrostatic precipitators or other particle filtration equipment before the flue gases reach the pipes of coal-fired power stations. Nearly 70% of the byproduct consists of fly ash, which is the most difficult to handle. Approximately 10–12% of the by-product is bottom ash, which individual particles are much larger than fly ash particles. Bottom ash particle size typically ranges from fine sand to gravel in size. The combination of fly ash with bottom ash is known as coal ash (Kalyoncu, 2000; Li et al., 2009; Fan et al., 2005).

2.2.1 Occurrence and genesis of minerals in coal fly ash

Since it is a sedimentary rock, coal is a complex mixture of organic and inorganic matter. A significant portion of the coal may be inorganic in nature and difficult to remove from the organic material. The inorganic matter comprises minerals, and amorphous material

constituents which have detrital and authigenic origins (Vassilev and Vassileva, 1996). Mainly there are four groups of inorganic constituents for coal (Kleinhans, 2018):

1) **Dissolved salts** and other inorganic substances in the moisture of coal: they can come from contact with seawater, and are contained in the pore water. Elements are generally found as cations Na^+, Ca^{2+}, K^+, and anions $H_2PO_4^-$, HPO_4^{2-}, Cl^-, $Si(OH)_3O^-$, or SO_4^{2-}.
2) **Organically-bound ash-forming compounds**: inorganic elements that are combined with organic compounds. Usually these are cations comprising Na^+, K^+, Mg^{2+}, Ca^{2+}, Al^{3+}, and Fe^{3+}. A further group consists of covalently bonded non-metals such as organic Cl, P or S.
3) **Included minerals** are in the form of distinct inorganic particles inside the coal matrix, crystalline or non-crystalline, representing mineral components. These included mineral particles are often finely dispersed and intimately mixed with the organic substance and are therefore difficult to remove.
4) **Excluded minerals** are released from the organic structure. This can occur during the coalification process or during milling in the power plant. Generally, excluded mineral particles are pyrite, quartz or clay minerals.

The principal physicochemical processes of coal transformation during combustion consists of burning; volatilization of some compounds; decomposition; formation of new phases; transformation of some minerals and phases, or of the whole residue, to a partial or complete melting (Sarkar et al., 2005). The CFA is the residue resulting from the inorganic and organic matter during combustion of the coal. Some of the pre-existing coal minerals do not undergo physicochemical transformations during combustion. But several of original minerals in coal undergo important alteration and change; hence they do not represent the pre-existing minerals and phases in coal. Some minerals in CFA have an artificial source that results from the crystallization of liberated components from organic matter. Thus, CFA is a composite inorganic mixture that contains (Vassilev and Vassileva, 1996):

- Primary minerals which are the pre-existing minerals in coal that have not undergone phase changes including silicates and oxides.
- Secondary phases which are new phases produced during combustion, such as oxyhydroxides, silicates; some carbonates, sulphates and amorphous phases.

- Tertiary minerals consisting of new minerals formed during CFA storage, usually hydroxides and sulphates.

The CFA which is produced by oxidation and combustion of coal differs in amount and origin from the inorganic and mineral constituents present in the raw coal. Minerals in CFA belong to different classes than those found in the raw coal. Their variety in CFA generally consists of silicates and oxyhydroxides, to a lesser amount sulphates and carbonates, and more rarely phosphates and other mineral species (Sarkar et al., 2005). The approximate quantitative distribution of mineral classes in CFA is mainly, in decreasing order of significance: silicates > oxyhydroxides > sulphates > carbonates > phosphates > others. Generally, the most abundant minerals in the crystalline matter of CFA are quartz, kaolinite, plagioclase, K-feldspar, Ca silicates, hematite, corundum, lime, portlandite and anhydrite. Typically, sulphide minerals are not present in CFA (Vassilev and Vassileva, 1996).

The mechanism of coal combustion mineral matter transformation consists firstly of the conversion of the coal to char as seen in Figure 2.1. At lot higher temperatures, the char materials burn out. At higher temperature, the fine included minerals progressively reduce and are liberated from inside the char as it fragments. At this stage, the minerals decompose and convert to volatile maters and eventually condense to form solid ash particles (Sarkar et al., 2005). Homogeneous condensation produces ash particles between 0.02 and 0.2 µm and fragmentation of included mineral matter leads to the formation of particles between 0.2 and 10 µm. The excluded mineral mater goes through a succession of complex transformations to produce predominantly spherical particles in the size range 10-90 µm (Sarkar et al., 2005; Spears and Lee, 2015).

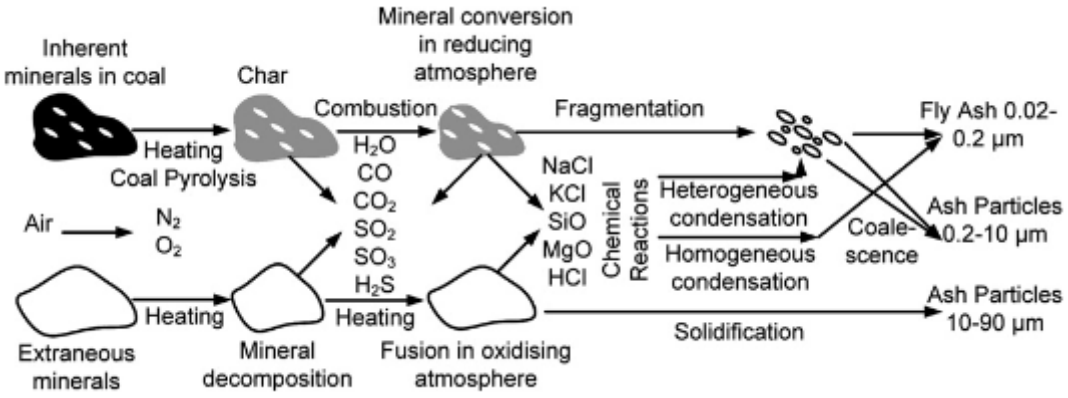

Figure 2.1: Mechanism of CFA formation during coal combustion (Blisset and Rowson, 2012).

The CFA is produced during the gasification process, where coal is fed into fluidized bed operating at higher temperature around 1200 ^{o}C. Figure 2.2 shows the schematic diagram of the CFA production. The CFA is a waste produced when coal reacts with the steam fed from the bottom side of the fluidized bed. As seen in the figure below, the gasification products leave from the top of the bed.

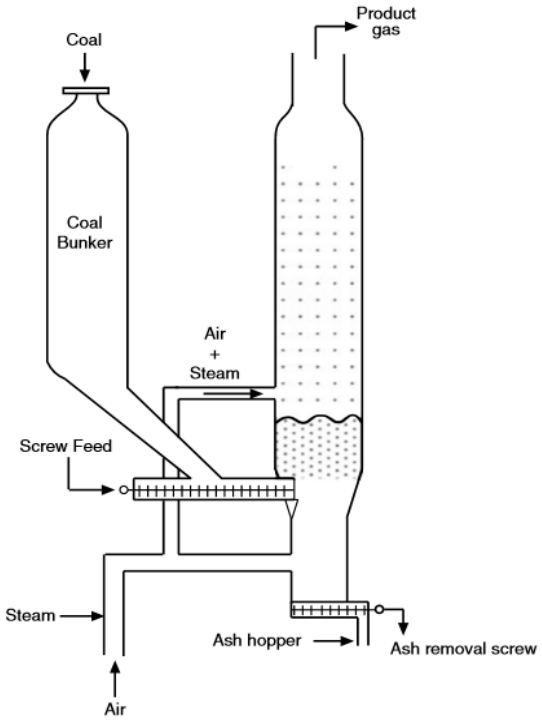

Figure 2.2: Schematic diagram of the coal fly ash production from coal-fired power plant (Basu, 2006).

2.2.2 Characteristics of coal fly ash

Physical properties

The CFA physical properties depend on the type of equipment used for collecting CFA. In general, CFA consists of fine spherical particles commonly ranging in diameter from 0.5 to 100 µm (Li et al., 2009). CFA particles exhibit smooth surface texture and are inhomogeneous (Fan et al., 2005). By studying the micro and nano-chemistry of CFA, Giere et al. (2003), showed that single CFA particles are hollow, empty spheres (cenospheres) or filled with smaller amorphous particles and crystals (plerospheres).

The CFA colour generally varies for each power plant and coal source. Depending on its chemical and mineral constituents, CFA ranges in colour from tan to dark grey (Figure 2.2). Tan and light colours are usually associated with elevated lime (CaO) content. A brownish colour is usually associated with the iron content. A dark grey to black colour is typically attributed to high unburned carbon content (Fan et al., 2005). Usually, CFA has a bulk density of 1.01–1.43 g/cm3, and the pH ranges from 4.2–11.8. The CFA pH largely depends on the sulphur content of the parent coal (Li et al., 2009).



Figure 2.3: Typical colours of coal fly ash (ACAA, 2015).

Chemical composition

The CFA, produced at 1200–1700 ^{o}C from different inorganic and organic constituents of the coal (Blisset and Rowson, 2012), is one of the most complex anthropogenic materials that can be characterized due to the range of the variety of components. Around 316 individual minerals and 188 mineral groups have been identified in various CFAs (Vassilev and Vassileva, 2005).

The CFA chemical composition is affected by the geographical and geological factors of the coal deposit, coal rank, boiler operation conditions, and fuel gas pollution control technology applied (Li et al., 2009; Fan et al., 2005). When coal is burned, the mineral matter forms fly ash that contains significant amounts of aluminium oxide (Al_2O_3), iron oxides (Fe_2O_3), silicon dioxide (SiO_2) (which are amorphous and crystalline), and calcium oxide (CaO) (Li et al., 2009). Besides, constituents can also include one or more of the following elements or substances found in trace concentrations (up to hundreds ppm): magnesium, manganese, chromium, hexavalent chromium, arsenic, cadmium, beryllium, mercury, boron, cobalt, lead, selenium, vanadium, strontium, molybdenum, potassium, sodium, carbon, sulphur, and thallium, along with very small concentrations of dioxins and PAH (polycyclic aromatic hydrocarbon) compounds (Sun et al., 2011). In general, oxides in CFA are found in the order: $SiO_2 > Al_2O_3 > Fe_2O_3 > CaO > MgO > K_2O > Na_2O > TiO_2$ (Blissett and Rowson, 2012). Normally, the constituents are reported in the form of compounds, which are principally mixtures of sulphates, oxides and silicates. Most sulphates are the product of the reaction between pyrite and oxygen (Fan et al., 2005; Sun et al., 2011). In CFA, pyrite is the major source of iron oxide. The silicates result from the shale and clay minerals. The calcium and magnesium oxides originate from the decomposition of carbonate minerals (Li et al., 2009; Fan et al., 2005).

The CFA mineralogy is very diverse. CFA has a complex heterogeneous mixture of amorphous and crystalline phases with an aluminosilicate glass matrix, together with crystalline quartz, mullite and the iron oxides hematite, magnetite and/or maghemite as the main identified phases (Dwivedi and Jain, 2014). Other phases often found are free lime, cristobalite, periclase, halite, calcite, anhydrite, portlandite, sylvite, anatase, and rutile. In Ca-rich CFA's, the Ca-bearing minerals gehlenite, anorthite, akermanite and various calcium aluminates and calcium silicates identical to those encountered in cement can be

identified. The content of mercury can reach 1 ppm, but is commonly included in the range 0.01–1 ppm for bituminous coal. Also, the concentrations of other trace elements vary according to the type of coal burned to form it (Vassileva et al., 2003). Based on the dominance of certain main elements, an experimental formula for CFA has been proposed as follows (Wang and Wu, 2006),

$Si_{1.0}Al_{0.45}Ca_{0.51}\ Na_{0.047}Fe_{0.039}Mg_{0.020}K_{0.013}Ti_{0.011}$.

Classification

Two categories of CFA are recognized for coal combustion, Class F fly ash and Class C fly ash. The main difference between these categories is the quantity of calcium, silica, alumina, and iron in the fly ash (Wang and Wu, 2006):

- ***Class F coal fly ash***

This type of CFA is typically produced from the combustion of anthracite or bituminous coal. This fly ash contains less than 7% lime (CaO) and contains more silica, alumina, and iron oxide (Spears and Lee, 2015; Iyer and Scott, 2001). This CFA is generally composed of aluminosilicate glass and mainly do not have any crystalline compounds of calcium (Manz, 1999; Sumer, 2012). Class F fly ash is recognized as a pozzolanic material. A pozzolan is a siliceous, or a siliceous and aluminous, material that has no intrinsic cementitious property (Blissett and Rowson, 2012; Alam and Akhtar, 2011). Containing pozzolanic properties, the glassy silica and alumina of class F fly ash needs a cementing agent such as hydrated lime mixed with water to react and form cementitious products (Iyer and Scott, 2001).

- ***Class C coal fly ash***

The burning of lignite and sub-bituminous coal usually produces type C fly ash which generally contains more CaO (15–30%) (Iyer and Scott, 2001). This CFA consists of calcium aluminosilicate glass with substantial amount of crystalline calcium compounds (Manz, 1999; Sumer, 2012). The high contents of CaO and sulfate (SO_4) of many of the lignite and sub-bituminous coal fly ashes results in the formation of cementitious products. In the presence of water, Class C fly ash becomes hard and gets stronger over time. The self-cementing Class C fly ash does not need an activator (Iyer and Scott, 2001, Blissett

and Rowson, 2012). The general concentration ranges as a function of coal type is presented in Table 2.1.

Table 2.1: Typical percent range of chemical composition of coal fly ash by coal type (Blissett and Rowson, 2012).

Compounds (wt. %)	**Bituminous**	**Sub-bituminous**	**Lignite**
SiO_2	20-60	40-60	15-45
Al_2O_3	5-35	20-30	10-25
Fe_2O_3	10-40	4-10	4-15
CaO	1-12	5-30	15-40
MgO	0-5	1-6	3-10
Na_2O	0-4	0-2	0-6
K_2O	0-3	0-4	0-4
SO_3	0-4	0-2	0-10
LOI*	0-15	0-3	0-5

*LOI: Loss on Ignition

2.2.3 World coal fly ash production

The global production of CFA was estimated to increase exponentially to an approximation of 750 million tons per annum (Vinai et al., 2013; Heidrich et al., 2013; Gollakota et al., 2019). In addition, worldwide CFA recycling average was estimated to be near 25% in 2008 (Wang, 2008). This clearly indicates that a significant amount of CFA must be disposed of properly. This is typically done by throwing away the ash to landfill or by arranging it in large ash lagoons. It was known that these very big lagoons break and provoke potential environmental issues as well as distress to the local community (Blissett and Rowson, 2012). In recent years, the major CFA producing countries are China 395 Mt, North America 118 Mt, India 105 Mt, Europe (EU 15) 52.6 Mt, Africa 31.1 Mt, and Middle East as minor contributor. Table 2.2 reports on estimated annual production by country.

Table 2.2: Estimated CFA annual production by country 2010 (Heidrich et al., 2013).

Country/Region	CFA production Mt
China	395.0
United State of America	118.0
India	105.0
Europe (EU 15)	52.6
Middle East and Africa	32.2
Russia	26.6
Australia	13.1
Japan	11.1
Canada	6.8
Other Asia	16.7
Total	777.1

2.2.4 Waste and disposal challenges

Disposal and management of CFA is a major issue in coal thermal power plants. The CFA discharges from a variety of coal combustion units contain an extensive range of composition. All the elements below atomic number 92 are present in CFA. A 500 MW coal combustion power plant releases 500 tons fly ash, 70 tons NO_2, and 200 million tons SO_2 almost every day. Coal fly ash is considered as a source of air pollution. Tiny particles of CFA reach the lungs and remain there for long periods of time; they act like increasing poisons. The submicron particles go deeper into the lungs and are deposited on the alveolar walls where the metals could be transported to the blood plasma across the cell membrane. Silica (40–73%) which is the remaining particles causes silicosis. Heavy metals (Ni, Cd, Sb, As, Cr, Pb, etc.) generally found in CFA are toxic in nature (Senapati, 2011). Globally, CFA is disposed-off either in a wet, slurried, or dry state (Heidrich et al 2013). Researches have shown that wet disposal of this waste does not protect the environment from migration of metal into the soil and heavy metals cannot be degraded biologically into non-toxic products like other organic waste. With the current practice of CFA disposal in ash ponds (usually in the form of slurry), the whole land necessary for ash disposal would be almost 82,200 ha by the year 2020 at an estimated 0.6 ha per MW. CFA can be considered as a by-product rather than waste (Dwivedi and Jain, 2014).

2.2.5 Uses of coal fly ash

From an electricity production aspect, CFA is a waste and source of air and water pollution till recent past, while from a coal use aspect, CFA is a resource material to be completely used and exploited. Thermal power producers are now looking for ways to valorise CFA (Kikuchi, 1999; Iyer and Scott, 2001). Possible utilizations of CFA based on its properties can be the following:

Cement: CFA discharged from power plant is used at present as a substitute material for cement and sand concrete, due to its pozzolanic properties (Sumer, 2012; Gonzalez et al., 2009).

Asphalt concrete: Asphalt concrete is a composite material consisting of a mineral aggregate and an asphalt binder. Both Class C and Class F fly ash may normally be used as a mineral filler to fill the cavities and give contact points between bigger aggregate particles in asphalt concrete mixes. This application is utilized in combination or as a replacement for, other binders such as cement or hydrated lime (Dwivedi and Jain, 2014; Gupta and Singh, 2013). The CFA has been shown to provide better resistance to stripping for asphalt pavements, due to its hydrophobic nature. In addition, the use of CFA raises the rigidity of the asphalt matrix (Alam and Akhtar, 2011).

Bricks: Recent investigations suggest that CFA can find better application in the manufacture of building bricks. CFA bricks have several advantages over the conventional burnt clay bricks (Senapati, 2011).

Roller compacted concrete: One more application of utilizing CFA is in roller compacted concrete dams. Several dams in the US have been constructed with high CFA contents. CFA decreases the heat of hydration permitting thicker placements to occur (Dwivedi and Jain, 2014).

Flowable fill: Flowable fill (also called controlled low strength material, or CLSM) is used as self-leveling, self-compacting backfill material instead of compacted earth or granular fill. Flowable fill consist of mixtures of cement and filler material, and can contain mineral admixtures (Nhan et al., 1996; Yao et al., 2015). Mines are backfilled to avoid rock falling. Since long time river sand and mill tailings were extensively used as back filling materials.

Studies showed that CFA is suitable to be used as backfill material because it has pozzolanic properties and also for its suitability as a cement substitute (Siriwardane et al., 2003; Mishra and Karanam, 2006).

Embankment: To certain degree, CFA properties are unique as an engineering material. Different to typical soils used for embankment construction, CFA has a large homogeneity coefficient consisting of clay-sized particles. Engineering properties that will influence CFA application in embankments consist of grain size distribution, compaction characteristics, permeability, compressibility, shear strength, and frost susceptibility. Almost all CFA used in embankments are Class F fly ashes (Senapati, 2011).

Soils stabilization: Soil stabilization process consists of the permanent chemical and physical modification of soils to improve their physical properties. Stabilization can enhance the shear strength of a soil and/or control the shrink-swell properties of a soil, consequently increasing the load-bearing capacity of a sub-grade to support pavements and foundations. A range of chemical additives such as Portland, cement CFA, and lime can be used for stabilization (Pandey and Singh; 2010).

Agriculture: CFA can be used as agricultural fertilizer and soil amendments. Because of its alkalinity, CFA can be used to improve the low pH of acidic soils (Jala and Goyal, 2006; Yao et al., 2015). This is explained by the release of minerals such as Na, Ca, Al, and OH ions from CFA (Pandey and Singh, 2010). Typically type C CFA (i.e. ash with high CaO content: > 15%) is used to raise the pH of acidic soil. In addition, due to its water absorption capacity, CFA can be utilized to enhance the water holding capacity of soils and hence the quantity of available water to the plant (Manoharan et al., 2010). In addition, due to its water absorption capacity, CFA can be utilized to enhance the water holding capacity of soils and hence the quantity of available water to the plant (Menzies and Aitken, 1996).

Catalyst: SiO_2 and Al_2O_3 are the major CFA components. These oxides are formed after high temperature combustion, with high thermal stability which makes CFA a good catalyst support. Besides, minor components of other metal oxides such as Fe_2O_3, CaO, K_2O, TiO_2, Na_2O, and MgO, can be used as active catalyst components. So, it is assumed that CFA can be used as catalyst and/or catalyst support for many catalytic reactions (Wang, 2008; Na et al., 2006).

Geopolymers: Geopolymerization is the alkali-activation of aluminosilicates consisting of a chemical reaction between aluminosilicate oxides and alkali metal silicate solutions under strongly alkaline conditions. This produces amorphous or semi-crystalline polymeric structures of Si-O-Al bonds (Panias et al., 2007). Geopolymers show good chemical, physical, and mechanical properties including good thermal stability, fire and chemical resistance, low density, micro and nano-porosity, low shrinkage, surface hardness, high mechanical strength, and durability. Due to these properties, geopolymers are considered as potential alternative material for industrial uses such as construction (e.g. flooring tiles, ceiling, door shutters, etc.), mining, metallurgy, transport, and aerospace (Barbosa and MacKenzie, 2003).

Metal matrix composites: Due to the low density of CFA, it can be mixed with molten metal and cast to reduce total weight and density. Study is underway to include CFA into lead acid batteries in a lead calcium tin CFA composite in order to reduce weight of the battery (Iyer and Scott, 2001).

Glass, glass-ceramics, and ceramics materials: Silicate-based natural raw materials (clays) are highly consumed by the ceramic, glass and glass–ceramic industry. However nowadays there is a worldwide deficiency of clay to produce ceramic materials (Haiying et al. 2007). There is a need to find other materials to substitute clay. Due to various oxide constituents, such as Al_2O_3, SiO_2, Fe_2O_3, and CaO, CFA can be used to replace raw materials for the manufacture of glass, glass–ceramics, and ceramics products (Erol et al., 2008; Peng et al., 2005).

Zeolite production: Zeolites include of a significant group of crystalline aluminosilicate minerals which possess an infinitely extending three-dimensional anion network consist of $(SiO_4)^{4-}$ and $(AlO_4)^{5-}$ tetrahedral that link at the corners by their shared oxygen atoms. The rise of the special properties of zeolitic materials is given by the three-dimensional nature of the structure. The internal channel and the empty space of the network let easy access of molecules leading to fast diffusion rates. This makes zeolites particularly appropriate materials for adsorption processes (Querol et al., 2002). The replacement of Si(IV) by Al(III) in the structure is what accounts for the overall negative charge; this indicates that the zeolites have the potential to show high cation exchange abilities leading to possible uses in ion exchange or as a molecular sieve. A source of Si and Al ions and an alkaline

environment are required for zeolites synthesis. The CFA has been used as source of Al and Si ions for zeolites synthesis (Querol et al., 2002; Inada et al., 2005).

Adsorbent: Several studies have been conducted on the use of CFA for adsorption of individual contaminants in flue gas (e.g. SO_x, NO_x, m-xylene and toluene vapours, and mercury) (Davini, 1995; Davini, 1996; Rubel et al., 2005; Rovatti et al., 1988; Karatza et al., 1998; Ahmaruzzaman, 2011). Alternatively, water treatment might be another interesting option. (Panday et al., 1985; Ahmaruzzaman, 2011; Wang and Wu, 2006). Recently the utilization of mixed CFAs with different chemical compositions was assessed to remove a variety of different metal from waste effluents: Cd, Zn, Cu, Ni, Pb, Cr, and Mn (Mohan and Gandhimathi, 2009; Cho et al., 2005; Itskos et al., 2010; Hequet et al., 2001).

Metals recovery: Usually aluminium is extracted from bauxite by the Bayer process. However, this process cannot cover the aluminium demand. Therefore, CFA could be an alternative source of aluminium. CFA also contains several other metals, some of which (iron and titanium) can be extracted as co-products (Kelmers et al., 1981).

Coagulant production: CFA is rich in Al_2O_3 and Fe_2O_3 which are essential raw materials for the production of coagulants for water and wastewater treatment (Li et al., 2009; Ahmaruzzaman, 2010; Fan et al., 2005).

2.3 Water and wastewater treatment coagulants

Treatment of the huge amount of wastewater released from various industries involves millions of tons of coagulants that are both economical and efficient in removing different contaminants. Chemically, water and wastewater treatments coagulants are either polymers or metallic salts. Polymers (polyelectrolytes such as polyacrylamide derivatives) are synthetic organic compounds made up of a long chain of smaller molecules (Bratby, 2006). They carry functional groups such as quaternary amine or carboxyl functionalities in the repeat units. The molecular weight of the polymer varies from a few thousands to millions of grams per mole. Based on the electric charge displayed by the polymer coagulants in the aqueous phase, polymers are classified as cationic (positively charged), anionic (negatively charged), and non-ionic (neutrally charged) coagulants (Choi et al., 2001; Bhatia et al., 2007). Metallic salts are inorganic compounds. Salts of iron and aluminium are two main inorganic coagulants used in water and wastewater treatment. Iron and aluminium-based

coagulants include ferric sulphate, ferrous sulphate ($FeSO_4.7H_2O$), ferric chloride ($FeCl_3.6H_2O$), ferrous chloride ($FeCl_2$), poly-ferric sulphate, aluminium sulphate (alum) ($Al_2(SO_4.14H_2O$), aluminium chloride, poly-aluminium sulphate, poly-aluminium chloride, and poly-alumino-iron sulphate (Fytianos et al., 1998; Menezes et al., 2010).

2.3.1 Ferrous sulphate

Ferrous Sulphate is acidic with green to brownish yellow in colour and existing in granules, crystals and lumps. Generally, it is fed in solution form with strength of 4 to 8 %. The pH value and alkalinity of natural water are very low to react with ferrous sulphate to form the wanted ferric hydroxide floc, since the reaction involves oxidation by the dissolved oxygen in the water, which does not happen when pH value is less than 8.5 (Nickel, 1946; Aziz et al., 2007; Leopold and Freese, 2009). Thus, it is necessary to add lime with ferrous sulphate to cause coagulation. For this reason, ferrous sulphate is not used in coagulation of high coloured water, which coagulates best at pH values less than 6.0. The concentration of lime required is almost 0.27 mg/L to react with 1.0 mg/L of ferrous sulphate and generally, the floc formed by the reaction of lime and ferrous sulphate is feathery and fragile, but has a high specific gravity (Nickel, 1946).

2.3.2 Ferric sulphate

Ferric sulphate is obtainable as a commercial water treatment coagulant in the form of an anhydrous material that can be transported and stored in wooden barrels. It readily dissolves in a limited amount of warm water so a special solution container must be used with chemical feeders, in which 1-part ferric sulphate by volume is dissolved in 2 parts waters to produce a solution of around 40% strength (Nickel, 1946). Ferric sulphate is an effective primary coagulant based on trivalent iron (Fe^{3+}), and is excellent in applications such as drinking water production, wastewater treatment, phosphorus removal uses. The products are also efficient in preventing odour and corrosion by controlling the formation of hydrogen sulphide (Aziz et al., 2007).

2.3.3 Aluminium sulphate

Aluminium sulphate ($Al_2(SO_4.14H_2O$), ordinarily known as alum, is one of the earliest, and still the most widely used coagulant. It is acid compound and light tan to grey colour

existing in blocks, lumps, and powder with a density of 1000–1100 kg/m^3 and specific gravity of 1.25 to 1.36. Aluminium sulphate can be bought in liquid form or dry form which readily dissolves with water (Aziz et al., 2007; Baskan and Pala, 2010). Aluminium sulphate reacts with water to form positively charged ions. The ions might have charges as high as +4, but are generally trivalent (with a charge of +3). The trivalent ion resulting from aluminium sulphate makes this a very effective coagulant (Krupinska, 2014).

Many factors influence the reaction between aluminium sulphate and natural constituents of various waters, so it is impossible to determine accurately the dosage of aluminium sulphate that will react with a given dosage of alkalinity. Theoretically, 1 mg/L of aluminium sulphate reacts with 0.45 mg/L of natural alkalinity expressed as $CaCO_3$, 0.30 mg/L of 85% quicklime as CaO, and 0.35 mg/L of 95% hydrated lime as $Ca(OH)_3$. Generally, aluminium sulphate is fed in solution form with 8 to 10% strength coagulant (Krupinska, 2014). If no alkali is added, then the acidity of 1.0 mg/L aluminium sulphate will decrease the natural alkalinity of the raw water by 0.45 mg/L. This lowering of natural alkalinity is wanted in most cases since the range of pH for coagulation of turbid waters being 5.7–8.0. Thus, the alkali required for corrosion prevention would be added to the filtered water, the required concentration being influenced but not governed by the aluminium sulphate concentration (Alaerts et al., 1982).

When compared with ferrous and ferric sulphates, 1 mg of aluminium sulphate will produce around 0.26 mg of insoluble $Al(OH)_3$ precipitates and will consume around 0.51 mg of alkalinity (expressed as $CaCO_3$). 1 mg of ferrous sulphate will produce around 0.64 mg of insoluble $Fe(HCO_3)_2$ precipitates and will consume 0.56 mg of alkalinity. 1 mg of ferric sulphate will produce around 0.54 mg of insoluble $Fe(OH)_2$ precipitates and will consume 0.75 mg of alkalinity. Due to the consumption of alkalinity, CO_2 is produced during coagulation. The pH value can also be decreased after the coagulation process, depending on the concentration of coagulant used and the total alkalinity in the raw water (Alaerts et al., 1982; Aziz, 2007; Krupinska, 2014).

2.3.4 Advantages and disadvantages of ferric and aluminium sulphates

The Advantages and disadvantages of ferric and aluminium sulphates (Sun et al., 2011) are presented in Table 2.3.

Table 2.3: Advantages and disadvantages of iron and aluminium coagulants.

Chemicals	Advantages	Drawbacks
Ferric sulphate or ferric chloride	- Best removal of organic and inorganic suspended solids. - Ferric coagulants can be used in colour removal at the high pH values required for the removal of manganese and iron. - Ferric hydroxide floc is produced at low pH values, so that coagulation is possible with ferric sulphate at pH values as low as 4.0. - Ferric hydroxide is insoluble within a wide range of pH values than aluminium hydroxide excluding the range of 7.0 to 8.5. - The floc produced with ferric coagulants is heavier than aluminium sulphate floc. - At high pH values, the ferric hydroxide floc does not redissolve. - Suitable for use in the lime-softening process (pH 9) - High iron residual is easy to detect. - pH sensitivity is slightly less than aluminium sulphate.	- Lower efficiency for attracting organic suspended solid than aluminium sulphate. - Rapid mixing is dangerous for correct functioning. - Must be used in the range of pH 5.5 to 8.5, generally requiring alkaline additives to achieve optimum pH. - Typically, large dose required. - Incorrect dosages cause reddish colour and high iron residual. - Very acidic, full protective equipment must be worn. - Sludge (brown) is aesthetically unpleasing
Aluminium sulphate	- Very effective at attracting inorganic suspended solids. - Less acidic (protective gear is recommended)	- Rapid mixing is dangerous to good functioning. - Non-optimal pH leads to excessive dose requirements, must be used in the range of pH 5.5 to 7.5, generally requiring alkaline additives to achieve optimum pH. - At lower temperatures, performance significantly decreases. - Effectiveness is poor for removal organic suspended solids. - Large concentration relatively required when used alone. - Lower DOC removal. Incorrect doses cause high aluminium residual and can cause a health risk.

2.4 Synthesis of coal fly ash-based coagulant

Due to distinct advantages and disadvantages of iron and aluminium-based coagulants for water and wastewater treatment, a complex coagulant composed of iron, aluminium, silicon, magnesium, and calcium constituents is ideal, as it has the advantages of both coagulants and avoids or lessen their disadvantages (Sun et al., 2011). Iron, aluminium, silicon, magnesium, and calcium salts-based CFA coagulant synthesis are commonly carried out using sulphuric acid (H_2SO_4) and/or hydrochloric acid (HCl) solutions (Bingtao and Li, 2011). The responsiveness of CFA to dissolution processes of its metals is determined by its composition (e.g. metal content and mineralogical composition) (Siedel and Zimmels, 1998). Usually a solution of iron-aluminium sulphates complex coagulant contains 1.5% iron and 3.0% aluminium (Fan et al., 2005).

This work intends to produce iron and aluminium sulphates complex coagulant from CFA. H_2SO_4 solution will be used to leach aluminium and iron in the CFA sample. Compared to HCl, H_2SO_4 was chosen because of it is cheaper than HCl (1L of H_2SO_4 costs $14.55 while 1L of HCl costs $23.75). Moreover, an investigation on the feasibility of the produced coagulant on the treatment of mining wastewater will be done.

2.5 Chemistry of leaching reactions

In general, most of the leaching process involves the formation of complex ion between the metal and the complexing agent or ligand in aqueous medium. Complexing reactions are presented as follows (Weiss, 1985; Senanayake, 2004),

$$M + L \leftrightarrow ML \qquad K_1 = \frac{[ML]}{[M][L]} \tag{2.1}$$

$$ML + L \leftrightarrow ML_2 \qquad K_2 = \frac{[ML_2]}{[ML][L]} \tag{2.2}$$

$$ML_{n-1} + L \leftrightarrow ML_n \qquad K_n = \frac{[ML_n]}{[ML_{n-1}][L]} \tag{2.3}$$

The overall reaction can be written as

$$M + nL = ML_n \qquad \beta_n = \frac{[ML_n]}{[M][L]^n K_1 K_2 K_n} \tag{2.4}$$

with *M*: the metal ion, *L*: the ligand, and *n*: a maximum number of ligands per metal ion in the dissolution process.

Economically dissolution reactions are time controlled. Time is needed to perform the wanted recovery. The leaching parameters must be optimized in order to perform a selective maximum leaching rate with minimum time and cost. Leaching parameters are: particle size, stirring speed, reagent concentration, redox potential, temperature, pulp density, and pulp viscosity (Weiss, 1985; Ntengwe, 2010; Hlabangana et al., 2018).

2.6 Kinetics of dissolution reactions

Kinetic gives information on the rate (speed) at which a given system reaches its equilibrium state. Kinetic is very important for the metallurgist, whose primary objective is to determine the maximum metal extraction at the lowest cost (Adamson, 1972; Meshram et al., 2015). The following primary steps are involved in the reaction mechanism between solutions and solids whose products are soluble (Adamson, 1972; Boudart and Djéga-Mariadassou, 2014):

1) Diffusion of the molecules of reactants to the solid surface,

2) Adsorption of the reactants at the solid surface,

3) Chemical reaction at the solid surface,

4) Desorption of the products,

5) Diffusion of the products from the solid surface.

If all the products are not soluble, stages 4 and 5 are not applied. Some steps involve more than one step, for example, the diffusion of the reactants to the surface of the solid consists of a convective mixing in the bulk solution and a diffusion through the boundary layer between the solution and the solid; and a reaction at the solid surface can occur involving a certain number of steps whose overall rate of reaction is determined by the rate of the slowest step of that stage (Adamson, 1972; Fernandez and Sanchez, 2002). The rate of

reaction can be defined as the speed at which the concentration of a reactant or product changes with time. It can be represented as a plot of reactant or product concentration versus time (Wright, 2005). It depends on the intensity of the agitation when the diffusion is controlling. For each primary step, the rate is proportional to the solid surface area available for the reaction. Any step is rate-controlling. The surface area is then an important variable. Thus, in particularly solid-liquid reactions, there is interference of side reactions leading to the formation of a film on the surface (Adamson, 1972; Forryan et al., 2005). A summary of rate equations is given in Table 2.4.

Table 2.4: Summary of the rate equations (Wright, 2005; and Pilling and Seakins, 1996).

Order	Rate equation		Units of rate constant	Graph to be drawn
	Differential form	Integrated form		
0	$dx/dt = k$	$k = x/t$	mol l^{-1} s^{-1}	$(a_0 - x)$ vs t slope $= -k$
½	$dx/dt = k(a_0 - x)^{1/2}$	$k = \frac{2}{t}\left[a_0^{1/2} - (a_0 - x)^{1/2}\right]$	$mol^{1/2}$ $l^{-1/2}$ s^{-1}	
1	$dx/dt = k(a_0 - x)$	$k = \frac{1}{t} ln \frac{a_0}{a_0 - x}$	s^{-1}	$ln(a_0 - x)$ vs t slope $= -k$
3/2	$dx/dt = k(a_0 - x)^{3/2}$	$k = \frac{2}{t}\left[\frac{1}{(a_0 - x)^{1/2}} - \frac{1}{a_0^{1/2}}\right]$	$l^{1/2}mol^{-1/2}$ sec^{-1}	
2	$dx/dt = k(a_0 - x)^2$	$k = \frac{1}{t} \frac{x}{a_0(a_0 - x)}$	l mol^{-1} sec^{-1}	$1/(a_0 - x)$ vs t slope $= +k$
3	$dx/dt = k(a_0 - x)^3$	$k = \frac{1}{2t} \frac{2a_0x - x^2}{a_0^2(a_0 - x)^2}$	l^2 mol^{-2} sec^{-1}	

The rate constant *k*, in each case, is relevant to the consumption of reactant. a_0 is the initial concentration of reactant A, *x* is the amount of A that is consumed per unit volume in time t, $a_0 - x$ is the amount of A that remaining.

Furthermore, for the leaching of minerals, the shrinking core model (Equation 2.12) is used which describes the reactions in which the solid particles are consumed by leaching and therefore the amount of material consumed is decreasing. Generally, the rate of leaching is

controlled diffusion through the porous layer, the leaching reaction at the mineral surface of un-reacted particles, or mixed controlled. Thus, classical models can be established as follows (Habashi, 1999; Rutto and Enweremadu, 2012): surface chemical reaction controlled kinetic model (Equation 2.12), internal diffusion controlled kinetic model (Equation 2.13), and mixed-controlled kinetic model (Equation 2.14).

$$1-(1-x)^{1/3}=\frac{kC}{r_0\rho}t=kt \tag{2.12}$$

$$1-\frac{2}{3}x-(1-x)^{2/3}=kt \tag{2.13}$$

$$[(1-x)^{-1/3}-1]+\frac{1}{3}\ln(1-x)=kt \tag{2.14}$$

Where x represents the fraction leached, k the rate constant (min^{-1}), t the leaching time, C the concentration of acid (It is supposed that the concentration of acid is kept constant), r_0 the initial radius of the solid particle, and ρ the density.

2.7 Thermodynamics of complex formation

In a chemical reaction, molecules must collide with proper orientation and with minimum energy in order to react to form a product. This energy is called activation energy, Ea (Sokić et al, 2009). As the activation energy of diffusion is low (less than 20 kjoule mol^{-1}), the temperature coefficient of rate is low. However, the reaction-controlled processes do not depend on stirring and have high temperature coefficients that correspond to the higher activation energies of reaction. In practice, it is very important to differentiate whether the transport or the reaction is rate-controlling. If transport is controlling, an increase in agitation increases the rate of reaction. If the reaction is rate-controlling, the reaction rate is significantly increased by increasing the temperature, and it is not important to intensify the agitation (Adamson, 1972). The activation energy can be calculated from the Arrhenius equation (Equation 2.15). In fact, the slope of the Arrhenius plot, which is obtained by plotting the logarithm of the rate constant, k, against the inverse temperature, 1/T, can be used determine the activation energy. Once the activation energy is obtained from the Arrhenius plot, the rate constant can be determined for any temperature using the Arrhenius equation. Furthermore, the resulting negatively-sloped line can be used to

determine the missing components of the Arrhenius equation. The value for ln A is found by the extrapolation of the line back to the y-intercept (Sokić et al, 2009).

$$k = A_e^{-\frac{E_a}{RT}} \quad (2.15)$$

where, k is the rate constant, A_e the pre-exponential factor (it is a constant for each chemical reaction, according to collision theory, A is the frequency of collisions in the correct orientation (different for every reaction), Ea the activation energy, R the gas constant (8.314 J mol^{-1} K^{-1}), and T the temperature (Kelvin).

If the metal ion, M, can bind n ligands L, to form a complex MLn, the complex will, if n>1, always be built up by step-by-step reactions. Therefore, all species MLj with 0≤j≤n exist in equilibrium with each other, which at saturation are described by the equilibrium constant (Schmidt et al., 2008). The formation of species is established by their free energy (**Equation 2.16**), which is a reference value that defines what the relative concentrations of products and reactants are at equilibrium for a particular temperature. As such, ΔG° can be linked to the equilibrium constant by the equation (Schmidt et al., 2008; Mohapatra et al., 2009).

$$-\Delta G_j^0 = RTlnk_j \quad (2.16)$$

Where, ΔG_j^0 refers to the free energies of the elements at 298 K, *R* is the gas constant = 8.314 J/mol·K, *T* the temperature in Kelvin, and *k* the equilibrium constant (must be molarity for concentrations of dissolved species).

$$k_j = \frac{[ML_j]}{[ML_{j-1}][L]} \quad (2.17)$$

From $ML_j \leftrightarrow ML_j + L$ (2.18)

ΔG_j^0 can also be determined by heats of formation and entropies of formation. Heats of formation and entropies of formation are determined in relation to the reference values. The value of the equilibrium constant for a process can be predicted by knowing the enthalpy (the amount of heat energy released/absorbed during a chemical process) as well as the change in entropy (the degree of randomness or disorder in a system).which is a measure of the difference in the number of ways the available heat energy can be distributed. So, the free energy can be determined by the relation

$$-\Delta G_j^0 = -\Delta H_j^0 + T\Delta S_j^0 \quad (2.19)$$

where, *H* represents the enthalpy and *S* the entropy.

ΔH_j^0 and ΔS_j^0 can be calculated using tabulated values for enthalpies of formation and entropies of formation using a Hess law formalism. The formation of a species is favoured by a great positive value of $-\Delta G_j^0$, which indicates a great value of $-\Delta H_j^0$ (an exothermic reaction) and a great value of $T\Delta S_j^0$. Equations 2.16 and 2.19 can be written (Mohapatra et al., 2009)

$$\Delta H_j^0 - T\Delta S_j^0 = RTlnk_j \quad (2.20)$$

After some algebra

$$lnk_j = -\frac{\Delta H_j^0}{RT} + \frac{\Delta S_j^0}{R} \quad (2.21)$$

A plot of lnk_j against 1/T must be a straight line with slope $= -\Delta H_j^0/R$

Intercept $= \Delta S_j^0/R$

In aqueous media, metal ions are hydrated by water molecules that bind to the metal ion to form a regular octahedron, while the outer shell of the molecules of water commands the structure by influencing the charge of the metal ion (Persson, 2010). When ligands are used in an aqueous solution containing hydrated metal ions, a complex is produced; one or more molecules of water are ejected from the inner shell and are substituted by the ligand. Therefore, the number of water molecules will decrease in the outer shell, particularly if the ligand is negatively charged. The amount of energy will be calculated as the difference between the energy gained from the binding of a ligand to a metal ion and the energy lost by breaking bonds between the metal ion and water molecules in the internal and external hydration spheres (Persson, 2010; Mahler and Persson, 2012; Jackson et al., 2015). So, to sum up here, complex formation follows the Equation 2.21.

$$M(H_2O)_x + L(H_2O)_y \leftrightarrow ML(H_2O)_z + (x+y-z)H_2O \quad (2.22)$$

Equations 2.22 and 2.18 being similar, the equation for the following step can be written as

$$M(H_2O)_x(L)_j + L \leftrightarrow M(H_2O)_y(L)_{j+1} + (x-y)H_2O \quad (2.23)$$

2.8 Typical required concentration of coagulant for water and wastewater treatment

The typical required concentration of coagulant for water and wastewater treatment is less than 100 and 200 ppm, respectively. This shows that the concentrations of impurities in water and wastewater could increase during coagulation (Fan et al., 2005). The addition of complex coagulant should not affect the levels of pollutants in water and wastewater. Compared with existing quality of water and wastewater and standards for drinking water and wastewater as shown in Table 2.5, the effect of the complex coagulant on the initial contaminant concentration would not be significant (Miller et al., 2008; Hendrawati et al., 2016). Being itself a good agent for removing the contaminant elements during coagulation process, it is expected that the complex coagulant would not result in an additional impurity input when used in water or wastewater (Fan et al., 2005). The maximum permissible contents of certain constituents in industrial wastewater are shown in Table 2.3.

Table 2.5: Maximum allowable concentrations of certain constituents in industrial effluent discharge (mg/l, except where otherwise stated) and health effects of various toxic heavy metals (Stander et al., 1970; Ahmaruzzaman, 2011).

Pollutants	South African standard	WHO*	Health hazards
pH (value)	5.5–9.5		
Colour, odour, taste	absent		
Dissolved Oxygen	min. 75% saturation		
Temperature	max 35°C		
Chem. Oxygen Demand (COD)	75		
Oxygen Absorbed (OA)	10		
Total Dissolved Solids (TDS)	not exceeding 500 above intakes		
Suspended Solids (SS)	25		
Sodium (as Na)	not more than 50 above intakes		
Soap, oil, grease	2.5		
Residual chlorine (as Cl)	0.1		
Free and saline ammonia (as N)	10		
Arsenic (as As)	0.5	-	Carcinogenic, producing liver tumours, and gastrointestinal effects
Copper (as Cu)	1		Long term exposure causes stomach ache, irritation of nose, mouth, eyes, headache
Lead (as Pb)	1	0.1	Suspected carcinogen, anaemia, muscle and joint pains, kidney problem and high blood pressure
Nickel	-		Causes chronic bronchitis, reduced lung function, cancer of lungs.

Table 2.5: Maximum allowable concentrations of certain constituents in industrial effluent discharge (mg/l, except where otherwise stated) and health effects of various toxic heavy metals (Stander et al., 1970; Ahmaruzzaman, 2011). (Continued).

Pollutants	South African standard	WHO*	Health hazards
Mercury	-	-	Excess dose may cause headache, abdominal pain, and diarrhea, paralysis, and gum inflammation, loosening of teeth, loss of appetite, etc.
Iron	-	0.1–1.0	Excess amounts cause rapid pulse rates, congestion of blood vessels, hypertension
Manganese	-	0.05–0.5	Excess amounts toxic, and causes growth retardation, fever, sexual impotence, muscles fatigue, eye blindness.
Cadmium	-	0.1	Carcinogenic, cause lung fibrosis, dyspnoea
Zinc (as Zn)	5	2	Causes short-term illness called “metal fume fever” and restlessness
Chromium hexavalent (as Cr)	0.05		
Total chromium (as Cr)	0.5	-	Suspected human carcinogen, producing lung tumours
Vanadium	-	-	Very toxic, and may cause paralysis
Boron (as B)	1		
Phenols	0.1		
Cyanides (as CN)	0.5		
Sulphides (as S)	1		
Fluoride (as F)	1		

*WHO: World Health Organization

2.9 Acid mine drainage

The AMD which is one of the main pollutants of water in several countries, is metal-rich water produced from the chemical reaction between water and ore containing sulphur-bearing minerals such as pyrite (Kuyucak, 1999; Costello, 2003). During the reaction, sulphide minerals oxidize producing sulphuric acid that mobilizes the constituents of rock (Johnson and Hallberg, 2005).

Generally, AMD is highly acidic (pH 2–4), often contains high sulphate concentrations (1–20 g/L), and dissolves high concentrations of Cu, Pb, Al, Fe, Zn, Mn and Cd into ground and surface water. It is highly toxic due to high acidic pH and high ionic content. Expensive storage, remediation and disposal techniques are needed for its control (Kuyucak, 1999; Costello, 2003; Johnson and Hallberg, 2005; Gitari et al., 2008; Yan et al., 2012). Metals such as Cu, Hg, Pb, Cr, Ni, Cd, As, Zn, Ag, and Se have been known as harmful heavy metals. Heavy metals are not biodegradable and can be accumulated in living organisms, causing various diseases and disorders (Chen, 2012).

For the treatment of metal-contaminated waste streams, various processes are presented, such as ion exchange, solvent extraction, reverse osmosis, coagulation, membrane filtration, chemical precipitation, photo catalytic degradation, biological systems, oxidation with ozone/hydrogen peroxide, ultra-filtration, and adsorption (Ahmaruzzaman, 2011). At the present time, physical and chemical processes such as adsorption, membrane filtration, chemical precipitation, ion-exchange, coagulation are the main methods of industrial effluent treatment. Many of these conventional methods for wastewater treatment have not been extensively applied at large scale because of the high cost and disposal problems (Aboulhassan, 2006).

It was found that coagulation is a promising process compared to the other techniques for wastewater treatment in terms of initial cost, simplicity of design, and ease of operation. Furthermore, coagulation does not produce harmful substances (Ahmaruzzaman, 2011) and high removal efficiency can be obtained with the use of coagulation process. Coagulation process is used to remove organics together with suspended solids, without being affected by the toxicity in the wastewater (Semerjian et al., 2003; Golob, et al., 2005). The main advantage of the processes such as coagulation-flocculation is the

destabilization of colloidal and suspended solids from the waste stream (Aboulhassan et al., 2006).

2.10 Coagulation of wastewater

2.10.1 Coagulation description

Coagulation (or flocculation) process in water treatment has been practiced from ancient times by the Egyptians, as earlier as 2000 BC. By 1757, coagulation process using aluminium sulphate was applied in England for water treatment (Bratby, 2006). Coagulation is the process in which destabilization (or neutralization of charges) of a given suspension or solution is produced. That is, coagulants neutralize the charges that keep the colloidal particles away from each other, inducing them to collide into larger particles or flocs (Bhatia et al., 2007; Bratby, 2006). Flocculation is the process in which destabilized particles (or flocs), are brought together and agglomerated into larger size particles that can subsequently be removed through filtration (Shammas, 2005).

The coagulation process can be divided into the following four distinct and successive steps:

1. Coagulant addition,
2. Particle destabilization,
3. Interparticle collisions (or flocculation),
4. Sedimentation.

The first two steps are generally fast with a rapid mixing to dissolve the coagulant and distribute it evenly throughout the water. The third step is a slower process that is accomplished by fluid flow and slow mixing. (Amirtharajah and Jones, 2006). This flocculation stage is named perikinetic flocculation. Nevertheless, for considerable floc formation, some method induced turbulence in the suspending medium is required. This stage, named orthokinetic flocculation, is achieved by mechanical agitation or by inducing a tortuous flow pattern to the suspension by passage over granular filter media or around baffles installed in a flocculation tank (Rao, 2005). Sedimentation step is the final phase of coagulation process where finer suspended particles formed earlier into larger particles of required size and characteristic are removed in a settling tank where flocs are either filtered from liquid or separated by gravity. The accumulated material can then be further treated

to facilitate final disposal. At this stage, polyelectrolytes are often added to increase the dewatering characteristics of the material. In this case, one denotes to the polyelectrolyte's conditioner (Rao, 2005; Bratby, 2006).

Coagulation is generally performed using inorganic coagulants (primary coagulants) such as iron or aluminium salts, and/or synthetic organic polymers commonly known as polyelectrolytes. Coagulant aids (polymeric additives) are used to help in the destabilization and to accelerate the rate of agglomeration of difficult and slow to settle particles. Sludge conditioners are used to promote and strengthen flocs before thickening or dewatering processes (Aguilar et al., 2002; Aguilar et al., 2005; Aboulhassan, 2006).

Generally, particles in solution are removed by settling followed by filtration. Small particles are not removed efficiently by settling because they settle too slowly; they can also pass through filters (Bratby, 2006). They would be easier to remove if they collide (coagulated) to form larger particles; however, they do not because they possess a negative charge and repulse each other. In coagulation, a coagulant like ferric sulphate which produces positive charges to neutralize the negative charges on the particles is used. So, the particles can attach together, forming larger particles which are more easily removed (Aguilar et al., 2005; Rao, 2005; Aboulhassan, 2006). Monomeric metallic salts (inorganic) coagulants destabilize the colloidal and suspended particles through compression of the electrical double layers surrounding the particles (Figure 2.3). While polymeric coagulants destabilize particles by adsorption and successive formation of a particle–polymer–particle bridge (Joo et al., 2003; Aboulhassan et al., 2006). Sections 2.9.6 will deal with coagulation mechanisms.

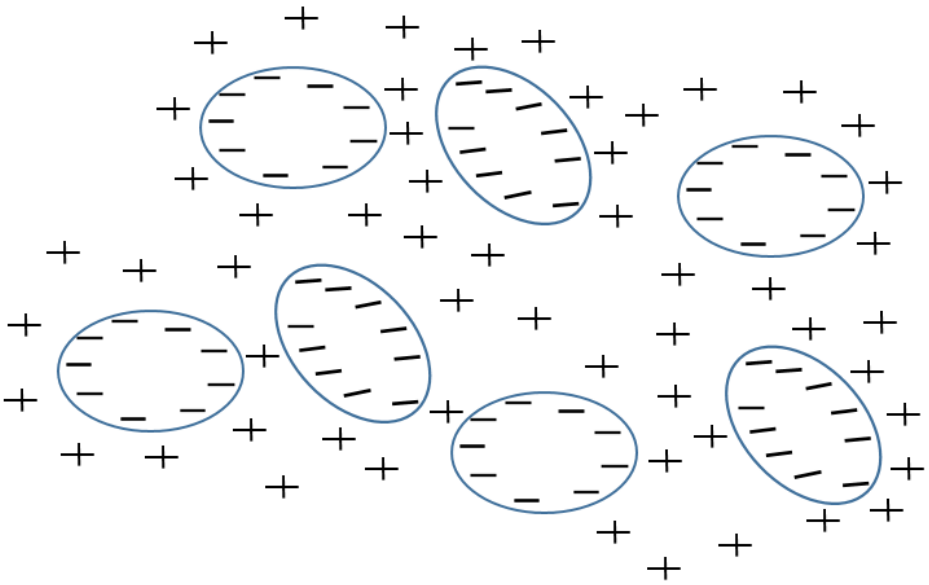

Figure 2.4: Illustration of negatively charged colloidal particles surrounded in solution by positively charged counter-ions, forming an electrical double layer (colloidal particles suspended in water may hold either a negative or a positive charge) (Manahan, 2009).

The process of coagulation is influenced by the following factors (Rao, 2005):

- The pH of water is important for selecting a coagulant
- Coagulant dosage
- Coagulation time
- Temperature
- Addition of activated silica or polyelectrolytes possessing characteristics of polymer or electrolytes, aid the coagulation process.

Coagulation has been shown to be an effective process for the removal of contaminants such as turbidity (Babu and Chaudhuri, 2005; Liew et al., 2006; Assad et al., 2007; Dihang et al., 2008), colloidal suspensions, suspended solids, toxic organic matter (Sun et al., 2011; Hu et al., 2005), heavy metals (Assad et al., 2007; Jonhson et al., 2008), colour (Verma et al., 2012), and viruses (Abbaszadegan et al., 2007).

2.10.2 Colloidal suspensions

The materials in wastewaters arise from industrial and domestic waste discharges, the dissolution of minerals, the deterioration of vegetation, and land erosion. For a given wastewater, such material can include suspended and/or dissolved organic and/or inorganic substance, and several biological forms like algae, bacteria, and viruses (Tatsi et al. 2003; Rao, 2005; Renou et al. 2008). As presented in Table 2.6, considerable amount of the suspended matter present in wastewaters is in microscopic to submicroscopic size range. Substances smaller than around 10^{-5} mm are considered as colloids. Colloidal matter includes mineral substances, biopolymers, small aggregates of precipitated and flocculated matter, macromolecules, silt, viruses, bacteria, and plankton. Particles less than approximately 10^{-6} mm are referred to as solutions. Such material includes inorganic simple and complex ions, polyelectrolytes, molecules and polymeric species, un-dissociated solutes, organic molecules, and small aggregates (Shammas, 2005; Bratby, 2006).

Table 2.6: Classification of particle sizes (Bratby, 2006).

Particle size (mm)	Classification	Examples	Total surface area (m^2/cm^3)	Time required to settle 100 mm if specific gravity = 2.65
10	Coarse dispersion (visible to naked eye)	Gravel, coarse sand, mineral substances, precipitated and flocculated particles, silt, macroplankton.	6×10^{-4}	0.1 s
1			6×10^{-3}	1 s
10^{-1}			6×10^{-2}	13 s
10^{-2}	Fine particulate dispersion (visible under microscope)	Mineral substances, precipitated and flocculated particles, silt, bacteria, plankton, and other organisms.	0.6	11 min
10^{-3}			6	20 h
10^{-4}			60	80 days
10^{-5}	Colloidal dispersion (submicroscopic)	Mineral substances, hydrolysis and precipitated products, macromolecules, biopolymers, viruses.	600	2 years
10^{-6}			6000	20 years
$<10^{-6}$	solution	Inorganic simple and complex ions, molecules and polymeric species, polyelectrolytes, organic molecules, undissociated solutes.		

In water, colloidal particles or smaller sizes can retain a dispersed state due to some inherent characteristics that promote their stability. The term stability denotes the capacity of such particles to remain independent entities inside a given dispersion (Shammas, 2005; Amirtharajah and Jones, 2006; Bratby, 2006). In aqueous solution, all particles possess some properties associated with interfacial phenomena which comprise the effects of the surface charge carried by the particles and the degree of hydration (or solvation) of the particles' surface layers (Ohshima, 2006).

It is because of the dominant impact of surface phenomena that colloids, which possess a huge surface area to mass ratio, have the capacity to exist as stable dispersions (Ohshima, 2006). For example, Table 2.6 presents the total surface area for an initial particle of diameter 10 mm fragmented into spheres of progressively smaller diameters. Since the size of particles becomes increasingly smaller, the total surface area becomes extremely large for a given total particle mass. Therefore, for a given total mass, the smaller the particles the more predominant become the impacts of phenomena associated with interfaces. Furthermore, the smaller become the impacts of gravity effects associated with mass. With the size of particles in the range of that of colloidal, it can be seen from Table 2.6 that, considering hydrodynamic effects alone, duration of up to several years can be required for colloidal material to settle through a significant distance (Bratby, 2006).

There are three main ways in which a colloidal particle can acquire a surface charge. The first is by *chemical reaction at the particle surface*. This reaction involves hydrogen ions and is dependent on pH, and is typical of oxides and hydroxides (Manahan, 2009). For example, the impacts of pH on the surface charge of hydrated manganese oxide [$MnO_2(H_2O)_{(S)}$]. In an acidic medium, the reaction in Equation 2.24 can happen on the surface, conferring the particle a positive charge.

$$MnO_2(H_2O)_{(s)} + H^+ \rightarrow MnO_2(H_3O)^+_{(s)} \qquad (2.24)$$

Contrarily, in a basic medium, a proton can be lost from the hydrated oxide surface to produce negatively charged particles as follows:

$$MnO_2(H_2O)_{(s)} \rightarrow MnO_2(HO)^-_{(s)} + H^+ \qquad (2.25)$$

The second way in which particles gain a charge is by the process of *ion absorption* which includes attachment of ions onto the colloidal particle surface by hydrogen bonding and van der Waals interactions. *Ion replacement* is the third way in which a colloidal particle can become charged. As an illustration, the substitution of Si^{4+} by Al^{3+} in the SiO_2 chemical unit in the crystalline lattice of clay minerals (Equation 2.26) results in sites with a negative charge. The same, the substitution of Al^{3+} by a divalent metal ion such as Mg^{2+} in the clay crystalline lattice gives a negative charge (Bratby, 2006).

$$SiO_2 + Al^{3+} \rightarrow AlO_2^- + Si^{4+} \quad (2.26)$$

2.10.3 Water and wastewater impurities

The coagulation process is used to enhance the degree of removal of water and wastewater impurities particles (colloids) which are classified in categories such as total suspended solids (TSS), total dissolved solids (TDS), turbidity, biochemical oxygen demand (BOD), and chemical oxygen demand (COD).

Total suspended solids (TSS) are solids in water that cannot pass through a filter with 2 µm pores and are indefinitely suspended in solution. Suspended particles often include silt, clay, algae and other microorganisms, organic matter and other minute particles (Manios et al., 2003). The TSS can be defined as a measure of the total amount of all suspended solids (organic and inorganic) per volume of water. Total suspended solids are reported in mg/L (Verma et al., 2013).

Turbidity is a measure of the relative clarity of water. Turbidity as well as TSS makes allusion to particles present in the water column. However, turbidity is not a direct measurement of suspended particles in water but, a measure of the scattering effect such particles have on light. Turbidity is expressed by NTU. It is important to measure the turbidity because it is an incontestable indicator of water quality change (Annadurai et al., 2004; Muthurama and Sasikala, 2014). In the water treatment process, a sudden change in turbidity may indicate another contamination source (biological, organic or inorganic) (Sadar, 1998; Mandal, 2014).

Total dissolved solids (TDS) are inorganic salts and small amounts of organic matter present in solution in water. It can be described as a measure of the total content of all ion particles that are smaller than 2 µm. This consist of all of the disassociated electrolytes that

make up salinity concentrations, also other compounds like dissolved organic matter. The TDS are expressed in mg/L (Basha et al., 2008; Broséus et al., 2009). In clean water TDS are almost equal to salinity, while in wastewater TDS can include organic solutes (like urea and hydrocarbons) in addition to the salt ions. Calcium, sodium, phosphates, chloride, nitrates, and potassium are the most common chemical constituents of TDS. They can be anions, cations, molecules or agglomerations (1000 or less molecules) (Basha et al., 2008). Conductivity and gravimetric analysis are two main techniques of measuring TDS. The former is a measure of electrical conductivity of water which is proportional to the concentration of dissolved ionized solids in the water. Conventional conductivity meter or TDS meter can be used to measure the electrical conductivity of water. Gravimetric techniques include evaporating the liquid solvent and measuring the mass of residues left (Dahm, 1981; Broséus et al., 2009).

2.10.4 Colloid stability and destabilization

In aqueous suspensions, several ways of interactions between particles can occur. These interactions determine whether the dispersion is stable or not. Thus, stability involves the particles remaining in a dispersed state for long times, rather than forming agglomerations (coagulation or flocculation). For stability, some form of repulsion exists between particles; if not, collisions of particle would result in attachment resulting from the universal van der Waals forces of attraction. Particles in water are nearly always charged and their electrical repulsion between them may be liable for their stability. A quantitative theory of the stability of colloids was developed by Derjaguin and Landau (Derjaguin and Voropayeva, 1964) and Verwey and Overbeek (Verwey and Overbeek, 1999) and known as DLVO theory. Other forms of interaction between particles, such as hydration and hydrophobic forces and effects associated with adsorbed polymers, are also known (Israelachvili, 1992).

The DLVO theory describes the stability of colloids in terms of equilibrium between van der Waals attraction and electrical repulsion between particles. Practically, only the latter can be greatly modified, and repulsion can be significantly affected by changing the ionic strength of the suspending medium or by modifying the surface charge of the particles (Bleier and Matijevic, 1976; Missana and Adell, 2000). The increase in ionic strength effectively hides the electrical repulsion and allows the particles to approach each other

more closely, so that van der Waals attraction can prevail. Adding salts having specifically adsorbing counterions (the charge is opposite to that of the particles), the surface charge of the particles can be reduced or neutralized so that repulsion between particles is reduced or totally eliminated. This is used in practice as an effective way of promoting coagulation. However, addition of excess coagulant can result in charge setback and restabilization of particles (Horn, 1990; Kragh and Langston, 1962; Benítez et al., 2007).

The action of adsorbing polymers constitutes another very important method of destabilizing particles. In fact, polymers of high molecular weight are able to adsorb simultaneously on two or more particles and attach them together by a process called polymer bridging. Therefore, the action of the hydrolysing metal coagulants may be via the effects of charge neutralization or involve the binding of particles together by precipitated hydroxide (Dickinson and Eriksson, 1991; Snowden et al., 1991; Hosny et al., 2016).

2.10.5 Chemical aspects of metal and silicon cation (Fe^{3+}, Al^{3+}, Si^{x+}, Mg^{2+}, and Ca^{2+}) salts as coagulants

Hydrolysis and precipitation processes

In aqueous solution, free metal ions and other cations hydrolyse to produce a series of monomeric (mononuclear) and polymeric (polynuclear) complexes. Hydrolysis is a main chemical factor of the chemistry of cation salts because cations are easily hydrolyzed in aqueous solutions in the absence of competing ligands (Horn, 1990; Barnum, 1983; Fiol et al., 2006; Hosny et al., 2016).

Monomeric hydrolysis products: In water, all ions are hydrated to some level. There is a primary hydration shell, where molecules of water are in direct contact with the central ion, and more lightly detained water molecules in a secondary hydration shell. A metal ion (cation) in aqueous solution, has a chemical formula $M(H_2O)_n^{z+}$, with n the hydration (or solvation) number and z the electrical charge of the metal ion (Stumm and Morgan, 1962). For Fe^{3+}, Al^{3+}, and Mg^{2+}, there is a primary hydration shell with six water molecules in octahedral co-ordination $Fe(H_2O)_6^{3+}$, $Al(H_2O)_6^{3+}$, and $Mg(H_2O)_6^{2+}$, respectively (Duan and Gregory, 2003; Ikeda et al., 2007). While Si^{4+} is dissolved as a hydroxocomplex, $Si(OH)_4$ in a tetrahedral lattice. However, H_4SiO_4 is generally used to indicate that the complex can

cede H^+ ions and thus behave as an acid [$Si(OH)_4 = H_4SiO_4$]. H_4SiO_4 and/or $Si(OH)_4$ are commonly called silicic acid (Mirsal, 2008). In the case of Ca^{2+}, a hydration number is not well established (Ikeda et al., 2007; Pálinkás and Heinzinger, 1986).

Metal ions in water are subject to hydrolysis. Commonly, hydrolysis reactions of metal cations used as coagulants is represented as a successive substitution (complexation reaction) of the water molecules in the first hydration shell by hydroxyl ions providing a lower positive charge. Also, the hydrolysis reactions of metal cations can be viewed as a series of consecutive deprotonation of water molecules in the primary hydration shell (Richens, 1997; Henry et al., 1992; Ikeda et al., 2007). Considering a substitution reaction, the illustration for a trivalent metal cation, omitting co-ordinated water molecules for simplicity, is:

$$M^{3+} \rightarrow M(OH)^{2+} \rightarrow M(OH)_2^{+} \rightarrow M(OH)_3 \rightarrow M(OH)_4^{-} \quad (2.27)$$

A single step of the substitution (complexation) reaction is given by

$$[M(H_2O)_n]^{z+} + OH^- \rightleftharpoons [M(H_2O)_{n-1}(OH)]^{(z-1)+} + H_2O \quad (2.28)$$

With M: metal ion.

The hydrolysis representation in Equation 2.27, which is simplified form, occur from left to right as the pH is increased, producing first the doubly- and singly-charged cationic species and then the uncharged metal hydroxide, $M(OH)_3$. With more increase in pH, the soluble anionic form $M(OH)_4^-$ becomes dominant (Barnum, 1983; Duan and Gregory, 2003).

Considering the deprotonation reaction, hydrolysis reaction of a trivalent metal cation can be described for successive deprotonations according to the following generalized equations (Barnum, 1983; De Abreu et al., 2006), omitting H_2O ligands coordinated to the M^{3+} ions:

$$M^{3+} + H_2O \leftrightarrow M(OH)^{2+} + H^+ \quad K_1 \quad (2.29)$$

$$M(OH)^{2+} + H_2O \leftrightarrow M(OH)_2^{+} + H^+ \quad K_2 \quad (2.30)$$

$$M(OH)_2^{+} + H_2O \leftrightarrow M(OH)_3 + H^+ \quad K_3 \quad (2.31)$$

$$M(OH)_3^{+} + H_2O \leftrightarrow M(OH)_4^{-} + H^+ \quad K_4 \quad (2.32)$$

Generally, a single step can be defined as

$$[M(H_2O)_n]^{z+} - H^+ \rightleftharpoons [M(H_2O)_{n-1}(OH)]^{(z-1)+} \quad (2.33)$$

With M: metal ion.

Polymeric hydrolysis products: Hydrolysis of cations can occur by showing the characteristics of multiple hydrolysis reactions. Therefore, dimeric, trimeric and

polynuclear hydrolysis species can form. The concentrations of various hydrolysis products, including polynuclear species with bridging hydroxide ions, change with the pH increase until the formation of an insoluble hydroxide (Barnum, 1983). The formation of polymer (polynuclear) products is done by the reduction of the charge density in the molecule as a whole. Polynuclear species of the hydrolysis of Fe and Al include $Fe_2(OH)_2^{4+}$ and $Fe_3(OH)_4^{5+}$ for Fe and $Al_2(OH)_2^{4+}$ and $Al_3(OH)_4^{5+}$ for Al (Rose and Waite, 2003). Furthermore, the polynuclear hydrolysis species $Al_{13}O_4(OH)_{24}^{7+}$ (or Al_{13}) is also known. This tridecamer has the structure containing of a central tetrahedral AlO_4^{5-} unit surrounded by 12 Al octahedra with shared edges (Bottero et al., 1982). For Mg, the polymeric hydrolysis product includes $Mg_4(OH)_4^{4+}$. Table 2.7 presents some general formula of polynuclear hydrolysis products (Grosjean and Roué, 2006). In the case of Si, $Si(OH)_4$ combine, at high concentration, to form a polymer (polynuclear complex) or dimer. In fact, the bridging O_2^- is bound to two Si_4^+ ions and consequently loses its H^+. The loss of this H^+ and an OH^- (whose sum represents an H_2O) shows that the dimer formation is a dehydration reaction (Equations 2.34 and 2.35) (Rimstidt and Barnes, 1980; Tossell, 2005).

$$Si(OH)_4 + Si(OH)_4 \rightarrow Si_2O(OH)_6 + H_2O \quad (2.34)$$

This can also be written as

$$H_4SiO_4 + H_4SiO_4 \rightarrow H_6Si_2O_7 + H_2O \quad (2.35)$$

Table 2.7: Some polynuclear hydrolysis species.

Species formula	Cations	Structure
$M_2(OH)_2^{(2z-2)+}$	Al^{3+}, Fe^{3+}	double hydroxide bridge between two cations
$M_3(OH)_4^{(3z-4)+}$	Al^{3+}, Fe^{3+}	Cube with alternate vertices of M^{n+} and OH^-groups, one vertex missing
$M_4(OH)_4^{4+}$	Mg^{2+}	Cube with alternate vertices of M^{n+} and OH^-groups

The general reaction for the loss of two protons from coordinated water molecules, can be expressed as (Barnum, 1983; De Abreu et al., 2006)

$$[M(H_2O)_n]^{z+} - 2\ H^+ \rightleftharpoons [M(H_2O)_{n-2}(OH)_2]^{(z-2)+} \quad (2.36)$$

Nevertheless, the equilibrium constant for the loss of two protons applies similarly well to the following equilibrium (Barnum, 1983).

$$[M(H_2O)_n]^{z+} - 2\ H^+ \rightleftharpoons [MO(H_2O)_{n-2}]^{(z-2)+} + H_2O \qquad (2.37)$$

In general, as expressed in Equations 2.29 to 2.32, 2.36, and 2.37, on transferring a proton to a solution water molecule, a coordinated H_2O is transformed to a hydroxyl ion. Thus, the hydrated metal ions produced by the reactions are acids according to the Bronsted theory of acids that a donor of proton is defined as an acid. Since the hydrolysis reaction depends on the acid-base reactions, the pH of the solution greatly influences the rate and distribution of the different hydrolysis products (Barnum, 1983; Eigen, 1964; Mohammed et al., 2005).

Practically it is not simple to describe the hydrolysis behaviour of metal cation salts because of the number and diversity of the hydroxide complexes which can be formed in solution. For given metal cation, the resulting chemical behaviour may be a complicated function of pH and concentration; and, if the identity and stability of the hydrolysis products are not known, this can be somewhat unpredictable (Baes and Mesmer, 1981, Barnum, 1983; Bratby, 2016).

2.10.6 Mechanisms of wastewater coagulation

Even if the terms coagulation and flocculation are used in different ways depending on the area of usage and on the assumed mechanism of aggregation, in this work the term coagulation is used to represent the overall process of coagulation, including flocculation and sedimentation. The wide variety of particulate impurities found in natural waters (inorganic substances such as metal oxides and clays, organic colloids and microbes such as bacteria, viruses, and algae) cover a wide range of particle size, from nm to mm sizes (Tatsi et al. 2003; Rao, 2005; Renou et al. 2008; Bratby, 2006). This constitutes a substantial challenge in water treatment method. Coagulation (flocculation) process includes aggregation of particles into larger, more readily removable aggregates. Generally, coagulation process involves two distinct stages: particle transport to achieve interparticle contact and particle destabilization to allow attachment when contact happens (Stumm, 1992). Furthermore, there are four secondary mechanisms that describe the coagulation in water treatment by hydrolysable metal salts (Duan and Gregory, 2003):

1) Electric double layer compression,
2) Adsorption and charge neutralization of negatively charged colloids by cationic hydrolysis products,
3) Adsorption and interparticle bridging,
4) Incorporation of pollutants in an amorphous hydroxide precipitate (commonly known as sweep coagulation).

The electric double layer compression is not probable to be important mechanism under water treatment conditions, but the other three mechanisms happen during water treatment depending on the specific conditions of treatment and water quality, and each of them can result in the removal of colloidal particles. Colloid destabilization can only remove particles from water and cannot remove dissolved pollutants, while the other two mechanisms can remove only dissolved pollutants in water and wastewater. Precipitation mechanism is often defined in a general way as any process resulting in the production of solids, as well as the destabilization of colloids and their subsequent agglomeration into settleable solids (Randtke, 1988). In the context of wastewater treatment, precipitation indicates the conversion of a dissolved substance into a solid by causing its solubility product to be exceeded. This definition causes the mechanisms of colloid destabilization and precipitation to be mutually exclusive (Randtke, 1988; Teh et al., 2016).

Adsorption and charge neutralization

In coagulation process, the mechanism for neutralization of negatively charged particles consists of the specific adsorption of cationic species from solution. Since iron, magnesium, aluminium, calcium, and silicon salts produce cationic hydrolysis species, charge destabilization is a possible reason for the action of these materials as coagulants. Adsorption of cations on negative surfaces can happen due to electrostatic forces or by some form of surface complex formation, consequently reducing the repulsive energy barrier and causing rapid coagulation (Matijević, 1973; Shammas, 2005). It is improbable that a single adsorption interaction is responsible as hydrolysing coagulants can destabilize the negative surface charge of several types of particles. Generally, small amounts of hydrolyzing coagulant are able to destabilize particles and optimum destabilization corresponds with the neutralization of particle charge. Higher amounts of coagulant reverse the charge at colloidal surfaces. Thus, the colloidal particles become positively charged and are restabilized. In the case of relatively low particle concentrations, destabilization

and restabilization usually happen with micromolar concentrations of coagulant (Stumm, 1992; Stumm and Morgan, 1962; Stechemesser and Dobiáš, 2005).

Even if the species accountable for charge neutralization could be dissolved cationic hydrolysis products, evidence exists which suggest that neutralization could occur by charged precipitate. This can either happen by a form of surface precipitation or by the adsorption of colloidal hydroxide precipitated in bulk solution and carried to the particles (Bratby, 2016; Farley et al., 1985).

Sweep flocculation

The addition of a metal salt such as Fe^{3+}, Al^{3+}, or Mg^{2+} salt to water in dosage sufficiently high to cause precipitation of metal hydroxide, impurity particles can be enmeshed in these precipitates as they are produced (as shown in Figure 2.4) and also collide with them subsequently, and hence can be removed from water by settling. This process is known as sweep flocculation, as particles are "swept out" of water by an amorphous hydroxide precipitate (Packham, 1965; Ghernaout and Ghernaout, 2012).

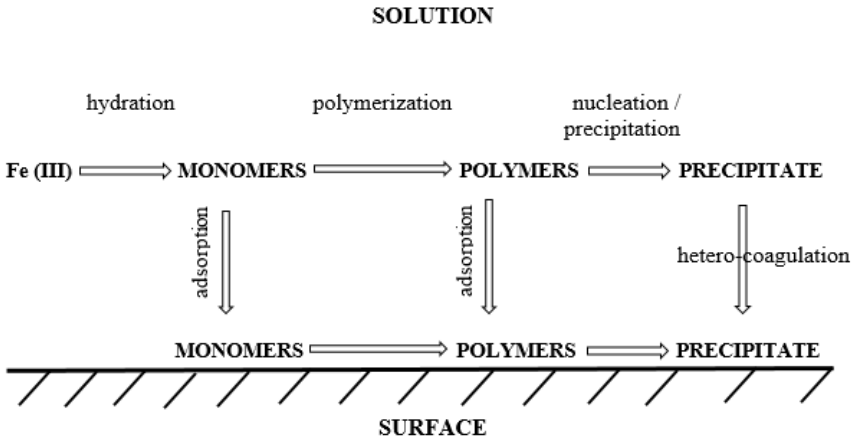

Figure 2.5: Schematic illustration of the various ways followed by cation hydroxide species in solution or at a surface in contact with the solution (Dentel, 1991).

Generally, significantly improved particle removal can be obtained by Sweep flocculation than when colloidal particles are destabilised just by charge neutralisation. The rate of aggregation is greatly improved due to the increased concentration of solids (Ghernaout and Ghernaout, 2012; Packham, 1965). The rather open structure of hydroxide precipitates does that even a small mass may cause a large effective volume concentration and

therefore a high possibility of capturing other particles. Furthermore, bridging (binding) of particles by precipitated hydroxide can lead to stronger aggregates. Increasingly larger volumes of sediment can be obtained by increasing the coagulant dose in the sweep region. However, beyond the experimental optimum dose, there is little more improvement in the removal of particle (Gregory and Dupont, 2001).

Four zones of coagulant dose are defined from the different mechanisms outlined above, with the following effect on negatively charged particles:

- Very low dose of coagulant; particles still negative and hence stable
- Dose enough to cause charge neutralization and hence coagulation
- Higher dose causing charge neutralization and restabilization
- Still higher dose causing hydroxide precipitate and sweep flocculation

2.11 Adsorption isotherms and mechanism

In general, an adsorption isotherm is an important curve defining the phenomenon governing the retention (or release) or movement of a substance from the aqueous porous media or aquatic environments to a solid-phase at a constant pH and temperature (Limousin et al., 2007; Allen et al., 2004). The adsorption equilibrium (the ratio between the adsorbed quantity with the residual in the solution) is established when a phase containing the adsorbate has been brought into contact with the adsorbent for a sufficient time, its adsorbate concentration in the Bulk solution being in dynamic equilibrium with interface concentration (Kumar and Sivanesan, 2007). Usually, mathematical correlation, which plays an important role in modeling analysis, operational design, and applicable practice of adsorption systems, is generally described by graphically expressing the solid-phase against its remaining concentration (Ncibi, 2008).

Assessment of a solid-liquid adsorption system commonly depends on two types of investigations: equilibrium batch adsorption and dynamic continuous-flow adsorption studies. Table 2.8 presents a summary of empirical models that are reported for single solute adsorption systems (Ahmaruzzaman, 2011). The Langmuir and Freundlich isotherm models are the most widely used (Rengaraj and Moon, 2002). The BET model assumes that the Langmuir isotherm applies to each layer and describes multi-layer adsorption on the surface of the adsorbent. These models are able to give information on the adsorption

capacity of metals from their aqueous solution. In most of the cases, Langmuir and Freundlich models can describe several adsorption isotherms. The automatic conclusion resulting from a good fit of the observed experimental data with the empirical models must be avoided. Nevertheless, the adsorption isotherms may show an irregular pattern due to the complex nature of both adsorbents and its multiple and varied active sites, as well as the complex solution chemistry of certain metallic compounds.

The mechanism of adsorption of metal ions on various industrial wastes is very complicated and appears to be due to electrostatic attraction, adsorption-precipitation, ion exchange, hydrogen bonding, and interaction between the metal ions and the surface functional groups of the various adsorbents. The main generally accepted adsorption mechanism is the chemical interaction between metal ions and surface functional groups of various industrial wastes (Ngah and Hanafiah, 2008; López-Delgado et al., 1998).

Table 2.8 Single-component adsorption isotherm models used.

Isotherm types	Equations		Plot to be drawn	Nomenclature
	Nonlinear form	**Linear form**		
Langmuir (Bellot and Condoret, 1993)	$q_e = \frac{q_m b C_e}{1 + bC_e}$	$\frac{C_e}{q_e} = \frac{1}{q_m b} + \frac{C_e}{q_m}$ $\frac{1}{q_e} = \frac{1}{bq_m C_e} + \frac{1}{q_m}$ $q_e = q_m - \frac{q_e}{bC_e}$ $\frac{q_e}{C_e} = bq_m - bq_e$	$\frac{C_e}{q_e}$ vs C_e $\frac{1}{q_e}$ vs $\frac{1}{C_e}$ q_e vs $\frac{q_e}{bC_e}$ $\frac{q_e}{C_e}$ vs q_e	q_e represents the equilibrium metal adsorption capacity; C_e is the equilibrium solute concentration in solution; q_m and b are Langmuir constants associated to maximum adsorption capacity (monolayer capacity) and bonding energy of adsorption (or "affinity"), respectively.
Freundlich (Zewail and Yousef, 2015)	$q_e = kC_e^{1/n}$	$\log q_e = \log k + \frac{1}{n}\log C_e$	$\log q_e$ vs $\log C_e$	k represents the adsorption equilibrium constant, it represents the sorption capacity; and n is a constant indicating the intensity of the adsorption.
Sips Isotherm (Combination of Langmuir–Freundlich) (Foo and Hameed, 2010)	$q_e = \frac{k_s C_e^{\beta_s}}{1 + a_s C_e^{\beta_s}}$	$\beta_s \ln(C_e) = -\ln\left(\frac{k_s}{q_e}\right) + \ln(a_s)$	$\ln\left(\frac{k_s}{q_e}\right)$ vs $\ln(C_e)$	β_s is the Sips constant

Table 2.8 Single-component adsorption isotherm models used (continued).

Isotherm types	Equations		Plot to be drawn	Nomenclature
	Nonlinear form	Linear form		
Brunauer (BET) (multilayer sorption) (Brunauer, 1938)	$q_e = \frac{q_s C_{BET} C_e}{(C_s - C_e)\left[1 + (C_{BET} - 1)\left(C_e/C_s\right)\right]}$	$\frac{C_e}{q_e(C_s - C_e)} = \frac{1}{q_s C_{BET}} + \frac{(C_{BET} - 1)}{q_s C_{BET}} \frac{C_e}{C_s}$	$\frac{C_e}{q_e(C_s - C_e)}$ vs $\frac{C_e}{C_s}$	C_{BET}, C_s, q_s, and q_e represent the BET adsorption isotherm (L/mg), adsorbate monolayer saturation concentration (mg/L), theoretical isotherm saturation capacity (mg/g) and equilibrium adsorption capacity (mg/g), respectively.
Radke–Prausnitz (Radke and Prausnitz, 1972)	$q_e = \frac{a_{RP} T_R C_e^{\beta_R}}{a_{RP} + r_R C_e^{\beta_R - 1}}$	-	-	The model exponent is represented by a_{RP}, where a_R and r_R are the model constants.
Redlich–Peterson (Ho, 2002)	$q_e = \frac{k_R C_e}{1 + a_R C_e^{\beta}}$	$\ln\left(K_R \frac{C_e}{q_e} - 1\right) = g \ln(C_e) + \ln(a_R)$	$\ln\left(K_R \frac{C_e}{q_e} - 1\right)$ vs $\ln(C_e)$	k_R is the Redlich–Peterson isotherm constant (l/g), a_R is also a constant having unit of $(l/mg)^{\beta}$, and β is an exponent having a value between 0 and 1. For β=1 the model is transformed to the Langmuir form.
Frenkel-Halsey-Hill (FHH) (Pierce, 1960)	$\ln\left(\frac{C_e}{C_s}\right) = -\frac{\alpha}{RT}\left(\frac{q_s}{q_e^d}\right)^r$	-	-	α, d, and r are isotherm constant (Jmr/mole), the sign of the interlayer spacing (m), and inverse power of distance from the surface (about 3), respectively.
MacMillan–Teller (MET) (Foo and Hameed, 2010)	$q_e = q_s \left(\frac{k}{\ln\left(C_s/C_e\right)}\right)^{1/3}$	-	-	k is an isotherm constant

Table 2.8 Single-component adsorption isotherm models used (continued).

Isotherm types	Equations		Plot to be drawn	Nomenclature
	Nonlinear form	Linear form		
Toth equation (Limousin, 2007)	$q_e = \frac{K_T C_e}{(a_T + C_e)^{1/T}}$	$\ln\left(\frac{q_e}{K_T}\right) = \ln(C_e) - \frac{1}{t}\ln(a_r + C_e)$	$\ln\left(\frac{q_e}{K_T}\right)$ vs $\ln(C_e)$	K_T and a_T are the constants. If a_T=1, Toth isotherm converts to the Langmuir-type isotherm equation.
Flory–Huggins (Jnr and Spiff, 2005)	$\frac{\theta}{C_0} = k_{FH}(1-\theta)^{n_{FH}}$	$\log\left(\frac{\theta}{C_0}\right) = \log(K_{FH}) + n_{FH}\log(1-\theta)$	$\log\left(\frac{\theta}{C_0}\right)$ *vs* $\log(1-\theta)$	θ represents the degree of surface coverage, k_{FH} and n_{FH} represent the equilibrium constant and model exponent.
Koble–Corrigan (Han et al., 2005)	$q_e = \frac{AC_e^n}{1 + BC_e^n}$	$\frac{1}{q_e} = \frac{1}{AC_e^n} + \frac{B}{A}$	-	A, B and n are the isotherm constants. They can be determined from the linear plot using a trial and error optimization.
Dubinin–Radushkevich (Jnr and Spiff, 2005)	$q_e = (q_s)exp(-k_d\varepsilon^2)$	$\ln(q_e) = \ln(q_s) - K_d\varepsilon^2$	$\ln(q_e)$ vs ε^2	k_d is the isotherm constant and the parameter ε can be correlated as: $\varepsilon = RT\ln\left(1 + \frac{1}{C_e}\right)$,where R, T and C_e represent the gas constant (8.314 J/mol K), absolute temperature (K) and adsorbate equilibrium concentration (mg/L), respectively.
Temkin (Jnr and Spiff, 2005)	$q_e = \frac{RT}{b_T}\ln A_T C_e$	$q_e = \frac{RT}{b_T}\ln A_T + \left(\frac{RT}{b_T}\right)\ln C_e$	q_e vs $\ln C_e$	A_T (L/g) and b_T represent the Temkin constants and they can be determined from a plot of q_e against $\ln C_e$.
Khan (Foo and Hameed, 2010)	$q_e = \frac{q_s b_k C_e}{(1 + b_k C_e)^{a_k}}$	-	-	b_k and a_k are the model constant and model exponent, respectively.

2.12 Kinetic modelling of adsorption in a batch system

Several kinetic models were proposed to describe data of adsorption, which can be classified in general as adsorption reaction models and adsorption diffusion models. Both models are used to describe the kinetic process of adsorption; nevertheless, they are somewhat different in nature. The adsorption diffusion models are established on the basis of three successive steps (Lazaridis and Asouhidou, 2003; Ho, 2003; Wu et al., 2009 Zewail and Yousef, 2015):

- Diffusion through the liquid film surrounding the adsorbent particles (i.e. external diffusion or film diffusion.
- Diffusion in the liquid contained in the pores and/or beside the walls of the pores which is named internal diffusion or intra-particle diffusion.
- Adsorption and desorption between the adsorbate and the active sites (i.e. mass action).

Nevertheless, the adsorption reaction models creating from chemical reaction kinetics are based on the whole process of adsorption and does not take into account the above stated steps. Adsorption diffusion models such as the linear driving force rate law was proposed for liquid film diffusion model; homogeneous solid diffusion model (HSDM), the Weber-Morris model, and the Dumwald-Wagner model for intraparticle diffusion model; and the double-exponential model (DEM) was also proposed. Furthurmore, kinetic models based on the adsorption reaction such as the pseudo-first-order expression (Zewail and Yousef, 2015), Ho's second-order equation (Ho, 2003), Elovich equation, and second-order rate equation were proposed. Currently, adsorption reaction models are extensively used to describe the kinetic process of adsorption (Banat et al., 2003; Shin et al., 2004; Hamadi et al., 2004; Aksu and Kabasakal, 2004; Jain et al., 2004; Hameed, 2008; Chen et al., 2008; Tan et al., 2008) and they are reported in Tables 2.9 and 2.10. The advantage of utilizing this kinetic model is that there is no need to know the equilibrium capacity from the experiments, since it can be determined from the model (Ho, 2003; Zewail and Yousef, 2015). Also, the initial rate of adsorption can be calculated from the model. Furthermore, for the design of adsorption process, kinetics studies and dynamic continuous-flow investigations are very important since they provide information on the rate of adsorption uptake of adsorbents, together with the hydrodynamic parameters. According to the

published literature, the adsorption kinetics is very important since it controls the efficiency of the process.

Table 2.9: Reaction kinetic models used for the adsorption reactions (Zewail and Yousef, 2015; Ho, 2003; Wu et al., 2009).

Isotherm types	**Rate equations**		**Graph to be drawn**	**Nomencalture**
	Non-linear form	**Linear form**		
Pseudo-first-order kinetic model	-	$ln(q_e - q_t) = ln\, q_e - k_1 t$	$ln(q_e - q_t)$ vs t	k_1 (min^{-1}) is the pseudo first-order rate constant, q_t and q_e (mg/mg) are the adsorption capacities at time t and equilibrium, respectively, and t (min) is the coagulation time.
Pseudo-second-order kinetic model	$\frac{dq_t}{dt} = k_2(q_e - q_t)^2$	$\frac{t}{q_t} = \frac{1}{k_2 q_e^2} + \frac{1}{q_e} t$	t/q_t vs t	k_2 (L/mg min) is the pseudo-second-order rate constant, q_e (mg/mg) the adsorption capacity of impurity at equilibrium, and q_t (mg/mg) is the adsorption capacity of impurity at time t, and t (min) is the time.
Elovich Equation	$\left(\frac{dq_t}{dt}\right) = aexp(-bq_t)$	$q_t = \left(\frac{1}{b}\right)\ln(ab) + \left(\frac{1}{b}\right)\ln t$	q_t vs $\ln t$	q_t is the amount of impurity removed at time t, and a and b are the constants for this model obtained from the slope and intercept of the linear plot of q_t versus $\ln t$. The constant a is considered as the initial rate.
Second-order kinetic model	$\frac{dC}{dt} = -k_2 C_t^2$	$\frac{1}{C_t} = k_2 t + \frac{1}{C_0}$	$1/C_t$ versus t	C_0 (mg/L) is the initial concentration of solute, C_t (mg/L) the concentration of solute at time t, k_2 (L/mg·min) the rate constant, and t the time (min).

Table 2.10: Diffusion kinetic models used for the adsorption reactions (Tsibranska and Hristova, 2011; Qiu et al., 2009; Boyd et al. 1947).

Isotherm types	Rate equations		Graph to be drawn	Nomencalture
	Non-linear form	Linear form		
Weber–Morris model or intraparticle diffusion model	$= k_{in}\, t^{n} + C$	$q_t = k_{in}\, t^{0.5}$	q_t versus $t^{0.5}$	k_{in} (mg $L^{-1}min^{-1/2}$) is the intraparticle diffusion rate constant, q_t (mg/mg) is the concentration of impurity at time *t*, and *t* (min) is the coagulation time.
Bangham's model	-	$log\left[log\left(\frac{C_0}{C_0 - q_t m}\right)\right] = log\left(\frac{K_0\, m}{2.303\, V}\right) + \alpha \log t$	$log\left[log\left(\frac{C_0}{C_0 - q_t m}\right)\right]$ versus $\log t$	C_0 (mg/L) is the initial concentration of adsorbate in solution, *V* (mL) is the volume of wastewater used, *m* (g/L) is the amount of adsorbent, q_t is the amount of impurity at time *t*, and α (< 1) and K_0 are constants.
Boyd's model	-	$\ln(1 - F) = kt$	-	*k* is the external mass transfer coefficient, $F = \frac{q}{q_e}$ is the fractional approach to equilibrium, and *t* is the time (min)

2.13 Process modelling

Modelling is the use of techniques to analyze complex real-world problems in order to make predictions about what might happen with various actions (Borjeson et al., 2006). Mathematical models development, which forms a better representation of real processes, is the basis for the further development of numerical software for solving complex problems (Saeger and Bishnoi, 1986; Kellner et al., 1999; Law et al., 2000; Bendraou et al., 2005). The objective of every process modelling operation is to optimize, scale-up, and/or design the process under investigation (Robinson, 2004). The Basic requirements for advance process models are a detailed knowledge of the chemical and physical properties of pure components and mixtures involved in the reactions, and mathematical models which in combination allows for the calculation of a process using computers (Rhodes, 1996). The use of predictive methods in process modelling is greatly cheaper than experimental work; predicted properties are normally only used in the early steps of the process development to find first suitable solutions and to reject wrong pathways (Mallaya et al., 1997; Casavant and Coˆté, 2004). In general, models can be categorized as either mechanistic or empirical. In both, leaching of Fe, Al, Si, Mg, and Ca from CFA and pollutants removal from AMD studies, empirical models will be considered.

Furthermore, optimization includes adjusting a process in order to regulate some specified set of parameters without violating some constraints so as to minimize cost, maximizes output, and or effectiveness (Kellner et al., 1999; Bendraou et al., 2005). This constitutes one of the main tools used in most industrial decision making. In the synthesis of CFA–based coagulant, the Fe, Al, Si, Mg, and Ca leaching process using H_2SO_4 solutions will be optimized to obtain high Fe, Al, Si, Mg, and Ca recoveries. Additionally, in wastewater treatment, the coagulation process using CFA–based coagulant will be optimized to obtain high pollutants removal capacity.

2.14 Anterior works

The reaction kinetics between Fe_2O_3 and Al_2O_3 in CFA with H_2SO_4 for the production of a complex sulphate-based coagulant was studied by Fan et al. (2003). It was found that the reaction orders of both Fe_2O_3 and Al_2O_3 in CFA ash with H_2SO_4 are second-order overall with respect to H_2SO_4 concentration, which indicates that the changes of H_2SO_4

concentration have similar effect on the rate of extracting Fe and Al from CFA under certain temperatures. The pre-exponential factor and activation energy of the extracting reaction of Fe from CFA with H_2SO_4 are less than those of the extracting reaction of Al from CFA. Therefore, the reaction temperatures have bigger effects on the extraction of Al than on the extraction of Fe. The empirical Arrhenius expressions of extracting reactions of Fe and Al were derived based on the rate constants obtained at different temperatures.

The production of a sulphate–based complex coagulant containing ferric sulphate and aluminium sulphate from CFA as a raw material was investigated by Fan et al. (2005). Reaction temperature and time strongly affected the concentrations of Fe^{3+} and Al^{3+} in the complex coagulant and the conversion efficiencies for iron and aluminium oxides in CFA. The maximum concentrations of 0.93 M Al^{3+} and 0.58 M Fe^{3+} in the synthesized complex coagulant were obtained at 120 ℃ and after 4 h of reaction time. The prepared coagulant was shown to be effective in reducing the turbidity of kaolin in water suspensions, arsenic concentration in dilute solutions, and chemical oxygen demand (COD) in dilute solutions.

Sui et al. (2009) assessed the feasibility of CFA–based coagulant on tanning wastewater treatment. The coagulant made by CFA and blast furnace iron sludge was prepared using 60 g CFA, 30 g iron sludge, and 150 mL of 3.5 mol/L H_2SO_4 under slow heating conditions; and then combined with polysilicate aluminium (PSA) flocculants. The effects of pH, coagulant concentration, and temperature on coagulation were investigated. It was found that the coagulant was efficient to treat tanning wastewater under the following optimum conditions: pH values in the range of 6 - 9, coagulant concentration: 70 mg/L, stirring speed: 120 rpm, time: 19 min, at room temperature. The rate of removal of COD_{cr}, Cr^{3-}, SS, S^{2-}, and colority in tanning wastewater was 83.3 %, 87.6 %, 93.1 %, 92.8 %, and 90.8 % respectively. The temperature had little impact on the removal rate of COD_{cr}. The produced coagulant was found to be more effective than the conventional coagulants polyaluminium chloride (PAC) and polyferric sulphate (PFS).

Studies were conducted by Li et al. (2009) to produce a complex wastewater coagulant by reacting CFA with sulphuric acid. Authors analysed factors causing conversion effectiveness of Al_2O_3 and Fe_2O_3 from CFA to Al^{3+} and Fe^{3+} ions and evaluated the ability of the produced complex coagulant in the removal of total suspended solid (TSS) and turbidity from wastewater. The effect of pH and coagulant concentration on turbidity and

total suspended solid (TSS) removal were studied. Reaction time and temperature greatly affected the conversion of Al_2O_3 and Fe_2O_3 in CFA. After 6 h of reaction at 130 ^oC the conversion efficiency (ratio of the mass of Al^{3+} or Fe^{3+}in the product to the mass of Al or Fe in CFA) of Al_2O_3 and Fe_2O_3 were 37.48 % and 73 %, respectively. The prepared coagulant was effective in removing turbidity in kaolinite suspended in tap water and TSS in an ethanol fermentation wastewater. The removal of TSS (99 %) occurred at neutral pH 7 with coagulant concentration of 150 - 200 ppm. The turbidity was removed (98.7 - 98.8 %) in the pH range of 7.5 to 8.5 and coagulant concentration of 20 ppm. The coagulation performance of the produced coagulant was higher than the conventional iron and aluminium sulphates at low concentrations.

Menezes et al. (2010) precipitated Fe and Al from acidic coal mine drainage at pH 5.0 and leached them in H_2SO_4 to produce a coagulant consisting of 8.7% Fe and 3.3% Al. Water treatment tests showed that this inexpensive produced coagulant was as effective as the coagulant chemicals conventionally used in water treatment plants. It was also found that the process reduces the sludge waste issues.

Bingtao and Li (2011) investigated the efficiency of CFA–based complex coagulant in removing turbidity and organic impurities in papermaking wastewater and tannage wastewater. CFA was successively leached in H_2SO_4 (2 mol/L), HCl (2 mol/L), and a mixture of H_2SO_4 (1 mol/L) and HCl (1 mol/L) to produce a complex coagulant. It was found that better results can be obtained when H_2SO_4 alone is used to extract Al, and HCl alone to extract Fe and Si from CFA. Therefore, mixture of H_2SO_4 (1 mol/L) and HCl (1 mol/L) were used to produce a CFA coagulant with high content of Al, Fe, and Si. Consequently, high polymeric complex, containing $Fe_2(SO_4)_3$, $Al_2(SO_4)_3$, $FeCl_3$, $AlCl_3$, and H_2SiO_3, can be formed during coagulation process. Results showed that removal rates of ~ 90.0 %, ~ 69.7 %, and ~ 98.6 % for SS, COD, and chrominance respectively can be reached when using coagulant produced from the CFA treated with mixture of H_2SO_4 and HCl. This was much better than the coagulants produced from CFA treated with single H_2SO_4 or HCl. It was also found that the coagulation performance of the produced coagulant is higher than a single $FeCl_3$ and $Al_2(SO4)_3$.

Yan et al. (2012) leached CFA in hydrochloric acid to synthesize coagulants for the treatment of coal washing wastewater. The first coagulant was produced by leaching raw

CFA in HCl solution, the second coagulant was prepared by first calcining the raw CFA in the oven at 800 ˚C for 2 h prior to leaching in HCl solution, and the third coagulant was prepared by first calcining the raw CFA mixed with Na_2CO_3 (100:6 weight ratio of raw CFA: Na_2CO_3) at 800 ˚C for 2 h prior to leaching in HCl solution. Best coagulation performances were obtained using the third coagulant. It was reported that optimum conditions for coal washing wastewater treatment at ambient temperature may be obtained using a coagulant dosage of 10 g/L, initial pH of 9 adjusted by CaO, for 40 min reaction time. Removal efficiency of 99.61 % and 96.48 % were obtained for a solid suspension (SS) and chemical oxygen demand (COD), respectively. The introduced Ca^{2+} and leached Al^{3+} and Fe^{3+} may have improved the coagulation process. However, the distribution of fine particle in the coal washing wastewater makes the wastewater treatment a difficult process and expensive.

Fair and Geramell (1964) developed a simplified mathematical model of floc growth in a stirred suspension using the Smoluchowski equation for orthokinetic coagulation. Particles were supposed to be spherical and to conjoin into spheres of proportionate volume upon contact. The growth of particle is limited to different maximum sizes or multiple volumes, larger particles breaking up into smaller ones which are returned to the system. A smooth growth pattern asymptotically approaching steady-state mean size outcomes when a model parameter of gross contact opportunity is less than 0.04 in magnitude; as it approaches 0.10, the growth pattern becomes oscillatory.

2.15 Summary

Having regard to the literature cited in this chapter, iron and aluminium coagulant production and the AMD treatment processes have been highlighted. Understanding the behavior of H_2SO_4 aqueous solutions containing iron and aluminium is important. It can be noticed from reported studies that process parameters such as reagent concentrations, temperature, and time influence the recovery of these metals. In the other hand, process variables such as coagulant concentrations, pH, time, and stirring speed affect the performance of the coagulant in treating wastewater. The present study will be focusing on the recovery of iron, aluminium, silicon, magnesium, and calcium in H_2SO_4 solution and the treatment of AMD using this solution.

It can also be noticed from previous studies on coagulant synthesis from CFA leaching that the goal of process modelling has not been encouraging. It is necessary to develop mathematical models of Fe, Al, Si, Mg and Ca from CFA, able to predict their dissolution in H_2SO_4 medium. Such mathematical models to be investigated in this research, is by using the Eureqa Newtonian software which is expected to give fitting model equations. Also, the use of the first principle of material balance to predict the dissolution of CFA with time. The development of mathematical models could provide an alternative to laboratory experiments to determine the leaching behaviour of CFA elements for coagulant production, which would encourage an expansion of investment in coagulant synthesis and make the process more economically feasible.

In addition, the performance of the CFA-based complex coagulant in wastewater treatment has limitations in terms of equilibrium capacities and adsorption kinetics of CFA-based coagulant for Al, Fe, Mn, Mg, Ca, Si, Zn, and Ni in aqueous solution. In general, available information on the thermodynamic and kinetic aspects of the adsorption of other elemental compounds onto other hydroxide precipitate-based adsorbents is also very limited. In order to better understand the adsorption process equilibrium and kinetics, a comprehensive study will be conducted in a controlled batch system. Furthermore, using Eureqa Newtonian, this research will attempt to develop mathematical models that will predict the coagulation behaviours of Al, Fe, Mn, Mg, Ca, Si, Zn, and Ni in AMD.

References

Abbaszadegan, M., Mayer, B.K., Ryu, H. and Nwachuku, N., 2007. Efficacy of removal of CCL viruses under enhanced coagulation conditions. *Environmental science & technology*, 41 (3), 971–977.

Aboulhassan, M.A., Souabi, S., Yaacoubi, A., Baudu, M., 2006. Improvement of paint effluents coagulation using natural and synthetic coagulant aids. *Journal of Hazardous Materials* 138, 40–45.

ACAA, 2015. Sustainability Improving Product Performance and Longevity with Coal Ash. *Ash at work.* 42–44.

Adamson, R.J., 1972. Gold Metallurgy in South Africa. Cape & Transvaal Printers Ltd., Cape Town.

Aguilar, M.I., Saez, J., Llorens, M., Soler, Ortuno, J.F., 2002. Nutrient removal and sludge production in the coagulation–flocculation process. *Water Research* 36, 2910–2919.

Aguilar, M.I., Saez, J., Llorens, M., Soler, Ortuno, J.F., Meseguer, V., Fuentes, A., 2005. Improvement of coagulation–flocculation process using anionic polyacrylamide as coagulant aid. *Chemosphere* 58, 47–56.

Ahmaruzzaman, M., 2010. A review on the utilization of fly ash. *Progress in Energy and Combustion Science* 36, 327–363.

Ahmaruzzaman, M., 2011. Industrial wastes as low-cost potential adsorbents for the treatment of wastewater laden with heavy metals. *Advances in Colloid and Interface Science* 166, 36–59.

Aksu, Z. and Kabasakal, E., 2004. Batch adsorption of 2, 4-dichlorophenoxy-acetic acid (2, 4-D) from aqueous solution by granular activated carbon. *Separation and Purification Technology*, 35 (3), 223–240.

Alaerts, G., Wilms, D., Van Haute, A., 1982. Physicochemical Methods for Water and Wastewater Treatment. In: Pawlowski, H (Editor), Studies in Environmental Science 19. Elsevier, Amsterdam, pp 13–41.

Alam, J., Akhtar, M.N., 2011. Fly ash utilization in different sectors in Indian scenario. *International journal of emerging trends in Engineering and Development* 1(1), 1–14.

Allen, S.J., Mckay, G. and Porter, J.F., 2004. Adsorption isotherm models for basic dye adsorption by peat in single and binary component systems. *Journal of colloid and interface science, 280* (2), 322–333.

Amirtharajah, A., Jones, S.C., 2006. Chemical Water and Wastewater Treatment IV. Springer.

Annadurai, G., Sung, S.S., Lee, D.J., 2004. Simultaneous removal of turbidity and humic acid from high turbidity stormwater. *Advances in environmental research* 8 (3–4), 713–725.

Assaad, E., Azzouz, A., Nistor, D., Ursu, A.V., Sajin, T., Miron, D.N., Monette, F., Niquette, P., Hausler. R., 2007. Metal removal through synergic coagulation–flocculation using an optimized chitosan–montmorillonite system. *Applied Clay Science* 37, 258–274.

Aziz, H.A., Alias, S., Assari, A., Adlan, M.N., 2007. The use of alum, ferric chloride and ferrous sulphate as coagulants in removing suspended solids, colour and COD from semi-aerobic landfill leachate at controlled pH. *Waste Manage Resources* 25, 556–565.

Babu, R., Chaudhuri. M., 2005. Home water treatment by direct filtration with natural coagulant. *Journal of Water and Health*, 27–30.

Baes Jr, C.F. and Mesmer, R.E., 1981. Thermodynamics of cation hydrolysis. *American Journal of Science. 281* (7), 935–962.

Banat, F., Al-Asheh, S. and Makhadmeh, L., 2003. Preparation and examination of activated carbons from date pits impregnated with potassium hydroxide for the removal of

methylene blue from aqueous solutions. *Adsorption Science & Technology*, 21 (6), 597–606.

Barbosa, V.F.F., MacKenzie, K.J.D., 2003. Thermal behaviour of inorganic geopolymers and composites derived from sodium polysialate. *Material Research Bulletin* 38, 319–331.

Barnum, D.W., 1983. Hydrolysis of cations. Formation constants and standard free energies of formation of hydroxy complexes. *Inorganic Chemistry*, *22* (16), 2297–2305.

Basha, C.A., Ghosh, P.K., Gajalakshmi, G., 2008. Total dissolved solids removal by electrochemical ion exchange (EIX) process. *Electrochimica Acta* 54 (2), 474–483.

Baskan, M.B. and Pala, A., 2010. A statistical experiment design approach for arsenic removal by coagulation process using aluminum sulfate. *Desalination*, 254 (1-3), 42–48.

Basu, P., 2006. *Combustion and gasification in fluidized beds*. CRC press.

Bellot, J.C., Condoret, J.S., 1993. Modelling of liquid chromatography equilibria. *Process Biochemistry*, *28* (6), 365–376.

Bendraou, R., Gervais, M.P. and Blanc, X., 2005, October. UML4SPM: A UML2. 0-based metamodel for software process modelling. In *International Conference on Model Driven Engineering Languages and Systems* (17–38). Springer, Berlin, Heidelberg.

Benítez, E.I., Genovese, D.B. and Lozano, J.E., 2007. Effect of pH and ionic strength on apple juice turbidity: Application of the extended DLVO theory. *Food hydrocolloids*, 21 (1), 100–109.

Bhatia, S., Othman, Z., Ahmad, A. L., 2007. Coagulation-flocculation process for POME treatment using *Moringa oleifera* seed extract: Optimisation studies. *Chemical Engineering Journal* 133, 205–212.

Bingtao, L., Li, Z., 2011. Experimental Study on Wastewater Treatment by Fly ash Coagulant. *Environmental sciences*, 1363–1366.

Bleier, A. and Matijevic, E., 1976. Heterocoagulotion. I. Interactions of monodispersed chromium hydroxide with polyvinyl chloride latex. *Journal of Colloid and Interface Science*, *55* (3), 510–524.

Blissett, R.S., Rowson, N.A., 2012. A review of the multi-component utilisation of coal fly ash. *Fuel* 97, 1–23.

Borjeson, L., Hojer, M., Dreborg, K.H., Ekvall, T., Finnveden, G., 2006. Scenario types and techniques: Towards a user's guide. *Futures* 38, 723–739.

Bottero, J.Y., Tchoubar, D., Cases, J.M., Fiessinger, F., 1982. Investigation of the hydrolysis of aqueous solutions of aluminum chloride. 2. Nature and structure by small-angle X-ray scattering. *The Journal of Physical Chemistry*, *86* (18), 3667–3673.

Boudart, M., Djéga-Mariadassou, G., 2014. Kinetics of heterogeneous catalytic reactions. Princeton University Press.

Boyd, G.E., Adamson, A.W. and Myers Jr, L.S., 1947. The exchange adsorption of ions from aqueous solutions by organic zeolites. II. Kinetics1. *Journal of the American Chemical Society*, 69 (11), 2836–2848.

Bratby, J., 2006. Coagulation and Flocculation in Water and Wastewater Treatment, Second Edition. Iwa, London.

Bratby, J., 2016. *Coagulation and flocculation in water and wastewater treatment*. IWA publishing.

Broséus, R., Cigana, J., Barbeau, B., Daines-Martinez, C., Suty, H., 2009. Removal of total dissolved solids, nitrates and ammonium ions from drinking water using charge-barrier capacitive deionisation. *Desalination* 249 (1), 217–223.

Brunauer, S., Emmett, P.H. and Teller, E., 1938. Adsorption of gases in multimolecular layers. *Journal of the American chemical society* 60 (2), 309–319.

Casavant, T.E. and Coˆté, R.P., 2004. Using chemical process simulation to design industrial ecosystems. *Journal of Cleaner Production*, *12*(8-10), 901–908.

Chen, Z., Ma, W. and Han, M., 2008. Biosorption of nickel and copper onto treated alga (Undaria pinnatifida): application of isotherm and kinetic models. *Journal of hazardous materials*, 155 (1-2), 327–333.

Chen, J.P., 2012. Decontamination of heavy metals, Processes, Mechanisms, and Applications, CRC Press, US.

Cho, H., Oh, D., Kim, K., 2005. A study on removal characteristics of heavy metals from aqueous solution by fly ash. *Journal of Hazardous Materials* B127, 187–195.

Choi, J.H., Shin, W.S., Lee, S.H., Joo, D.J., Lee, J.D., Choi, S.J., Park, L.S., 2001. Application of Synthetic Polyamine Flocculants for Dye Wastewater Treatment. *Separation Science and Technology* 36, 2945–2958.

Costello, C, 2003. Acid Mine Drainage: Innovative Treatment Technologies, U.S. Environmental Protection Agency Office of Solid Waste and Emergency Response Technology Innovation Office Washington, DC, pp. 1–29.

Dahm, C.N., 1981. Pathways and mechanisms for removal of dissolved organic carbon from leaf leachate in streams. *Canadian journal of fisheries and aquatic sciences* 38 (1), 68–76.

Davini, P., 1995. Investigation of flue gas desulphurization by fly ash and calcium hydroxide mixtures. *Resources, Conservation and Recycling* 15, 193–201.

Davini, P., 1996. Investigation of the SO_2 adsorption properties of $Ca(OH)_2$-fly ash systems. *Fuel* 75, 713–6.

De Abreu, H.A., Guimaraes, L. and Duarte, H.A., 2006. Density-functional theory study of iron (III) hydrolysis in aqueous solution. *The Journal of Physical Chemistry A*, *110* (24), 7713–7718.

Dentel, S.K., 1991. Coagulant control in water treatment. *Critical Reviews in Environmental Science and Technology*, *21*(1), 41–135.

Derjaguin, B.V., Voropayeva, T.N., 1964. Surface forces and the stability of colloids and disperse systems. *Journal of Colloid Science*, *19* (2),113–135.

Dickinson, E., Eriksson, L., 1991. Particle flocculation by adsorbing polymers. *Advances in Colloid and Interface Science*, *34*, 1–29.

Dihang, D., Aimar, P., Kayema, J., Koungou, S.N., 2008. Coagulation and flocculation of laterite suspensions with low levels of aluminium chloride and polyacrylamids. *Chemical Engineering and Processing* 47, 1509–1519.

Duan, J., Gregory, J., 2003. Coagulation by hydrolysing metal salts. *Advances in Colloid and Interface Science* 100–102, 475–502.

Duan, J., Gregory, J., 1998. The influence of silicic acid on aluminium hydroxide precipitation and flocculation by aluminium salts. *Journal of Inorganic Biochemistry, 69* (3), 193–201.

Dwivedi, A., and Jain, M.K., 2014. Fly ash–waste management and overview: A Review. *Recent Research in Science and Technology* 6 (1), 30–35.

Eigen, M., 1964. Proton Transfer, Acid-Base Catalysis, and Enzymatic Hydrolysis. Part I: Elementary processes. *Angewandte Chemie International Edition in English* 3 (1), 1–19.

Erol, M., Kucukbayrak, S., Ersoy-Mericboyu, A., 2008. Comparison of the properties of glass, glass–ceramic and ceramic materials produced from coal fly ash. *Journal of Hazardous Materials* 153, 418–425.

Fair, G.F., and Geramell, R.S., 1964. A Mathematical Model of Coagulation. *Journal of Colloid Science* 19, 360-372.

Fan, M., Brown, R.C., Leeuwen, J.H.V., Nomura, M., Zhuang, Y., 2003. The kinetics of producing sulfate-based complex coagulant from fly ash. *Chemical Engineering and Processing* 42, 1019–1025.

Fan, M., Brown, R.C., Wheelock, T.D., Cooper, A.T., Nomura, M., Zhuang, Y.,2005. Production of a complex coagulant from fly ash. *Chemical Engineering Journal* 106, 269–277.

Farley, K.J., Dzombak, D.A., Morel, F.M., 1985. A surface precipitation model for the sorption of cations on metal oxides. *Journal of Colloid and Interface Science 106* (1), 226–242.

Fernandez, J.F. and Sanchez, C.R., 2002. Rate determining step in the absorption and desorption of hydrogen by magnesium. *Journal of Alloys and Compounds*, 340 (1-2), 189–198.

Fiol, N., Villaescusa, I., Martínez, M., Miralles, N., Poch, J. and Serarols, J., 2006. Sorption of Pb (II), Ni (II), Cu (II) and Cd (II) from aqueous solution by olive stone waste. *Separation and Purification technology*, 50 (1), 132–140.

Foo, K.Y. and Hameed, B.H., 2010. Insights into the modeling of adsorption isotherm systems. *Chemical engineering journal*, *156* (1), 2–10.

Forryan, C.L., Klymenko, O.V., Brennan, C.M. and Compton, R.G., 2005. Reactions at the Solid− Liquid Interface: Surface-Controlled Dissolution of Solid Particles. The Dissolution of Potassium Bicarbonate in Dimethylformamide. *The Journal of Physical Chemistry B*, 109 (7), 2862–2872.

Fytianos, K., Voudrias, E., Raikos, N., 1998. Modelling of phosphorus removal from aqueous and wastewater samples using ferric iron. *Environmental Pollution* 101, 12–130.

Ghernaout, D. and Ghernaout, B., 2012. Sweep flocculation as a second form of charge neutralisation—a review. *Desalination and Water Treatment*, 44 (1-3), 15–28.

Giere, R., Carleton, L.E., Lumpkin, G.R., 2003. Micro and nanochemistry of fly ash from a coal fired power plant. *American Mineralogist* 88, 1853–1865.

Gitari W.M., Petrik L.F., Etchebers O., Key D.L., Okujeni C., 2008. Utilization of fly ash for treatment of coal mines wastewater: Solubility controls on major inorganic contaminants. *Fuel* 87, 2450–2462.

Gollakota, A.R., Volli, V. and Shu, C.M., 2019. Progressive utilisation prospects of coal fly ash: A review. *The Science of the total environment*, 672, 951-989.

Golob, V., Vinder, A., Simonic, M., 2005. Efficiency of the coagulation/flocculation method for the treatment of dye bath effluents. *Dyes Pigments* 67, 93–97.

Gonzalez A, Navia R, Moreno, N., 2009. Fly ashes from coal and petroleum coke combustion: current and innovative potential applications. *Waste Manage Resources* 27(10), 976–987.

Gregory, J., Dupont, V., 2001. Properties of flocs produced by water treatment coagulants. *Water Science and Technology*, *44* (10), 231–236.

Grosjean, M.H., Roué, L., 2006. Hydrolysis of Mg–salt and MgH2–salt mixtures prepared by ball milling for hydrogen production. *Journal of alloys and compounds*, *416* (1–2), 296–302.

Gupta, M., Singh, S.P., 2013. Fly ash production and its utilization in different countries. *Ultra Chemistry* 9(1), 156–160.

Habashi, F., 1999. Kinetics of the Metallurgical Processes. Les copies de la Capitale, Québec City.

Haiying, Z., Youcai, Z., Jingyu, Q.,2007. Study on use of MSWI fly ash in ceramic tile. *Journal of Hazardous Materials* 141, 106–114.

Hamadi, N.K., Swaminathan, S. and Chen, X.D., 2004. Adsorption of paraquat dichloride from aqueous solution by activated carbon derived from used tires. *Journal of Hazardous Materials*, 112 (1-2), 133–141.

Hameed, B.H., Mahmoud, D.K. and Ahmad, A.L., 2008. Equilibrium modeling and kinetic studies on the adsorption of basic dye by a low-cost adsorbent: Coconut (Cocos nucifera) bunch waste. *Journal of Hazardous Materials,* 158 (1), 65–72.

Han, R., Zhang, J., Zou, W., Shi, J. and Liu, H., 2005. Equilibrium biosorption isotherm for lead ion on chaff. *Journal of Hazardous materials 125* (1-3), 266–271.

Heidrich, C., Feuerbon, H.J., Weir, A., 2013. Coal Combustion Products: a Global Perspective. *2013World Coal Ash (WOCA) Conference.* http://www.flyash.info/.

Hendrawati, Yuliastri, I.R., Nurhasni, Rohaeti, E., Effendi, H., Darusman, L.K., 2016. The use of Moringa Oleifera Seed Powder as Coagulant to Improve the Quality of Wastewater and Ground Water. *Earth and Environmental Science* 31,1–10.

Henry, M., Jolivet, J.P., and Livage, J., 1992. Aqueous chemistry of metal cations: hydrolysis, condensation and complexation. In *Chemistry, Spectroscopy and Applications of Sol-Gel Glasses*. Springer, Berlin, Heidelberg.

Hequet, V., Ricou. P., Lecuyer. I., Le Cloirec. P., 2001. Removal of Cu^{2+} and Zn^{2+} in aqueous solutions by sorption onto mixed fly ash. *Fuel* 80, 851–856.

Hlabangana, N., Bhebhe, S., Mguni, N.G., Danha, G. and Tshuma, J., 2018. Optimisation of the leaching Parameters of a gold ore in sodium cyanide solution. *International Journal of Engineering Research and Reviews*, 1–10.

Ho, Y.S., Huang, C.T. and Huang, H.W., 2002. Equilibrium sorption isotherm for metal ions on tree fern. Process Biochemistry, 37 (12), pp.1421-1430.

Ho, Y.S., 2003. Removal of copper ions from aqueous solution by tree fern. *Water research 37* (10), 2323–2330.

Horn, R.G., 1990. Surface forces and their action in ceramic materials. *Journal of the American Ceramic Society*, *73* (5), 1117–1135.

Hosny, R., Fathy, M., Ramzi, M., Moghny, T.A., Desouky, S.E.M. and Shama, S.A., 2016. Treatment of the oily produced water (OPW) using coagulant mixtures. *Egyptian Journal of Petroleum*, 25 (3), 391-396.

Hu, C., Liu, H., Qu, J., 2005. Preparation and characterization of polyaluminum chloride containing high content of Al13 and active chlorine. *Colloids and Surfaces A: Physicochem. Eng. Aspects* 260, 109–117.

Inada, M., Tsujimoto, H., Eguchi, Y., Enomoto, N. and Hojo, J., 2005. Microwave-assisted zeolite synthesis from coal fly ash in hydrothermal process. *Fuel*, 84 (12-13), 1482–1486.

Ikeda, T., Boero, M., Terakura, K., 2007. Hydration properties of magnesium and calcium ions from constrained first principles molecular dynamics. *The Journal of Chemical Physics*, 127, 1–8.

Israelachvili, J., 1992. Intermolecular and Surface Forces 2nd edn (New York: Academic).

Itskos, G, Koukouzas, N, Vasilatos, C, Megremi, I, Moutsatsou, A., 2010. Comparative uptake study of toxic elements from aqueous media by the different particle size-fractions of fly ash. *Journal of Hazardous Materials* 183, 787–792.

Iyer, R.S., Scott, J.A., 2001. Power station fly ash—a review of value-added utilization outside of the construction industry. *Resources, Conservation and Recycling* 31, 217–228.

Jackson, V.E., Felmy, A.R., Dixon, D.A., 2015. Prediction of the pKa's of Aqueous Metal Ion +2 Complexes. *Journal of Physical Chemistry* 119, 2926−2939.

Jain, A.K., Gupta, V.K., Jain, S. and Suhas, 2004. Removal of chlorophenols using industrial wastes. *Environmental science & technology*, 38 (4), 1195–1200.

Jala, S., Goyal, D., 2006. Fly ash as a soil ameliorant for improving crop production—a review. *Bioresource Technology* 97, 1136–1147.

Jnr, M.H. and Spiff, A.I., 2005. Equilibrium sorption study of Al3+, Co2+ and Ag+ in aqueous solutions by fluted pumpkin (Telfairia occidentalis HOOK f) waste biomass. *Acta Chimica Slovenica 52*, 174–181.

Johnson, D.B., Hallberg, K.B., 2005. Acid mine drainage remediation options: a review. *Science of the Total Environment* 338, 3–14.

Johnson, P.D., Girinathannair, P., Ohlinger, K.N., Ritchie, S., Teuber, L., Kirby, J., 2008. Enhanced Removal of Heavy Metals in Primary Treatment Using Coagulation and Flocculation. *Water Environment Research* 80, 472–479.

Joo, D.J., Shin, W.S., Young-Hun Kim, Y.H., Kim, J.H., Choi, J.H., Choi, S.J., Park, L.S., 2003. Effect of Polyamine Flocculant Types on Dye Wastewater Treatment. *Separation Science and Technology* 38, 661–678.

Kalyoncu, R.S., 2000. Coal Combustion Products. U.S. Geological Survey Minerals Yearbook.

Karatza, D., Lancia, A., Musmarra, D., 1998. Fly ash capture of mercuric chloride vapors from exhaust combustion gas. *Environmental Science and Technology* 32, 3999–4004.

Kellner, M.I., Madachy, R.J., Raffo, D.M., 1999. Software process simulation modeling: Why? What? How? *Journal of Systems and Software* 46, 91–105.

Kelmers, A.D., Egan, B.Z., Seeley, F.G., Campbell, G.D., 1981. Direct acid dissolution of aluminium and other metals from fly ash. *The Metallurgical Society of AIME, TMS paper A* 81–24.

Kikuchi, R., 1999. Application of coal ash to environmental improvement—transformation into zeolite, potassium fertilizer, and FGD absorbent. *Resources, Conservation and Recycling* 27, 333–346.

Kleinhans, U., Wieland, C., Frandsen, F.J. and Spliethoff, H., 2018. Ash formation and deposition in coal and biomass fired combustion systems: Progress and challenges in the field of ash particle sticking and rebound behaviour. *Progress in energy and combustion science*, 68, 65–168.

Kragh, A.M., Langston, W.B., 1962. The flocculation of quartz and other suspensions with gelatine. *Journal of Colloid Science*, *17* (2), 101–123.

Krupinska, K., 2014. Effect of the type of aluminium coagulant on effectiveness at removing pollutants from groundwater in the process of coagulation. *The 9th International Conference "Environmental Engineering,* Article number: enviro.2014.082.

Kumar, K.V. and Sivanesan, S., 2007. Sorption isotherm for safranin onto rice husk: Comparison of linear and non-linear methods. *Dyes and Pigments*, *72* (1), 130–33.

Kuyucak, N., 1999. Acid mine drainage prevention and control options, Mine. *Water and Environment*, IMWA Congress.

Law, A.M., Kelton, W.D. and Kelton, W.D., 2000. *Simulation modeling and analysis* (Vol. 3). New York: McGraw-Hill.

Lazaridis, N.K. and Asouhidou, D.D., 2003. Kinetics of sorptive removal of chromium (VI) from aqueous solutions by calcined Mg–Al–CO3 hydrotalcite. *Water Research*, 37 (12), 2875–2882.

Leopold, P. and Freese, S., 2009. *A simple guide to the chemistry, selection and use of chemicals for water and wastewater treatment*. Pretoria: Water Research Commission.

Li, L., Fan, M., Brown, R.C., Koziel, J.A., Leeuwen, J. H., 2009. Production of a new wastewater treatment coagulant from fly ash with concomitant flue gas scrubbing. *Journal of harzardous Materials* 162, 1430–1437.

Liew, A.G., Noor, M.J. M. M., Muyibi, S.A. Fugara, A.M.S., Muhammed, T.A., Iyuke, S.E., 2006. *International Journal of Environmental Studies* 63 (2), 211–219.

Limousin, G., Gaudet, J.P., Charlet, L., Szenknect, S., Barthes, V. and Krimissa, M., 2007. Sorption isotherms: a review on physical bases, modeling and measurement. *Applied geochemistry*, *22* (2), 249–275.

López-Delgado, A., Pérez, C. and Lopez, F.A., 1998. Sorption of heavy metals on blast furnace sludge. *Water Research*, *32* (4), 989–996.

Mahler, J., Persson, I., 2012. A Study of the Hydration of the Alkali Metal Ions in Aqueous Solution. *Inorganic chemistry* 51, 425−438.

Mallaya, J.U., Zitney, S.E., Choudhary, S., Stadtherr, M.A., 1997. Parallel frontal solver for large-scale process simulation and optimization. *AIChE Journal* 43, 1032–1040.

Manahan, S.E., 2009. Fundamentals of environmental chemistry, Third edition. CRC Press, New York.

Mandal, H.K., 2014. Influence of wastewater pH on turbidity. *International Journal of Environmental Research and Development*, 4 (2), 105–114.

Manios, T., Stentiford, E.I., Millner, P., 2003. Removal of Total Suspended Solids from Wastewater in Constructed Horizontal Flow Subsurface Wetlands. *Journal of environmental science and health* 38 (6), 1073–1085.

Manoharan, V., Yunusa, I.A.M., Loganathan, P., Lawrie, R., Skilbeck, C.G., Burchett, M.D., Murray, B.R., Eamus, D., 2010. Assessments of Class F fly ashes for amelioration of soil acidity and their influence on growth and uptake of Mo and Se by canola. *Fuel* 89, 3498–3504.

Manz O.E, 1999. Coal fly ash: a retrospective and future look. *Fuel* 78 (2): 133–136.

Matijević, E., 1973. Colloid stability and complex chemistry. *Journal of Colloid and Interface Science*, *43* (2), 217–245.

Menezes, J.C.S.S., Silva, R.A., Arce, I.S., Schneider, I.A.H., 2010. Production of a polyalumino-iron sulphate coagulant by chemical precipitation of a coal mining acid drainage. *Minerals Engineering* 23, 249–251.

Menzies, N.W., Aitken, R.L., 1996. Evaluation of fly ash as a component of potting substrates. *Scientia Horticulturae* 67, 87–99.

Meshram, P., Pandey, B.D. and Mankhand, T.R., 2015. Recovery of valuable metals from cathodic active material of spent lithium ion batteries: Leaching and kinetic aspects. *Waste management*, 45, 306–313.

Miller, S.M., Fugate, E.J., Craver, V.O., Smith, J.A., Zimmerman, J.B., 2008. Toward Understanding the Efficacy and Mechanism of Opuntia spp. as a Natural Coagulant for Potential Application in Water Treatment. *Environmental Science & Technology* 42, 4274–4279.

Mirsal, I., 2008. *Soil pollution: origin, monitoring & remediation*. Springer Science & Business Media.

Mishra, M.K., Karanam, U.M.R., 2006. Geotechnical characterisation of fly ash composites for backfilling mine voids. *Geotechnical and Geological Engineering* 24, 1749–1765.

Missana, T. and Adell, A., 2000. On the applicability of DLVO theory to the prediction of clay colloids stability. *Journal of Colloid and Interface Science*, *230* (1), 150–156.

Mohammed, O.F., Pines, D., Dreyer, J., Pines, E. and Nibbering, E.T., 2005. Sequential proton transfer through water bridges in acid-base reactions. *Science*, *310* (5745), 83–86.

Mohan, S, Gandhimathi, R., 2009. Removal of heavy metal ions from municipal solid waste leachate using coal fly ash as an adsorbent. *Journal of Hazardous Materials* 169, 351–359.

Mohapatra, M., Khatun, S. and Anand, S., 2009. Kinetics and thermodynamics of lead (II) adsorption on lateritic nickel ores of Indian origin. *Chemical Engineering Journal*, 155 (1), 184–190.

Muthuraman, G., Sasikala, S., 2014. Removal of turbidity from drinking water using natural coagulants. *Journal of Industrial and Engineering Chemistry* 20 (4), 1727–1731.

Na, J.G., Jeong, B.H., Chung, S.H., Kim, S.S., 2006. Pyrolysis of low-density polyethylene using synthetic catalysts produced from fly ash. *Journal of Material Cycles and Waste Management* 8, 126–132.

Ncibi, M.C., 2008. Applicability of some statistical tools to predict optimum adsorption isotherm after linear and non-linear regression analysis. *Journal of Hazardous Materials, 153* (1-2), 207–212.

Ngah, W.W. and Hanafiah, M.A.K.M., 2008. Removal of heavy metal ions from wastewater by chemically modified plant wastes as adsorbents: a review. *Bioresource technology*, 99 (10), 3935–3948.

Nhan, C.T., Graydon, J.W., Kirk, D.W., 1996. Utilizing coal fly ash as a landfill barrier material. *Waste Managemen*t 16, 587–595.

Nickel, J.B., 1946. Coagulation with Ferric Sulfate. *American Water Works Association* 38, 755–760.

Ntengwe, F.W., 2010. The leaching of dolomitic-copper ore using sulphuric acid under controlled conditions. *Open Mineral Processing Journal*, *3*, 60-67.

Ohshima, H., 2006. Theory of Colloid and Interfacial Electric Phenomena. Academic Press, London.

Packham, R.F., 1965. Some studies of the coagulation of dispersed clays with hydrolyzing salts. *Journal of colloid science*, *20* (1), 81–92.

Pálinkás, G., Heinzinger, K., 1986. Hydration shell structure of the calcium ion. *Chemical Physics Letters*, 126 (3–4), 251–254.

Panday, K.K., Prasad, G., Singh, V.N., 1985. Copper(II) removal from aqueous solutions by fly ash. *Water Research* 19, 869 HYDRATION SHELL STRUCTURE OF THE CALCIUM ION 873.

Pandey, V.C., Singh, N., 2010. Impact of fly ash incorporation in soil systems. *Agriculture, Ecosystems and Environment* 136, 16–27.

Panias, D., Giannopoulou, I.P., Perraki, T., 2007. Effect of synthesis parameters on the mechanical properties of fly ash-based geopolymers. *Colloids and Surfaces A: Physicochem. Eng. Aspects* 301, 246–254.

Peng, F., Liang, K.M., Hu, A.M., 2005. Nano-crystal glass–ceramics obtained from high alumina coal fly ash. *Fuel* 84, 341–346.

Persson, I., 2010. Hydrated metal ions in aqueous solution: How regular are their structures? *Pure and Applied Chemistry* 82 (10), 1901–1917.

Pierce, C., 1960. The Frenkel-Halsey-Hill adsorption isotherm and capillary condensation. *The Journal of Physical Chemistry*, *64* (9) 1184–1187.

Pilling, M.J. and Seakins, P.W., 1996. *Reaction kinetics*. Oxford University Press.

Querol, X., Moreno, N., Umana, J.C., Alastuey, A., Hernandez, E., Lopez-Soler, A., Plana, F., 2002. Synthesis of zeolites from coal fly ash: an overview. *International Journal of Coal Geology* 50, 413–423.

Qiu, H., Lv, L., Pan, B.C., Zhang, Q.J., Zhang, W.M. and Zhang, Q.X., 2009. Critical review in adsorption kinetic models. *Journal of Zhejiang University-Science A*, 10 (5), 716–724.

Radke, C.J. and Prausnitz, J.M., 1972. Thermodynamics of multi-solute adsorption from dilute liquid solutions. *AIChE Journal*, *18*(4), 761–768.

Randtke S.J., 1988. Organic Contaminant Removal by Coagulation and Related Process Combinations. *American Water Works Association*, 41–56.

Rao, P.V., 2005. Textbook of Environmental Engineering. Jay Print Pack, New Delhi.

Rengaraj, S., Moon, S.H., 2002. Kinetics of adsorption of Co (II) removal from water and wastewater by ion exchange resins. *Water research 36* (7), 1783–1793.

Renou, S., Givaudan, j.g., Poulain, S., Dirassouyan, F., Moulin, P., 2008. Landfill leachate treatment: Review and opportunity. *Journal of Hazardous Materials* 150, 468–493.

Rhodes, C.L., 1996. The Process Simulation Revolution: Thermophysical Property Needs and Concerns. *Journal of Chemical Engineering Data* 41, 947-950.

Richens, D.T., 1997. The Chemistry of Aqua Ions, Wiley, Chichester.

Rimstidt, J.D., Barnes, 1980. The kinetics of silica-water reactions. *Geochimica et Cosmochimica Acta*, *44* (11), 1683–1699.

Robinson, R., 2004. Simulation: The Practice of Model Development and Use. John Wiley & Sons, England.

Rose, A.L., Waite, T.D., 2003. Kinetics of hydrolysis and precipitation of ferric iron in seawater. *Environmental science & technology*, *37* (17), 3897–3903.

Rovatti, M., Peloso, A., Ferraiolo, G., 1988. Susceptibility to regeneration of fly ash as an adsorbent material. *Resources, Conservation and Recycling* 1, 137–143.

Rubel, A., Andrews, R., Gonzalez, R., Groppo, J., Robl, T., 2005. Adsorption of Hg and NOx on coal by-products. *Fuel* 84, 911–916.

Rutto, H. and Enweremadu, C., 2012. Dissolution of a South African calcium-based material using urea: An optimized process. *Korean Journal of Chemical Engineering* 29 (1), 1–8.

Sadar, M.J., 1998. Turbidity science. Technical Information Series—Booklet no. 11. *Hach Co. Loveland CO*, *7*, 8.

Saeger, R.B., and Bishnoi, P.R., 1986. A modified “inside-out” algorithm for simulation of multistage multicomponent separation processes using the UNIFAC group-contribution method. *Canadian Journal of Chemical Engineering* 64, 759–767.

Sarkar, A, Rano, R., Mishra, K., Sinha, I., 2005. Particle size distribution profile of some indian fly ash – a comparative study to assess their possible uses. *Fuel Processing Technology* 86, 1221–1238.

Schmidt, T., Lothenbach, B., Romer, M., Scrivener, K., Rentsch, D., Figi, R., 2008. A thermodynamic and experimental study of the conditions of thaumasite formation. *Cement and Concrete Research*, 38 (3), 337–349.

Seidel, A., Zimmels, Y., 1998. Mechanism and kinetics of aluminum and iron leaching from coal fly ash by sulfuric acid. *Chemical Engineering Science* 53 (22), 3835–3852.

Semerjian, L., Ayoub, G.M., 2003. High-pH-magnesium coagulation-flocculation in wastewater treatment. *Advances in Environmental Research* 7, 389–403.

Senanayake, G., 2004. Gold leaching in non-cyanide lixiviant systems: critical issues on fundamentals and applications. *Minerals Engineering*, *17* (6), 785–801.

Senapati, M. R., 2011. Fly ash from thermal power plants–waste management and overview. *Current Science* 100 (12), 1791–1794.

Shammas, N.K., 2005. Physicochemical Treatment Processus, Handbook of Environmental Engineering 3. Springer.

Shin, E.W., Han, J.S., Jang, M., Min, S.H., Park, J.K. and Rowell, R.M., 2004. Phosphate adsorption on aluminum-impregnated mesoporous silicates: surface structure and behavior of adsorbents. *Environmental science & technology*, 38 (3), 912–917.

Siriwardane, H.J., Kannan, R.S.S., Ziemkiewicz, P.F., 2003. Use of Waste Materials for Control of Acid Mine Drainage and Subsidence. *Journal of Environmental Engineering* 129 (10), 910–915.

Snowden, M.J., Clegg, S.M., Williams, P.A. and Robb, I.D., 1991. Flocculation of silica particles by adsorbing and non-adsorbing polymers. *Journal of the Chemical Society, Faraday Transactions*, *87* (14), 2201–2207.

Sokić, M.D., Marković, B. and Živković, D., 2009. Kinetics of chalcopyrite leaching by sodium nitrate in sulphuric acid. *Hydrometallurgy*, 95 (3), 273–279.

Spears D.A., Lee S., 2015. Geochemistry of leachates from coal ash. Available at http://sp.lyellcollection.org/. Accessed March 2018.

Stander G. J., Se., D., Henzen, M.R., Se., M., Funke, J.W., 1970. The disposal of polluted effluents from Mining, Metallurgical and Metal Finishing Industries, their effects on receiving water and remedial measures. *Journal of the South African Institute of Mining and Metallurgy*, 95–103.

Stechemesser, H. and Dobiáš, B., 2005. *Coagulation and flocculation*. Taylor & Francis.

Stumm, W. and Morgan, J.J., 1962. Chemical aspects of coagulation. *Journal-American Water Works Association*, *54* (8), 971–994.

Stumm, W., 1992. Chemistry of the solid-water interface: processes at the mineral-water and particle-water interface in natural systems. John Wiley & Son Inc.

Sui, Z., Qiao, C., Zhao, X., Qiang, X., 2009. Application of Fly ash-based coagulant in tanning wastewater treatment. Available at http://www.aaqtic.org.ar/congresos/china2009/download/2-5/2-196.pdf. Accessed Jun 2019.

Sumer, M., 2012. Compressive strength and sulfate resistance properties of concretes containing Class F and Class C fly ashes. *Construction and Building Materials*, 34, 531–536.

Sun, T., Sun, C.H., Zhu, G.L., Miao, X.J., Wu, C.C., Lv, S.B., Li, W.J., 2011. Preparation and coagulation performance of poly-ferric-aluminum-silicate-sulfate from fly ash. *Desalination* 268, 270–275.

Tan, I.A.W., Ahmad, A.L. and Hameed, B.H., 2008. Adsorption of basic dye on high-surface-area activated carbon prepared from coconut husk: Equilibrium, kinetic and thermodynamic studies. *Journal of hazardous materials*, 154 (1-3), 337–346.

Tatsi, A.A., Zouboulis, A.I., Matis, K.A., Samaras, P., 2003. Coagulation-flocculation pretreatment of sanitary landfill leachates. *Chemosphere*, 53, 737–744.

Teh, C.Y., Budiman, P.M., Shak, K.P.Y. and Wu, T.Y., 2016. Recent advancement of coagulation–flocculation and its application in wastewater treatment. *Industrial & Engineering Chemistry Research*, 55 (16), 4363–4389.

Tossell, J.A., 2005. Theoretical study on the dimerization of Si (OH) 4 in aqueous solution and its dependence on temperature and dielectric constant. *Geochimica et Cosmochimica Acta*, 69 (2), 283–291.

Tsibranska, I. and Hristova, E., 2011. Comparison of different kinetic models for adsorption of heavy metals onto activated carbon from apricot stones. *Bulg Chem Commun*, 43 (3), 370–377.

Vassilev S.V., Vassileva C.G., 2005. Methods for characterization of composition of fly ashes from coal-fired power stations: a critical overview. *Energy Fuels* 19 (3),1084–1098.

Vassileva, S.V., Menendez, R., Alvarez, D., Diaz-Somoano, M., Martinez-Tarazona, M.R., 2003. Phase-mineral and chemical composition of coal fly ashes as a basis for their multicomponent utilization. 1. Characterization of feed coals and fly ashes. *Fuel* 82, 1793–1811.

Vassilev, S.V., Vassileva, C.G., 1996. Occurrence, abundance and origin of minerals in coals and coal ashes. *Fuel Processing Technology* 48, 85–106.

Verma, A.K., Dash, R.R. and Bhunia, P., 2012. A review on chemical coagulation/flocculation technologies for removal of colour from textile wastewaters. *Journal of environmental management*, 93 (1), 154–168.

Verma, A., Wei, X. and Kusiak, A., 2013. Predicting the total suspended solids in wastewater: a data-mining approach. *Engineering Applications of Artificial Intelligence*, 26 (4), 1366–1372.

Verwey, E.J.W., Overbeek, J.T.G. and Overbeek, J.T.G., 1999. *Theory of the stability of lyophobic colloids*. Courier Corporation.

Vinai, R., Lawane, A., Minane, J.R., Amadou, A., 2013. Coal combustion residues valorisation: Research and development on compressed brick production. *Construction and Building Materials* 40, 1088–1096.

Wang, S., 2008. Application of solid ash-based catalysts in heterogeneous catalysis. *Environmental Science Technology* 42(19), 7055–7063.

Wang, S., Wu, H., 2006. Review Environmental-benign utilisation of fly ash as low-cost adsorbents. *Journal of Hazardous Materials* B136, 482–501.

Weiss, N.L., 1985. SME Mineral Processing Handbook, volume 2. Kingsport, TN, USA.

Wright, M.R., 2005. *Introduction to chemical kinetics*. John Wiley & Sons.

Yan, L., Wang, Y., Ma, H., Han, Z., Zhang, Q., Chen, Y., 2012. Feasibility of fly ash-based composite coagulant for coal washing wastewater treatment. *Journal of Hazardous Materials* 203–204, 221–228.

Yao, Z.T., Ji, X.S., Sarker, P.K., Tang, J.H., Ge, L.Q., Xia, M.S. and Xi, Y.Q., 2015. A comprehensive review on the applications of coal fly ash. *Earth-Science Reviews*, 141, 105–121.

Wu, F.C., Tseng, R.L., Juang, R.S., 2009. Characteristics of Elovich equation used for the analysis of adsorption kinetics in dye-chitosan systems. *Chemical Engineering Journal 150* (2–3), 366–373.

Zewail, T.M., Yousef, N.S., 2015. Kinetic study of heavy metal ions removal by ion exchange in batch conical air spouted bed. *Alexandria Engineering Journal*, *54* (1), 83–90.

CHAPTER 3
EXPERIMENTAL METHODOLOGY

3.1 Introduction

This chapter provides the basic concepts and experimental techniques used in this study. Furthermore, fundamental principles and practical applications of instrumental techniques used are discussed. Coagulant synthesis experiments done in this study were applied to the coal fly ash (CFA) sample. X-ray diffraction spectroscopy (XRD), x-ray fluorescence spectroscopy (XRF), fourier-transform infrared spectroscopy (FTIR), scanning electron microscopy combined with energy dispersive x-ray spectrometry (SEM/EDS), and particle size distribution (PSD), inductively coupled plasma optical emission spectroscopy (ICP-OES), and optical microscopy techniques were used for characterization of the raw and treated CFA, the raw and treated acid mine drainage (AMD), and the flocs size. The coagulant was produced in the laboratory of the School of Mining, Metallurgy and Chemical Engineering at the University of Johannesburg by direct sulphuric acid pressure leaching method for the recovery of iron, aluminium, and other elements from CFA. Coagulation tests carried out in this research were applied to AMD sample in the laboratory of the School of Mining, Metallurgy and Chemical Engineering at the University of Johannesburg.

3.2 Materials and methods

The CFA was the raw material used for the coagulant synthesis process, whereas AMD was the raw material for the coagulation process. The CFA sample was collected from the electrostatic precipitators of the Kendal power plant located in Mpumalanga province, South Africa; while the AMD sample was obtained from the comprehensive wastewater discharged from coal mine of Witbank in Mpumalanga Province of South Africa. Before coagulant synthesis and coagulation performance tests, both the CFA and AMD samples were characterized. A summary of the experimental methods and analytical techniques used in this study is illustrated in Figure 3.1.

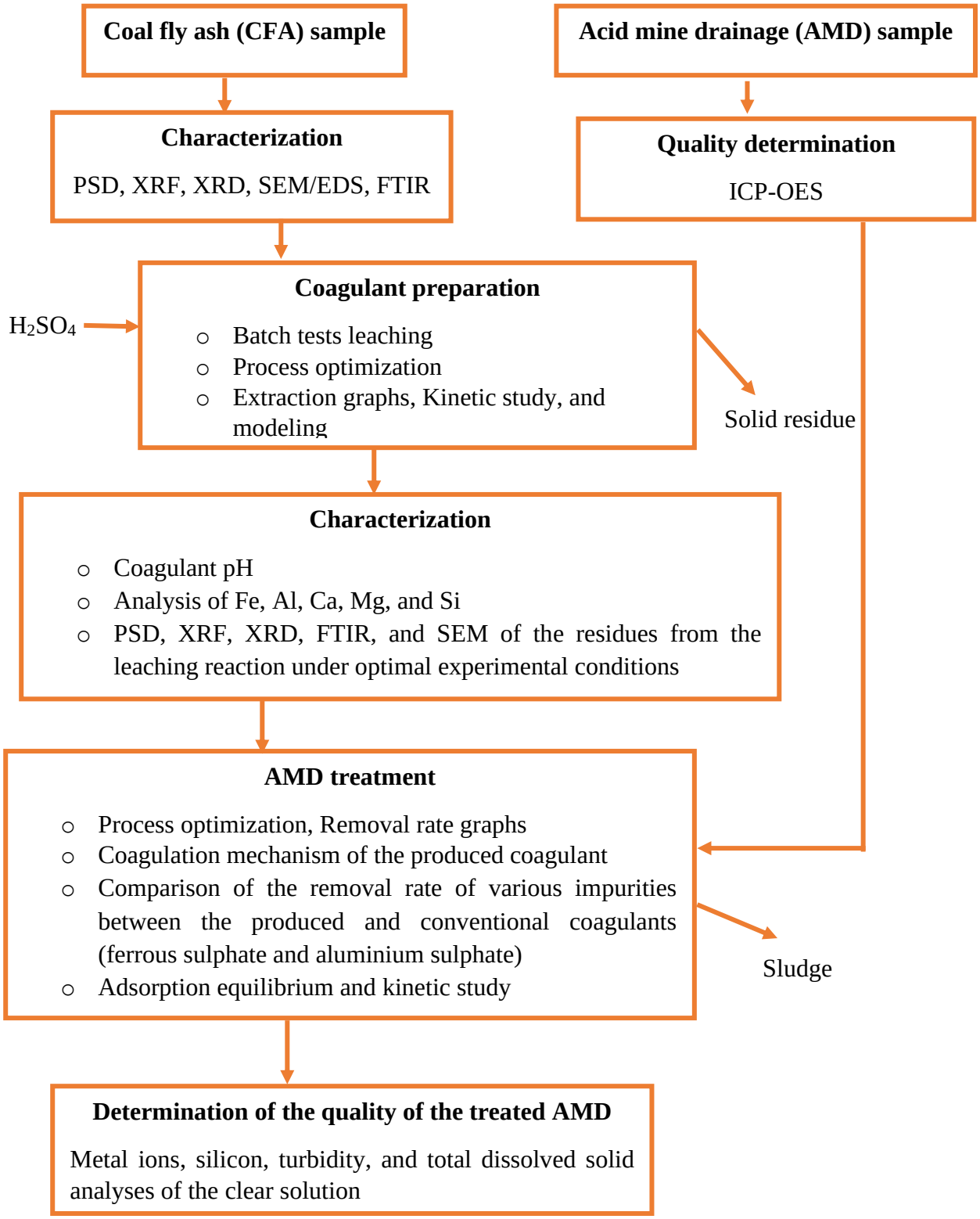

Figure 3.1: Flow diagram depicting the experimental and analytical methods.

3.3 Analytical techniques

The following analytical techniques were used for the characterization of raw and treated CFA:

- Particle size distribution (PSD),
- X-ray diffraction spectroscopy (XRD),
- X-ray fluorescence spectroscopy (XRF),
- Fourier-transform infrared spectroscopy (FTIR),
- Scanning electron microscopy combined with energy dispersive x-ray spectrometry (SEM/EDS),

And for the raw and treated AMD, an inductively coupled plasma optical emission spectroscopy (ICP-OES) technique was used. Optical microscopy was used for the floc size measurement.

3.3.1 Coal fly ash sample preparation

The sample preparation for chemical analysis, such as XRD, XRF and FTIR was performed by splitting a large amount of CFA into smaller quantities, in order to provide a representative sample for characterization. The spinning riffler was used to produce the representative sample used in this investigation. The bulk CFA sample was poured evenly into the hopper (funnel). The material flows through the vibratory dispenser for distribution to the dividing head and collection vessels. At each operation, the feed sample is divided into representative subsamples. The operation was repeated three times to obtain a representative sample which was used in further analytical techniques. The spinning rifflers uses the rotational motion, which provide an efficient, accurate and equal sampling for bulk materials (Allen, 2013). The fed amount of CFA sample in the spinning rifflers varied from the amount collected from the equipment after the splitting process of each run. The starting amount for the first run was 1000 g of CFA.

The CFA sample used for the synthesis of coagulant by H_2SO_4 leaching process contains a wide particle size distribution. The surface area of the interface is an important factor in the rate of electrons transfer during the dissolution process; the rate of leaching is fast with the finely ground particles than with coarse particles because of the large surface area in the fine

particles. In order to release the minerals so that they are accessible to the lixiviant, the CFA was milled to fine particles. The size for CFA particle was determined later during the particle size distribution.

3.3.2 Particle size distribution

The PSD was determined using Microtrac S3500 particle size analyzer. The Microtrac S3500 conforms to ISO 13320 and consists of different modules for dry and wet analysis. The Sample Distribution Controller (SDC) allows measurements using water or any organic solvent. The operation is entirely controlled by software. The S3500 uses patented Tri-laser (solid state diode) technology to illuminate particles from which scattered light is detected between 0.02 and 163 degrees. This allows a measurement over the entire size range of 0.02 to 2800 µm. The system uses Microtrac FLEX intuitive software to apply the Mie scattering theory to calculate the PSD of samples (Kefeni and Okonkwo, 2014). It also provides key features such as measurement statistics, trend analysis, average volume, as well as number and area distribution.

In this study, CFA sample was analysed for particle size measurement in wet (fluid dispersion) mode. For the measurement, the SDC is automatically filled with dispersion medium which for CFA was distilled water. Before the measurement, a blank measurement is performed. The CFA powder is then transferred to the SDC and the measurement is started. The PSD was reported in a graph of % passing vs particle diameter. The reproducibility was assessed by performing separate transfers of the CFA sample to the SDC. An acceptable value for the % RSD (standard deviation/average of the measurements) is 3%, whereas the international methods require 10%.

3.3.3 X-ray diffraction spectroscopy

The XRD technique is used to find out the mineralogical composition of the crystalline materials. Ideally, it is a non-destructive analysis tool used in mining and mineral processing for phase identification of minerals and ores. It constitutes a necessary analytical technique in engineering for characterization of sample and quality control.

The fundamental principle in XRD technique is that an interaction between x-rays and a crystalline material generates a diffraction pattern which is always the same for the same

material. In other words, each material in a mixture of materials gives its unique diffraction pattern. Diffraction process consists of incident beam that makes an angle theta (θ) with fixed crystal planes and generates a diffracted beam at an angle 2-θ from the incident beam. A typical diffraction pattern contains a plot of diffracted x-rays intensities (area under the peak) against the detector angle 2-θ. Values of the 2-θ for the peak are related to the wavelength of the anode material of the x-ray tube (1.54 angstrom for copper) (Fewster, 2015). The diffractometer used in this study is a Rigaku Ultima IV model. Initially, the fine powder sample was pressed in a sample holder with a smooth plane surface, and mounted onto the sample chamber. Thus, X-rays hit it and diffract from the sample. The diffraction pattern we obtained in this study was prepared as step-scans. The anode material was Cu. Before running the steps-scan, we set the generator at 40 mA and the voltage at 40 kV, and the following parameters:

- A start position [^{o}2-θ angle] : 3.5084

- A step-size [^{o}2-θ angle] : 0.0170

- A scan step time [s] : 51.0345

- An end position [^{o}2-θ angle]: 79.9914

In this research, there are diffraction patterns of the raw and treated CFA. The vertical axis displays the diffracted X-rays intensities whilst the horizontal axis shows the detector angles 2-θ in degrees.

3.3.4 X-ray fluorescence spectroscopy

The XRF is a qualitative and quantitative analytical technique which is used to measure the elemental composition of materials in ores, ceramics, etc. The XRF technique uses basically the principle that when materials are exposed to high-energy (short-wavelength) x-ray tube, x-rays are either absorbed by the atoms or scattered through the material. Generally, there are two types of analysis of the fluorescent x-ray emitted: wavelength–dispersive analysis and energy-dispersive analysis. In wavelength–dispersive analysis, wavelengths of the radiation are separated. The fluorescent radiations released by the material sample are directed into a

diffraction grating monochromator. Usually, a single crystal is utilized as diffraction grating. A single x-ray wavelength can be selected by changing the angle of incidence in which the x-rays hit the crystal. Bragg's law (Equation 3.1) gives the wavelength obtained (Tertian and Claisse, 1982; Klockenkämper and Von Bohlen, 2014).

$$n\lambda = 2d\ \sin(\theta) \tag{3.1}$$

where n is an integer 1, 2, 3, ... (it is assumed that n = 1), λ represents the wavelength of the incident x-ray in angstroms (1.54 for copper), d is the interatomic spacing in angstroms, and θ the diffraction angle in degrees.

In energy-dispersive analysis, the energies of the photons are arranged and then the intensity of each characteristic radiation is immediately associated to the quantity of each element in the substance. Therefore, dispersion and detection are a single process. The wavelength of the light (fluorescent photon) emitted by a transition can be calculated by the Planck's law (Equation 3.2), and its intensity is proportional to the concentration of the elements (Jekins, 1988; Beckhoff, 2007).

$$\lambda = hc/E \tag{3.2}$$

where h represents the Planck's constant, c is the velocity of the electromagnetic radiation ($c = 3 \times 10^8 ms^{-1}$), and E represents the energy per quantum of radiation.

A Rigaku ZSX Primus II model x-ray fluorescence spectrometer was used in this study to achieve a dispersive wavelength analysis. The standard diffraction crystal used was lithium fluoride LiF (220), and the procedure was as follows. Firstly, around 8 g of the fine powder sample was weighed and mixed with an amorphous binder (cellulose) in order to enhance homogenization. The obtained homogeneous mixture was filled into an aluminium cap and pressed by applying 15 MPa of pressure, using a hydraulic press for approximately 1 minute. The purpose of this process was to produce a smooth flat surface. Subsequently, the sample was oven dried at 80 ºC for 30 minutes to remove all moisture and, lastly, the sample was mounted onto the sample chamber. The x-ray tube that provided primary radiation was operated at a high voltage of approximately 60 kV. The high voltage helped to get a continuous spectrum that allowed excitation of a large range of atoms.

In the XRF analysis of the raw and treated CFA samples used in this research (sample type: pressed pellet), only transitions Kα were considered. Quantification (%) of different elements present in the minerals sample was given.

3.3.5 Fourier-transform infrared spectroscopy

The FTIR is an analytical technique in which a beam of infrared light passes through the sample, thus causing vibration of chemical bond. This leads to the absorption of infrared by the sample. Light is transmitted and shows the amount of energy that was absorbed at each wavelength. This process is done by means of a monochromatic beam that changes in wavelength over time, or by using a Fourier transform instrument which measures all of infrared wavelengths instantly. Subsequently, an absorbance or transmittance spectrum will be done, revealing at which infrared wavelengths the sample absorbs. The absorbed wavelength is characteristic for the chemical group (Griffiths and Haseth, 2007; Mackenzie, 1988; Smith, 2011). Almost exclusively, the infrared method works on samples with covalent bonds. Infrared spectroscopy detects characteristic vibrations of chemical bonds, and molecular bonds have specific frequencies at which they vibrate or rotate. A specific type of bond has a characteristic frequency of the vibrations which may be associated to chemical group (Socrates, 2000; Saikia, 2008).

The wavelength of the radiation is represented by λ (cm) whilst its wavenumber (cm^{-1}) is denoted as follows (Griffiths and Haseth, 2007; Mackenzie, 1988; Fan, 2012):

$$\text{Wavenumber} = {}^{1}/_{\lambda} \qquad (3.3)$$

A typical FTIR spectrum contains the plot of % transmittance (infrared intensity) versus wavenumber (wavelength) of light. The FTIR spectrum of the CFA was obtained using a Thermo Scientific Nicolet iS10 spectrometer which is designed for accurate and fast use. A sufficient CFA sample was loaded to obtain a transmittance spectrum. The FTIR spectrometer generated a graph in the form of a transmittance spectrum, which shows the unique chemical bonds and the molecular structure of the sample material. This transmittance spectrum has peaks that indicate functional groups present. Different types of bonds, and therefore different functional groups, absorb infrared radiation of different wavelengths. The analytical spectrum was then compared in a reference library program to identify the

functional groups or to find a "best match" for unknown material using catalogued spectra for known materials. The obtained FTIR spectrum of the CFA was in the wavenumber region of 500–4000 cm^{-1}. The vertical axis shows the percentage of transmitted light while the horizontal axis indicates wavenumbers of the infrared wavelength at which the sample has absorbed infrared. The resulting spectrum denotes the molecular absorption and transmission, which is a molecular fingerprint of the sample.

3.3.6 Scanning electron microscopy coupled with energy dispersive spectroscopy

The SEM/EDS is an analytical technique that uses a beam of electrons to produce high resolution and high magnification image of sample surface. This technique gives detailed imaging information about the morphology and surface texture of individual particles. In this technique, the back-scattering electron (BSE) gives information about the elemental composition of the specimen. In this work, a Vega3 Tescan model XMU Scanning Electron Microscope equipped with secondary electron (SE) and backscattered electron (BSE) detectors combined with EDS was used to study the microstructure of the CFA sample.

For the SEM sample preparation and analysis, 1 to 2 g of CFA sample was dispersed onto double-sided carbon tape. It was then coated with a thin layer of carbon to render the surface electrically conductive and to avoid charging. The coating technique was done under vacuum. The coated piece was then placed in a SEM microscope to determine the particle morphology and external surface structure, and external elemental composition of individual CFA particles using EDS. The elemental analysis using EDS was carried out in a ‘spot mode’ by randomly selecting 4 spots or areas of view and investigating all the CFA particles observed within the selected areas. The morphology and elemental composition were noted for each particle and compiled.

3.3.7 Inductively coupled plasma optical emission spectroscopy

The ICP-OES is a quantitative analytical technique in which a liquid sample is sucked through a plastic tube into a source of energy (plasma) so that the sample is taken by a peristaltic pump and transported into a nebulizer by means of an inert argon gas as a carrier. The sample is then ionized by the plasma and emits radiation at the characteristic wavelengths of the elements involved. The light intensity of each element is compared to measured intensities of known concentrations of the elements. Along the calibration lines, the

concentrations are calculated by extrapolation. In this study, 15 mL of sample were used for the analysis. Element's concentrations in the raw and treated AMD were analysed with a Spectro Arcos ICP-OES spectrometer. The instrument was calibrated with standard solutions at 1, 5, 10, 20, 40, 60, and 80 ppm prior to each analysis. An instrument blank was run before each sample set.

3.3.8 Optical microscopy

The optical microscopy is used to produce a magnified image of small object sample. This technique uses visible light and an objective lens to create a magnified image which is further magnified by a second lens system (the eyepiece) to allow the user to observe it by the naked eye. The final image to be observed is an inverted virtual image (Humphreys et al., 2014). The optical microscope used in this research is an Olympus GX41 model. To study the floc growth characteristics, a drop of the treated AMD from coagulation experiment using the composite coagulant under optimal conditions were collected at selected times during the sedimentation phase and placed on a slide which was then mounted onto the microscope, centred so that the sample is underneath the objective lens. The image was then obtained. After adjusting the brightness and contrast of the illumination and engaging the desired magnification objective, the floc size was measured.

3.4 Chemical equilibrium diagrams

In this study the Eh-pH diagrams for the systems Fe–SO_4^{2-}–H_2O, and Al–SO_4^{2-}–H_2O were drawn.

3.4.1 Eh-pH diagram for the Fe–SO_4^{2-}–H_2O system

In the present research work, iron from CFA sample had to be dissolved with H_2SO_4 to generate its soluble forms. In the purpose to show the stability regions of different iron species in an aqueous solution, an Eh-pH diagram for the system iron–sulphate at 25 °C (for a solution of total sulphate concentration = 1.5 M) was drawn using the Hydra/Medusa chemical equilibrium software. The vertical axis indicates the potential (E) in Volt and the horizontal axis shows the pH.

3.4.2 Eh–pH diagram for the Al–SO_4^{2-}–H_2O system

The prediction of predominance regions of aluminium species in an aqueous solution was made by the construction of an Eh–pH diagram for the system Al–SO_4^{2-}–H_2O at 25 °C (for a solution of total sulphate concentration = 1.5 M) using the Hydra/Medusa software. The vertical axis displays the potential (E) in Volt whilst the horizontal axis indicates the pH.

3.5 Coagulant synthesis

Batch leaching tests were conducted in a 750 mL high pressure reactor as shown in Figure 3.2. The autoclave used in this study is a Celsius Scientific Amar equipment PVT. The autoclave was equipped with a variable speed stirrer, temperature control system, a heating mantle, a thermocouple, and a water-cooled condenser to minimize the loss of solution by vaporization. In a test, the reactor was charged with 200 mL of H_2SO_4 leaching solution and required amount of CFA sample. Once the solution was heated to the test temperature, the reaction was allowed to proceed. At the end of the test, the solution was filtered and the residue was washed and dried. Required quantities of H_2SO_4 solution and 40 g of CFA were used with a stirring speed of 300 rpm. Leaching parameters such as H_2SO_4 concentration from 0.5–6.0 M, temperature range of 25–190 °C, solid to liquid ratio from 0.17–0.40, leaching time in the range of 1–6 h, and stirring speed of 300 rpm, were investigated to obtain optimal experimental conditions. The justifications of using these experimental values are the following:

- H_2SO_4 concentration: the work done by Fan et al. (2005), Sui et al. (2009) and Sun et al. (2011) used a fixed concentration (3.83, 3.5 and 4 M, respectively). This investigation explored a large range (0.5 to 6.0 M) that includes previous works concentrations in order to evaluate the effect of concentration.
- Temperature: in the work done by Fan et al. (2005) and Li et al. (2009), a small temperature range (70 to 130^oC) was used. In this study, the range was widened to see the effect of temperature.
- Solid to liquid ratio: in the investigation by Fan et al. (2005), a fixed solid to liquid ratio of 1:0.4 was used. In study, a wide range (0.17–0.40) was used to assess the effect of solid to liquid ratio.

- Dissolution time: the work done by Fan et al. (2005), Li et al. (2009) and Sun et al. (2011) used a fixed dissolution time (4, 6 and 4.5 hours, respectively). This investigation explored a large range (1 to 6 h) that includes previous works dissolution time in order to evaluate the effect of dissolution time.
- Stirring speed: the work done by Fan et al. (2005) used a stirring speed of 180 rpm (with low production yield) to leach iron and aluminium from CFA. The stirring speed has an effect on the reaction rate (increasing the stirring rate up to an optimum speed, increases the reaction rate (Singh et al., 2016). In this investigation, the stirring speed was chosen to 300 rpm for the sake of working close or after the optimum (as the optimum speed was not determined, and a plateau is reach after the optimum stirring speed) in order to improve the production of the coagulant.

For the effect of temperature, as soon as the temperature reaches the selected value, the time is started to be counted for the reaction. After filtration, a sample of the treated CFA was washed three times with deionized water, dried in the oven at 50 °C overnight, re-ground, and analyzed by XRF. Percentages of iron, aluminium, silicon, magnesium, and calcium leached were, respectively, calculated in relation to the iron, aluminium, silicon, magnesium, and calcium percentages in CFA sample (Equation 3.5). The leaching rate graphs were drawn. Furthermore, leach residues samples from the optimal experimental conditions were collected, washed three times with deionized water, dried in the oven at 50 °C overnight, re-ground prior to PSD, XRF, XRD, FTIR, and SEM/EDS analysis. The schematic diagram and pictorial representation of the process is depicted in Figure 3.2. The dissolution recoveries of elements were determined using the following equation:

$$\text{w}\ (\%) = \frac{[(m_{feed} \times C_0) - (m_{res} \times C)] \times 100}{(m_{feed} \times C_0)} \qquad (3.5)$$

where w (%) represents the dissolution recovery of elements, m_{feed} (g) the mass of sample used in the leaching, C_0 (%) the element % in the feed, m_{res} (g) the mass of the leaching residue, C (%) the concentration of the element in the residue.

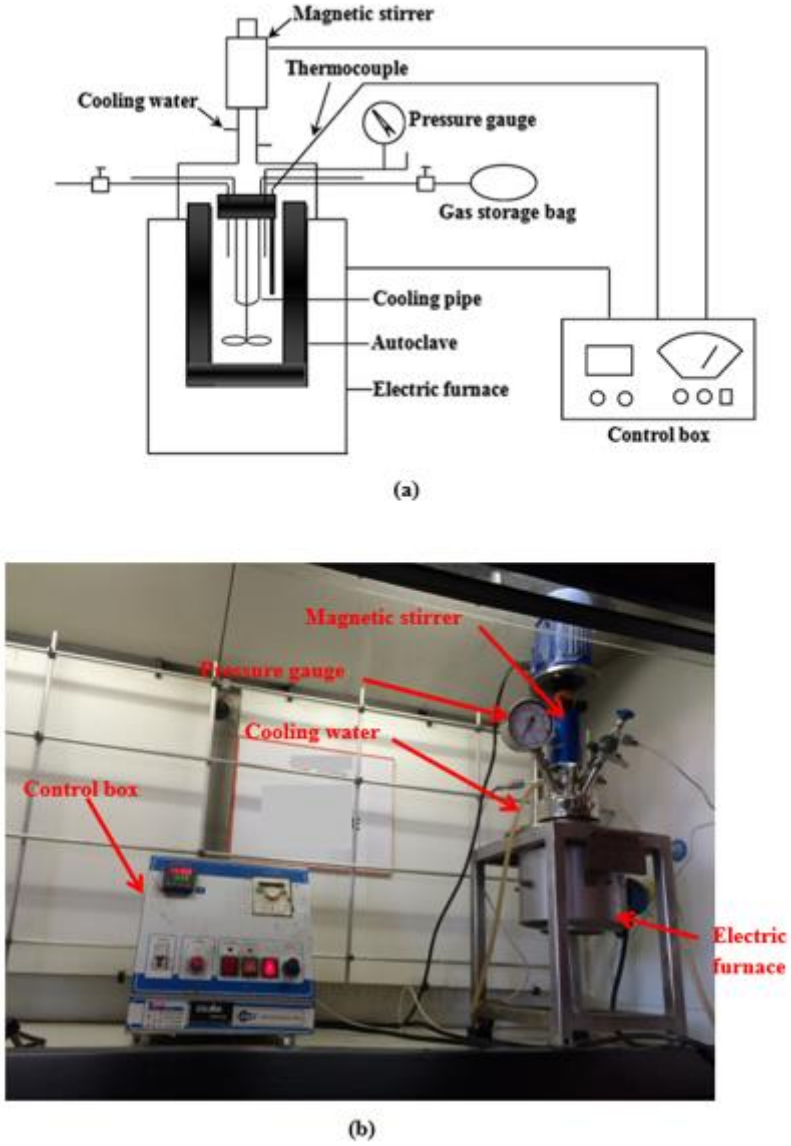

Figure 3.2: (a) Schematic and (b) pictorial set-up of batch sulphuric acid leaching of Fe and Al from CFA in the Chemical Engineering laboratory of the University of Johannesburg.

3.6 Leaching kinetic study

Kinetic mechanism of the leaching process of CFA particles by H_2SO_4 was determined by means of four standard equations of the shrinking core model (film diffusion factor, chemical reaction factor, product layer diffusion factor, mixed - controlled factor (Equations 4.11–

4.14) and the activation energies of elements extracted from CFA were determined using Arrhenius equation (Equation 4.15). Kinetic models were investigated using six reaction kinetic models, viz., zero-order, half-order, first-order, second-order, Hixson and Crowell, and Gompertz model equations, to determine the suitability of these reaction kinetic models to experimental data (Equations of each model can be seen in equations 4.23, 4.27, 4.31, 4.35, 4.36 and 4.39).

3.7 Fitting model analysis and mathematical modelling of the leaching process

The fitting model analysis was explored using Eureqa Newtonian software which is artificial intelligence-based scientific data software that automatically builds predictive and analytic models from experimental data. The input and output variables were time and concentration, respectively. Mathematical modelling development of leaching of CFA was performed based on the first principle of material balance.

3.8 Coagulation study

The coagulant obtained from the dissolution process of CFA was used for the coagulation process according to the set up shown in Figure 3.3 (a) and (b).

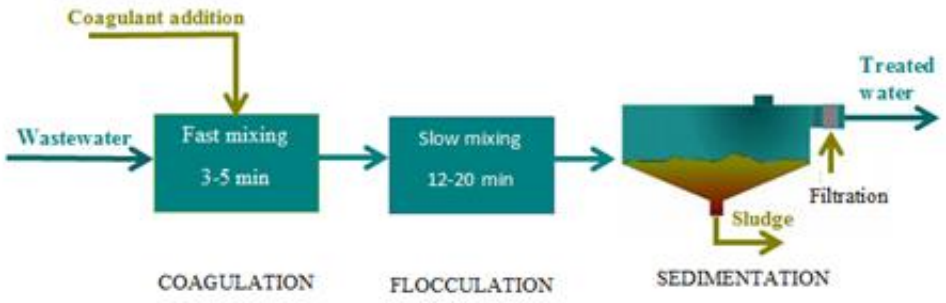

(a)

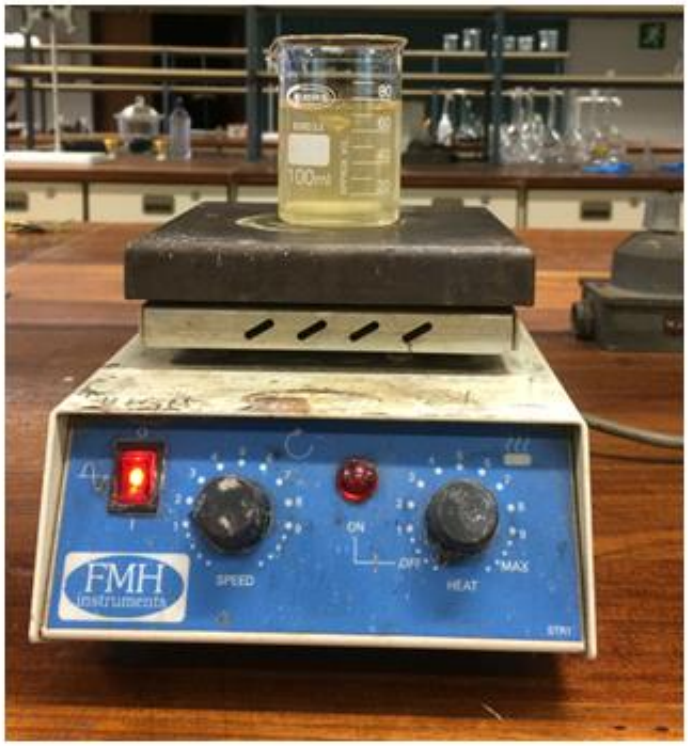

(b)

Figure 3.3: (a) Schematic and (b) pictorial set-up of coagulation process of coagulant from CFA.

Prior to coagulation experiments, the quality of the acid mine wastewater sample was determined. The TDS were measured using a conductivity meter, the toxic elements (Fe, Al, Mn, Mg, Ca, Si, Zn, and Ni) concentrations using ICP-OES, and the turbidity by means of a turbidity meter. The coagulation tests were conducted in glass beakers containing AMD. As the pH of the wastewater plays an important role in the treatment efficiency, the initial pH of

the AMD was adjusted near 7 using concentrated NaOH solution to minimize the volume change. The appropriate volume of synthesized coagulant was added to the AMD samples. Thereafter, a rapid mixing of approximately 5 minutes was done in order to dissolve the coagulant and distribute it evenly throughout the wastewater. Subsequently, a slow mixing of 20 minutes was accomplished in order to allow aggregation of particles. Once the test has been carried out, the mixture of wastewater–coagulant was poured into a measuring cylinder. After 150 minutes of settling, the supernatant sample was filtered through a 0.45 µm microfilter and the final value of pH was measured, the TDS was determined in the filtered water sample by a conductivity meter (912 conductometer Metrohm), the concentrations of toxic elements (Fe, Al, Mn, Mg, Ca, Si, Zn, and Ni) using an ICP-OES spectrometer (Spectro arcos ICP-OES spectrometer), and the residual turbidity by a turbidimeter (Eutech TN-100 Turbidimeter). The volume of sludge was determined by direct reading as mL of sludge / 25 mL of waste effluent treated. Data from this method was then used to draw/plot the removal rate graphs. The residual TDS, concentrations of toxic elements, and turbidity % at time t, were calculated using Equation 3.6.

$$R\ (\%) = \left(\frac{C_t}{C_0}\right) \times 100 \qquad (3.6)$$

where, $R\ (\%)$ represents the residual efficiency of TDS, concentrations of toxic elements, and turbidity; C_0 (mg/L) the initial concentration in the raw effluent for TDS, toxic elements, and turbidity; and C_t (mg/L) the concentration in the wastewater at time *t* (min).

The following coagulation parameters were investigated in order to determine the optimum experimental conditions.

1) The synthesized coagulant was added at different concentrations ranging from 2 to 50 mg/L.
2) Different pH values were selected from 4 to 12 to evaluate its effect on the coagulation process.
3) Different reaction temperatures were selected from to 20 to 50 °C to study its effect.
4) The optimum time of reaction was determined by varying the reaction time (slow mixing) from 1 to 50 minutes.

3.9 Adsorption study

Adsorption mechanisms of impurities were explored by evaluating the description of experimental data by published isotherm models. The Langmuir, Freundlich, Temkin, and Brunauer–Emmett–Teller (BET) isotherm models were used in this study. The linear equations of these isotherm models were used to assess the best suitable model to describe either the adsorption of impurity particles on the hydroxide precipitates formed, as a uniform or in a random distribution layer. Adsorption experiments were carried out under optimal process conditions. Coagulant dosage 20 mg/L (as Fe + Al + Si + Mg + Ca) at coagulation pH 7 using 25 mL of wastewater containing 720.2, 1.64, 13.86, 0.42, 13.52, 0.91, 0.93, 30.18, and 31.13 mg/L concentration of TDS, Fe, Al, Ni, Mn, Si, Zn, Mg, and Ca, respectively. Samples were withdrawn at different time intervals (0–50 minutes) and residual pollutant concentrations were analysed. The fitness of each isotherm model was calculated by linear regression method (comparison of coefficients of determination, R^2) from the experimental data at optimum pH and optimum coagulant dose. The adsorption capacity (q_e) of impurity at time *t* was determined using the following equation (Hussain et al., 2013):

$$q_e = \frac{(C_0 - C_t) \times V}{D} \tag{3.7}$$

where q_e is in mg/mg; C_0 and C_t (mg/L) represent the initial and final concentrations of impurity, respectively, *V* (mL) represents the volume of wastewater, and *D* (mg/L) is the coagulant dosage (as Fe + Al + Si + Mg + Ca).

3.10 Coagulation kinetics study

The determination of the kinetic mechanism of the adsorption (coagulation) process of AMD by the complex coagulant was conducted using two types of kinetic models, namely the adsorption reaction kinetic models and the diffusion kinetic models. Four reaction kinetic models, namely, pseudo-first-order, pseudo-second-order, Elovich model, and second order model equations, were used. Furthermore, three diffusion kinetic models namely Weber-Morris (intra-particle diffusion), Boyd's, and Bangham's model equations were investigated. The experimental data were used to fit these kinetic models to determine the suitable model for the coagulation process and the diffusion behaviour of the elements implicated in the process.

Kinetic studies for different metals and silicon were conducted using optimal coagulation conditions (i.e., complex coagulant dosage: 20 mg/L, pH: 7 using 25 mL of wastewater containing 720.2, 1.64, 13.86, 0.42, 13.52, 0.91, 0.93, 30.18, and 31.13 mg/L concentration of TDS, Fe, Al, Ni, Mn, Si, Zn, Mg, and Ca, respectively). The treated AMD samples were collected at predefined time intervals ranging from 1 to 50 minutes, and the pollutant concentrations were determined in the same way. The amount of impurity removed at time *t*, q_t (mg/mg), was calculated using the following equation (Hussain et al., 2013):

$$q_t = \frac{(C_0 - C_t) \times V}{D} \quad (3.8)$$

where C_0 (mg/L) is the initial concentration and C_t (mg/L) represents the concentration of the impurity at time *t* in the wastewater, *V* (mL) is the volume of the wastewater, and *D* (mg/L) represents the coagulant dosage (as Fe + Al + Si + Mg + Ca). The amount of impurity removed at saturation (or equilibrium),q_e (mg/mg), were determined by equation (3.8) with q_e = maximum value of q_t for each impurity.

3.11 Comparison of the performance of the produced composite coagulant with the conventional coagulants

The performance of the produced composite coagulant was compared to those of the available conventional coagulants (aluminium sulphate and ferric sulphate). The comparison was done using optimal experimental conditions obtained from the coagulation using the produced coagulant.

3.12 Fitting models analysis of the coagulation process

Experimental optimal conditions from the coagulation process using the produced complex coagulant were used for the fitting models analysis. The fitting model's analysis was performed using the Eureqa Newtonian software, which is an artificial intelligence-based scientific data software that automatically builds predictive and analytic models from experimental data. The input and output variables were time and concentration, respectively.

3.13 Summary

This chapter has dealt with experimental techniques that were used in this study. These involved techniques to characterize the raw and treated CFA, the produced coagulant, the raw and treated AMD, and the floc size measurement. Coagulant production and coagulation performance procedures were also discussed in this chapter. In addition, kinetic mechanisms,

fitting models, and mathematical modelling for both coagulant production and coagulation processes are discussed.

References

Allen, T., 2013. Particle size measurement. Springer.

Beckhoff, B., Kanngießer, B., Langhoff, N., Wedell, R. and Wolff, H. eds., 2007. *Handbook of practical X-ray fluorescence analysis*. Springer Science & Business Media.

Fan, M., Brown, R.C., Wheelock, T.D., Cooper, A.T., Nomura, M., Zhuang, Y., 2005. Production of a complex coagulant from fly ash. *Chemical Engineering Journal* 106, 269–277.

Fan, M., Dai, D. and Huang, B., 2012. Fourier transform infrared spectroscopy for natural fibres. In *Fourier transform-materials analysis*. Intechopen.

Fewster, P.F., 2015. X-Ray Scattering from Semiconductors and Other Materials, 3rd Edition. World Scientific, London.

Griffiths, P. R., Haseth, J. A., 2007. Fourier Transform Infrared Spectrometry. John Wiley & Sons, USA.

Humphreys, J., Beanland, R., Goodhew, P.J., 2014. *Electron microscopy and analysis*. CRC Press.

Hussain, S., van Leeuwen, J., Chow, C., Beecham, S., Kamruzzaman, M., Wang, D., Drikas, M. and Aryal, R., 2013. Removal of organic contaminants from river and reservoir waters by three different aluminum-based metal salts: Coagulation adsorption and kinetics studies. *Chemical Engineering Journal* 225, 394–405.

Jenkins, R., 1988. X-Ray Fluorescence Spectrometry, John Wiley & Sons, USA.

Kefeni, K.K. and Okonkwo, J.O., 2014. Distribution of polybrominated diphenyl ethers and dust particle size fractions adherent to skin in indoor dust, Pretoria, South Africa. *Environmental Science and Pollution Research*, 21 (6), 4376–4386.

Klockenkämper, R. and Von Bohlen, A., 2014. *Total-reflection X-ray fluorescence analysis and related methods*. John Wiley & Sons.

Li, L., Fan, M., Brown, R.C., Koziel, J.A., Leeuwen, J. H., 2009. Production of a new wastewater treatment coagulant from fly ash with concomitant flue gas scrubbing. *Journal of harzardous Materials* 162, 1430–1437.

Mackenzie, M.W., 1988. Advances in Applied Fourier Transform Infrared Spectroscopy. John Wiley & Sons, Great Britain.

Saikia, B.J., Parthasarathy, G. and Sarmah, N.C., 2008. Fourier transform infrared spectroscopic estimation of crystallinity in SiO 2 based rocks. *Bulletin of Materials Science*, 31 (5), 775–779.

Smith, B.C., 2011. *Fundamentals of Fourier transform infrared spectroscopy*. CRC press.

Socrates, G., 2000. Infrared and Raman Characteristic Group Frequencies: Tables and Charts, Third Edition. John willey & Sons, England.

Singh, G., Nakade, P.G., Mishra, P., Jha, P., Sen, S. and Mondal, U., 2016. Kinetic investigation on liquid–liquid–solid phase transfer catalyzed synthesis of dibenzyl disulfide with H_2S-laden monoethanolamine. *Journal of Molecular Catalysis A: Chemical*, *411*, 78-86.

Sui, Z., Qiao, C., Zhao, X., Qiang, X., 2009. Application of Fly ash-based coagulant in tanning wastewater treatment. Available at http://www.aaqtic.org.ar/congresos/china2009/download/2-5/2-196.pdf. Accessed Jun 2019.

Sun, T., Sun, C.H., Zhu, G.L., Miao, X.J., Wu, C.C., Lv, S.B., Li, W.J., 2011. Preparation and coagulation performance of poly-ferric-aluminum-silicate-sulfate from fly ash. *Desalination* 268, 270–275.

Tertian, R., Claisse, F., 1982. Principles of Quantitative X-Ray Fluorescence Analysis. Heyden, UK.

CHAPTER 4
PRODUCTION OF A COMPLEX COAGULANT FROM COAL FLY ASH

4.1 Introduction

In this chapter, findings from the research work conducted on the complex coagulant production are presented and discussed. A sample of coal fly ash (CFA) was studied. It was used for the production of coagulant by leaching process. Prior to leaching, the mineralogical composition of the CFA sample was determined by X-ray diffraction (XRD), X-ray fluorescence (XRF), Fourier transform infrared spectroscopy (FTIR), Scanning electron microscopy coupled with energy dispersive X-ray spectroscopy (SEM/EDS). Particle size distribution (PSD) analysis was also applied for the characterization of the CFA sample. After leaching, specific residues were characterized by PSD, XRD, XRF, FTIR, and SEM.

Part of the results of this section was published in the *Materials Science and Technology* 2018, Conference proceeding, DOI 10.7449. Another part of the results of this section was submitted for publication in the *Journal of Chemical and Metallurgy*.

4.2 Results and discussion

4.2.1 Coal fly ash characterization

Particle size distribution

The PSD of the CFA sample in Figure 4.1 shows that the sample has a P80 particle diameter of 49 µm (i.e., 80% of the volume distribution of the sample having particle sizes less than 49 µm). In the synthesis of the complex coagulant, which consists of dissolution process of iron, aluminium, and other elements (such as silicon, magnesium, and calcium) in CFA, inclusions of all these elements bearing minerals are to be leached from the CFA particles. Since the smaller the particle size, the better the recovery efficiency (due to the exposure of the iron, aluminium, and other elements mineral grains) (Chu et al., 2012; Nemati et al., 2000), particle size smaller than 49 µm is suitable for the dissolution of elements in CFA.

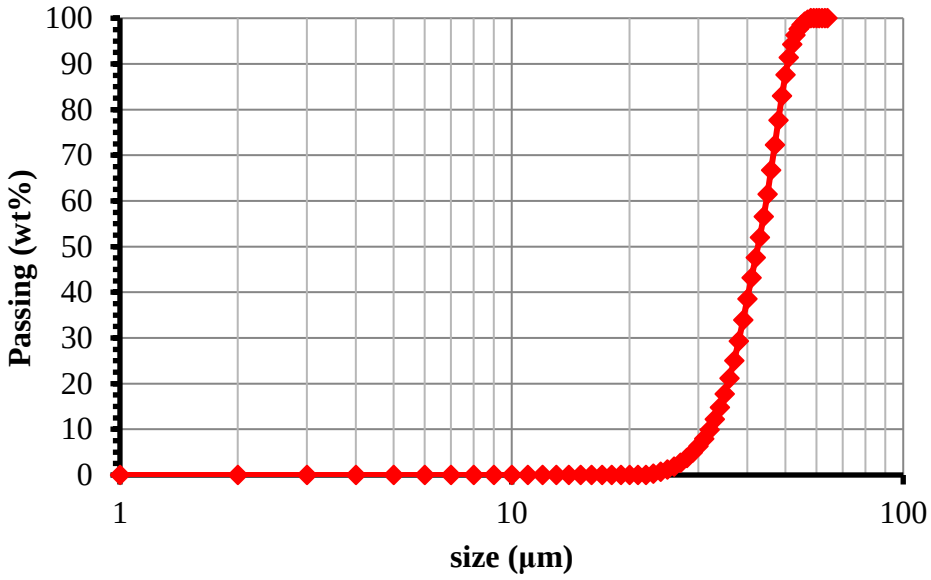

Figure 4.1: Curve of particle size distribution (PSD) of CFA sample shows that the sample has a P80 particle diameter of 49 µm.

Mineralogical study

The CFA sample was characterized by XRD, XRF, FTIR, and SEM/EDS. While XRD was used in order to identify different mineral phases present in the sample, XRF was used for the quantification of various elements present in the material, FTIR was used to determine the chemical functional bonds in the sample, SEM/EDS was used for microstructural study and the determination of the elemental composition of the sample.

X-ray diffraction and X-ray fluorescence analyses of the coal fly ash: The XRD pattern (Figure 4.2) obtained from the analysis of the CFA sample showed that the main crystalline phases were quartz (SiO_2), mullite ($Al_{5.65}Si_{0.35}O_{9.175}$), and hematite ($Fe_2O_3$). The XRF results reported in Table 4.1 show that the CFA sample contains mainly 49.92% silica (SiO_2), 32.15% alumina (Al_2O_3), 4.16% hematite (Fe_2O_3), 6.25% lime (CaO), and 2.15% titanium dioxide (TiO_2). Elements found by XRF are in agreement with phases found by XRD analysis particularly with the predominance of silicon compound (quartz) and aluminium compound (mullite). Furthermore, the XRF results showed that the sample belongs to class F CFA due to the low content of CaO. Ideally, the XRD and XRF results indicate that the

following were the main elements: Al, Fe, Si, Ca, and Ti. These results are consistent with the findings of Van der Merwe et al., (2014).

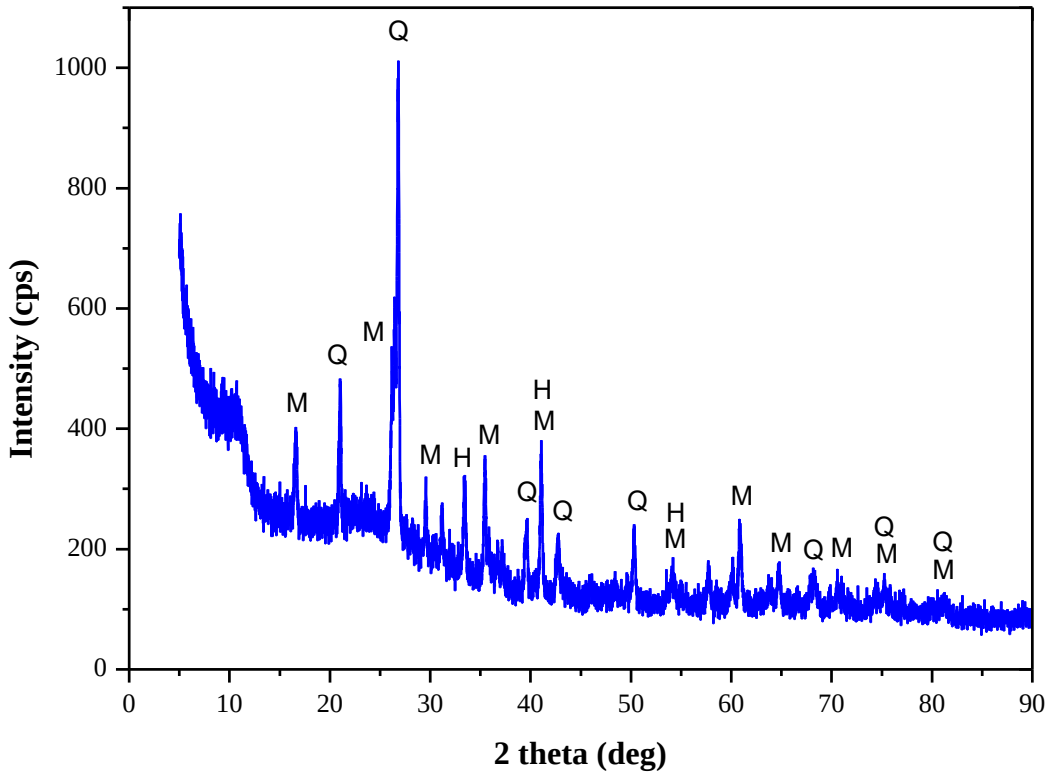

Figure 4.2: XRD pattern of CFA. Q, M, and H indicate quartz (SiO_2), mullite ($Al_{5.65}Si_{0.35}O_{9.175}$), and hematite ($Fe_2O_3$), respectively.

Table 4.1: Chemical composition of CFA sample. Only important elements from important phases are presented.

Chemical composition	Content (wt%)
Al_2O_3	32.15
Fe_2O_3	4.16
SiO_2	49.92
CaO	6.25
TiO_2	2.15
MgO	1.40
K_2O	1.00
P_2O_5	1.04

Mineralogical study confirmed that CFA contains essential mineral elements (Fe, Al, Mg, Si, and Ca) in oxide form, which can be used to produce coagulants. Therefore, the pulverized CFA has a huge potential for usage in the production of coagulant for wastewater treatment (Bottero et al., 1987; Siedel and Zimmels, 1998; Bidhendi et al., 2007; Semerjian and Ayoub, 2003; Teringo, 1986).

Fourier transform infrared analysis of the coal fly ash: The FTIR spectrum in Figure 4.3 displays the impact of combustion on the CFA sample. Characterization of the chemical functional bonds as displayed in FTIR spectrum was carried out by comparing principal peak frequencies with the typical infrared absorption frequencies of functional groups as presented in Table 4.2.

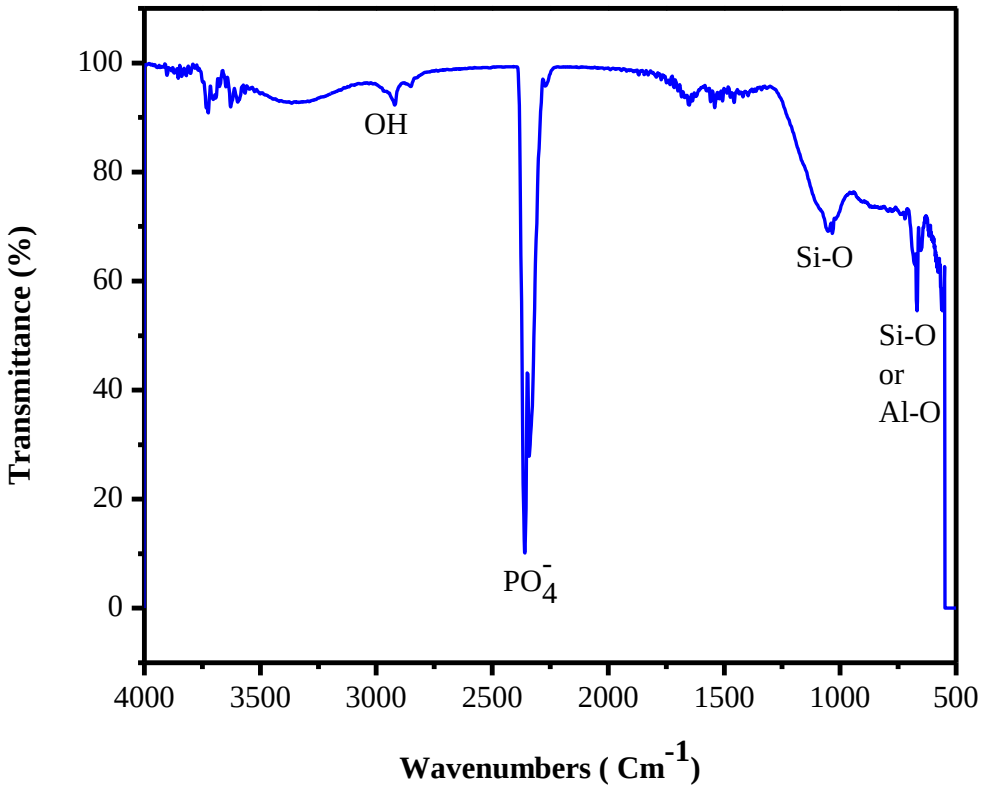

Figure 4.3: FTIR spectrum for CFA.

In Figure 4.3, the peak at 669.14 cm^{-1} was related to Si–O or Al–O bending vibrations and has contributions from quartz (SiO_2) and mullite ($Al_{5.65}Si_{0.35}O_{9.175}$). This is in agreement with the findings of the studies by van der Merwe et al. (2014) and Mackenzie (1972). The broad

band observed at around 1032.97 cm^{-1} originates from Si-O stretching vibrations. This also agrees well with the findings of the investigations by van der Merwe et al. (2014), Vempati et al. (1994), Fernandez and Palomo (2005), and Voll et al. (2002). This broad band indicated the high quartz content as shown by XRD, XRF, SEM/EDS, and ICP-OES. The bands appearing in the wavenumber values from 2400 to 2200 cm-^{1} may be attributed to the P=O bonds of the phosphate PO_4^- group. The OH stretching vibrations of Si–OH group occured at the wavenumber range of 2900–3400 cm^{-1}. This is supported by the works by Kaur and Goyal (2016), Andini et al. (2008), Thonsang and Sombatsompop (2006), and Vempati et al. (1994). From the FTIR results, major components of CFA were found to be mullite and quartz. The later can be used for the synthesis of aluminium type coagulants that may help in the treatment of wastewater.

Table 4.2: Band assignment for coal fly ash compounds related to the band positions in cm^{-1}.

Wavenumber range (cm^{-1})	**Band assignment for coal fly ash**
450–520	Si–O
550–920	Si–O, Al–O
950–1168	Si–O
2200–2400	P=O
2500–3400	O–H

Scanning electron microscopy coupled with energy dispersive x-ray spectroscopy analysis of the coal fly ash: Morphology study using SEM indicates that particles in CFA have smooth spherical surfaces as shown in Figure 4.4. Ideally, the single CFA particles were found to be hollow, empty spheres (cenospheres) or filled with smaller amorphous particles and crystals (plerospheres) (Giere et al., 2003).

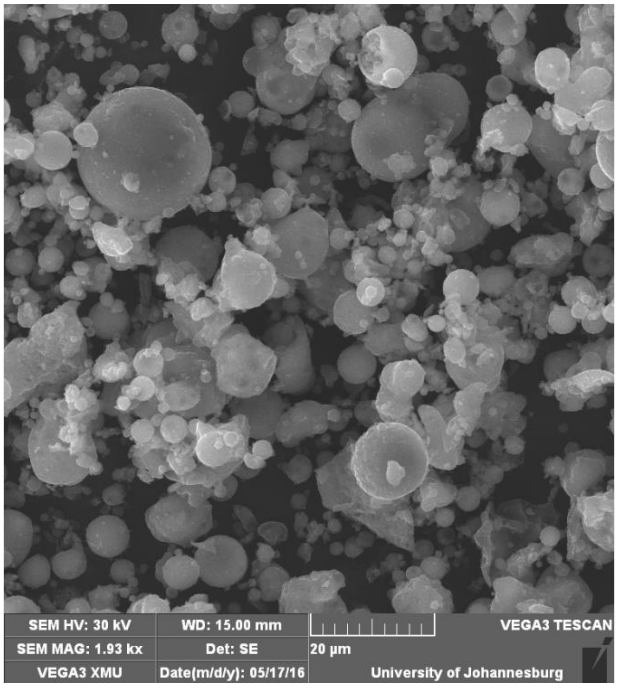

Figure 4.4: Scanning electron micrograph (SEM) of the CFA showing smooth spheres.

The EDS results of surface of CFA presented in Figure 4.5 and Table 4.3 were in agreement with XRD and XRF data, i.e., the CFA sample has high mineralogical content rich in Al, Fe, Si, and Ca and minor amounts of the elements: Ti, K, Mg, Na, and S. The SEM and EDS results show that CFA sample contains essential mineral oxides like Al_2O_3 and Fe_2O_3 that are essential in the synthesis of coagulants for the treatment of water and wastewater effluents.

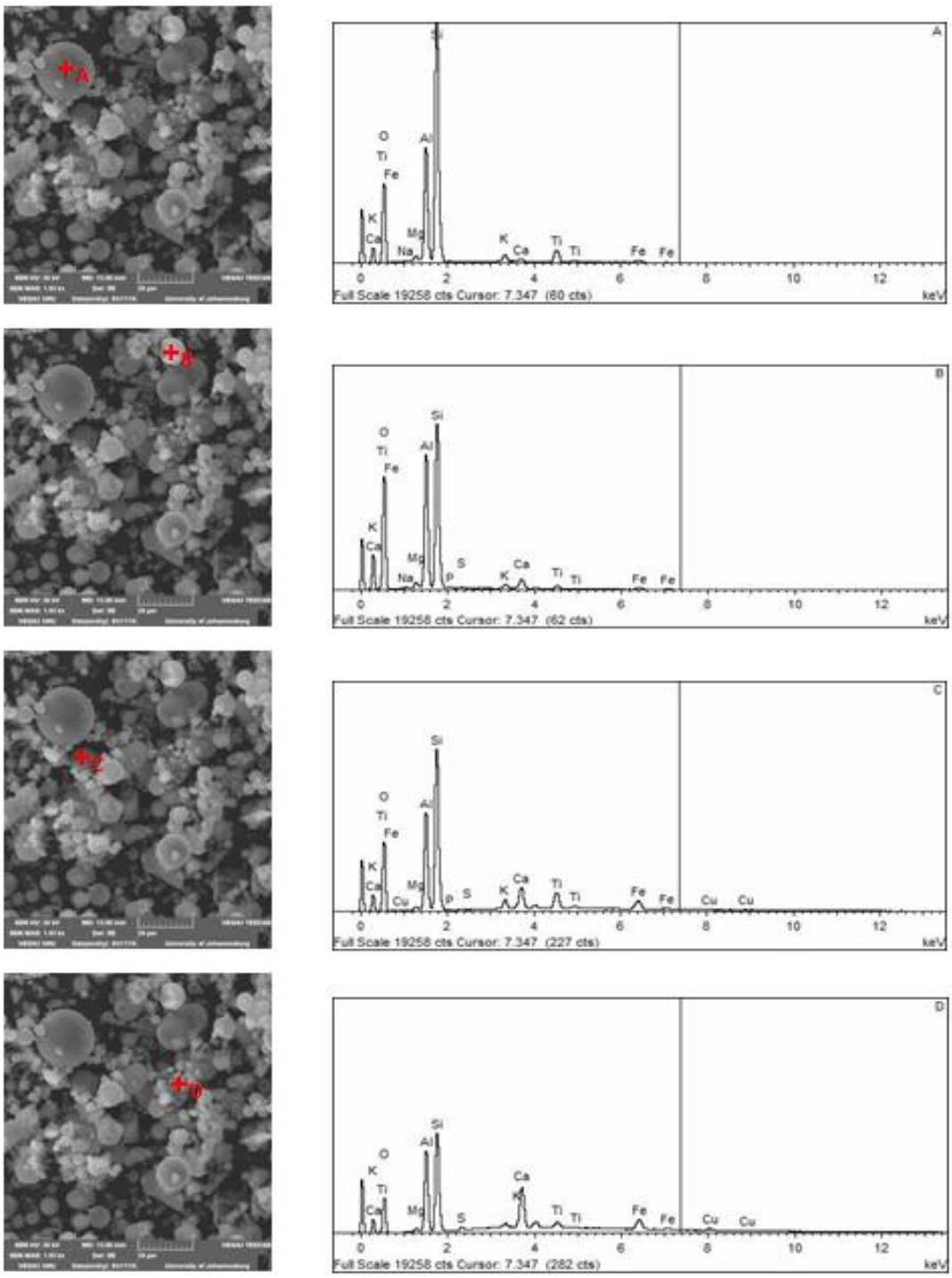

Figure 4.5: SE images with elemental spectra of the CFA spheres (spots A, B, C, and D). These CFA particles have small variations in proportions of Al, Fe, and Si.

Table 4.3: Energy dispersive spectrometry (EDS) w% of elements in CFA.

Spectrum	Na	Mg	Al	Si	P	S	K	Ca	Ti	Fe	Cu	O	Total
A	0.28	0.55	12.42	32.28			1	0.34	2.17	0.69		50.27	100
B	0.24	0.69	16.92	28.08	0.34	0.24	0.67	1.62	0.67	0.71		49.81	100
C		0.61	13.27	26.36	0.21	0.2	1.44	3.55	3.4	2.86	0.4	47.71	100
D		0.65	14.93	21.91		0.78	0.83	8.59	1.57	4.02	0.86	45.85	100
Max.	0.28	0.69	16.92	32.28	0.34	0.78	1.44	8.59	3.4	4.02	0.86	50.27	
Min.	0.24	0.55	12.42	21.91	0.21	0.2	0.67	0.34	0.67	0.69	0.4	45.85	

4.2.2 Leaching of iron, aluminium, and other elements from coal fly ash

Batch dissolution experiments were performed for each selected parameter to study the dissolution behaviour of iron, aluminium, and other elements from CFA material. Leaching solution used for the dissolution of elements from CFA sample was an aqueous solution of sulphuric acid (H_2SO_4). A sample of CFA with contents of 2.91% iron and 17.01% aluminium was used. Usually, iron and aluminium in CFA are found with other elements such as silicon, magnesium, calcium, potassium, and titanium. Among these elements, the dissolutions of silicon, calcium, and magnesium were investigated.

In order to show the predominance areas of different iron and aluminium species in an aqueous solution, Eh-pH diagrams for the Fe–SO_4^{2-}–H_2O system and Al–SO_4^{2-}–H_2O system at 25 °C (for a solution of total sulphate concentration = 1.5 M) were drawn and presented in Figures 4.6 and 4.7. The total sulphate concentrations of 1.5 M were selected according to diluted H_2SO_4 solutions. It is shown from Figure 4.6 that for a solution of total sulphate concentration of 1.5 M, Fe^{3+} (i.e. $Fe(SO_4)_2^-$complex) is the most predominant species at pH less than 3.9 and Eh between 0.67 and 1.00 V; hydrolysis of $Fe(SO_4)_2^-$ occurs when pH increases forming species such FeS_2, Fe_2O_3, and $Fe(HS)_3$ which are predominant species at pH values greater than 4. Figure 4.7 shows that dissolved aluminium species Al^{3+}, $AlSO_4^+$ and $Al(SO_4)^{2-}$ are stable in the region of pH less than 5 and Eh range from -1.00 to 1.00 V.

Figure 4.6: Eh–pH diagram for the Fe–SO_4^{2-}–H_2O system at 25 °C; Total SO_4^{2-} concentration = 1.5 M. This diagram has been drawn using the Hydra/Medusa software.

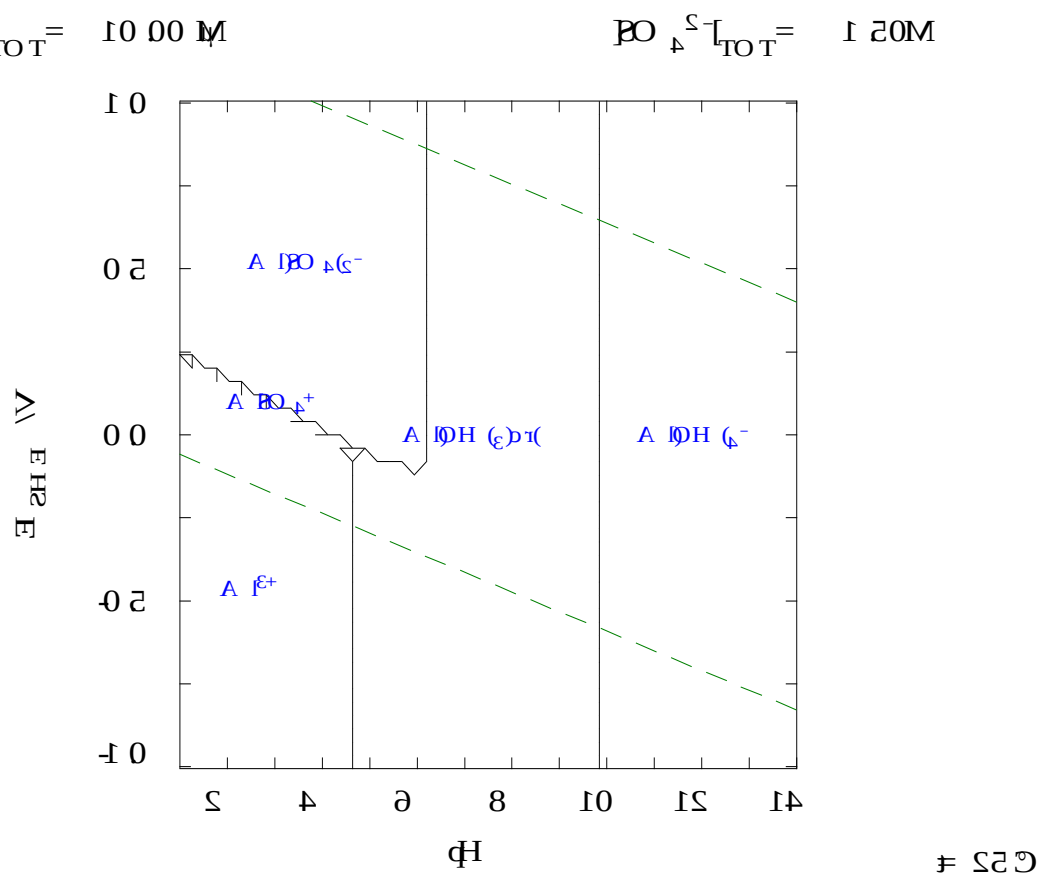

Figure 4.7: Eh–pH diagram for the Al–SO_4^{2-}–H_2O system at 25 °C; Total SO_4^{2-} concentration = 1.5 M. This diagram has been drawn using the Hydra/Medusa software.

In general, aqueous equilibrium reactions of iron and aluminium in H_2SO_4 media are presented in Equations 4.1–4.6 (Barrett et al., 1993; Stumm and Morgan, 1996; Langmuir, 1997). In aqueous H_2SO_4 solutions (Equation 4.6), iron distributes as Fe(II) and Fe(III) soluble species such as free ions ($Fe^{2+}$and Fe^{3+}) or complex compounds [$FeSO_4^0$, $FeSO_4^+$, $Fe(SO_4)_2^-$] (Equations 4.1–4.3) (Casas et al., 2005; Yue et al., 2014). Whilst, aluminium goes into solution as Al (III) species such as simple cations (Al^{3+}) or charged complexes [$AlSO_4^+$, $Al(SO_4)_2^-$] (Equations 4.4 and 4.5) (Rubisov and Papangelakis, 2000). The concentrations of iron and aluminium depend highly on the initial total amount of iron, aluminium, acidity, and temperature (Yue et al., 2014).

$$Fe^{2+} + SO_4^{2-} \leftrightarrow FeSO_4^0 \qquad (4.1)$$

$$Fe^{3+} + SO_4^{2-} \leftrightarrow FeSO_4^{+} \quad (4.2)$$

$$Fe^{3+} + 2SO_4^{2-} \leftrightarrow Fe(SO_4)_2^{-} \quad (4.3)$$

$$Al^{3+} + SO_4^{2-} \leftrightarrow AlSO_4^{+} \quad (4.4)$$

$$Al^{3+} + 2SO_4^{2-} \leftrightarrow Al(SO_4)_2^{-} \quad (4.5)$$

$$H^{+} + SO_4^{2-} \leftrightarrow HSO_4^{-} \quad (4.6)$$

Chemistry of H_2SO_4 leaching of iron, and aluminium from Fe_2O_3 and Al_2O_3 in coal fly ash

The aim was to leach iron and aluminium from Fe_2O_3 and Al_2O_3, respectively, in the CFA sample with H_2SO_4 solutions. During the leaching of iron and aluminium with H_2SO_4, the mechanism that describes complexation of iron and aluminium is given by Equations 4.2–4.6. The overall reactions are expressed by Equations 4.7 and 4.8 for iron and aluminium, respectively (Fan et al., 2005).

$$Fe_2O_3 + 3H_2SO_4 \leftrightarrow Fe_2(SO_4)_3 + 3H_2O \quad (4.7)$$

$$Al_2O_3 + 3H_2SO_4 \leftrightarrow Al_2(SO_4)_3 + 3H_2O \quad (4.8)$$

H_2SO_4 reacts with iron and aluminium in CFA to, respectively, form $FeSO_4^{+}$ and $AlSO_4^{+}$ complexes on the surface of iron and aluminium metals (Equation 4.2 and 4.4). Then $FeSO_4^{+}$ undergoes another complexation with sulphate ion to form $Fe(SO_4)_2^{-}$ (Equation 4.3) which goes into solution whilst $AlSO_4^{+}$ enters in complexation with sulphate ion forming $Al(SO_4)_2^{-}$ which moves in solution (Equation 4.5). Theoretically, the dissolution of iron and aluminium occurs as depicted in Equations 4.2–4.6 at pH < 3.9. Further, the effects of reaction factors on dissolution of elements from CFA are studied in order to optimize the process.

Effect of time

Leaching parameters selected from the chemical equilibrium diagrams in Figures 4.6 and 4.7 were: pH from 0.5 to 3.9. In the present study, the effects of time on the dissolutions of iron, aluminium, and other elements from CFA were carried out at RT (23±2 °C), S/L ratio of 0.33, particle size: –49 µm, stirring speed of 300 rpm, and leaching period in the range of 1 to

6 hours. The results are shown in Figure 4.8. It was mainly noticed that the dissolution of iron, aluminium, silicon, and magnesium at the concentration of 1 M H_2SO_4 at RT is completed within 1hour. It is shown that recoveries of iron, aluminium, silicon, and magnesium after 1hour leaching period at RT reached 7.97, 10.25, 10.21 and 60.15% respectively with no calcium reported after 6 hours. Practically, 1 hour of dissolution time was found to be optimum.

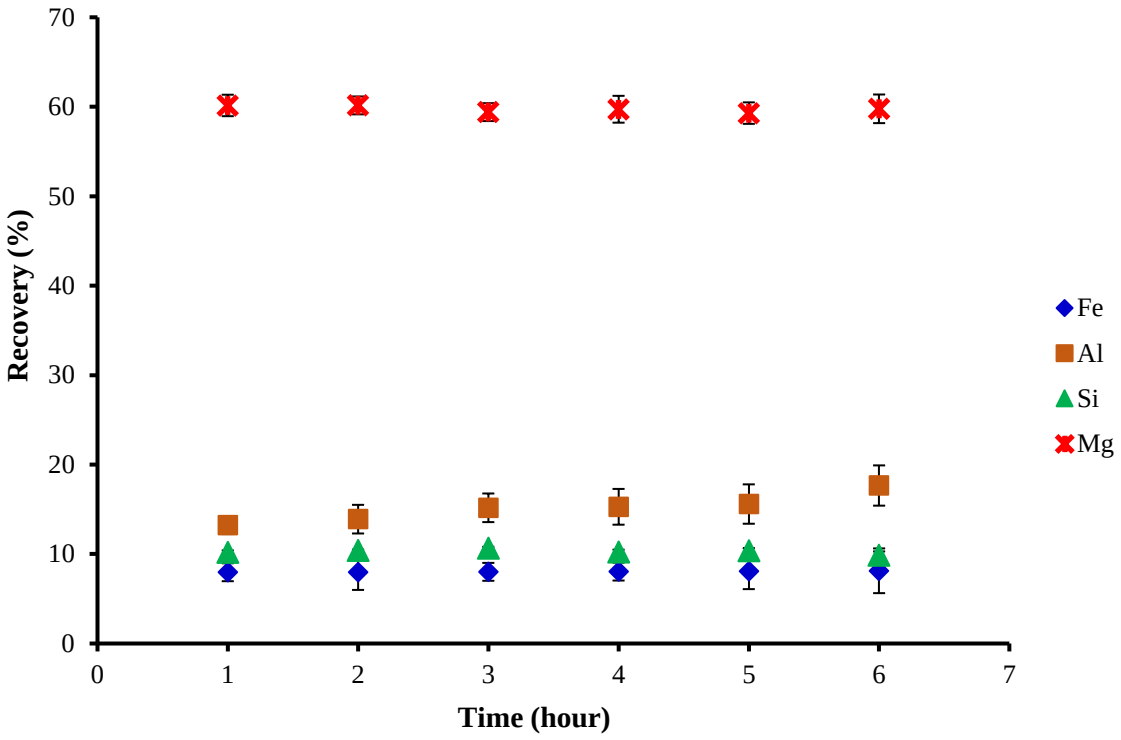

Figure 4.8: Effect of time on the leaching of elements from CFA sample (particle size: −49 µm, RT (23±2 °C), 1 M H_2SO_4, 300 rpm, S/L = 0.33).

Effect of sulphuric acid concentrations

Reagent concentration plays an important role in the dissolution process. Dissolution tests were conducted with different H_2SO_4 concentrations including 0.5, 1.0, 1.5, 2.0, 3.0, 4.0, 5.0, and 6.0 M. Figure 4.9 displays % iron, aluminium, silicon and magnesium recoveries = f (H_2SO_4 concentration) at RT at 1hour leaching period. When the H_2SO_4 concentration was less than 1.5 M, it is noticed that the extraction efficiency gradually increases in iron from

10.83% to 14.96% and in aluminium from 14.08% to 16.00% with the H_2SO_4 concentration. Then with H_2SO_4 concentration of 1.5 M, the concentrations of iron and aluminium reached a plateau. Mainly, it was observed from Figure 4.9 that the iron leaching, like the dissolution of aluminium is completed when 1.5 M sulphuric acid was used.

Throughout the H_2SO_4 concentration range, elements such as silicon and magnesium are also dissolved together with iron and aluminium. Maximum concentrations of 11.52% and 42.32% were obtained for silicon and magnesium, respectively. Under these conditions no calcium was detected in the leachate. Practically, the concentration of 1.5 M H_2SO_4 was found to be optimum for both iron and aluminium dissolutions.

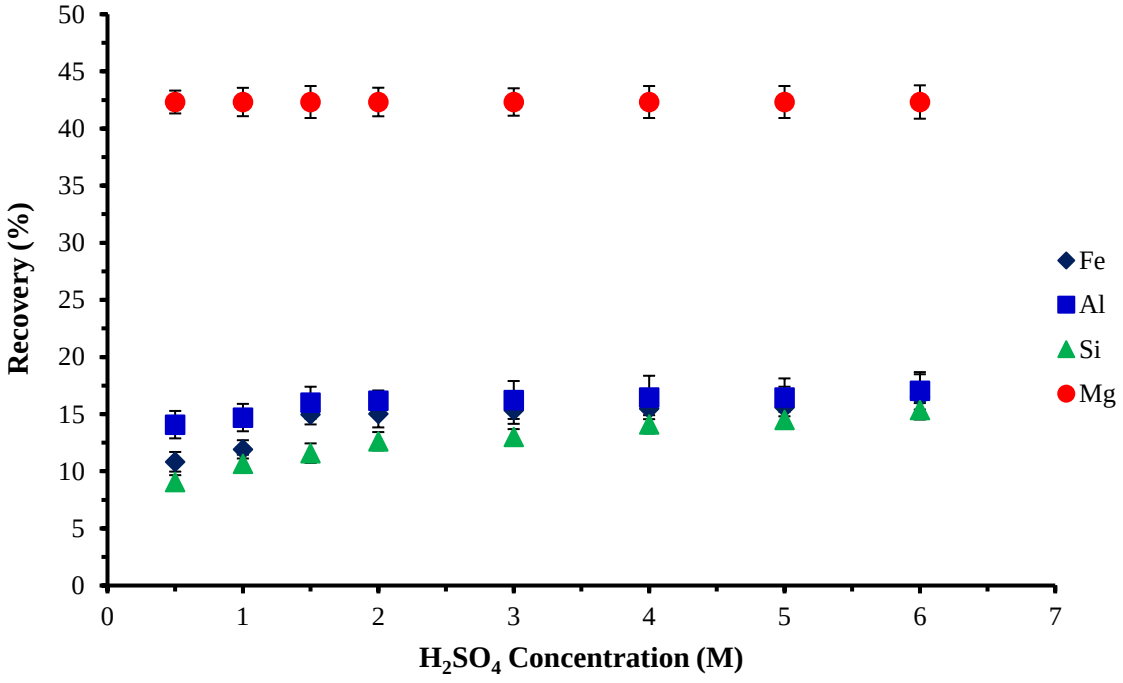

Figure 4.9: Effect of H_2SO_4 concentration on the leaching of elements from CFA sample (particle size: −49 µm, RT (23±2 °C), 300 rpm, S/L= 0.33, 1 hour).

Effect of temperature

From Figure 4.10, the variation of temperature on iron dissolution is found to be very effective than the dissolution of aluminium. The CFA sample displayed widely varying iron and aluminium dissolution behaviour at different temperatures. When the leaching was

carried out at ambient temperature, the leaching of iron and aluminium was slower. The dissolution of iron increases significantly with increasing temperature from 120 to 190 °C, but there is no noticeable increase at lower temperatures. For aluminium, from 90 °C, the extraction efficiency is 10.72%. There is no obvious change in the aluminium dissolution when the temperature increases from 90 to 150 °C. Then, the dissolution decreases until the temperature reaches 190 °C. The fused structure of aluminosilicate is probably the reason of relatively lower dissolution of aluminium. This result is consistent with the reaction rate theory which argues that the rate of a chemical reaction increases with temperature (Parravano et al., 2000; Fan et al., 2005). Similar results have been reported by others (Li et al., 2009; Kelmers et al., 1981). The maximum dissolution of aluminium is reached with a temperature of 150 °C.

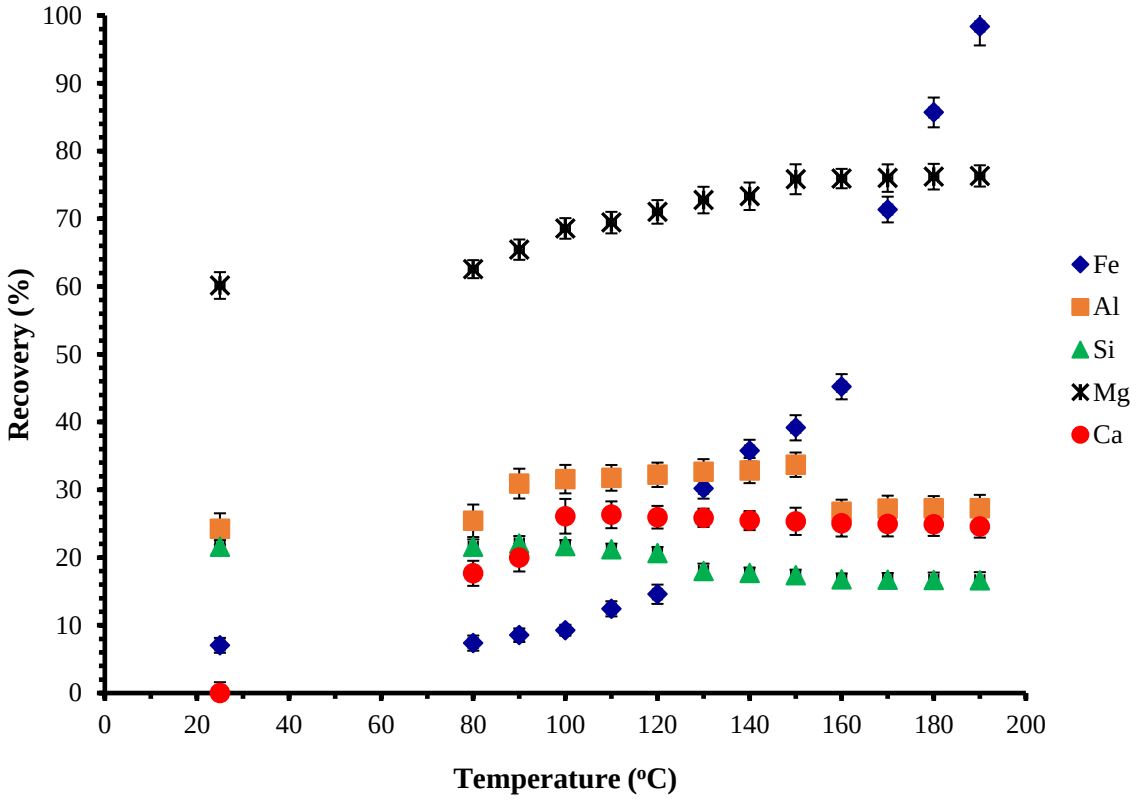

Figure 4.10: Effect of temperature on the leaching of elements from CFA sample (particle size: −49 µm, 1.5 M H_2SO_4, 300 rpm, S/L= 0.33, 1 hour).

Effect of solid to liquid ratio

It can be seen in Figure 4.11 that S/L ratio has a greater effect on the leaching of iron and magnesium than the dissolution of other elements with H_2SO_4. There is an increase in iron concentration in the complex coagulant with increasing S/L ratio from 0.17 to 0.20. At higher S/L ratios, the dissolution of iron dramatically decreases. This may be explained by the fact that high S/L leads to a lack of reagent. Hence, at S/L of 0.20 more than 90% of iron was extracted with 1.5 M H_2SO_4. Similar tendency was noticed in the dissolutions of aluminium, silicon, magnesium, and calcium for different S/L ratio under identical conditions. Maximum recoveries of 28.88, 7.81, 78.67, and 27.11% were obtained for aluminium, silicon, magnesium, and calcium respectively at 0.20 S/L ratio. In this study, based on the experimental data, an S/L ratio of 0.20 is appropriate. Compared to leaching behaviour of iron, the low extraction efficiencies of aluminium and silicon (<30%) is possibly due to the structure and property of aluminium and silicon oxides in CFA. The CFA mineralogy is extremely varied. The identified phase of iron oxide is hematite which could be easily dissolved in H_2SO_4 medium (Blissett and Rowson, 2012). In CFA, the Al_2O_3 either exists in crystalline mullite form and non-crystalline amorphous form or is bound in an aluminosilicate glass matrix (Matjie et al., 2008; Blissett and Rowson, 2012). The glass matrix and mullite phase are not easily accessible to direct acid leaching (Shemi et al., 2012).

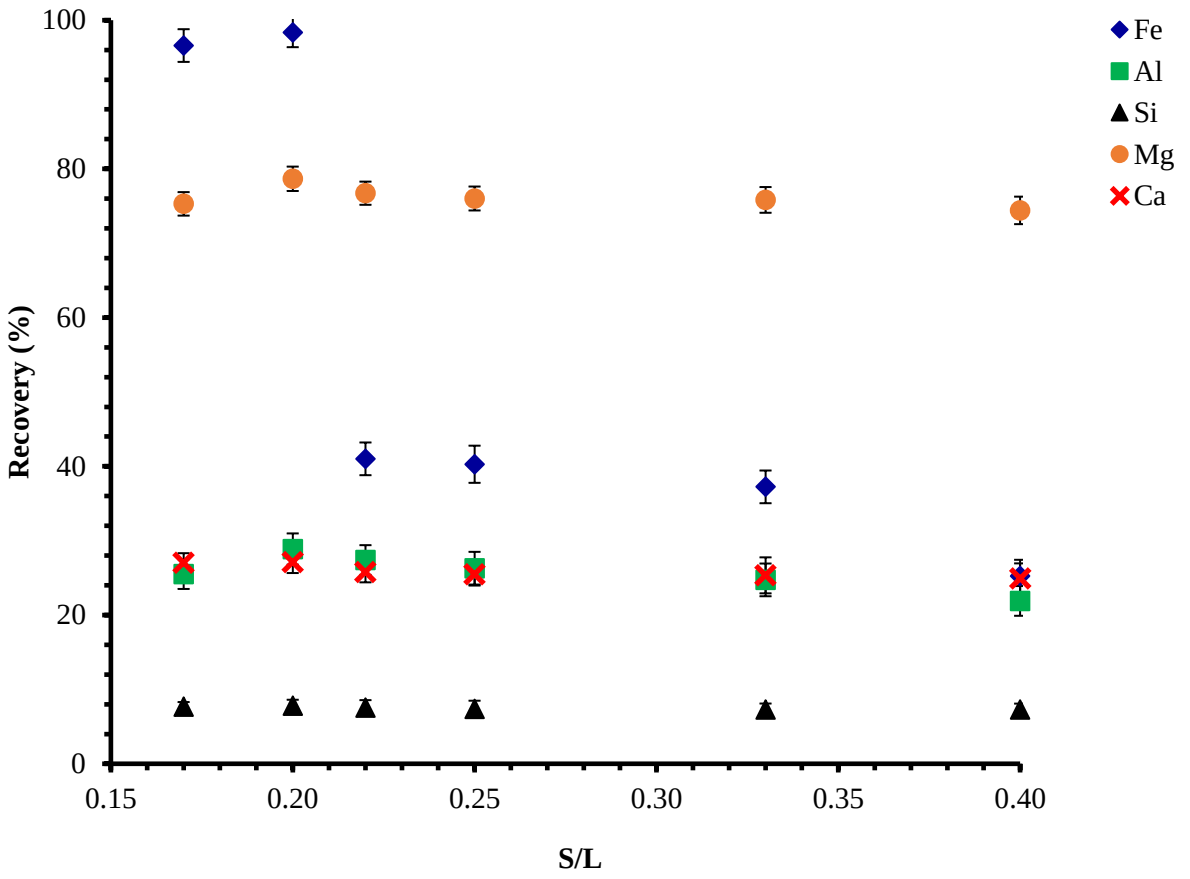

Figure 4.11: Effect of S/L on the leaching of elements from CFA sample (particle size: −49 µm, 1.5 M H_2SO_4, 150 °C, 300 rpm, 1 hour).

Effect of time on the optimal experimental conditions

The effect of time on optimal experimental conditions was studied and results are shown in Figure 4.12. It can be seen that magnesium dissolved more quickly than iron and aluminium, while silicon and calcium showed a surprising difference in dissolution behaviour. After 6 hours' dissolution process, the concentrations of iron and aluminium in the complex coagulant solution reach values of 57.90, and 33.86%, respectively. It is shown that below 3 hours of dissolution time, the concentration of iron decreased substantially in the produced composite coagulant solution. This behaviour can be explained by the dissolution and precipitation of iron, which can be related to many factors such as solution concentration, temperature, and the presence of some ions in the solution. Furthermore, it is established that depending on solution concentration and temperature, a large number of iron minerals in aqueous H_2SO_4 solutions could precipitate, such as hydronium jarosite [$H_3OFe_3(SO_4)_2(OH)_6$]

and hydrous ferric oxides (Fe_2O_3 nH_2O) (Linke, 1958; Stumm and Morgan, 1996; Welham et al., 2000; Casas et al., 2005). This fact is further established by results from XRD analysis of the treated CFA (Figure 4.15). After 3 hours, the self- inhibition effect of iron to the mass transfer is influenced by the dissolution of other ions from the solid site. Then extraction efficiency of iron is increased. The lower dissolution of aluminium may be caused by the presence of an unfavourable structure of aluminium oxides, resulting from burning coal at high temperatures. The concentrations of silicon, magnesium, and calcium in the composite coagulant solution increased with time up to 11.12, 73.21, and 25.43% respectively for 6 hours' dissolution process. Low silicon extraction is common in an acidic solution and may be due to the mineral structure of CFA which promotes an alkaline solution to leach silicon (Mazzocchitti et al., 2009). Furthermore, the treated CFA samples (leach residues) are characterized and compared with the raw CFA (Section 4.2.2.8) in order to see the impact of H_2SO_4 dissolution of iron, aluminium, silicon, magnesium, and calcium; which provide an additional support to the dissolution behaviour of these elements.

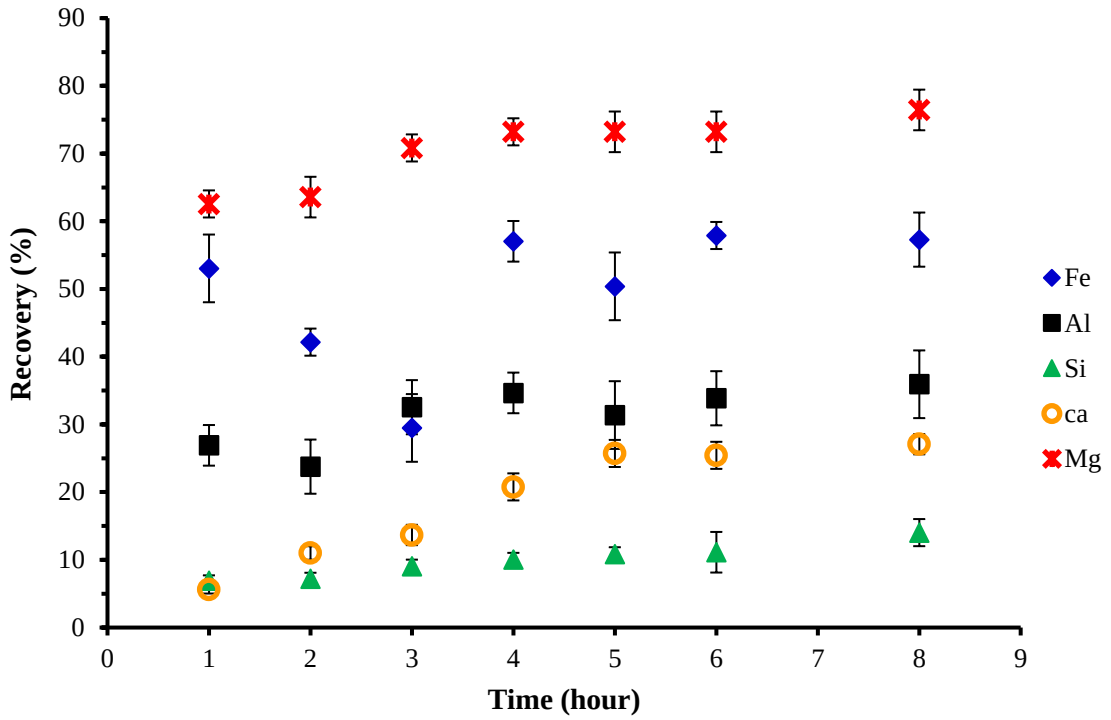

Figure 4.12: Effect of time on optimal experimental conditions (particle size: −49 µm, 1.5 M H_2SO_4, 150 °C, S/L, 0.20, 300 rpm).

Characteristics of the produced coagulant solution

The complex coagulant produced from leaching of CFA (shown in Figure 4.13) was a dark green colour liquid. The coagulant (produced using optimal experimental conditions, at 150 °C for 6 hours) was characterised in terms of chemical properties as presented in Table 4.4. It is shown that the constituent elements of the composite coagulant are iron (21731.89 mg/L), aluminium (603.18 mg/L), silicon (96 mg/L), magnesium (1366.70 mg/L), and calcium (796.70 mg/L). Other elements such as Mn, S, Ni, Co, and Cr are also present in the produced coagulant.

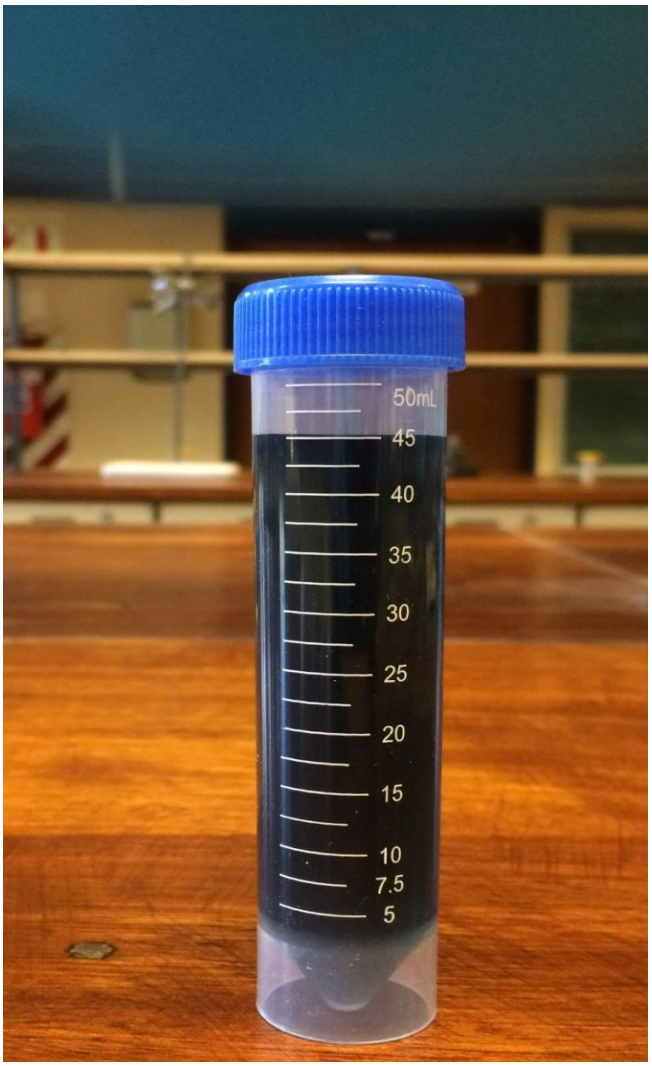

Figure 4.13: Complex coagulant. (Conditions: particle size: −49 µm, 1.5 M H_2SO_4, 150 °C, S/L= 0.20, 300 rpm, and 6 hours).

Table 4.4: Chemical composition of the coagulant produced by H_2SO_4 leaching of the CFA sample.

Properties of the synthesized complex coagulant at 150 °C for 6 hours	
pH	0.68–0.75 (< 4)
Colour	dark green
Fe	21731.89 mg/L
Al	603.18 mg/L
Si	96.00 mg/L
Mg	1366.70 mg/L
Ca	796.70 mg/L
S	4612.00 mg/L
Mn	402.15 mg/L
Ni	2696.06 mg/L
Co	27.35 mg/L
Cr	4397.15 mg/L
Cd	0.00 mg/L
Cu	0.00 mg/L
Pb	0.00 mg/L

Analysis of treated coal fly ash

Leach residues from the optimal experimental conditions were analysed using PSD, XRD, XRF, FTIR, and SEM in order to compare to raw CFA and measure the impact of H_2SO_4 dissolution.

Particle size distribution: The CFA ash leach residues obtained from H_2SO_4 leaching under optimal experimental conditions at 1, 3, and 6 hours were subjected to PSD analysis. The PSD (Figure 4.14) was similar for all CFA leach residues measured. Mainly, the average diameter at 80% of weight was 47 µm. These results were compared to the PSD of the raw CFA (Figure 4.1) for which an average diameter at 80% weight of 49 µm was determined. This shows that changes in particle size occurred during the dissolution process.

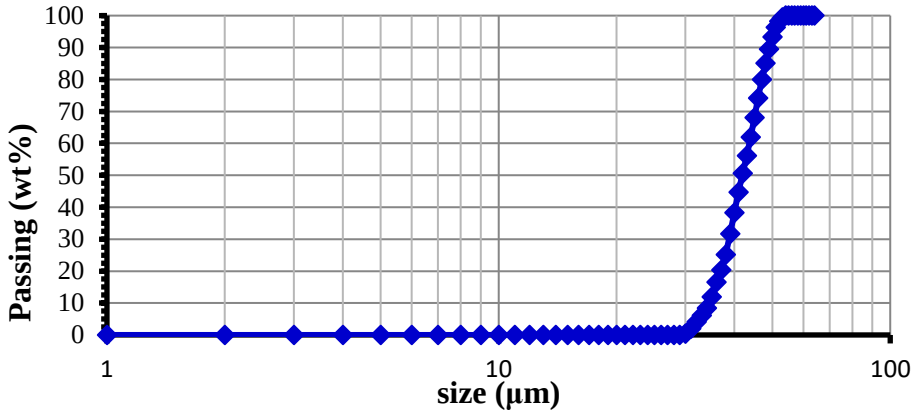

(a)

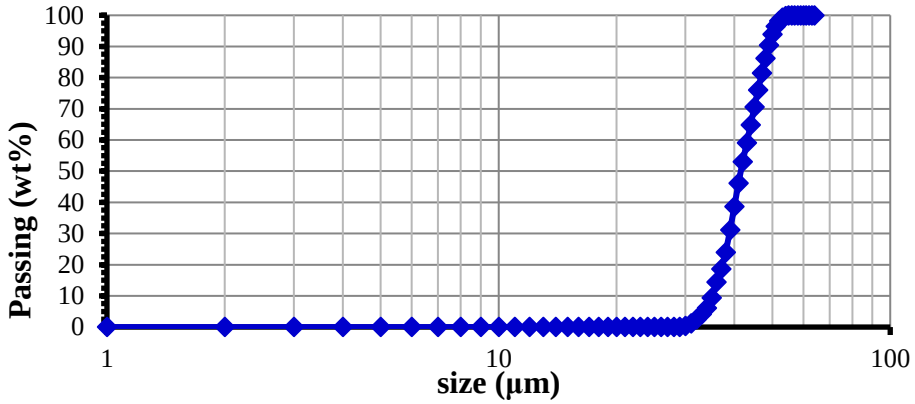

(b)

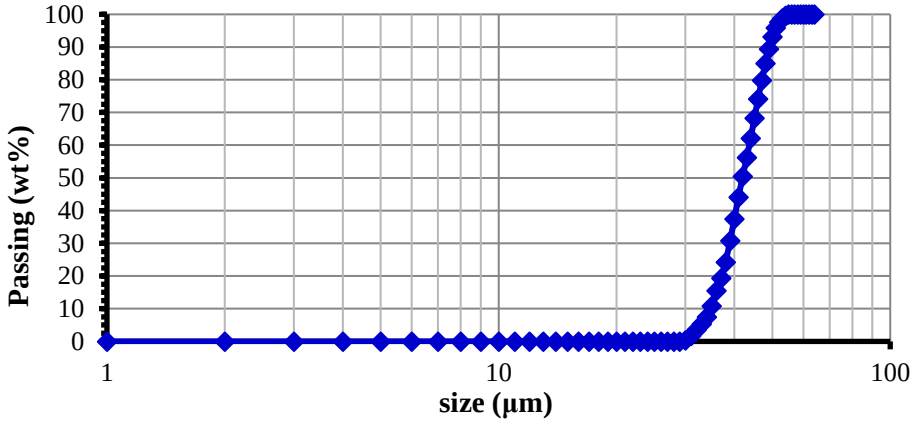

(c)

Figure 4.14: Particle size distribution of the treated CFA with H_2SO_4 under optimal experimental conditions at different leaching stages: (a) 1 hour leaching, (b) 3 hours leaching, and (c) 6 hours leaching.

X-ray diffraction and x-ray fluorescence: The XRD (Figure 4.15) and XRF (Table 4.4) analyses of residues were carried out for samples from the H_2SO_4 leaching under optimal experimental conditions with varying times.

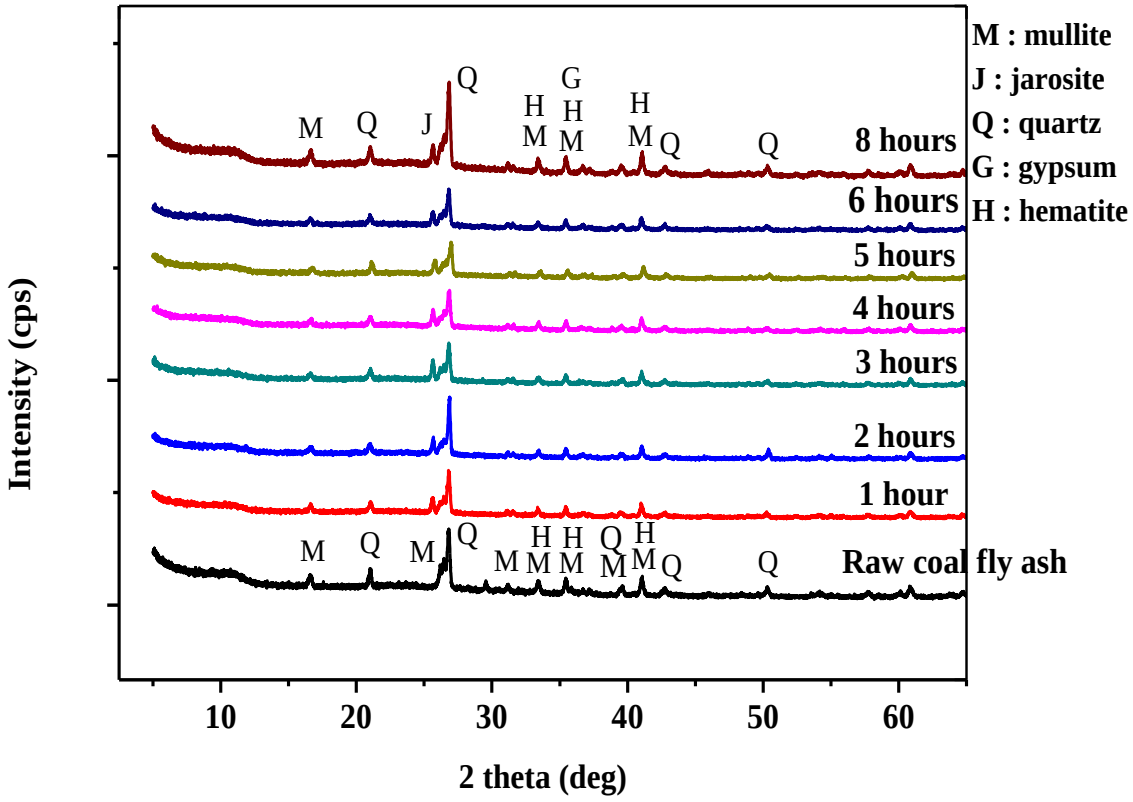

Figure 4.15: Comparison of XRD pattern of the raw to the treated CFA with H_2SO_4 leaching under optimal experimental conditions in different times.

The results from XRD and XRF obtained from the leached CFA samples were compared to the raw CFA sample. It can be seen from Figure 4.15 that the characteristics of the mineral matter in the raw CFA sample were revealed in the leach residues. However, during reaction with varying times secondary mineral phases such as jarosite ($2Fe_3(OH)_6(SO_4)_2$), and gypsum ($CaSO_4.2H_2O$) were formed. It is established that the formation of jarosite is based on the presence of iron in sulphate media and the tendency for iron sulphate to hydrolyse inside pH less than 3 and temperatures between 20 and 200 °C (Babcan, 1971; Roeland and Dijkhuis, 2009). Thus, in H_2SO_4 solution containing CFA, jarosite precipitate can be formed according to reaction in Equation 4.9 (Das et al., 1995; Roeland and Dijkhuis, 2009; Malenga et al., 2015). The XRD results of the leach residues are consistent with the leaching results in

Figure 4.12. Furthermore, the formation of gypsum is established on the presence of calcium in H_2SO_4 aqueous solution in which CaO (in CFA) tends to dissolve in water to form $Ca(OH)_2$ which will react with H_2SO_4 according to Equation 4.10 (Bellmann et al., 2006)

$$3Fe_2(SO_4)_3 + X_2SO_4 + 12H_2O \rightarrow 2Fe_3X(OH)_6(SO_4)_2\downarrow + 6H_2SO_4 \quad (4.9)$$

where X is the hydronium ion.

$$Ca(OH)_2 + 2H^+ + SO_4^{2-} + 2H_2O \rightarrow CaSO_4.2H_2O\downarrow + 2H^+ + 2OH^- \quad (4.10)$$

Table 4.5 shows that there is not much change in the XRF results of the raw and the treated CFA samples. These results agree well with XRD results in Figure 13.

Table 4.5: Chemical composition of the raw and treated CFA samples. Only important elements from important phases are presented.

Chemical composition	Content (wt%)							
	Raw CFA	Treated CFA						
		1 h	2 h	3 h	4 h	5 h	6 h	8 h
Al_2O_3	32.15	28.20	26.50	24.10	25.20	25.20	25.60	25.96
Fe_2O_3	4.16	2.34	2.60	3.26	2.14	2.36	2.10	2.19
SiO_2	49.92	49.50	49.40	49.30	49.26	49.10	49.50	49.22
CaO	6.25	5.59	5.03	5.18	5.95	6.17	5.60	4.81
TiO_2	2.15	2.13	2.15	2.15	2.14	2.14	2.15	2.15
MgO	1.40	0.46	0.56	0.57	0.45	0.46	0.45	0.42
K_2O	1.00	1.03	1.14	1.11	1.05	1.07	1.05	1.09
P_2O_5	1.04	0.16	0.18	0.21	0.17	0.19	0.17	0.19

Fourier transform infrared analysis: The FTIR spectra of the raw and treated CFA (residues of H_2SO_4 leaching under optimal experimental conditions at different times) are given in Figure 4.16 in which peaks in the wavenumber ranges from 950–1168 cm^{-1} and 550–920 cm^{-1} originated from quartz and mullite are practically unchanged after leaching, so that the identifiable chemical bonds remained practically unchanged. It can be seen the presence of the same mineral phases in the raw and treated CFA samples. This point was earlier established by results from XRD and XRF analyses (Figure 4.15 and Table 4.4).

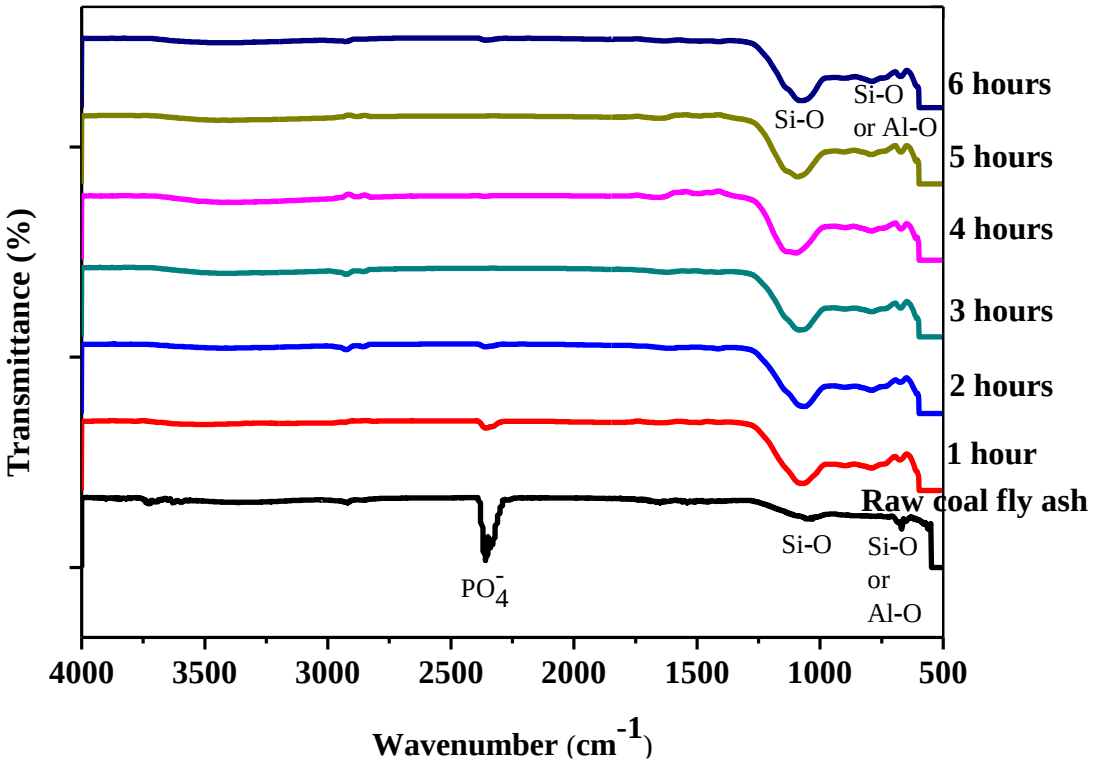

Figure 4.16: Comparison of FTIR spectrum of the raw to the treated CFA with H_2SO_4 leaching under optimal experimental conditions in different times.

Morphological analysis using SEM/EDS: The SEM of the feed and leach residues were used to support the dissolution behaviour of CFA. The SEM images of the raw and leached samples in Figure 4.17 show the marked effect of the H_2SO_4 solution. The surface morphology of the raw CFA particles (image a) looks relatively smooth. The morphologies in images (b), (c), and (d) are almost totally uniform compare to the agglomerations of particles in the feed (image a). Images (b), (c) and (d) reveal that a porous structure was formed after leaching. Moreover, the dissolution of H_2SO_4 produces a stem-like structure that denotes the formation of new phases. This aspect is previously established by results from XRD analysis (Figure 4.15).

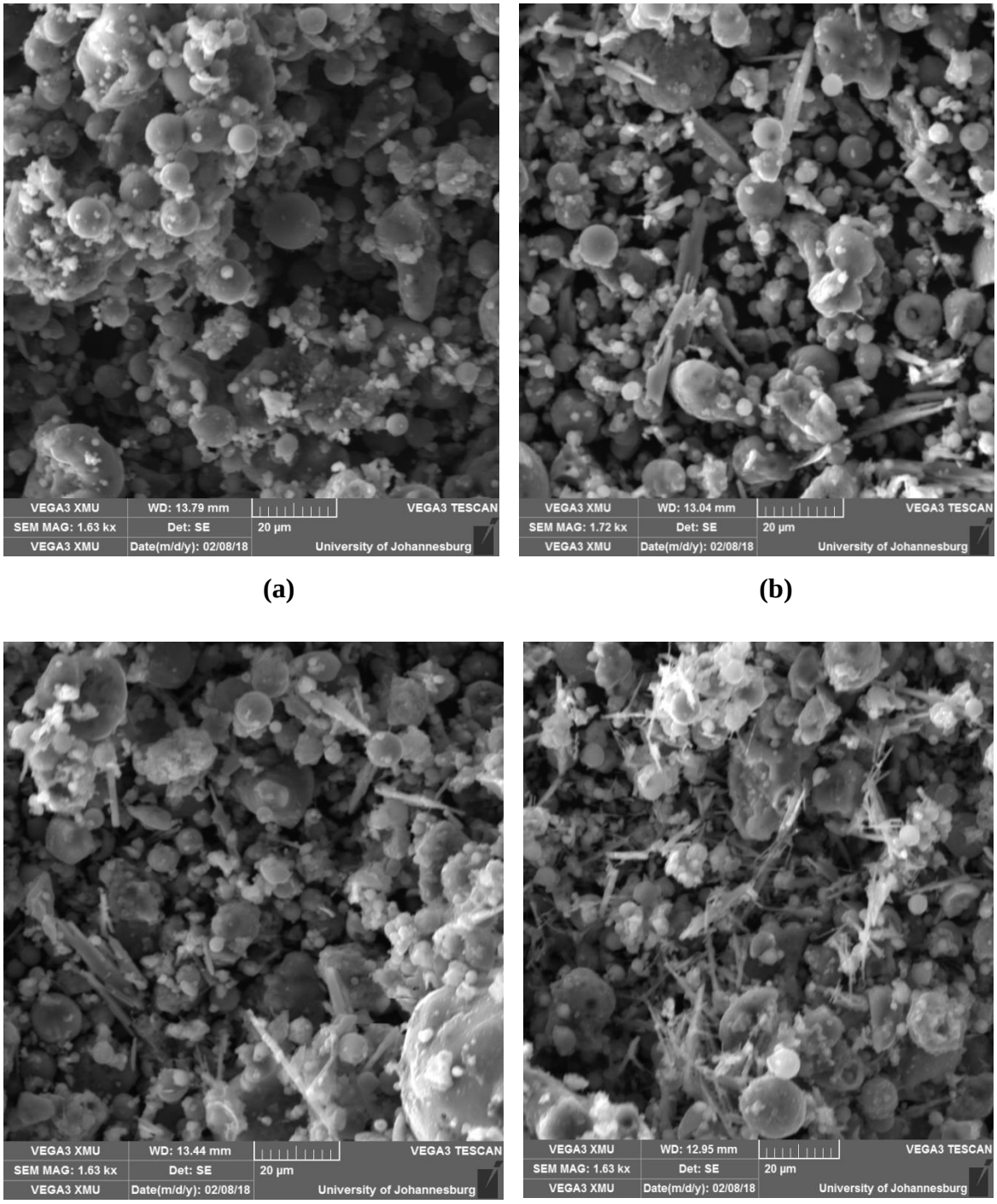

Figure 4. 17: SEM micrographs of CFA particles at different leaching stages. (a) raw CFA; (b) CFA after 1 hour leaching (c) CFA after 3 hours leaching, and (d) CFA after 6 hours leaching.

4.3 Leaching kinetics of coal fly ash

4.3.1 Kinetic mechanism

Rate controlling factor based on shrinking core model

In order to determine the rate controlling factor and the nature of the dissolution process of CFA particles with H_2SO_4, shrinking extraction type core model was used by assuming that the solid particles are spherical and the reaction occurs at a constant temperature (Habashi, 1999; Rutto and Enweremadu, 2012; Brouwers and Van Eijk, 2002; Koech et al., 2015). The rate controlling model is determined based on the standard equations of the shrinking core model below, and the more linear graph with higher R^2 value is the rate controlling factor.

- Film diffusion factor: $x = kt$ (4.11)
- Chemical reaction factor: $1 - (1 - x)^{1/3} = kt$ (4.12)
- Product layer diffusion factor: $1 - 3(1 - x)^{2/3} + 2(1 - x) = kt$ (4.13)
- Mixed - controlled factor: $\left[(1 - x)^{-1/3} - 1\right] + \left(\frac{1}{3}\right) ln(1 - x) = kt$ (4.14)

The conversion (x) was used to plot f {= x (for film diffusion control); = $1 - (1 - x)^{1/3}$ (for chemical reaction control); = $1 - 3(1 - x)^{2/3} + 2(1 - x)$ (for product layer (coal fly ash) diffusion control); and = $\left[(1 - x)^{-1/3} - 1\right] + \left(\frac{1}{3}\right) ln(1 - x)$ (for mixed-controlled)} against time for the extracted elements (iron, aluminium, silicon, calcium and magnesium).

Leaching of iron

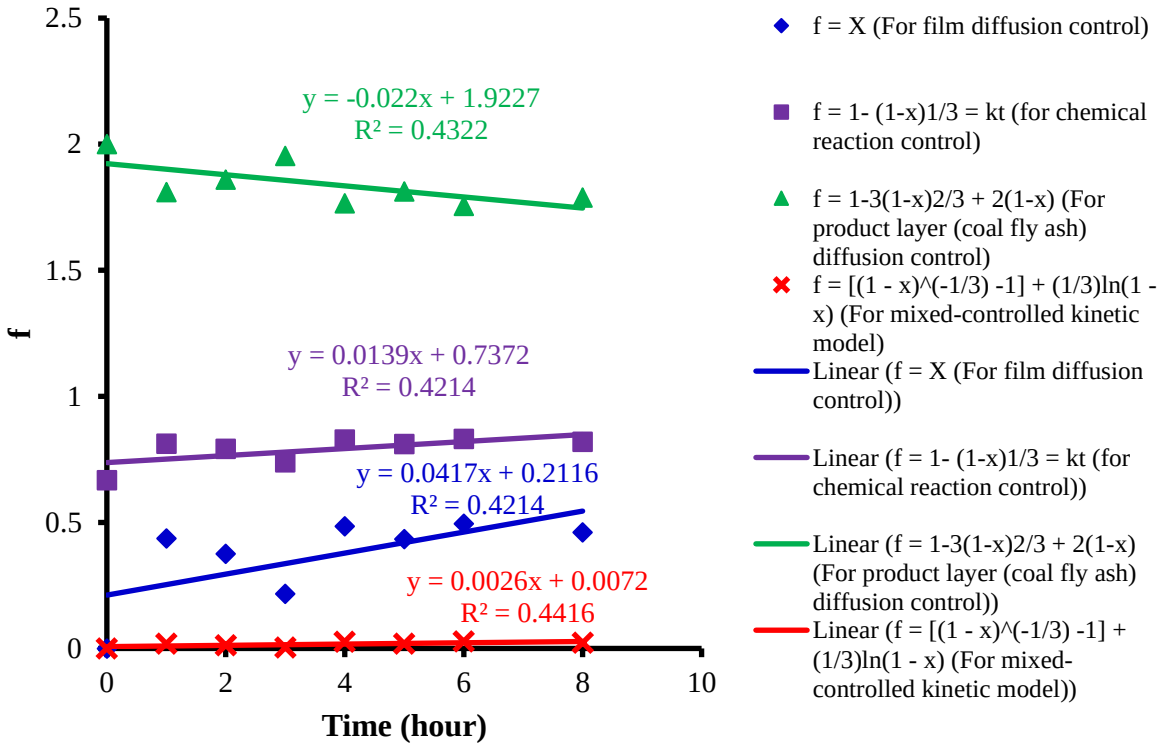

Figure 4.18: Determination of the rate controlling factor of leaching of iron.

Leaching of aluminium

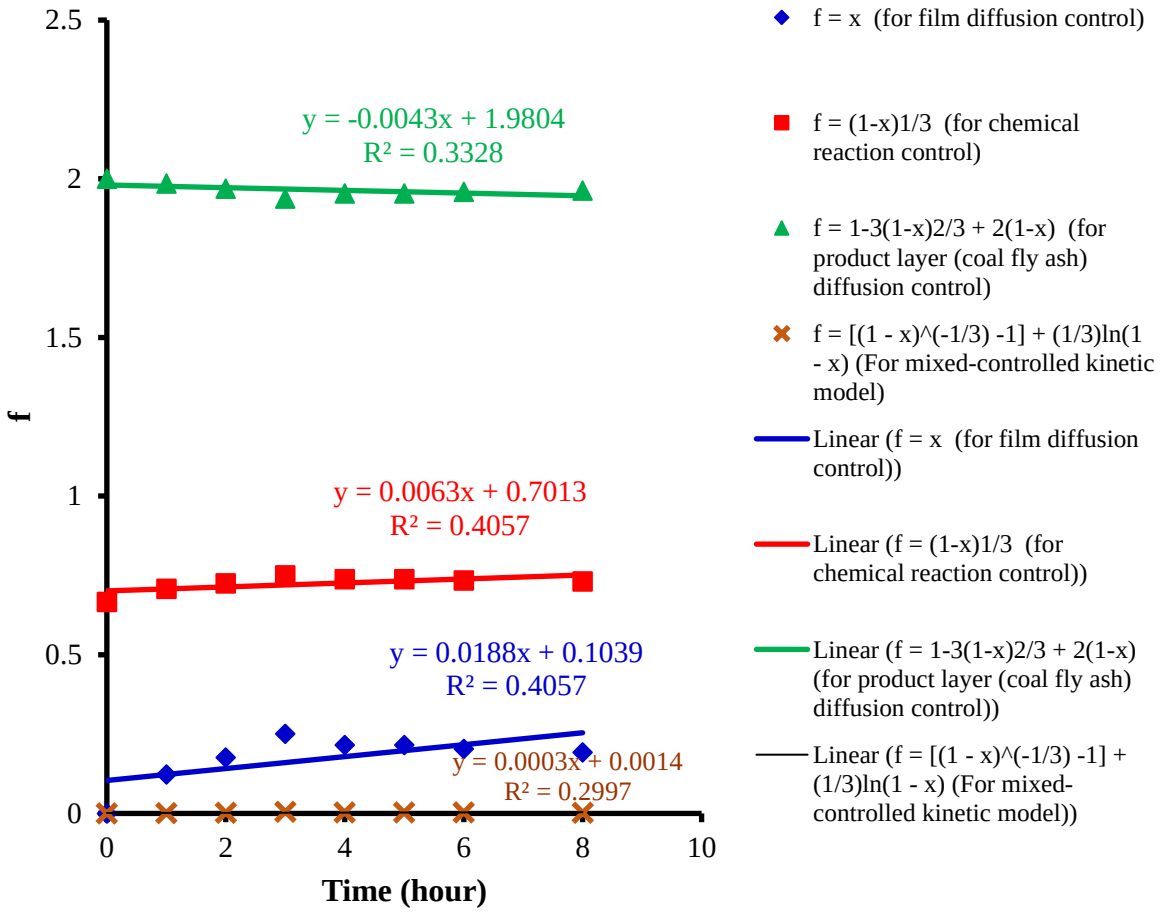

Figure 4.19: Determination of the rate controlling factor of leaching of aluminium.

Leaching of silicon

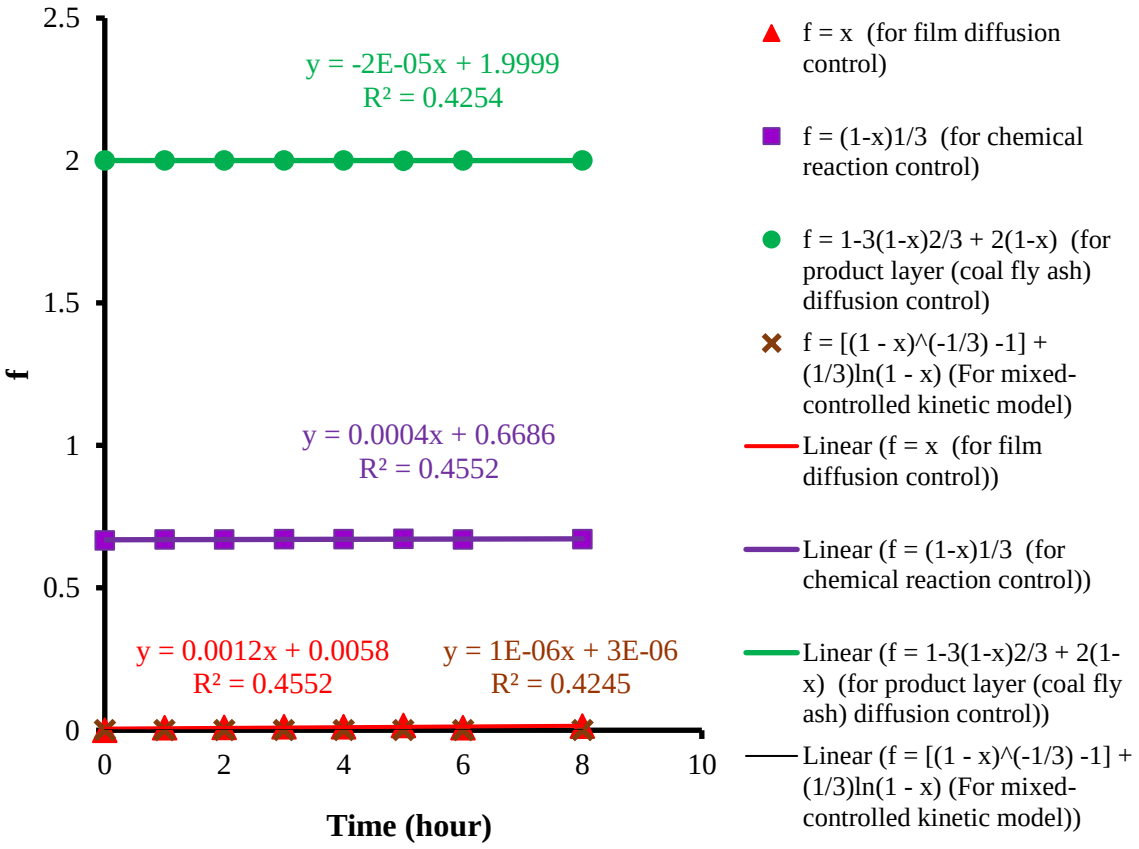

Figure 4.20: Determination of the rate controlling factor of leaching of silicon.

Leaching of calcium

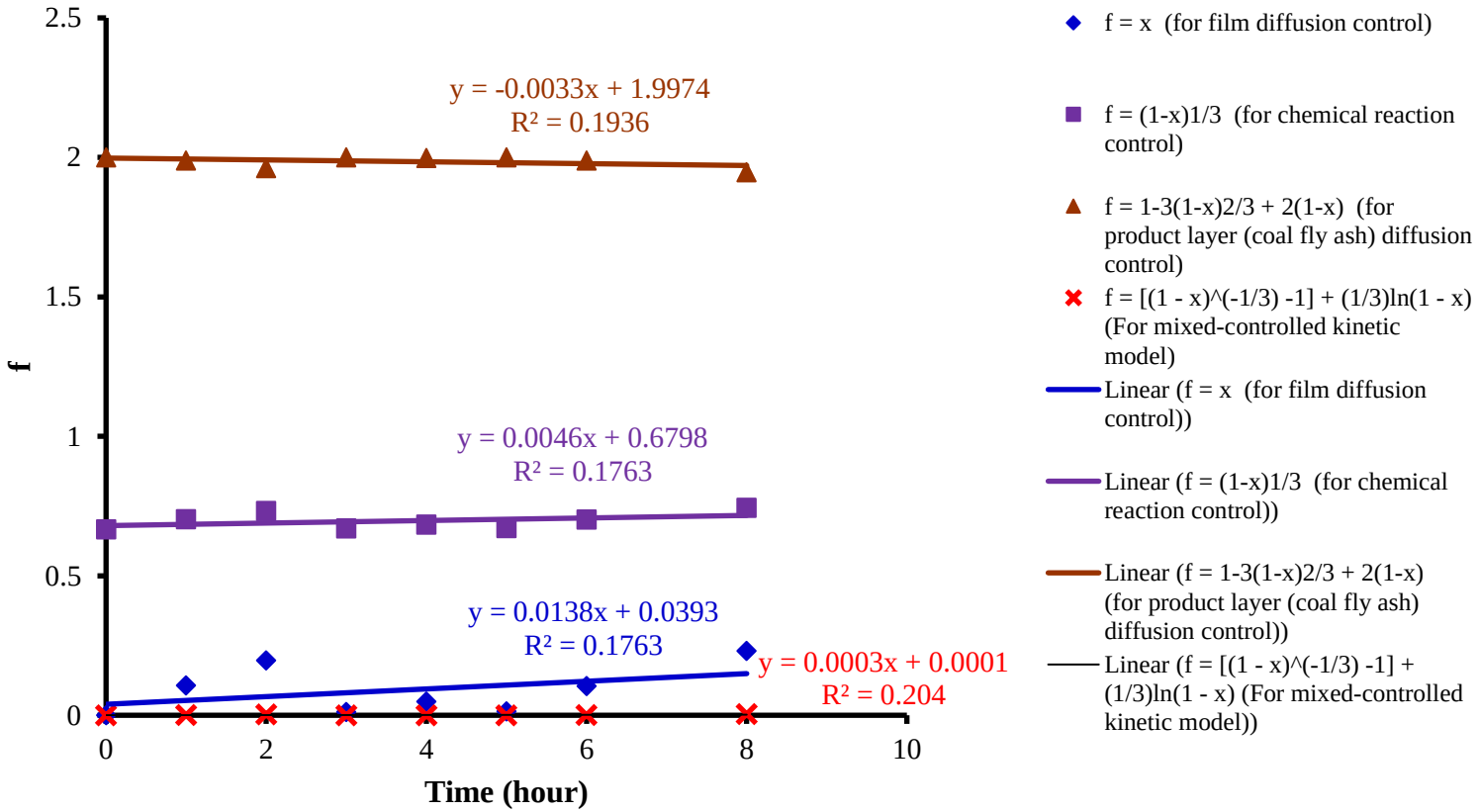

Figure 4.21: Determination of the rate controlling factor of leaching of calcium.

Leaching of magnesium

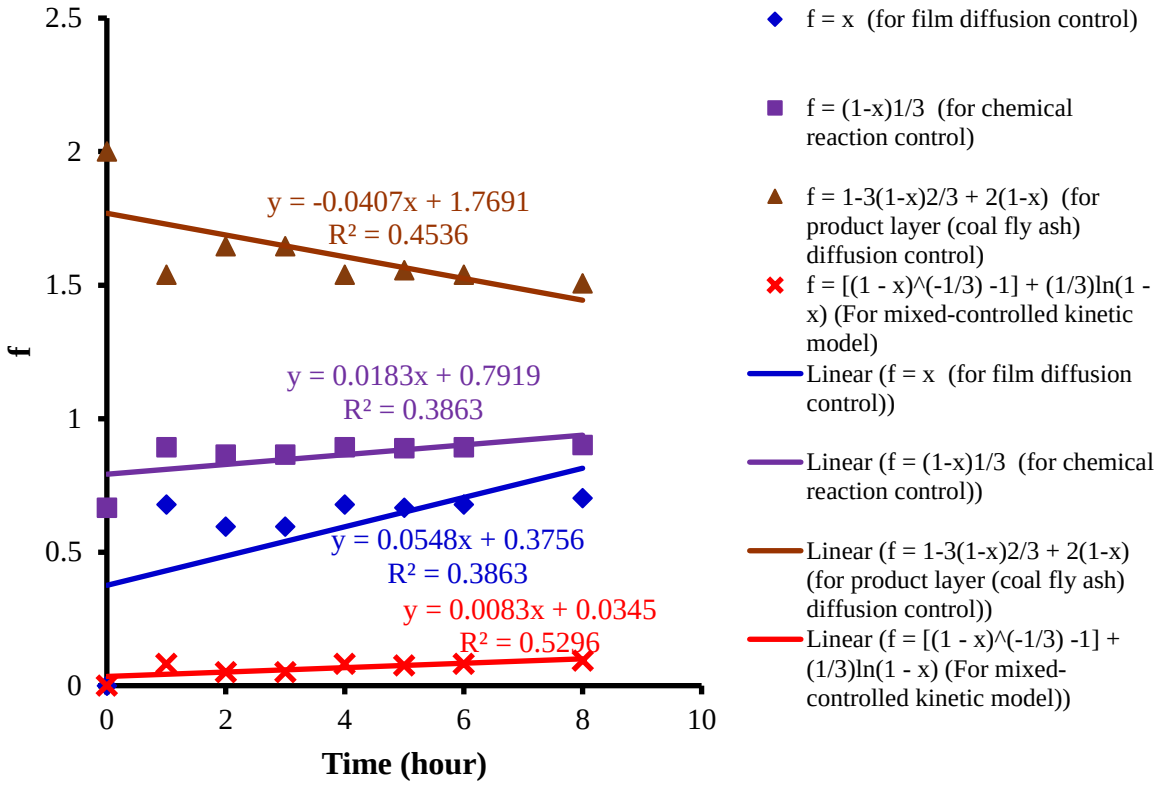

Figure 4.22: Determination of the rate controlling factor of leaching of magnesium.

The kinetic investigation of the leaching behaviour of CFA as seen in the above Figures 4.18 to 4.22 based on the shrinking core model showed that the rate of the dissolution is controlled by mixed controlled mechanism (diffusion and chemical reaction). Similar kinetic mechanisms were also found by leaching of rutile ore, Semi-Oxidized Manganese Ores and CFA (Baba et al., 2009; Wang et al., 2017; Shemi, 2013). The extraction of aluminium showed two step mechanisms (before and after the optimum dissolution temperature, which was 150 °C).

Rate controlling factor based on the activation energies

The activation energies of elements extracted from CFA were determined using Arrhenius equation given by the Equation 4.15.

$$k = A\, e^{\frac{-E_a}{RT}} \tag{4.15}$$

where A is the exponential factor, E_a is the activation energy, R is the gas constant (J mol $^{-1}$ K^{-1}), and T is the temperature (Kelvin).

From the above kinetic expressions (Equations 4.11, 4.12, 4.13, and 4.14) and at a constant time, f (x) is proportional to k. Therefore, conversion can be used to determine the activation energy using the following relationship

$$f\ (x = \text{conversion}) \sim k = A\, e^{\frac{-E_a}{RT}} \tag{4.16}$$

$$ln\ f\ (x = \text{conversion}) \sim ln\ k = lnA\ -\ \frac{E_a}{R}\frac{1}{T} \tag{4.17}$$

By plotting $ln\ f$ (x = conversion) against $^1/_T$, the activation energy can be determined from the slope of the graph (with R = 8.314 J mol $^{-1}$ K^{-1}). To determine the activation energy, the mixed-controlled kinetic model was used as discussed above. ln f (f = $\left[(1-x)^{-1/3}-1\right] + \left(\frac{1}{3}\right) ln(1-x)$) was plotted against $^1/_T$ as seen in Figure 4.23, and E_a was calculated from the slope of the graph ($E_a = R \times slope$)

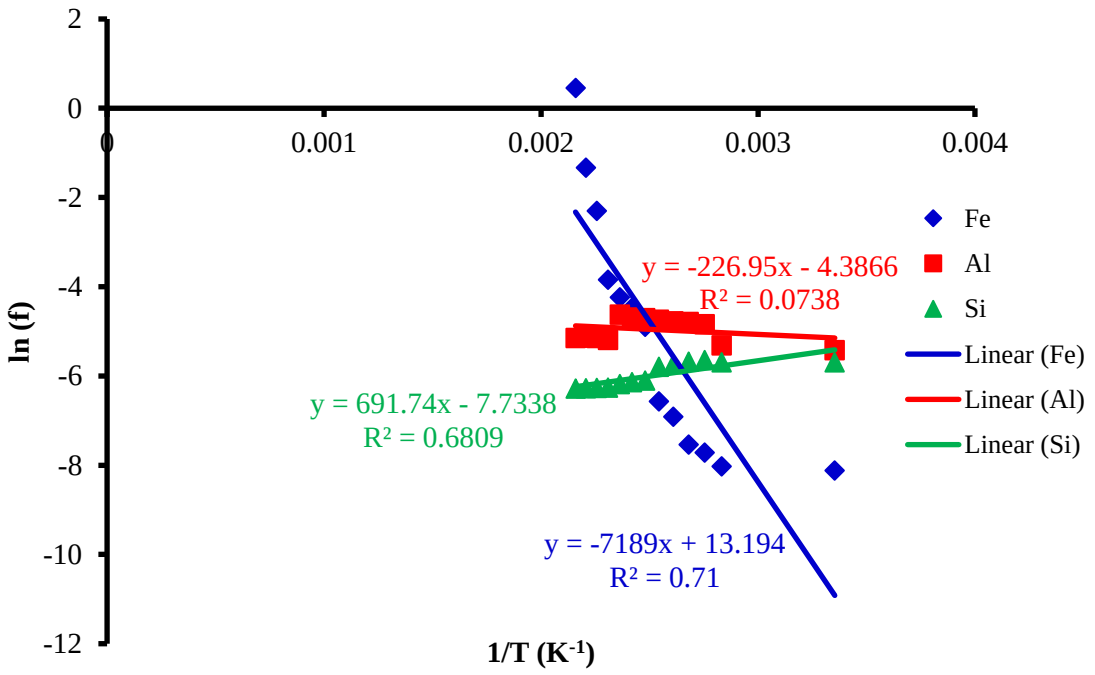

Figure 4.23: Determination of E_a.

As seen from the above Figures, two behaviours were observed from the dissolution of aluminium. The concentration of aluminium decreased after 150 °C; therefore, plotting *ln* f from 25 to 190 °C gave low R^2 value. Figure 4.24 below gives the activation energies E_{a1} and E_{a2} before and after the optimum temperature, respectively.

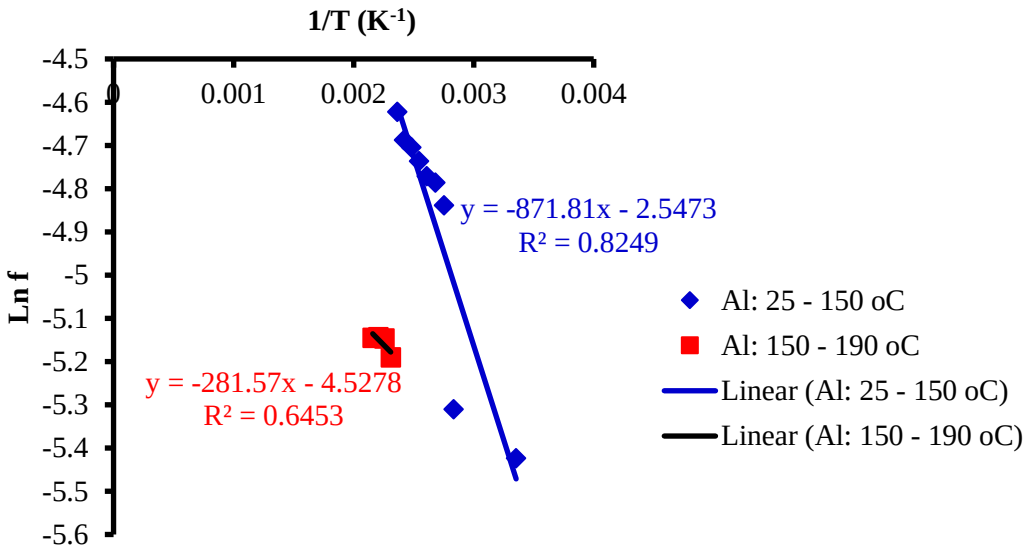

Figure 4.24: E_a for aluminium extraction.

Table 4.6 displays the E_a calculated from the above Figures.

Table 4.6: Calculated E_a for the dissolution of elements

Elements	**Fe**	**Al (before 150 °C)**	**Al (after 150 °C)**	**Si**
E_a (J/mole)	59769.35	7248.228	2340.973	5751.126

Iron required more activation energy for its acid dissolution, followed by aluminium and silicon. This result is in agreement with findings from Li et al. (2009). Furthermore, similar behaviours were observed with chemical reaction kinetic model (as seen in Appendix A: Figure A.1 to A.3) which confirms that the dissolution mechanism was mixed–controlled kinetics.

4.3.2 Kinetic models

In order to design and scale up the leaching process, it is essential to study the kinetic behaviour or models, because they describe the rate of dissolution of elements found in CFA by H_2SO_4 solutions as lixiviant. The experimental data were used to fit the currently known kinetic models to determine the suitable model for the leaching process. Six reaction kinetic models, namely, zero-order, half-order, first-order, second-order, Hixson and Crowell, and Gompertz model equations were used to investigate the suitability of those reaction kinetic models against the experimental data.

The kinetic studies for various elements were conducted by using the proposed leaching optimum conditions found in previous section ((Particle size: −49 μm, 1.5 M H_2SO_4, 150 °C, S/L= 0.20, 300 rpm, and 6 hours). The treated CFA samples were collected at pre-set time intervals ranging from 1 to 8 hours, and the concentrations of the elements were in the same way determined. Plots of metals and silicon dissolution versus time are previously presented in Figure 4.12.

Zero-order model

A zero-order equation for the dissolution (Magalhães et al., 2005) of elements in CFA may be expressed in the following form:

$$-\frac{d\,C}{dt} = K\,C^n \tag{4.18}$$

n = 0 for zero order kinetic model, therefore the above equation became

$$-\frac{d\,C}{dt} = K \tag{4.19}$$

$$-d\,C = K\ dt \tag{4.20}$$

Integration method was used to solve the above differential equation,

$$-\int_{C_t}^{C_0} d\,C = K\int_0^t dt \tag{4.21}$$

$$C_0 - C_t = Kt \tag{4.22}$$

$$C_t = C_0 - Kt \tag{4.23}$$

where C_t represents the concentration of element dissolved at time *t*, *t* (hour) is the leaching time, C_0 is the initial concentration of element in CFA, and *K* ($mol\ L^{-1}\ h^{-1}$) represents the zero-order dissolution rate constant. The plot of the element-dissolved fraction versus time should be linear if the dissolution reaction is zero order. Figure 25 shows the plot of C_t versus time for Fe, Al, Si, Ca, and Mg respectively. The slopes and intercepts of the curves in Figures 4.25 were used for determining the zero-order dissolution rate constants, K. The dissolution rate constants for Al, Si, Ca, and Mg are presented in Table 4.8.

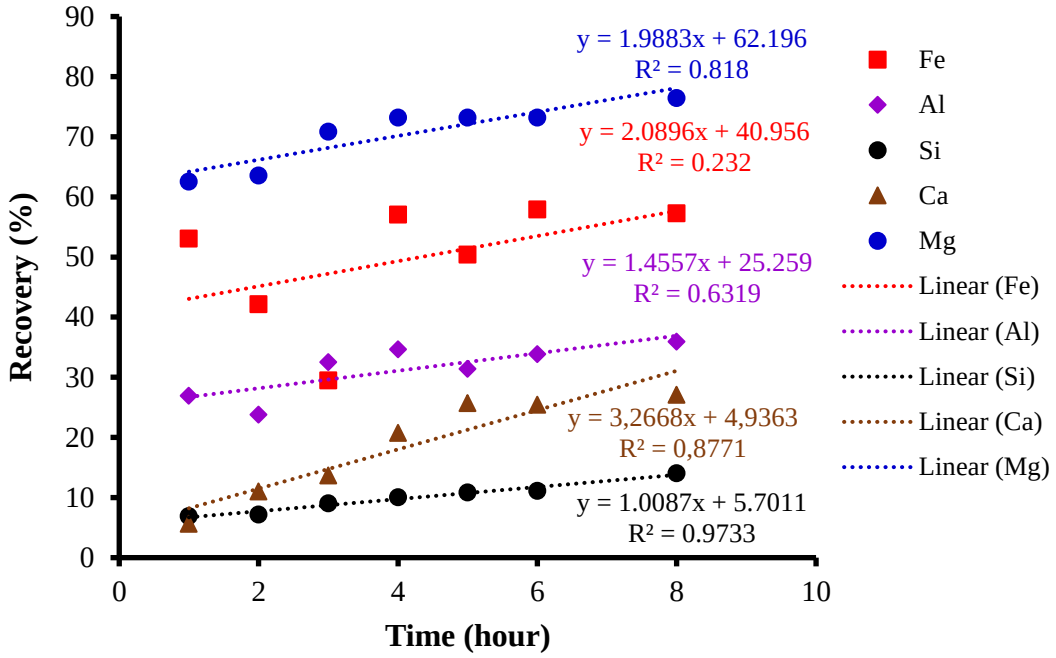

Figure 4.25: Zero-order kinetic model for the leaching of Fe, Al, Si, Ca, and Mg from coal fly ash. (Particle size: −49 µm, 1.5 M H_2SO_4, 150 °C, S/L= 0.20, 300 rpm, and 8 hours).

From Figure 4.25, it can be seen that silicon fit the zero-order model with R^2 value of 0.97 followed by calcium and magnesium. The deviations of experimental data from the fitting zero-order model of extracted metals (aluminium and iron) are greater, which indicate that other models should be investigated.

Half-order model

The Half-order model is defined as follows (Li and Miller, 2002):

$$\frac{dC}{C^{1/2}} = -Kdt \tag{4.24}$$

Integration method was used to solve the differential equation,

$$\int_{C_0}^{C_t} C^{-1/2}\ dC = -K\ \int_0^t dt \tag{4.25}$$

$$2\left(C_s^{1/2} - C_0^{1/2}\right) = -Kt \tag{4.26}$$

The linear form of the half-order equation can be expressed as follow:

$$C_s^{1/2} = C_0^{1/2} - \frac{1}{2}Kt \tag{4.27}$$

where, C_s represents the concentration of the element in solution, C_0 is the initial amount of the element, *K* ($mol^{1/2}\ L^{1/2}\ h^{-1}$) is the dissolution rate constant, and *t* (hour) is the leaching time. The dissolution rate constant *K* can be determined from the slope and y-intercept of the half-order plot of $C_s^{1/2}$ against time as seen in Figure 4.26.

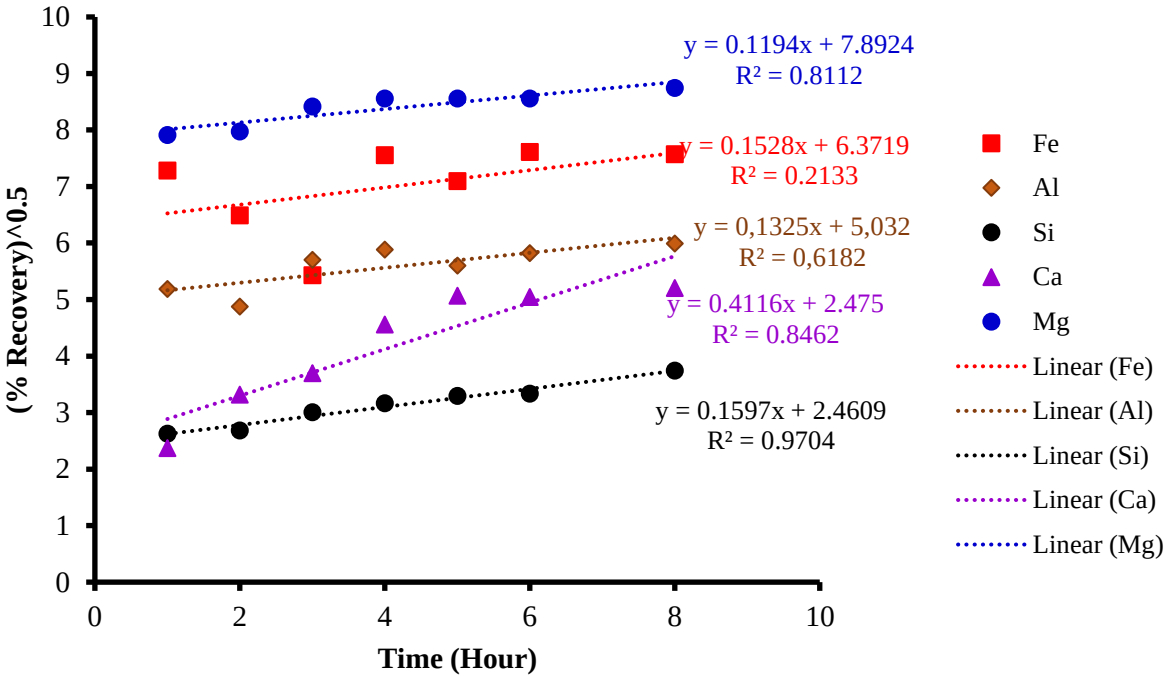

Figure 4.26: Half-order kinetic model for the leaching of Fe, Al, Si, Ca, and Mg from coal fly ash. (Particle size: −49 µm, 1.5 M H_2SO_4, 150 °C, S/L= 0.20, 300 rpm, and 8 hours).

Figure 4.26 showed that iron and aluminium dissolution behaviours deviated more from the fitting linear half order kinetic model. Therefore, they should be more investigated. For silicon, calcium and magnesium, experimental data fitted the half-order kinetic model.

First-order model

The first-order kinetic model (Li and Miller, 2002) can be expressed from the general kinetic equation given by

$$dC/dt = KC^n \tag{4.28}$$

By replacing n = 1 into the above equation, the differential equation can be solved as follows

$$dC/dt = KC \tag{4.29}$$

$$\int_{C_0}^{C_t} \frac{d\,C}{C} = K \int_0^t d\,t \tag{4.30}$$

After rearranging and integrating the equation,

$$\ln C_t = \ln C_t - Kt \tag{4.31}$$

where, C_t is the concentration of dissolved element at time t (hour) and *K* represents the first-order rate constant of dissolution (time^{-1} or per hour). Values of *K* can be calculated from the plots of $\ln C_t$ versus *t* (Figure 4.27) for different elements in CFA.

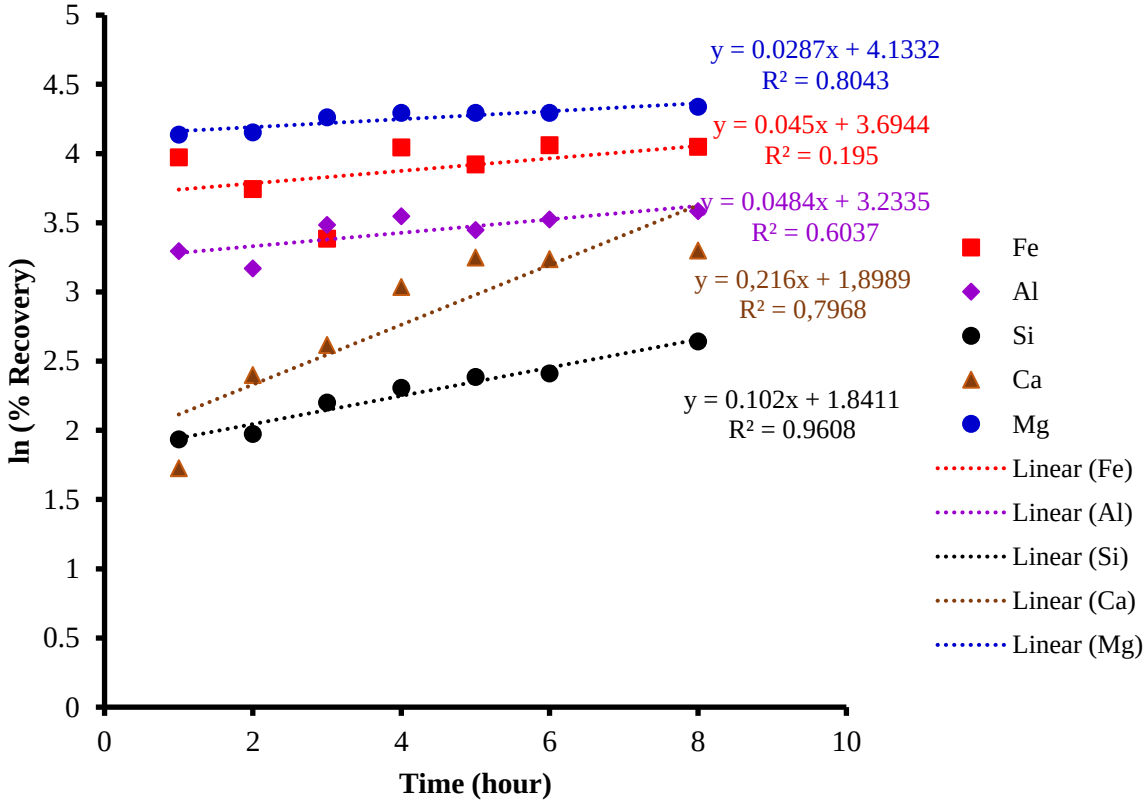

Figure 4.27: First-order kinetic model for the leaching of Fe, Al, Si, Ca, and Mg from coal fly ash. (Particle size: −49 µm, 1.5 M H_2SO_4, 150 °C, S/L= 0.20, 300 rpm, and 6 hours).

It can be seen from Figure 4.27 that silicon and magnesium fit the first order kinetic model. The experimental data of calcium, aluminium and iron deviate more from the linear form of the first order kinetic model. More discussion should be carried out in order to determine the leaching kinetic model.

Second-order model

The second-order kinetic model (Greenberg and Tomson, 1992) is described as follows

$$-\frac{dC}{dt} = KC^2 \tag{4.32}$$

$$-\frac{dC}{C^2} = Kdt \tag{4.33}$$

The above differential equation was solved using the integration method

$$\int_{C_0}^{C_t} C^{-2}\, dC = -K \int_0^t d\, t \tag{4.34}$$

$$\frac{1}{C_t} = \frac{1}{C_0} + K\, t \tag{4.35}$$

where, C_t and C_0 are the amounts of element dissolved at time *t* (hour) and *t* = 0,-respectively, and *K* is the rate constant of second-order dissolution (L/ mol h). The second order kinetic model accuracy is determined by the fitting level of the linear plot of $1/C_t$ against *t*. The second-order kinetic rate constant, *K*, may be calculated from the slope of the plots of $1/C_t$ against *t*. Figure 4.28 shows the plots of $1/C_t$ vs *t* for the elements in CFA.

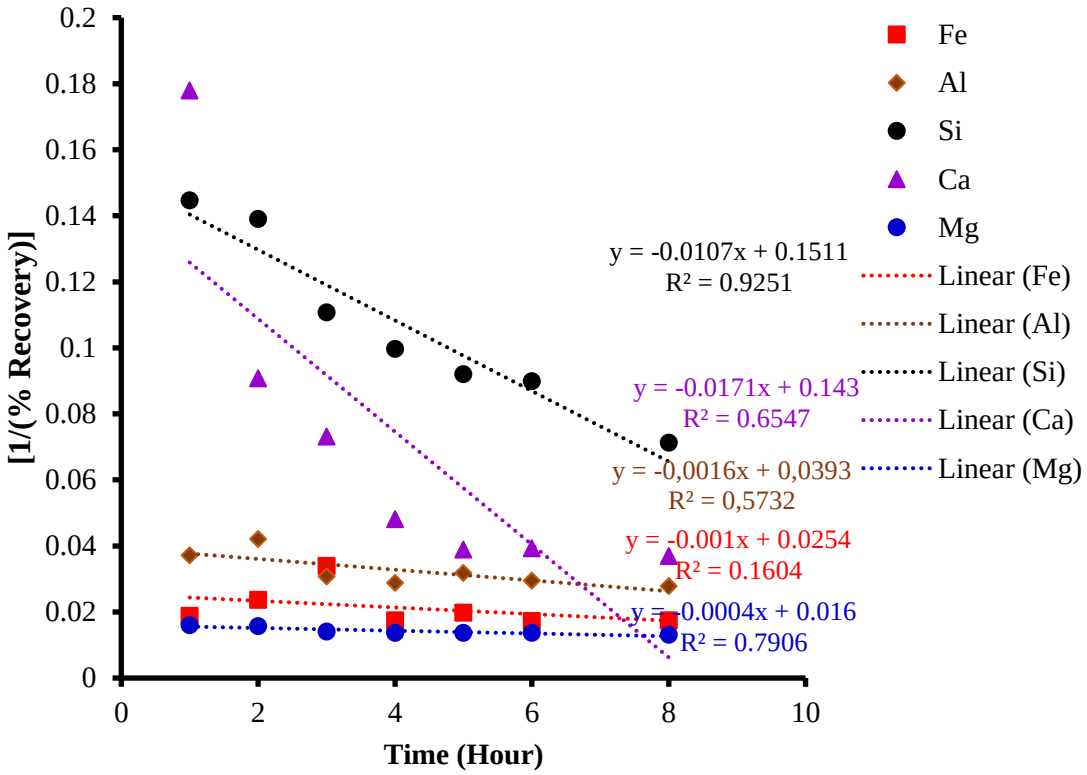

Figure 4.28: Second-order kinetic model for the leaching of Fe, Al, Si, Ca, and Mg from coal fly ash. (Particle size: −49 µm, 1.5 M H_2SO_4, 150 °C, S/L= 0.20, 300 rpm, and 6 hours).

Figure 4.28 shows a good agreement of experimental data with the second-order kinetic model for silicon and magnesium. The correlation coefficients for the second-order kinetic model are 0.93 and 0.79, respectively (Table 4.7). However, although the deviations are little in the case of iron and aluminium, it was observed that the second-order model was not suitable for iron, aluminium, and calcium in the tested leaching process.

Hixson and Crowell model

The Hixson-Crowell cubic root law describes the dissolution from systems in which the surface area and diameter of particles change. As a result, particles of regular area are proportional to the cube root of its volume. From the above concept, Hixson-Crowell established a relationship between particle dissolution and time, which can be represented by the following equation (Gouda et al., 2017; Jalal et al., 1989):

$$C_t^{1/3} = C_0^{1/3} - Kt \tag{4.36}$$

where, C_0 (%) is the initial amount of element in CFA, C_t (%) is dissolved amount of element at time *t*, and *K* is the Hixson-Crowell constant describing surface volume relation. To study the dissolution kinetics, experimental data were plotted as cube root of element percentage dissolved, $C_t^{1/3}$, versus time and are presented in Figure 4.29.

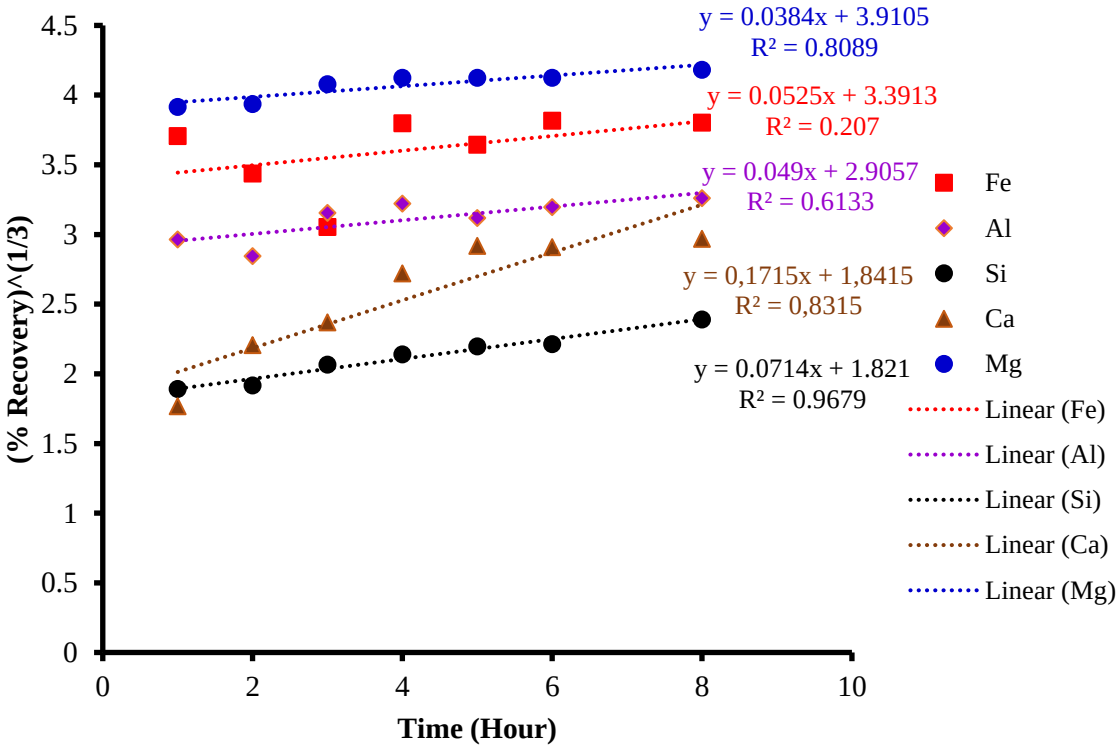

Figure 4.29: Hixson-Crowell kinetic model for the leaching of Fe, Al, Si, Ca, and Mg from coal fly ash. (Particle size: −49 µm, 1.5 M H_2SO_4, 150 °C, S/L= 0.20, 300 rpm, and 6 hours).

The results as shown in Figure 4.29 indicate that a linear relationship was obtained in the cases of silicon, calcium and magnesium. This implies that change in surface area and diameter of the CFA particles occurs with the progressive dissolution of matrix as a function of time. Nevertheless, the dissolution data of iron and aluminium did not fit the Hixson-Crowell cube root law.

Gompertz model

Leaching behaviour of CFA can also be described by the Gompertz model (Lokhandwala et al., 2013), expressed by the following equation:

$$C_t = C_{max} exp\left[-\alpha e^{\beta \log t}\right] \quad (4.37)$$

$$\ln\left(\frac{C_t}{C_{max}}\right) = -\alpha e^{\beta \log t} \quad (4.38)$$

The linear form can be expressed as follows:

$$\ln\left[-\ln\left(\frac{C_t}{C_{max}}\right)\right] = \ln \alpha + \beta \log t \quad (4.39)$$

where C_t is the amount of dissolved element at time *t*; C_{max} is the maximum dissolution; α represents the undissolved proportion at time t = 1 and described as location or scale parameter; β is the dissolution rate per unit of time described as shape parameter. This model has a strong increase at the beginning and converges gradually towards asymptotic maximal dissolution (Magalhães et al., 2005). Figure 4.30 shows the plot of $\ln\left[-\ln\left(\frac{C_t}{C_{max}}\right)\right]$ versus $\log t$. The values of α and β can be determined from y intercept and slope, respectively.

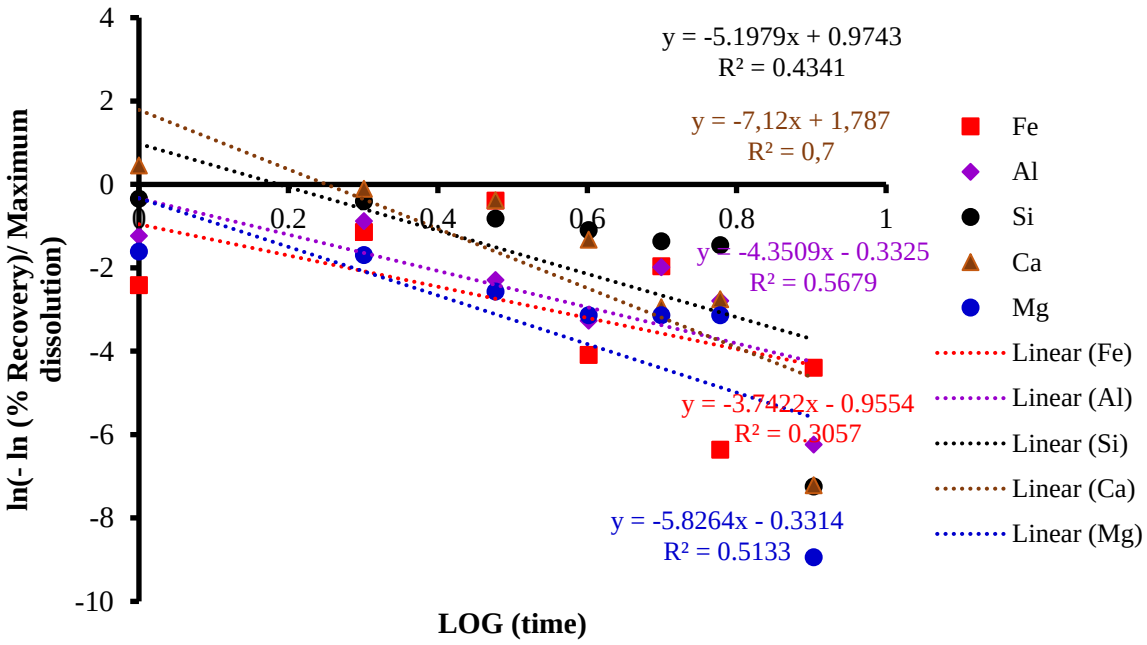

Figure 4.30: Gompertz model for the leaching of Fe, Al, Si, Ca, and Mg from coal fly ash. (Particle size: −49 µm, 1.5 M H_2SO_4, 150 °C, S/L= 0.20, 300 rpm, and 6 hours).

Kinetic models behaviour and determination of kinetic parameters

The behaviour of the sulphuric acid leaching of CFA was applied in different kinetic models and was interpreted in the form of graphical presentation and evaluated by correlation coefficient (R^2) represented in Table 4.7. The highest value of correlation coefficient determines the appropriate kinetic equation model that follows element dissolution. From the comparison in Table 4.7, it was found that zero-order kinetic model fitted mostly the investigated elements (Al: R^2 = 0.63; Si: R^2 = 0.9733; Ca: R^2 = 0.877 and Mg: R^2 = 0.8180). For Si and magnesium, the half-order kinetic R^2 values were closer to those of the zero order (0.9704 and 0.8112, respectively). More investigation should be carried out for iron behaviour. Table 4.8 displays the kinetic model parameters.

Table 4.7: Linear kinetic coefficients of determination (R^2)

Elements	Zero-order	Half-order	First-order	Second-order	Hixson and Crowell model	Gompertz model
Fe	0.2320	0.2133	0.1950	0.1604	0.2070	0.3057
Al	0.6319	0.6182	0.6037	0.5732	0.6133	0.5679
Si	0.9733	0.9704	0.9608	0.9251	0.9679	0.4341
Ca	0.8771	0.8462	0.7968	0.6547	0.8315	0.7000
Mg	0.8180	0.8112	0.8043	0.7906	0.8089	0.5133

Table 4.8: Kinetic model parameters

Elements	Zero-order	
	K (Kinetic constant) (mol L^{-1} h^{-1})	**R^2**
Al	1.4557	0.6319
Si	1.0087	0.9733
Ca	3.2668	0.8771
Mg	1.9883	0.8180

4.4 Conclusion

The CFA is composed of both crystalline and amorphous phases. In addition, the amorphous phase can be either clear glass beads or more irregular spongy material. Aluminium can occur in any or all of the three phases (Hulett and Weinberger, 1980). In CFA sample used in this study, aluminium-bearing phases must be in both crystalline and amorphous phases. Part of it is present as crystalline mullite. Iron in hematite was identified in individual crystallographic phases. The aluminium dissolution was dramatically different from the iron dissolution. More than 30% of Aluminium in the CFA sample was dissolved after 6 hours at 150 ^{o}C. This fraction of aluminium may be in the crystalline phase. The remaining aluminium was in a very refractory phase and can be present perhaps in high silica as glass constituent. For the iron dissolution, it was observed greater dissolution of iron then aluminium. Increased dissolution behaviour could be expected since the CFA sample contained a portion of the iron as the crystalline phase hematite (physically separated from the aluminium). In this study, the outcome of the use of CFA as a precursor for iron, alumimiun, and other strategic elements (Si, Mg, and Ca) in the synthesis of coagulant through pressure leaching method was achieved. The synthesised complex coagulant would be used in the AMD treatment.

Furthermore, the presence of porous layer is taken into account during the dissolution of the CFA particles. According to the shrinkage core model of the dissolution, the reaction is considered to occur first on the outer surface of the CFA particles. The porous zone enters the solid particles and the particles shrink during the dissolution process. The kinetics of the leaching process involves three steps that occur during leaching: (1) the outer diffusion of H_2SO_4 to the solid surface, (2) inside diffusion in the porous layer from the solution to the core surface and vice versa, and (3) dissolution reaction at the solid surface. Based on the Arrhenius equation, the activation energy of iron dissolution is higher than those of the leaching of aluminium and silicon. The investigation of the kinetic models revealed that zero-order kinetic model fitted mostly the investigated elements (Al: $R^2 = 0.6319$; Si: $R^2 = 0.9733$; Ca: $R^2 = 0.8771$ and Mg: $R^2 = 0.8180$). For silicon and magnesium, the half-order kinetic R^2 values were closer to those of the zero order (0.9704 and 0.8112, respectively).

References

Andini, S., Cioffi, R., Colangelo, F., Grieco, T., Montagnaro, F., Santoro, L., 2008. Coal fly ash as raw material for the manufacture of geopolymer-based products. *Waste Management* 28, 416–423.

Baba, A.A., Adekola, F.A., Toye, E.E. and Bale, R.B., 2009. Dissolution kinetics and leaching of rutile ore in hydrochloric acid. *Journal of Minerals and Materials Characterization and Engineering* 8 (10), 787–801.

Babcan, J., 1971. Synthesis of jarosite $KFe_3(SO_4)_2(OH)_6$. *Geology* Zb, 22 (2), 299–304.

Barrett, J., Ewart, D.K., Hughes, M.N., Poole, R.K., 1993. Chemical and biological pathways in the bacterial oxidation of arsenopyrite. *FEMS microbiology reviews* 11 (1-3), .57–62.

Bellmann, F., Moser, B., Stark, J., 2006. Influence of sulfate solution concentration on the formation of gypsum in sulfate resistance test specimen. *Cement and Concrete Research* 36, 358–363.

Bidhendi, N.G.R., Torabian, A., Ehsani, H., Razmkhah, H., 2007. Evaluation of industrial dyeing wastewater treatment with coagulants and polyelectrolyte as coagulant aid. *Iranian Journal of Environmental Health Science & Engineering* 4 (1), 29–36.

Blissett, R.S., Rowson, N.A., 2012. A Review of the Multi-Component Utilisation of Coal Fly Ash. *Fuel* 97, 1–23.

Bottero, J.Y., Axelos, M., Tchoubar, D., Cases, J.M., Fripiat, J.J., Fiessinger, F., 1987. Mechanism of formation of aluminum trihydroxide from keggin Al13 polymers. *Journal of Colloid Interface Science* 117 (1), 47–57.

Brouwers, H.J.H., Van Eijk, R.J., 2002. Fly ash reactivity: Extension and application of a shrinking core model and thermodynamic approach. *Journal of Materials Science* 37, 2129–2141.

Casas, J.M., Crisóstomo, G. and Cifuentes, L., 2005. Speciation of the Fe (II)–Fe (III)–H_2SO_4–H_2O system at 25 and 50 °C. *Hydrometallurgy*, 80 (4), 254–264.

Chu, K.R., Lee, E., Jeong, S.H. and Park, E.S., 2012. Effect of particle size on the dissolution behaviors of poorly water-soluble drugs. *Archives of pharmacal research*, *35* (7), 1187-1195.

Das, G.K., Anand, S., Acharya, S. and Das, R.P., 1995. Preparation and decomposition of ammoniojarosite at elevated temperatures in H_2O-$(NH_4)2SO_4$-H_2SO_4 media. *Hydrometallurgy* 38 (3), 263–276.

Fan, M., Brown, R.C., Wheelock, T.D., Cooper, A.T., Nomura, M., Zhuang, Y., 2005. Production of a complex coagulant from fly ash. *Chemical Engineering Journal* 106, 269–277.

Fernandez-Jimenez, A., Palomo, A., 2005. Mid-infrared spectroscopic studies of alkali-activated fly ash structure. *Microporous and Mesoporous Materials* 86, 207–214.

Giere, R., Carleton, L.E., Lumpkin, G.R., 2003. Micro and nanochemistry of fly ash from a coal fired power plant. *American Mineralogist* 88, 1853–1865.

Gouda, R., Baishya, H., Qing, Z., 2017. Application of Mathematical Models in Drug Release Kinetics of Carbidopa and Levodopa ER Tablets. *Journal of Developing Drugs*, 6 (2), 1–8.

Greenberg, J. and Tomson, M., 1992. Precipitation and dissolution kinetics and equilibria of aqueous ferrous carbonate vs temperature. *Applied Geochemistry*, 7 (2), 185-190.

Habashi, F., 1999, Kinetics of the Metallurgical Processes, Les copies de la Capitale, Québec City, 1–317.

Hulett, D.L., Weinberger, A.J., 1980. Some etching studies of the microstructure and composition of large aluminosilicate particles in fly ash from coal-burning power plants. *Environmental Science and Technology* 14 (8), 965–970.

Jalal, I., Zmaily, E., Najib, N., 1989. Dissolution kinetics of commercially available controlled-release theophylline preparations. *International Journal of Pharmaceutics*, 52 (1), 63–70.

Kaur, R., Goyal, D., 2016. Mineralogical comparison of coal fly ash with soil for use in agriculture. *Journal of Mater Cycles Waste Management* 18, 186–200.

Kelmers, A.D., Egan, B.Z., Seeley, F.G., Campbell, G.D., 1981. Direct acid dissolution of aluminum and other metals from fly ash (No. CONF-810203-6). Oak Ridge National Lab., TN (USA).

Koech, L., Everson, R., Neomagus, H., Rutto, H., 2015. Dissolution kinetics of south African coal fly ash and the development of a semi-empirical model to predict dissolution. *Chemical Industry & Chemical Engineering Quarterly* 21 (2), 319−330.

Langmuir, D., 1997. Aqueous environmental geochemistry (No. 551.48 L3.).

Li, J., Miller, J.D., 2002. Reaction kinetics for gold dissolution in acid thiourea solution using formamidine disulfide as oxidant. *Hydrometallurgy*, 63 (3), 215-223.

Li, L., Fan, M., Brown, R.C., Koziel, J.A., Leeuwen, J. H., 2009. Production of a new wastewater treatment coagulant from fly ash with concomitant flue gas scrubbing. *Journal of harzardous Materials* 162, 1430–1437.

Linke, W.F., 1958. Solubilities, Inorganic and Metal-Organic Compounds, 4th ed., vol. I. D. Van Nostrand Co, Princeton, N.J., USA.

Lokhandwala, H., Deshpande, A., Deshpande, S., 2013. Kinetic modeling and dissolution profiles comparison: an overview. *International Journal of Pharma and Bio Sciences,* 4 (1), 728-73.

MacKenzie, K.J.D., 1972. Infrared Frequency Calculations for Ideal Mullite ($3Al_2O_3.2SiO_2$). *Journal of the American Ceramic Society* 55, 68–71.

Magalhães, J.M., Silva, J.E., Castro, F.P. and Labrincha, J.A., 2005. Kinetic study of the immobilization of galvanic sludge in clay-based matrix. *Journal of hazardous materials*, 121(1-3), 69–78.

Malenga, E.N., Mulaba-Bafubiandi, A.F. and Nheta, W., 2015. Alkaline leaching of nickel bearing ammonium jarosite precipitate using KOH, NaOH and NH_4OH in the presence of EDTA and Na_2S. *Hydrometallurgy* 155, 69–78.

Matjie, R.H., Li, Z., Ward, C.R., French, D., 2008. Chemical composition of glass and crystalline phases in coarse coal gasification ash. *Fuel* 87, 857–859.

Mazzocchitti, G., Giannopoulou, I., Panias, D., 2009. Silicon and aluminum removal from ilmenite concentrates by alkaline leaching. *Hydrometallurgy* 96 (4), 327–332.

Nemati, M., Lowenadler, J. and Harrison, S.T.L., 2000. Particle size effects in bioleaching of pyrite by acidophilic thermophile Sulfolobus metallicus (BC). *Applied microbiology and biotechnology*, *53* (2), 173-179.

Parravano, G., Martin, J.J., Katz, D.L., 2000. Elements of Chemical Reaction Engineering, third ed., Prentice Hall PTR, NJ.

Roeland, J. and Dijkhuis, E. 2009. The minimisation of copper losses during iron and aluminium precipitation from zinc leach liquors. Technical University of Delft, The Netherlands.

Rubisov, D.H. and Papangelakis, V.G., 2000. Sulphuric acid pressure leaching of laterites—speciation and prediction of metal solubilities “at temperature*”. Hydrometallurgy* 58 (1), 13–26.

Rutto, H., Enweremadu, C., 2012. Dissolution of a South African calcium based material using urea: An optimized process. *Korean Journal of Chemical Engineering* 29 (1), 1–8.

Seidel, A., Zimmels, Y., 1998. Mechanism and kinetics of aluminum and iron leaching from coal fly ash by sulfuric acid. *Chemical Engineering Science* 53 (22), 3835–3852.

Semerjian, L., Ayoub, G.M., 2003. High-pH–magnesium coagulation–flocculation in wastewater treatment. *Advances in Environmental Research* 7 (2), 389–403.

Shemi, A., Mpana, R. N., Ndlovu, S., van Dyk, L. D., Sibanda, V., Seepe, L., 2012. Alternative Techniques for Extracting Alumina from coal fly ash. *Minerals Engineering* 34, 30–37.

Shemi, A., 2013. Extraction of aluminium from coal fly ash using a two-step acid leach process (Mastersl dissertation).

Stumm, W., Morgan, J.J., 1996. Aquatic Chemistry, 3rd ed. John Wiley and Sons, USA.

Teringo, J., 1986. Magnesium hydroxide for neutralizing acid waste containing metals. *Plating and surface finishing*, 36–39.

Thongsang, S., Sombatsompop, N., 2006. Effect of NaOH and Si69 treatments on the properties of fly ash/natural rubber composites. *Polymer Composites* 27 (1), 30–40.

van der Merwe, E.M., Prinsloo, L.C., Mathebula, C.L., Swart, H.C., Coetsee, E., Doucet, F.J., 2014. Surface and bulk characterization of an ultrafine South African coal fly ash with reference to polymer applications. *Applied Surface Science* 317, 73–83.

Vempati, R.K., Ajoy, R., Hess, T. R., Cocke, D. L., Lauer, H. V., Jr, 1994. Fractionation and characterization of texas lignite class F fly ash by XRD, TGA, FTIR and SEM. *Cement and Concrete Research* 24 (6), 1153–116.

Voll, D., Angerer, P., Beran, A., Schneider, H., 2002. A new assignment of IR vibrational modes in mullite. *Vibrational Spectroscopy* 30, 237–243.

Wang, Y., Jin, S., Lv, Y., Zhang, Y. and Su, H., 2017. Hydrometallurgical Process and Kinetics of Leaching Manganese from Semi-Oxidized Manganese Ores with Sucrose. *Minerals* 7 (2), 27.

Welham, N.J., Malatt, K.A., Vukcevic, S., 2000. The effect of solution speciation on iron–sulphur–arsenic–chloride systems at 298 K. *Hydrometallurgy* 57 (3), 209–223.

Yue, G., Zhao, L., Olvera, O.G., Asselin, E., 2014. Speciation of the H_2SO_4–$Fe_2(SO_4)_3$–$FeSO_4$–H_2O systemand development of an expression to predict the redox potential of the Fe^{3+}/Fe^{2+} couple up to 150 °C. *Hydrometallurgy* 147–148, 196–209.

CHAPTER 5
PERFORMANCE OF THE PRODUCED COMPLEX COAGULANT

5.1 Introduction

Findings from the research work conducted on the coagulation performance of the produced composite coagulant are presented and discussed in this chapter. Sample of acid mine drainage (AMD) from coal mine was studied. The AMD sample was used for its treatment by coagulation process. The quality of the raw AMD sample before coagulation process was determined in terms of elemental composition by inductively coupled plasma optical emission spectroscopy (ICP-OES), total dissolved solids (TDS), and turbidity. The quality of the treated acid mine wastewater was analysed for TDS, Mn, Fe, Al, Ca, Mg, Zn, Ni, Si, and turbidity.

5.2 Results and discussion

5.2.1 Coal mine wastewater characterization

The characteristics of the raw acid mine wastewater are as shown in Table 5.1.

Table 5.1: Chemical analysis of the coal mine wastewater sample.

Parameter	Value
pH (value)	2.60
Colour	Yellowish
Turbidity (NTU)	-
Conductivity (mS/cm)	12.90
Total Dissolved Solids (TDS) (mg/L)	5276.00 (18 °C)
S (mg/L)	1836.88
Fe (mg/L)	299.11
Al (mg/L)	14.82
Mn (mg/L)	175.29
As (mg/L)	16.48
Ca (mg/L)	441.04
Co (mg/L)	5.44
Mg (mg/L)	411.08
Ni (mg/L)	195.64
Si (mg/L)	19.92
Zn (mg/L)	13.02
Cr (mg/L)	0.09
Cu (mg/L)	0.26
Pb (mg/L)	0.07
Cd (mg/L)	0.42

5.2.2 Coagulation of toxic elements and turbidity from acid coal mine drainage

The aim of this investigation, through laboratory testing and analysis was to evaluate the efficiency of the produced composite coagulant from coal fly ash (CFA), as treating agent for AMD. Beaker tests were carried out to assess the effect of the composite coagulant on the reduction of total dissolved solids (TDS) and turbidity. A produced CFA–based coagulant bearing 21731.89 mg/L Fe, 603.18 mg/L Al, 96.00 mg/L Si, 1366.70 mg/L Mg, and 796.70 mg/L Ca was used for the coagulation of pollutants from AMD. The AMD used for the treatment was a sample of coal mine wastewater with 5291 mg/L TDS. Since TDS are related

to dissolved ions, the coagulations of toxic elements such as Mn, Fe, Al, Ca, Mg, Zn, Ni, and Si in the AMD were also studied.

In wastewater treatment by coagulation process, the selective precipitation of metal hydroxides by controlling change of pH is important. In order to show the solubility relationships of the hydroxides of different metals, the hydroxide precipitation diagram is presented in Figure 5.1. It is shown from Figure 5.1 (Monhemius, 1977; Abdullah et al., 1999) that Fe^{3+}, Al^{3+}, Ca^{2+}, and Mg^{2+} precipitate from pH 3, 5, 10, and 11, respectively.

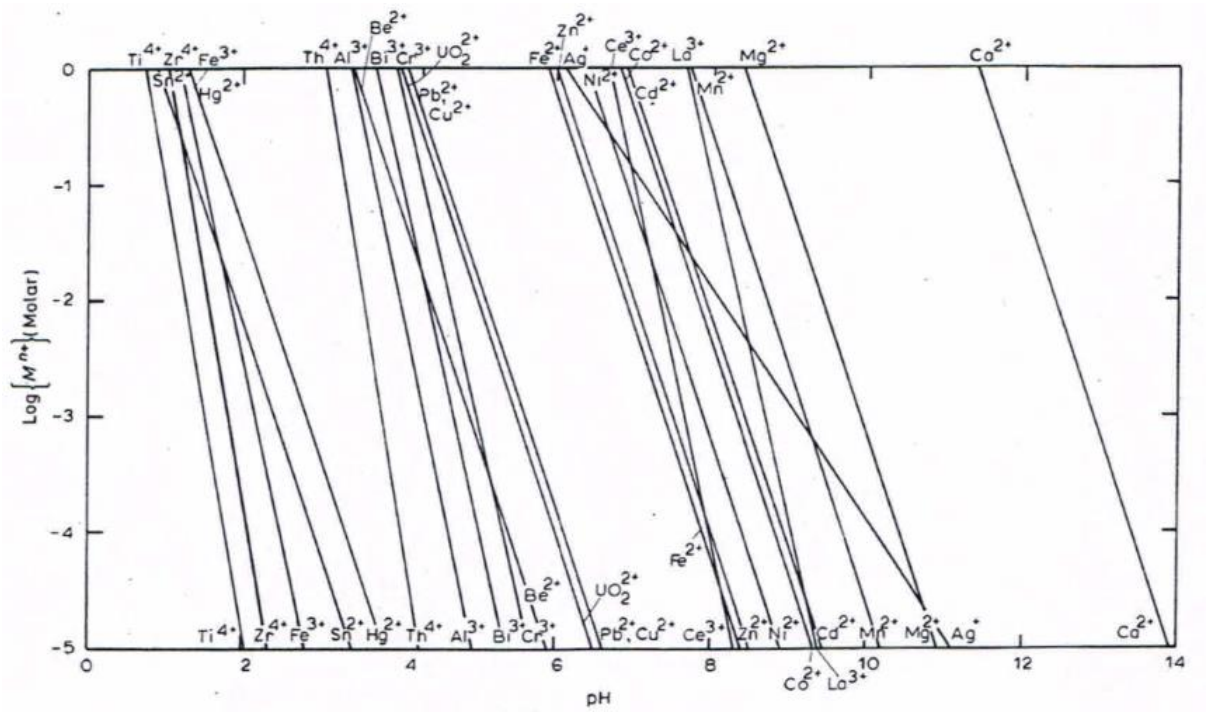

Figure 5.1: Hydroxide precipitation diagram, 25 ^{o}C.

Chemistry of Fe^{3+}, Al^{3+}, Mg^{2+}, Ca^{2+} and Si^{4+} as coagulants

It is known that in water all ions are hydrated at a certain level (Stumm and Morgan, 1962). Indeed, when treating wastewater from coal mine by the composite coagulant containing Fe, Al, Si, Mg, and Ca ions, the chemistry of Fe^{3+}, Al^{3+}, Mg^{2+}, and Si^{4+} as coagulants can be summarized in a very simplified manner as follows: there is a primary hydration layer, in which the water molecules are directly bound to the central ion, and water molecules slightly held in a secondary hydration layer. For Fe^{3+}, Al^{3+}, and Mg^{2+}, the primary hydration shell contains six molecules of water in octahedral co-ordination $[Fe(H_2O)_6]^{3+}$, $[Al(H_2O)_6]^{3+}$, and $[Mg(H_2O)_6]^{2+}$, respectively (Duan and Gregory, 2003; Ikeda et al., 2007). While Si^{4+} is

dissolved as a hydroxocomplex, Si $(OH)_4$ (or H_4SiO_4) in a tetrahedral network. H_4SiO_4 or $Si(OH)_4$ are commonly referred to as silicic acid (Mirsal, 2008). In the case of Ca^{2+}, the number of hydrations is not well established (Ikeda et al., 2007; Pálinkás and Heinzinger, 1986). Commonly, hydrolysis reactions of monomeric cation salts (used as coagulants) may be represented by successive-deprotonation of water molecules in the primary hydration shell providing a lower positive charge (Richens, 1997; Barnum, 1983; Henry et al., 1992). The general illustration for trivalent metals (Fe^{3+}, Al^{3+}), omitting H_2O ligands coordinated to the M^{3+} ions for simplicity, may be given as follows (Barnum, 1983; De Abreu et al., 2006), omitting:

$$M^{3+} + H_2O \leftrightarrow M(OH)^{2+} + H^+ \quad (5.1)$$

$$M(OH)^{2+} + H_2O \leftrightarrow M(OH)_2^{+} + H^+ \quad (5.2)$$

$$M(OH)_2^{+} + H_2O \leftrightarrow M(OH)_3 + H^+ \quad (5.3)$$

$$M(OH)_3^{+} + H_2O \leftrightarrow M(OH)_4^{-} + H^+ \quad (5.4)$$

A single step of deprotonation reaction is given by

$$[M(H_2O)_n]^{z+} - H^+ \rightleftharpoons [M(H_2O)_{n-1}(OH)]^{(z-1)+} \quad (5.5)$$

With M: metal ion.

From Equations 5.1–5.4, **t**he hydrolysis representation (simplified form) occur as the pH is increased, producing first the doubly- and singly-charged cationic species and then the uncharged metal hydroxide, $M(OH)_3$. With more increase in pH, the soluble anionic form $M(OH)_4^-$ becomes dominant (De Abreu et al., 2006).

However, in the complex coagulant (polymeric coagulant), hydrolysis of Fe, Al, Si, Mg, and Ca sulphates in water happen by multiple hydrolysis reactions resulting in the formation of dimeric, trimeric and polynuclear hydrolysis species. The concentrations of different hydrolysis products, including polynuclear species with bridging hydroxide ions, vary with the pH increase until the formation of an insoluble hydroxide (Barnum, 1983). The production of polymer (polynuclear) species is done by the reduction of the charge density in the molecule as a whole. Equation 5.6 gives an illustration for Al^{3+} (Rebhun and Lurie, 1993).

$$[Al(H_2O)_6]^{3+} \longrightarrow [Al(H_2O)_5OH]^{2+} \xrightarrow{OH^-} [Al_6(OH)_{15}]_{(aq)}^{3+} \longrightarrow [Al_8(OH)_{20}]_{(aq)}^{4+} \xrightarrow{OH^-} \text{Polymerization} \dashrightarrow [Al(OH)_3(H_2O)_3]_{(s)} \xrightarrow{OH^-} [Al(OH)_4]^- \quad (5.6)$$

Monomeric and polymeric species of the hydrolysis of Al include the following: (1) Monomers: $[Al(OH)]^{2+}$, $[Al(OH)_2]^{+}$, $[Al(OH)_4]^{-}$; and (2) Polymers: $[Al_2(OH)_2]^{4+}$, $[Al_3(OH)_4]^{5+}$, $[Al_6(OH)_{15}]^{3+}$, $[Al_7(OH)_{17}]^{4+}$, $[Al_8(OH)_{20}]^{4+}$, $[Al_{13}(O_4(OH)_{12}]^{7+}$, and $[Al_{13}(OH)_{34}]^{5+}$. Similar species exist for Fe^{3+} (Rebhun and Lurie, 1993; Cheng and Chi, 2002). For Mg and Si, the polynuclear hydrolysis products include $Mg_4(OH)_4^{4+}$ and $Si_2O(OH)_6$, respectively (Rose and Waite, 2003).

In general, as shown in Equations 5.1 to 5.4, when a proton is given to a solution water molecule, a coordinated H_2O is converted to a hydroxyl ion (Barnum, 1983). Consequently, the hydrated metal ions produced by the reactions are acids according to the Bronsted theory of acids according to which a proton donor is defined as an acid. Since the hydrolysis reaction depends on the acid-base reactions, the pH of the solution significantly impacts the rate and distribution of the different hydrolysis products (Eigen, 1964). In practice, it is not easy to describe the hydrolysis behaviour of metal cation and silicon salts because of the number and diversity of the hydroxide complexes that can be formed in solution. For given metal or silicon cation, the resulting chemical behaviour may be a complicated function of pH and concentration; and, if the identity and stability of the hydrolysis products are not known, this may be somewhat unpredictable (Baes and Mesmer, 1981, Barnum, 1983).

Furthermore, since the aim was to coagulate impurities (Al, Fe, Mn, Mg, Ca, Si, Zn, Ni, and TDS) in coal mine drainage sample by the produced polymeric coagulant, highly charged cations such as Si^{4+}, Fe^{3+}, Al^{3+}, Mg^{2+}, and Ca^{2+} are efficient in interacting specifically with negative colloids and neutralise their charge. However, over the optimal range of pH values in wastewater, as state above, in the complex coagulant these simple cations are not found in significant concentrations, as a result of hydrolysis, which can give a range of products. Several hydrolysis species are cationic and can strongly interact with negatively charged colloid particles, causing destabilisation and coagulation under the correct conditions of dosage and pH. Over-dosage can lead to charge reversal and re-stabilisation of colloids (Duan and Gregory, 2003).

Furthermore, the effects of reaction parameters on coagulation of impurities from coal mine wastewater are studied in order to optimize the process. Pre-experiments to find the suitable volume of coagulant and the appropriate initial concentration of coagulant were performed based on removal of TDS.

Effect of the volume of the composite coagulant

As the volume of coagulant plays an important role in the coagulation process, the suitable volume of the composite coagulant for TDS reduction was optimized under the following experimental conditions: 50 mL AMD, 10 mg/L composite coagulant dosage, pH = 7, RT (23 ± 2 ^{o}C), rapid mixing (300 rpm) for 5 minutes, slow mixing (30 rpm) for 20 minutes which has been demonstrated enough to obtain a good contact time (Sui et al., 2009). It was observed that 150 minutes were appropriate for a good sludge settling. Figure 5.2 shows the reduction of TDS versus the volume of coagulant at 5276 mg/L TDS concentration. It can be observed from Figure 5.2 that 86,92% of TDS could be remained in the AMD with a complex coagulant amount of 10 mL. The final optimized AMD/coagulant ratio was found to be 2.5.

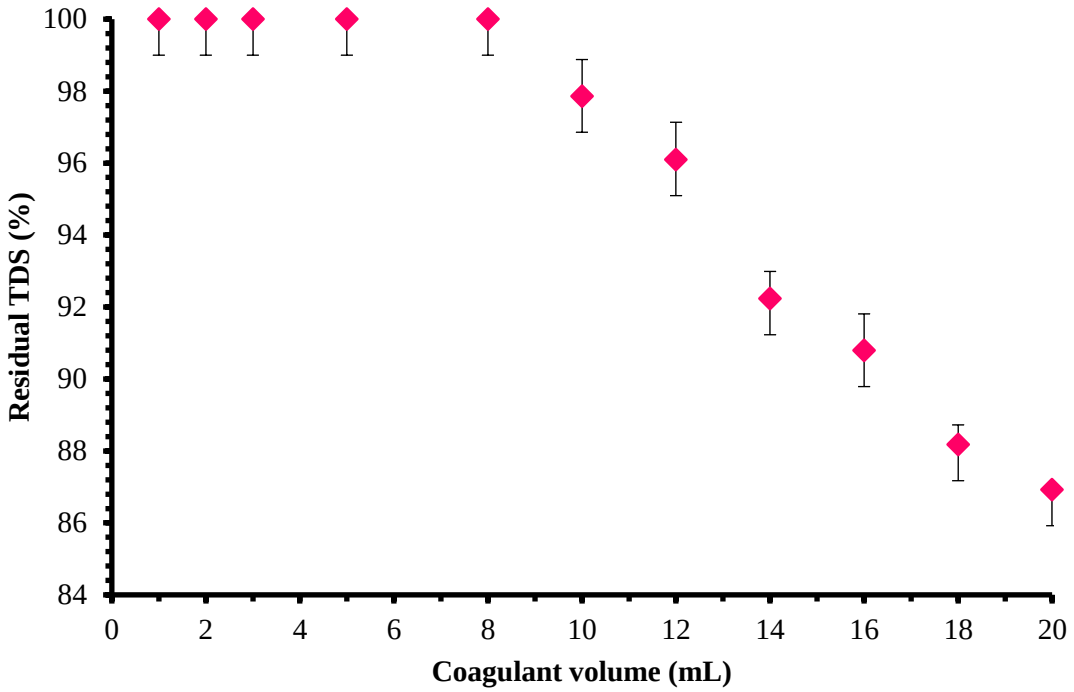

Figure 5.2: Evaluation of the effect of the amount of the synthesized coagulant in reducing TDS from AMD sample (Initial TDS: 5276 mg/L; pH: 7; RT (20±2 °C); coagulant dosage as $C_{Fe+Al+Si+Mg+Ca}$: 24594,48 mg/L; 5 minutes rapid mixing at 300 rpm; 20 minutes slow mixing at 30 rpm).

Effect of the initial concentration of the feed

In order to study the effect of the feed concentration on the reduction of TDS in the AMD, a series of dilution (0, 4, 8, 16, and 20 times dilutions) of the initial AMD was performed and the TDS concentrations of 5276, 1902, 1206, 720.2, and 578.8 mg/L were obtained, respectively. Experimental conditions used to study the effect of the volume of the composite coagulant were used for the effect of the initial concentration of the feed. The results are shown in Figure 5.3. It was observed from Figure 5.3 that 74.33, 100.00, 100.00, 53.21, and 100.00% residual TDS were obtained for the initial TDS concentrations of 5276, 1902, 1206, 720.2, 578.8 mg/L, respectively. The optimum feed concentration was found to be 720.2 mg/L TDS as it led to 53.21% residual TDS in the treated wastewater.

The TDS removal efficiency in the coagulation process could be affected by several factors including Fe, Al, Si, Mg, and Ca / TDS (elements molar in the coagulant) ratios and water chemistry (Meng et al., 2000; Mercer and Tobiason, 2008). The results showed that, for AMD with an initial concentration of 5276 mg / L TDS, 25.67% of TDS was removed by the initial Fe, Al, Si, Mg and Ca / TDS ratios (molar elements) reducing the initial concentration to 3921.4 mg/L (or 74.33% the residual TDS). Therefore, the coagulant dosage as well as the composite effects of the complex wastewater sample played an important role in TDS removal efficiency from AMD.

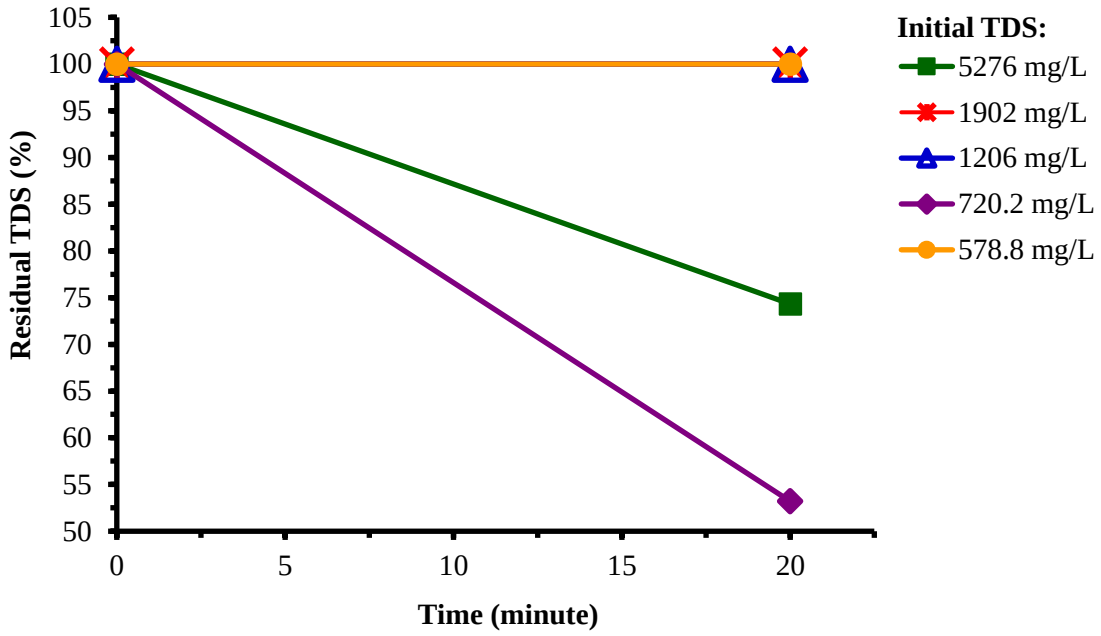

Figure 5.3: Evaluation of the effect of the feed concentration in reducing TDS from coal mine drainage sample (AMD/coagulant ratio: 2,5; pH: 7; RT (20±1 °C); 5 minutes rapid mixing at 300 rpm; 20 minutes slow mixing at 30 rpm).

Effect of composite coagulant dosage and pH

Coagulant dosage and pH are two of the important factors in coagulation process. Coagulation parameters selected from the hydroxide precipitation diagram in Figure 5.1 were: initial pH of the raw wastewater from 4 to 12. In the present study, the effects of pH and coagulant dosage in removing TDS, toxic elements (Fe, Al, Mn, Mg, Ca, Si, Zn, and Ni), and turbidity were conducted at RT (23±2 °C), 2–50 mg/L composite coagulant dosage, AMD/coagulant ratio of 2.5, and coagulation time of 20 minutes. Pre-experiments had shown that 150 minutes were suitable for a good sedimentation. Therefore, the formed flocs were allowed to settle for 150 minutes. Adsorption of TDS, Fe, Al, Mn, Si, Mg, Ca, Zn, and Ni onto cation (metal and silicon cations) hydroxide precipitates is a function of coagulant dosage and pH (Figures 5.4–5.12). The results for TDS, Fe, Al, Mn, Si, Mg, Ca, Zn, and Ni removal are shown in Figures 5.4–5.12, respectively, which indicate that coagulant dosage has a strong effect on the coagulation process.

The results for TDS removal in Figure 5.4 indicate that TDS removal was enhanced by increasing coagulant dosage and controlling the pH. The remaining TDS percentage reached at a dose of 20 mg/L was 42.78% (308.1 mg/L). As the coagulant dosage increases, the removal of TDS increases until coagulant dosage of 20 mg/L; and after that the removal of TDS decreases as the dosage of the coagulant increases. This behaviour was also observed for the removal of toxic elements (Fe, Al, Mn, Si, Mg, Ca, Zn, and Ni) (Figure 5.5–5.12). There was a direct relationship between TDS and toxic elements concentrations. Although the removals increased with increasing the coagulant dosage, the rate of pollutants remaining increased with increasing coagulant dosage beyond a certain coagulant dosage. Since maximum removal was reached at a dosage of 20 mg/L under the experimental conditions, this dosage was considered to be the optimum dosage for TDS removal (42.78% residual TDS or 308.1 mg/L). When the coagulant dose is very low, coagulation is insufficient, and therefore the efficiency of the coagulant is low. While coagulant dosage of 20 mg/L is sufficient to produce charge neutralization and hence achieve coagulation. When the coagulant dose is very high, particles present in the acid mine drainage are too surrounded by coagulant and, consequently, their surfaces are saturated so that the chances of colloidal particles to combine with each other diminish, and that they reach another state of stability in which particles are difficult to coagulate. Hence, a gradual decrease in adsorption capacity (q_e, mg/mg) was noticed with increasing coagulant dosage.

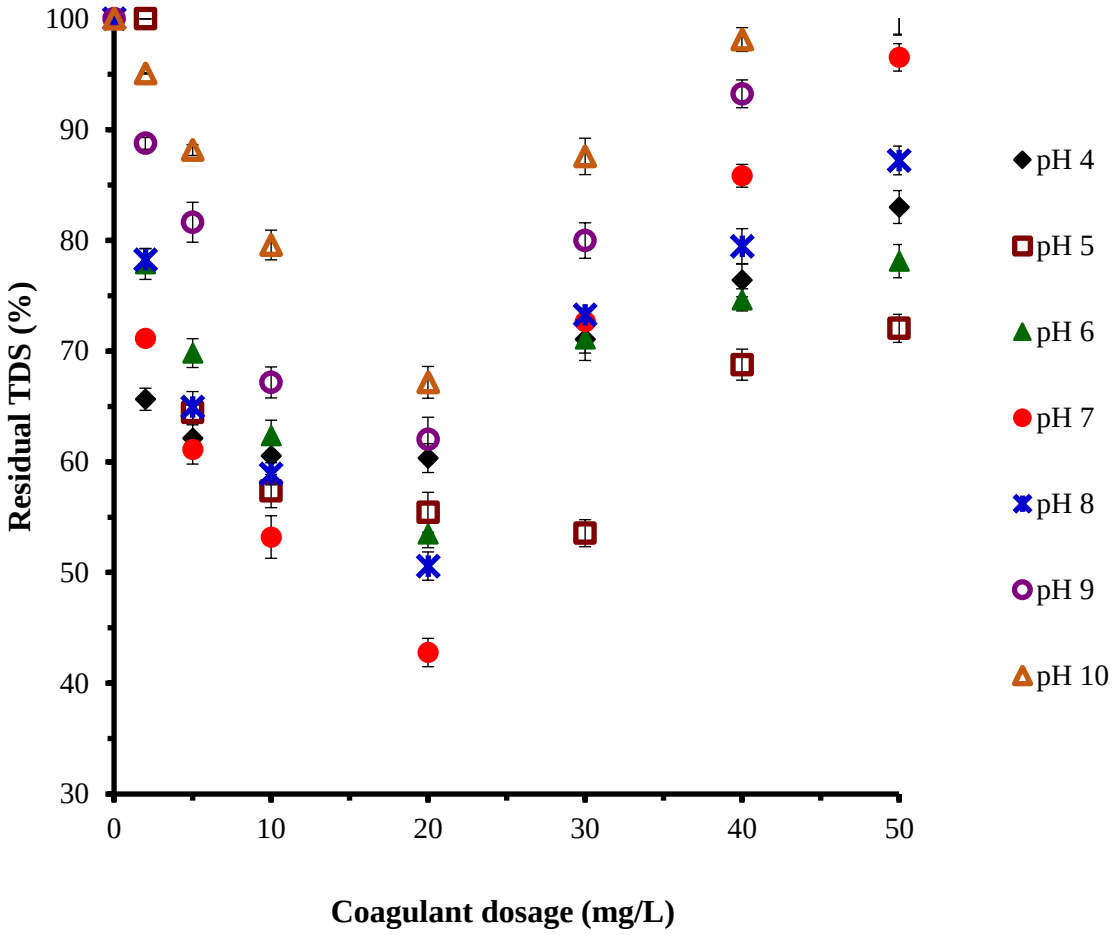

Figure 5.4: Effect of coagulant dosage (mg/L) and pH on removal of TDS from acid coal mine drainage (initial TDS concentration was 720.2 mg/L, initial pH: 4–10; AMD/coagulant ratio: 2.5; RT (23±2 °C); 5 minutes rapid mixing at 300 rpm; 20 minutes slow mixing at 30 rpm).

It can be seen from Figure 5.5 that coagulant dosage from 2–20 mg/L was optimum for the removal of iron as a maximum of 6% residual iron (0.10 mg/L) was reached.

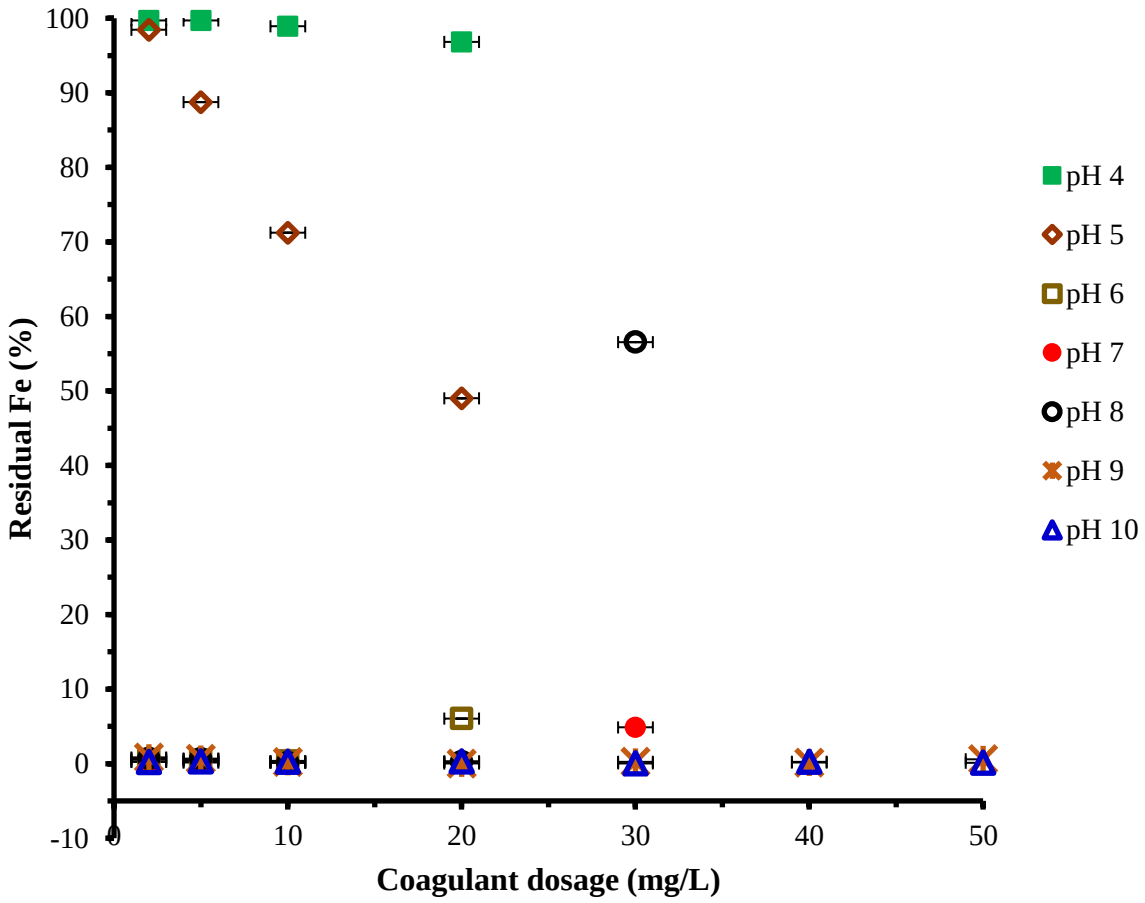

Figure 5.5: Effect of coagulant dosage (mg/L) and pH on removal of Fe from acidic coal mine drainage (initial Fe concentration was 1.64 mg/L; initial pH: 4–10; AMD/coagulant ratio: 2.5; RT (23±2 °C); 5 minutes rapid mixing at 300 rpm; 20 minutes slow mixing at 30 rpm).

Based on Figure 5.6, coagulant dosage of 20 mg/L was completely successful in removing aluminium from the wastewater. Maximum discharging aluminium was found to be 1.36% (0.19 mg/L).

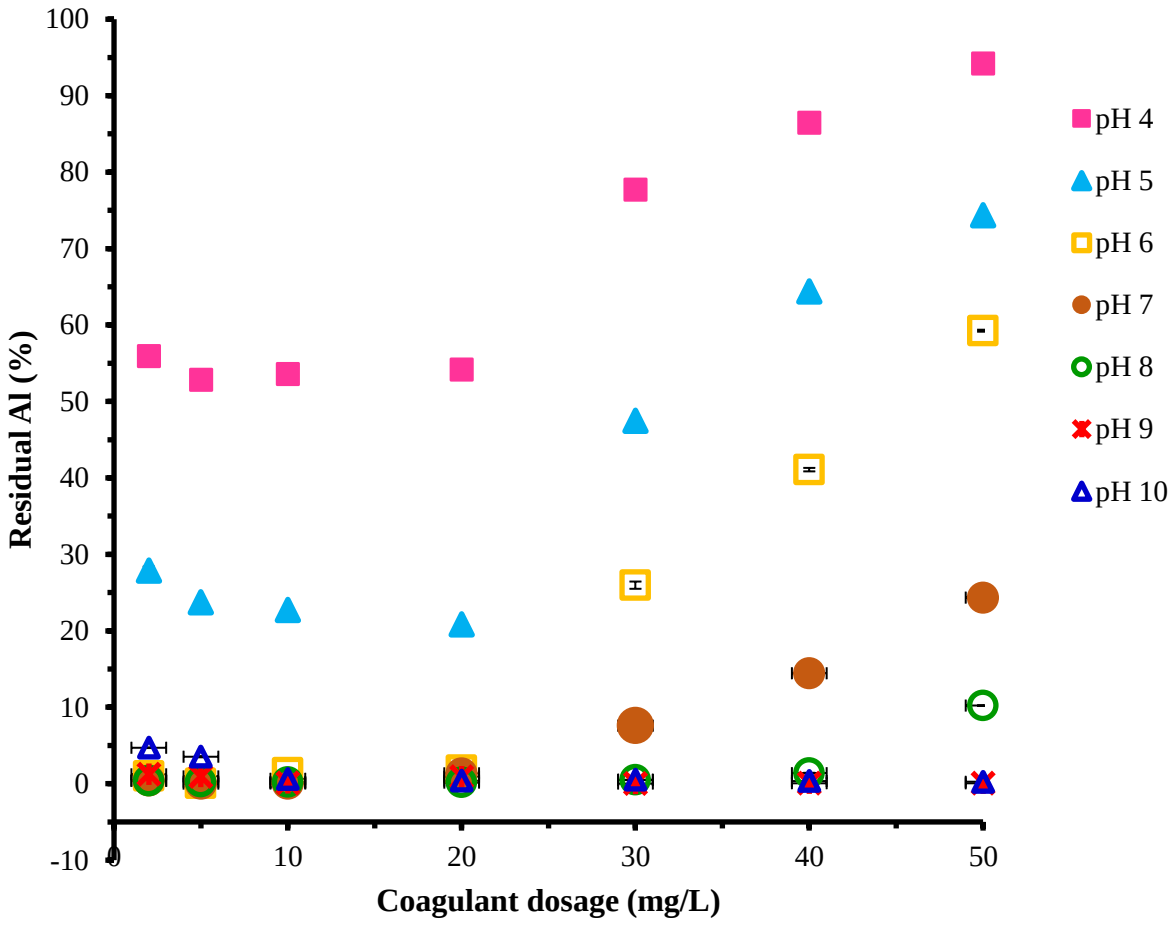

Figure 5.6: Effect of coagulant dosage (mg/L) and pH on removal of Al from acidic coal mine drainage (initial Al concentration was 13.86 mg/L; initial pH: 4–10; AMD/coagulant ratio: 2.5; RT (23±2 °C); 5 minutes rapid mixing at 300 rpm; 20 minutes slow mixing at 30 rpm).

Mainly, it can be seen from Figure 5.7 that maximum manganese removal (0.57% residual Mn or 0.08 mg/L) was obtained at 20 mg/L coagulant dosage.

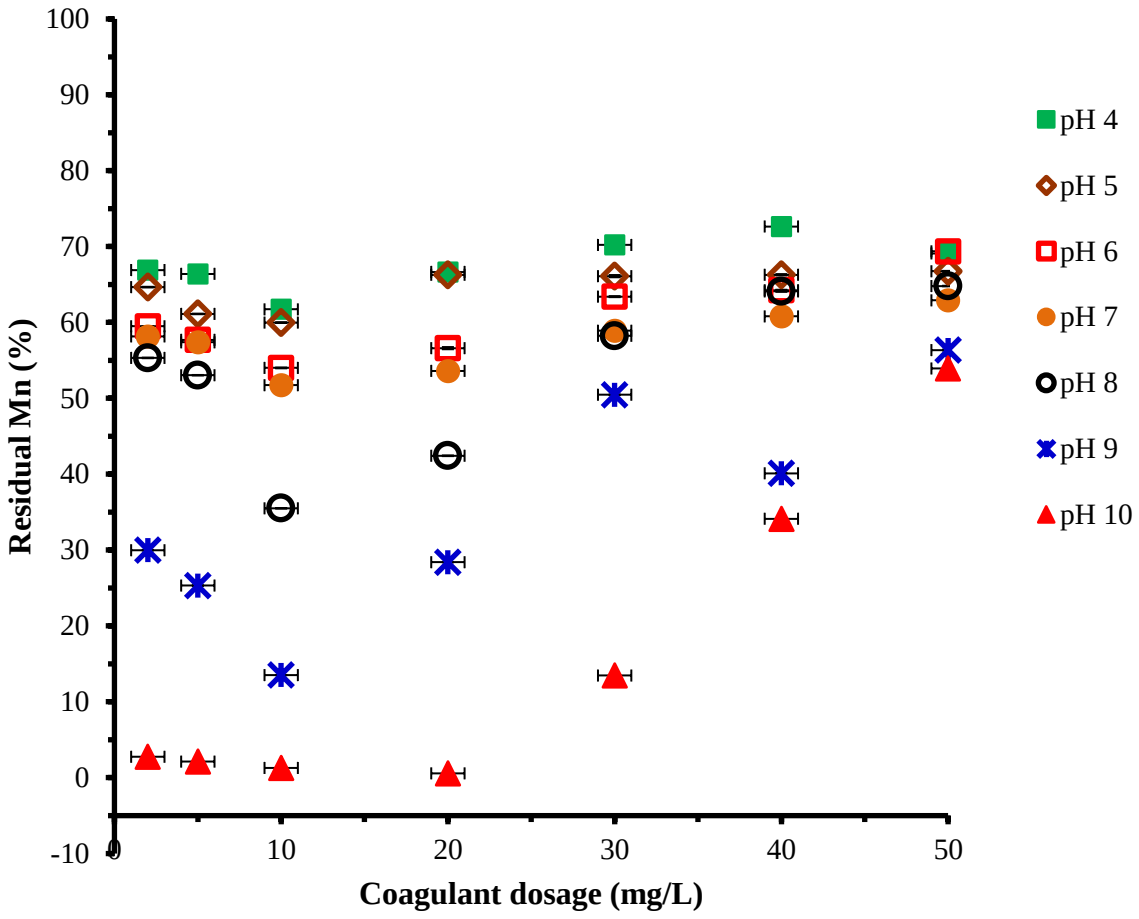

Figure 5.7: Effect of coagulant dosage (mg/L) and pH on removal of Mn from acidic coal mine drainage (initial Mn concentration was 13.52 mg/L; initial pH: 4–10; AMD/coagulant ratio: 2.5; RT (23±2 °C); 5 minutes rapid mixing at 300 rpm; 20 minutes slow mixing at 30 rpm).

According to Figure 5.8, the composite coagulant showed efficiency in removing silicon at less than 33% of residual silicon (less than 0.30 mg/L) at a coagulant dose of 20 mg/L.

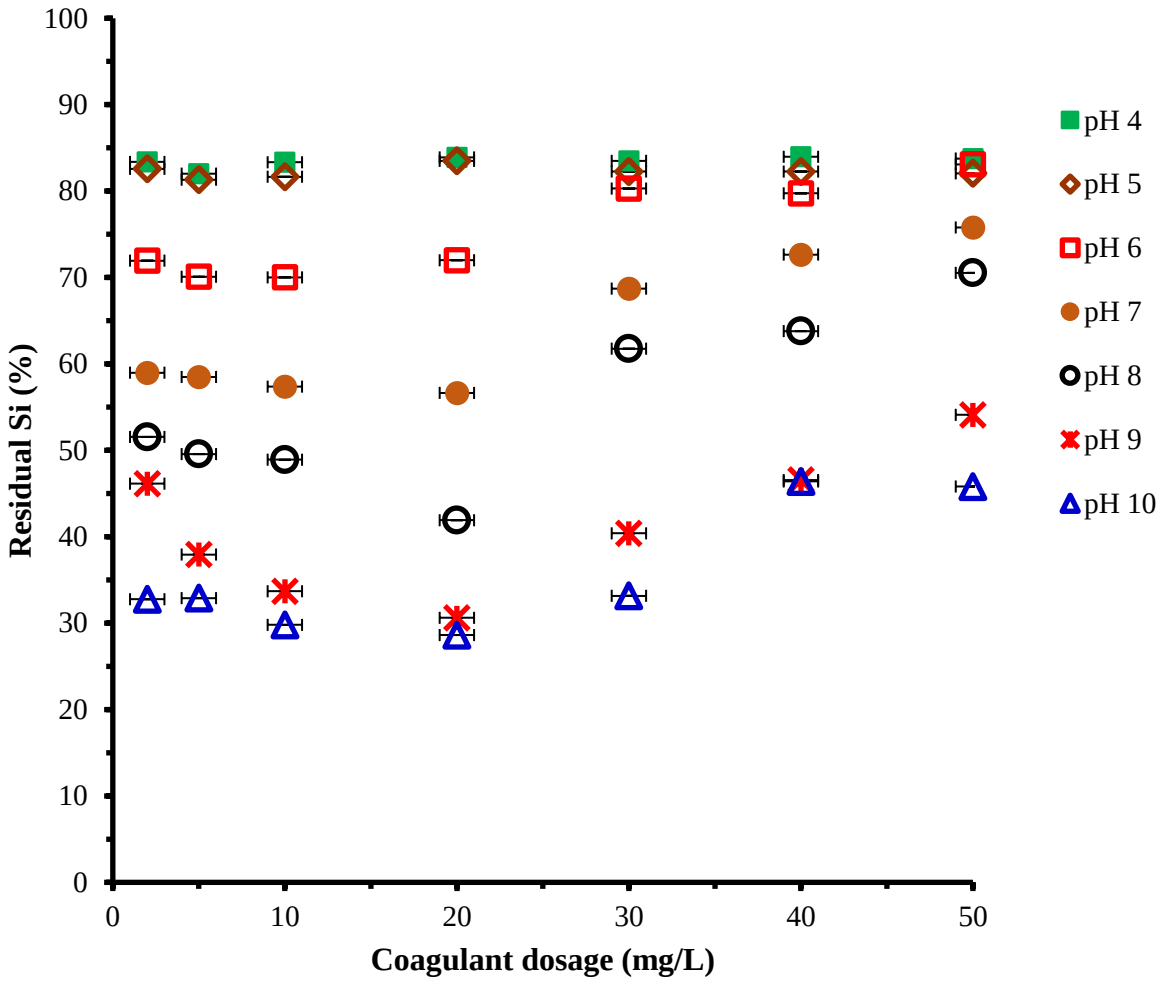

Figure 5.8: Effect of coagulant dosage (mg/L) and pH on removal of Si from acidic coal mine drainage: (initial Si concentration was 0.91 mg/L; initial pH: 4–10; AMD/coagulant ratio: 2.5; RT (23±2 °C); 5 minutes rapid mixing at 300 rpm; 20 minutes slow mixing at 30 rpm).

Figure 5.9 shows that at a dosage of 20 mg/L, the composite coagulant was efficient in removing magnesium from wastewater. The results showed that a residual magnesium concentration of 0.66% (0.20 mg/L) could be obtained using the complex coagulant.

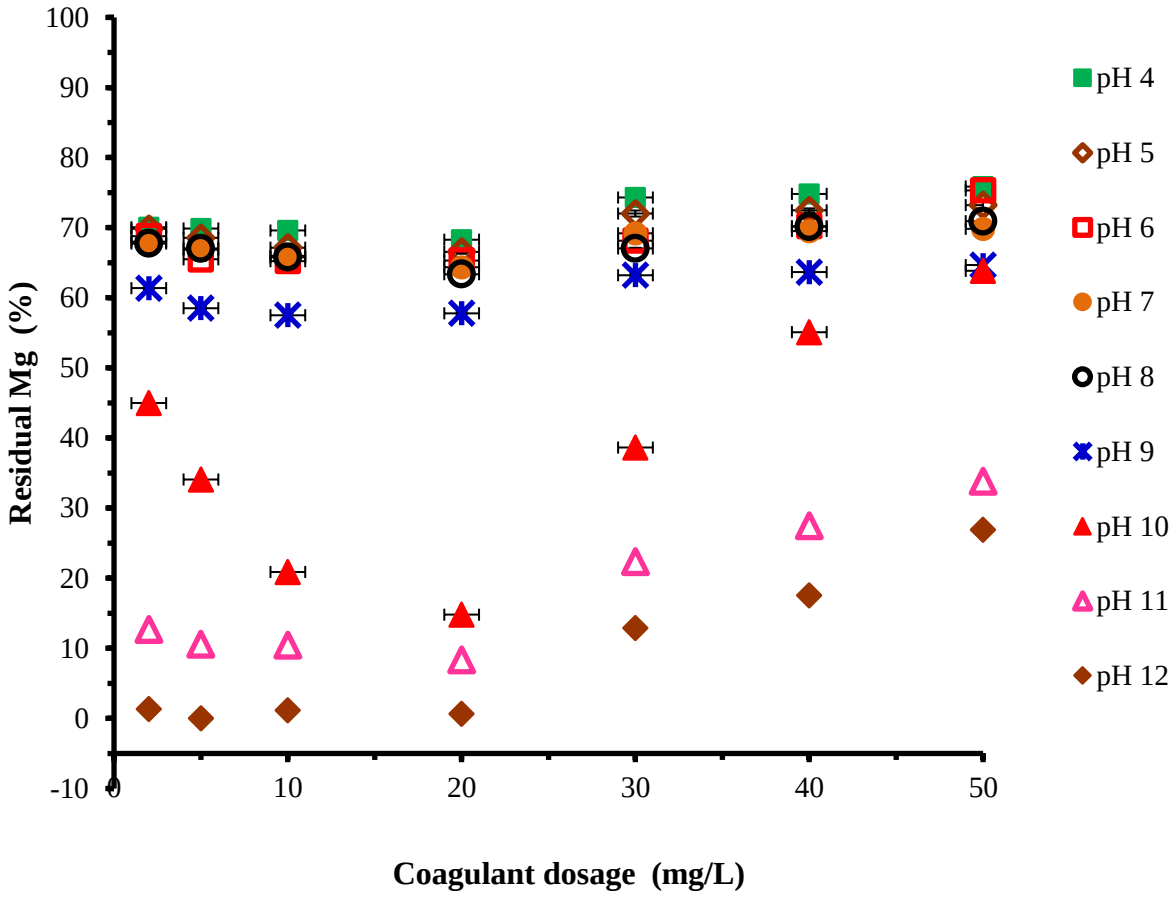

Figure 5.9: Effect of coagulant dosage (mg/L) and pH on removal of Mg from acidic coal mine drainage (initial Mg concentration was 30.18 mg/L; initial pH: 4–10; AMD/coagulant ratio: 2.5; RT (23±2 °C); 5 minutes rapid mixing at 300 rpm; 20 minutes slow mixing at 30 rpm).

According to Figure 5.10, the dosage of 20 mg/L was found optimal for maximum calcium removal as the results showed that 6.88% (2.14 mg/L) residual calcium could be reached.

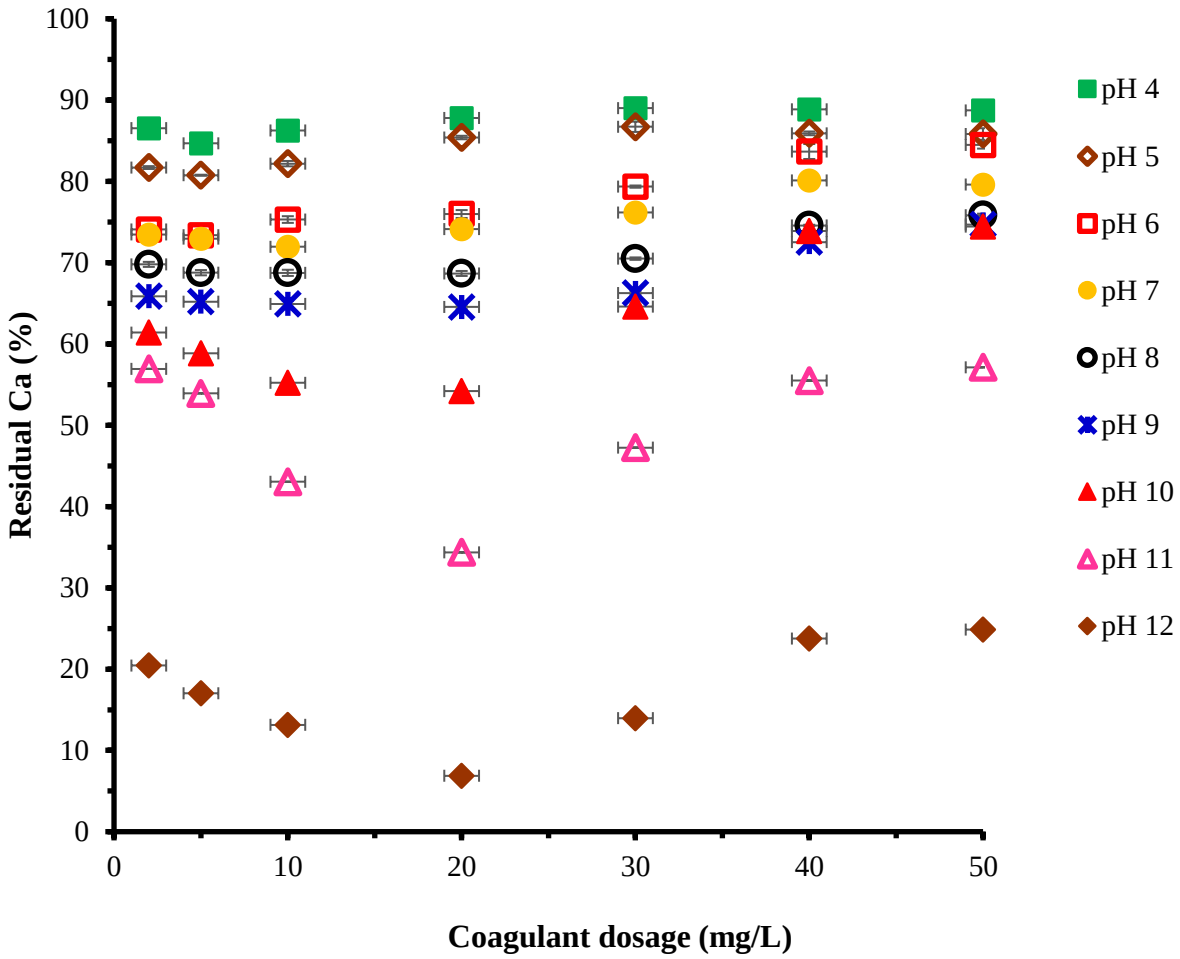

Figure 5.10: Effect of coagulant dosage (mg/L) and pH on removal of Ca from acidic coal mine drainage (initial Ca concentration was 31.13 mg/L; initial pH: 4–10; AMD/coagulant ratio: 2.5; RT (23±2 °C); 5 minutes rapid mixing at 300 rpm; 20 minutes slow mixing at 30 rpm).

In Figure 5.11, the composite coagulant showed excellent efficiency in removing zinc from wastewater at 20 mg/L coagulant dosage. Similar results were also reported in the literature (Fu and Wang, 2011). At 10 and 20 mg/L coagulant dosages, the obtained residual zinc was in the range of 0.36–1.13% (0.00–0.01 mg/L).

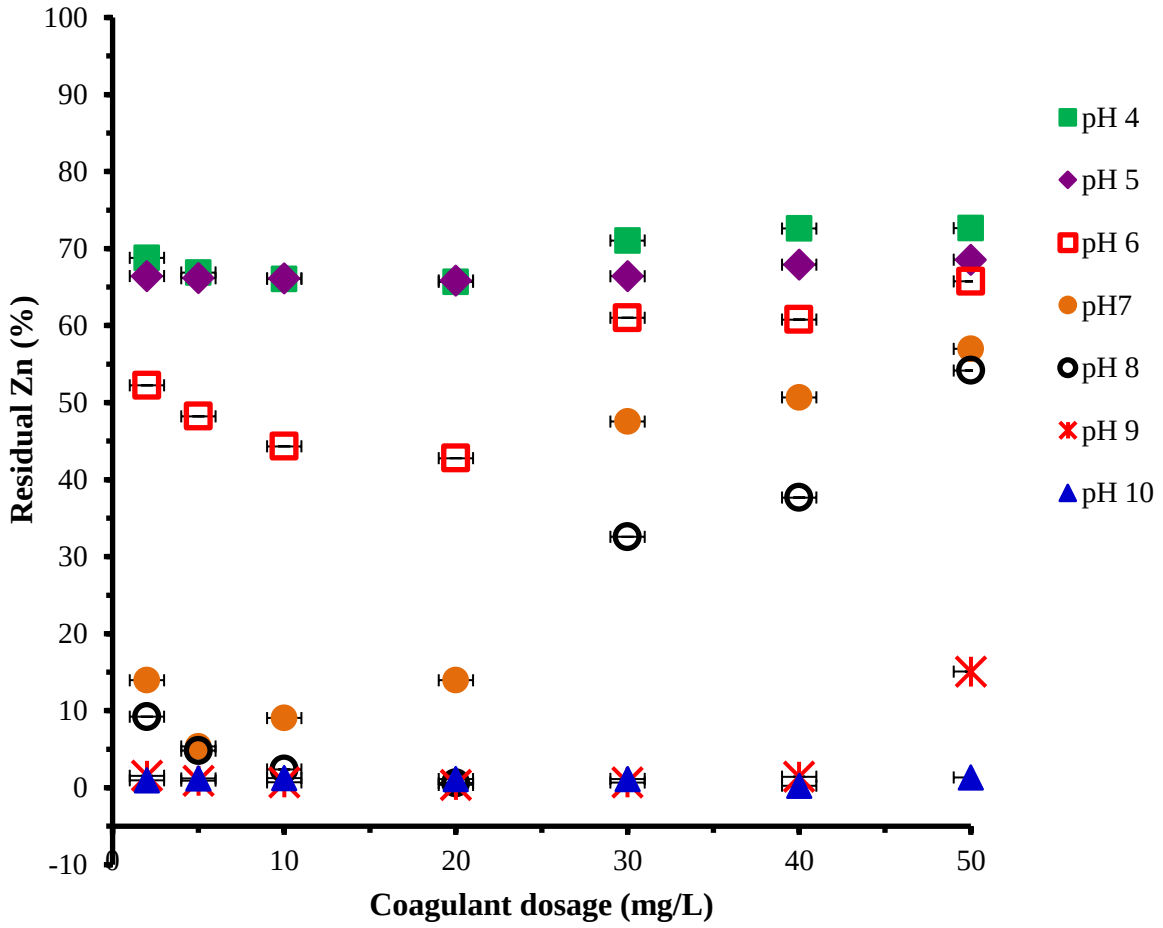

Figure 5.11: Effect of coagulant dosage (mg/L) and pH on removal of Zn from acidic coal mine drainage (initial Zn concentration was 0.93 mg/L; initial pH: 4–10; AMD/coagulant ratio: 2.5; RT (23±2 °C); 5 minutes rapid mixing at 300 rpm; 20 minutes slow mixing at 30 rpm).

According to Figure 5.12, 10–20 mg/L coagulant doses were found to be optimal in completely removing nickel from water since residual nickel concentration of less than 1.10% (0.01 mg/L) was reached.

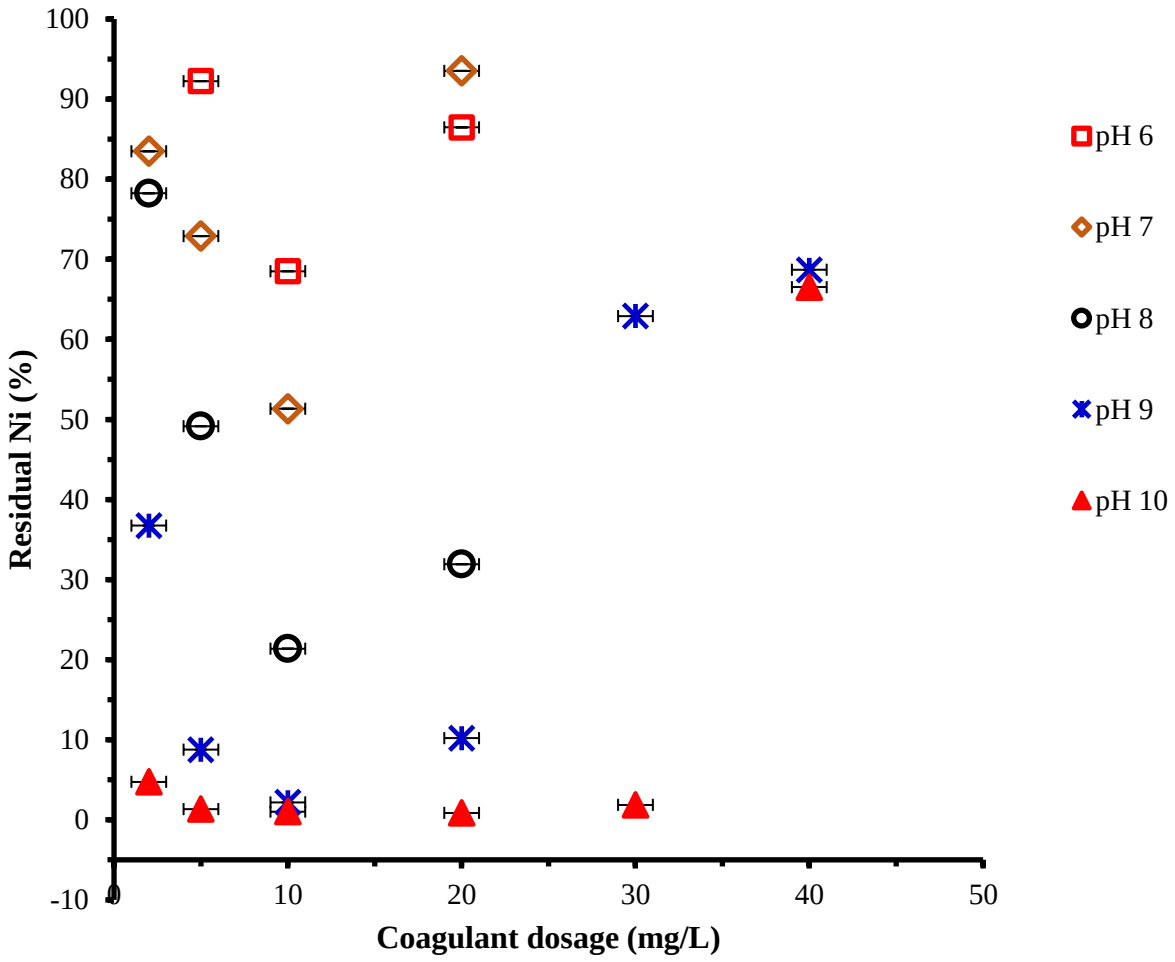

Figure 5.12: Effect of coagulant dosage (mg/L) and pH on removal of Ni from acidic coal mine drainage (initial Ni concentration was 13.86 (initial pH: 4–10; AMD/coagulant ratio: 2.5; RT (23±2 °C); 5 minutes rapid mixing at 300 rpm; 20 minutes slow mixing at 30 rpm).

Coagulation pH plays an important role in optimizing the removal of TDS and toxic elements, and results are shown in Figures 5.4–5.12. It can be seen from Figure 5.4 that the percentage of residual TDS increased as the coagulation pH increased, with maximum removal (42.78% residual TDS or 308.1 mg/L) achieved at neutral pH (pH 7). The colloidal particles in wastewater generally carry electrical negative charges, while the composite coagulant contains a large quantity of Fe^{3+}, Al^{3+}, Mg^{2+}, Si^{4+}, and Ca^{2+} ions. At optimum pH value, these ions (i.e., Fe^{3+}, Al^{3+}, Mg^{2+}, Si^{4+}, and Ca^{2+}) are hydrolyzed into monomeric and

polymeric hydroxy complex ions, which are capable to compress the electric double layer of particles and electrically neutralize for destabilization of the colloidal particles, and are capable to adsorb the colloidal particles. At higher pH values, generally above the optimum pH, hydrolysis of cations (Fe^{3+}, Al^{3+}, Mg^{2+}, Si^{4+}, and Ca^{2+}) happens decreasing the formation of positively charged ions as well as diminishing the ability of coagulant to neutralize the negative charge on TDS, this phenomenon decreases the TDS removal efficiency (Gregor et al., 1997; Gao and Yue, 2005). It is clear that the composite coagulant is effective for removal of TDS at neutral pH (pH 7); iron over the pH range 6–10 (Figure 5.5); aluminium at pH values from 7 to 10 (Figure 5.6); silicon and zinc at pH 9 and 10 (Figures 5.8 and 5.11, respectively); manganese, magnesium, and nickel at pH 10 (Figures 5.7, 5.9, and 5.12, respectively); and calcium at pH 12 (Figure 5.10). Rebhum and Lurie (1993) also found that both the coagulant dosage and the solution pH are important factors in coagulation. Coagulant dosage of 20 mg/L is much more effective due to extensive hydroxide precipitation and a process known as sweep flocculation which led to low TDS, silicon, and metal concentrations and pH values in the range of the permissible pH values for industrial effluent and drinking water. Hence, in the subsequent studies, experiments were performed in the solution pH 7 at coagulant dosage of 20 mg/L.

Effect of coagulant dosage (mg/L) and pH on turbidity removal

The residual turbidity of the treated wastewater was measured to show an indication of the level of particle removal achieved. The performance of the composite coagulant at different dosages for turbidity reduction at pH values from 4 to 10 is presented in Figure 5.13. The original turbidity was 87.7 NTU. Data from the experiments show that optimal conditions for turbidity removal were a dosage of 20 mg/L and pH range of 6–8. These conditions reduce the residual turbidity to 0.00 NTU (99.99% removal). Thus, slight acidic to slight alkaline conditions favoured the turbidity removal by the synthesized composite coagulant to reach required standards of drinking water (less than 1 NTU). This result was in agreement with previous reported results (Li et al., 2009; Fan et al., 2005).

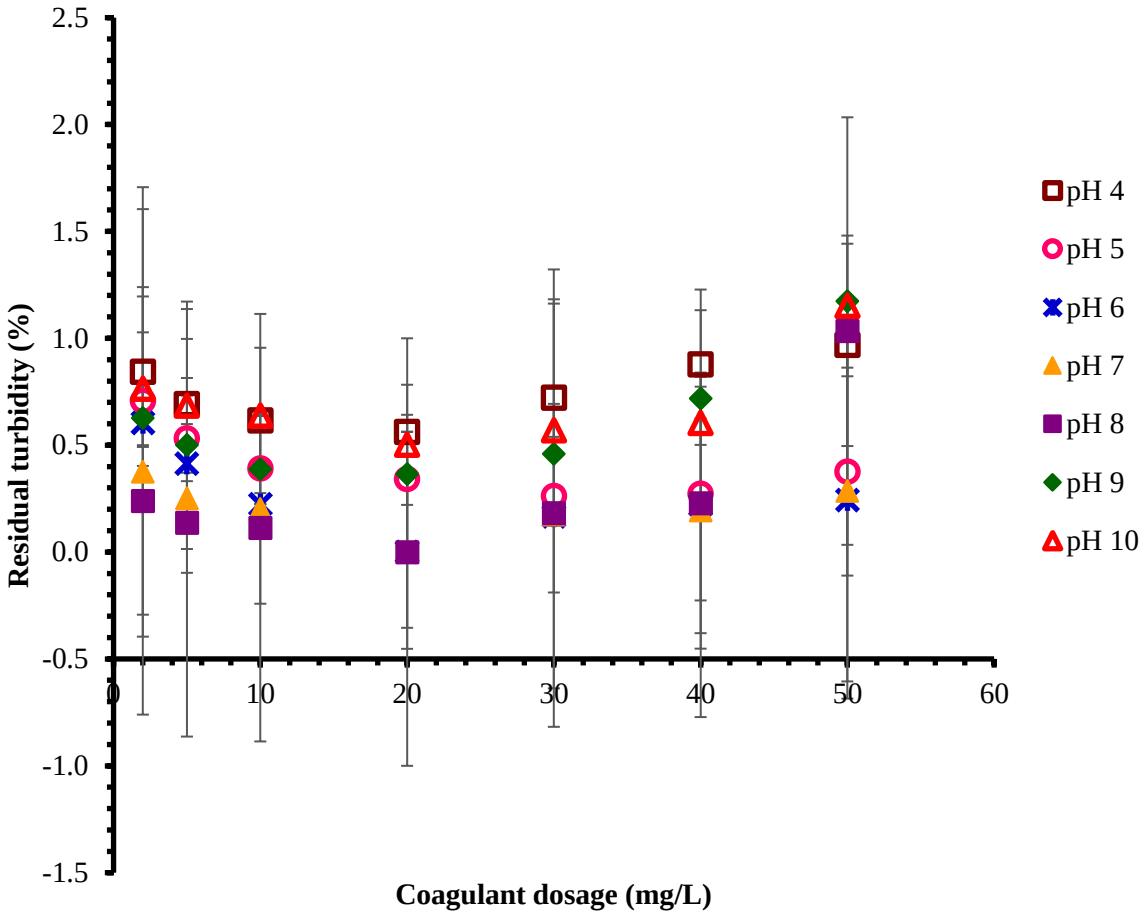

Figure 5.13: Turbidity reduction at different pH and coagulant dosage (mg/L) (initial turbidity 87.7 NTU; initial pH: 4–10; AMD/coagulant ratio: 2.5; RT (23±2 °C); 5 minutes rapid mixing at 300 rpm; 20 minutes slow mixing at 30 rpm).

Effect of coagulant dosage on the final pH of wastewater

The impact of coagulant dosage on the final pH was assessed and results are shown in Figure 5.14 which shows that the complex coagulant (24594.48 mg/L as Fe+Al+Si+Mg+Ca) has reduced the pH to below the initial pH values. The values of the final pH were almost constant as the dosages of coagulant were increased. This indicates that the solution had reached its saturation value. Decreases in pH may be due to several hydrolysis reactions that happen during the coagulation process leading to the formation of polyvalent charged hydroxide species and producing $H3O^{+}$ ions, at each step, thereby creating an acidic

condition and lower the final pH of the wastewater (Eigen, 1964, Stephenson and Duff, 1996). It was noticed from Figure 5.14 that the final pH was decreased with an increase pH value. This agrees with Aziz et al. (2007).

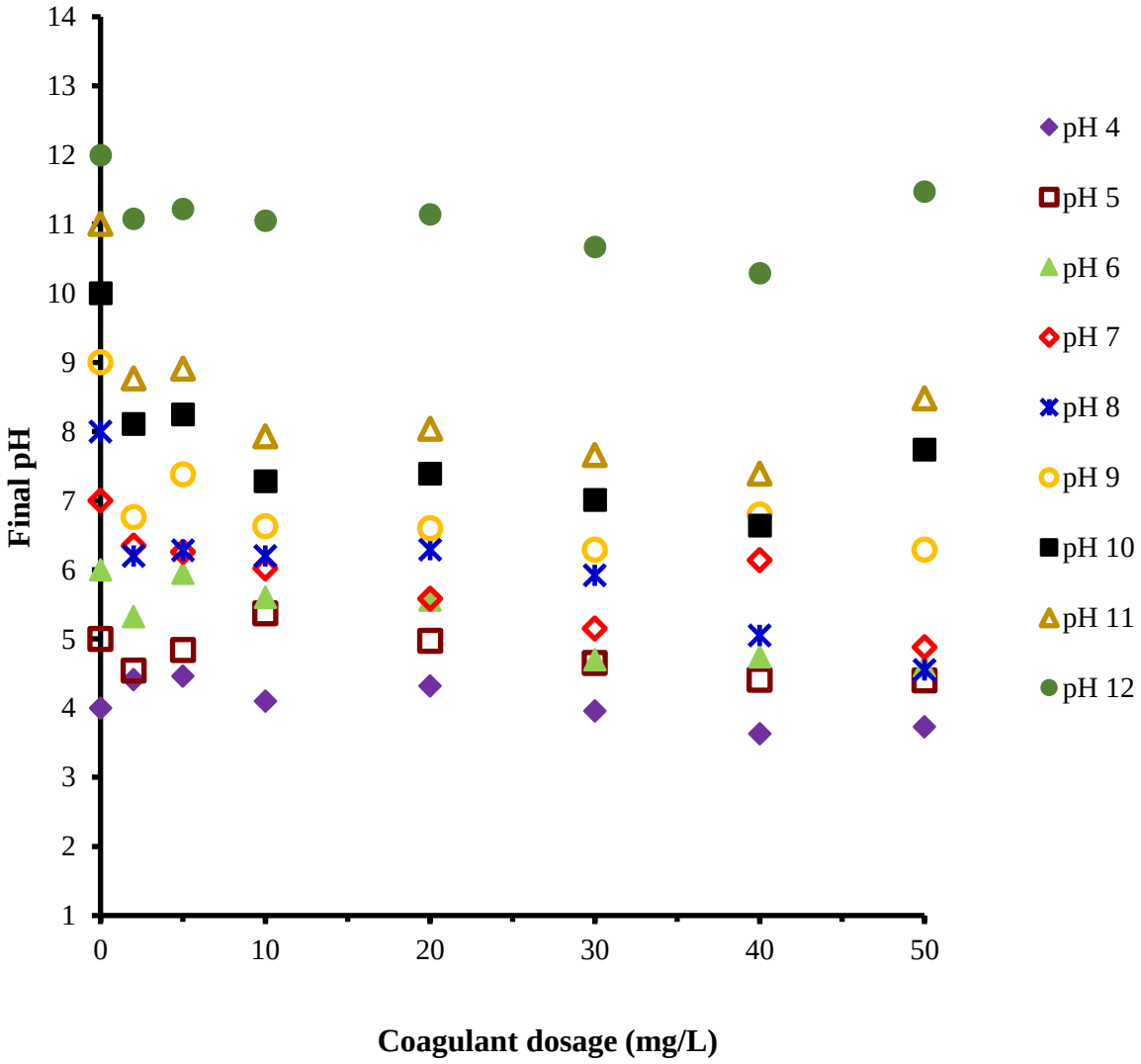

Figure 5.14: Change of pH after adding different doses of the composite coagulant in acid coal mine drainage sample.

Effect of temperature

The effects of temperature on pollutant removals were analysed using the obtained optimal values of pH and coagulant dose (pH 7 and 20 mg/L coagulant dose) and results are shown in

Figure 5.15. As the temperature increases, the viscosity of the AMD decreases, Brownian motion becomes intense and the inorganic coagulant hydrolyses rapidly, accelerating coagulation. Under the experimental conditions used in this study, the time required for the reaction and the settling is sufficient, but it was noticed that the temperature (temperature range: 20–50 °C) has very low effect on the removal of TDS and toxic elements (Fe, Al, Mn, Si, Mg, Ca, Zn, and Ni). During the coagulation process using a CFA-based coagulant, a similar trend was observed by Sui et al. (2009).

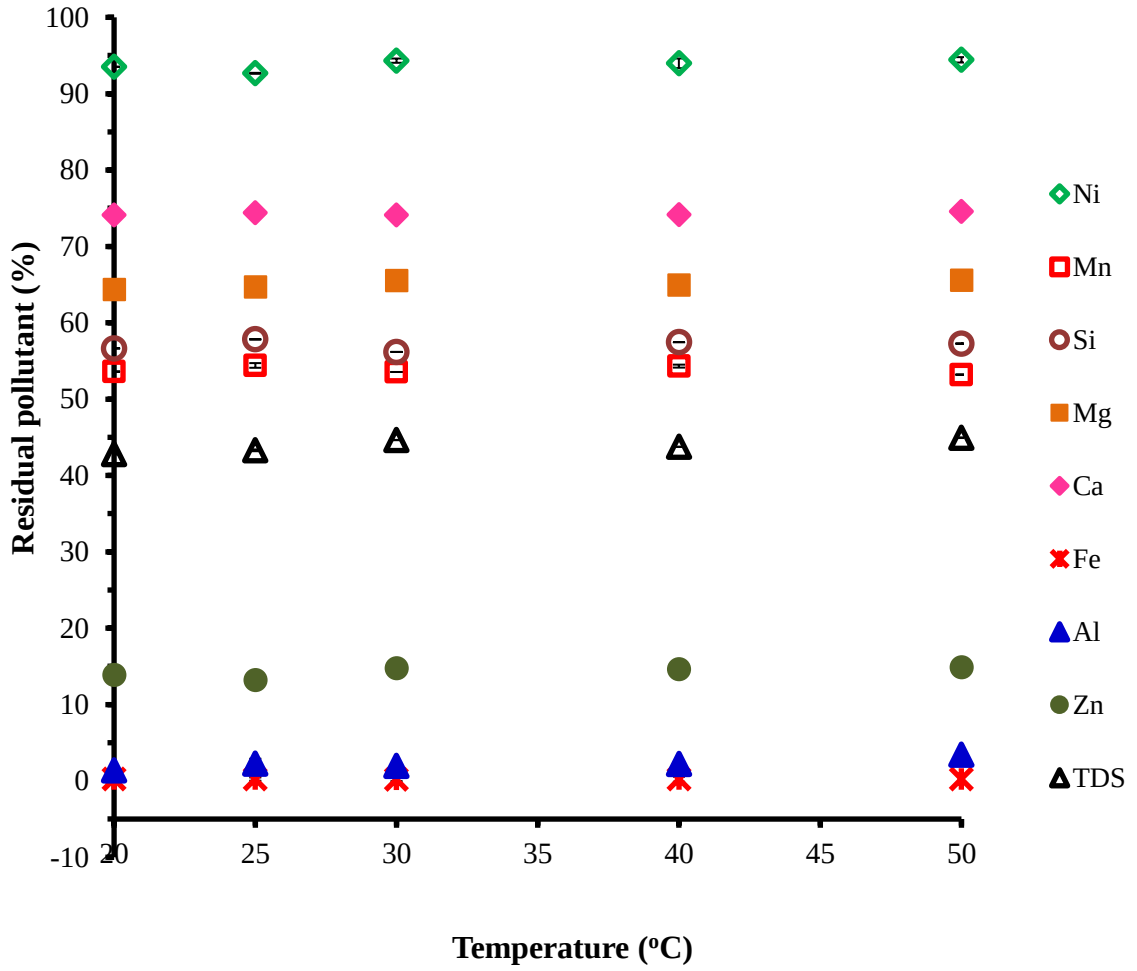

Figure 5.15: Change of total dissolved solids and toxic elements concentrations at different temperatures of coagulation process. Conditions: 20 mg/L coagulant dosage, pH 7, coagulation time = 20 minutes, temperature = 20–50 °C.

Effect of time

Predetermined optimal values of coagulant dosage and pH were used for analysing the effects of time on the removal process. Figure 5.16 shows the effect of coagulation time on the percentage of residual toxic elements and TDS by the produced complex coagulant. It can be seen that at pH 7 the produced composite coagulant did not have efficiency in removing TDS at time less and more than 20 minutes. While the residual pollutant percentage in the treated wastewater gradually decreased with time and attained saturation in 20 minutes for Fe, Zn, Ca, Si, and Ni. Beyond 20 minutes' coagulation time, the residual percentage gradually increased with increasing the coagulation time. The coagulation behaviour of Mg, Mn. and Al showed that the residual metal percentages in the wastewater somewhat decreased until 20 minutes and slightly increased until 50 minutes.

In general, it was noticed that the % of residual impurity decreases as the coagulation time increases up to 20 minutes, and then the % of residual impurity increases as the coagulation time increases. The initial decrease in % of residual impurity can be explained in terms of the high faster adsorption due to high driving force at the beginning. However, with increasing the coagulation time, slower adsorption is possible due to the decrease in the driving concentration difference between the bulk solution and the surface, which slows down transport of the impurity particles to the surface of adsorbent (hydroxide precipitate). At coagulant dosage of 20 mg/L, 60.83, 1.36, 0.23, 53.61, 74.13, 64.35, 56.57, 13.95, 65.29% residual TDS, Al, Fe, Mn, Ca, Mg, Si, Zn, and Ni, respectively, were observed after 20 minutes. The coagulation time of 20 minutes was found sufficient for TDS and toxic elements removal from AMD. Based on a survey of coagulation it was observed that no information on coagulation of studied pollutants is available in the literature.

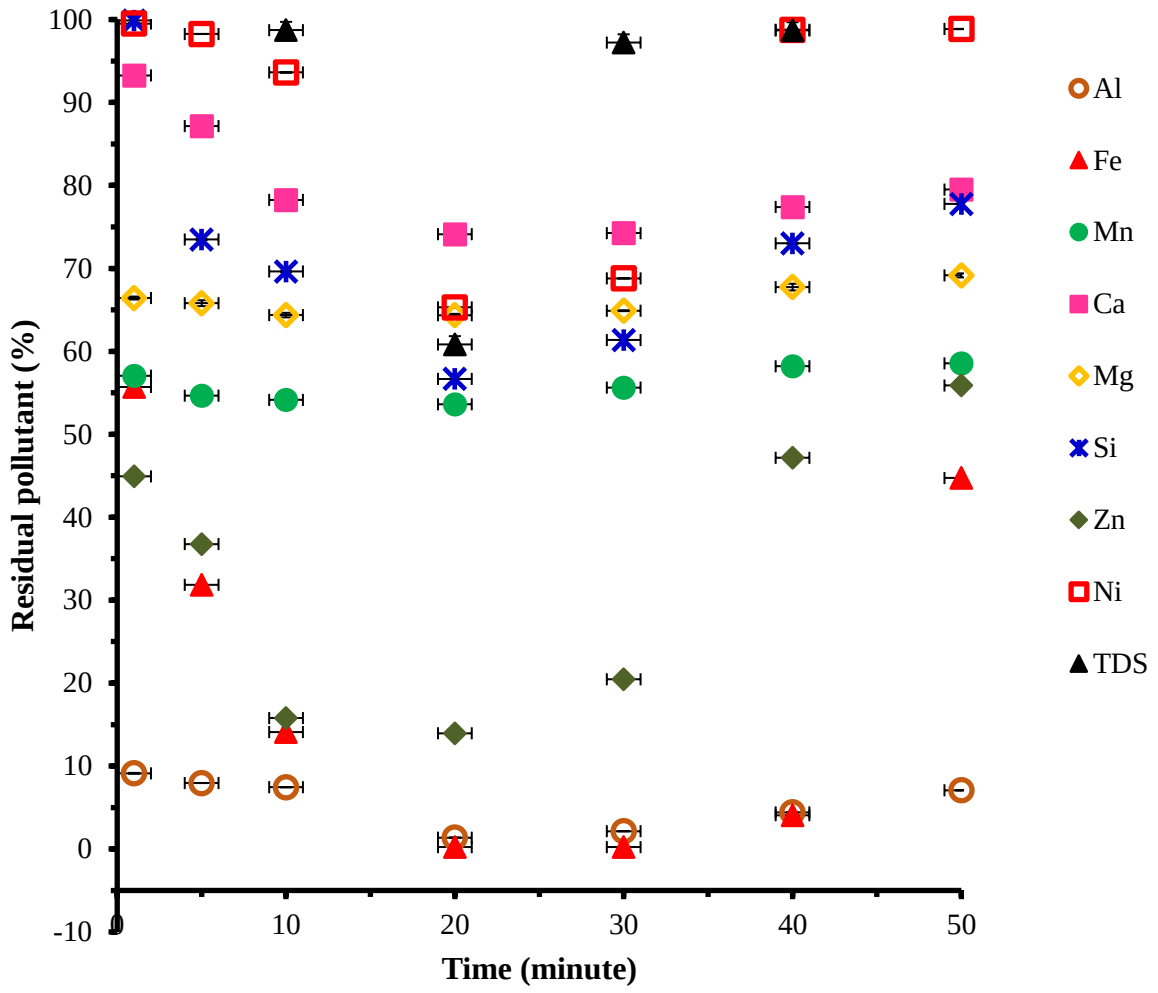

Figure 5.16: Change of toxic elements and total dissolved solids concentrations after different times of coagulation process. Conditions: 20 mg/L coagulant dosage, pH 7, RT (20±1 °C), coagulation time = 1–50 minutes.

In general, optimal coagulation process conditions were found to be 20 mg/L composite coagulant dosage, neutral to alkaline pH (pH 7–11), and 20 minutes' coagulation time. However, since the wastewater used in this study is a multi-component aqueous solution, pH value of 7 was considered as optimum.

These conditions were further used in each of the performances of conventional coagulants used in this study. Moreover, the treated coal mine wastewater sample was characterized and compared with the raw (Section 5.2.1) in order to see the effect of composite coagulant on

removal of TDS, Fe, Al, Si, Mn, Mg, Ca, Ni, and Zn; which provides an additional support to the coagulation behaviour of these impurities.

5.3 Characteristics of the treated coal mine wastewater after optimisation

The coal mine wastewater samples before and after treatment by the synthesized complex coagulant are shown in Figure 5.17. The treated coal mine wastewater (obtained using optimal process conditions, at pH 7, coagulant dosage of 20 mg/L, RT (23±2 °C) for 20 minutes) was characterised in terms of chemical properties as presented in Table 5.2. It is shown that the residual impurity concentrations of the treated coal mine wastewater are turbidity (0.00 NTU), TDS (308.1 mg/L), iron (0.00 mg/L), aluminium (0.19 mg/L), manganese (7.25 mg/L), silicon (0.52 mg/L), magnesium (19.42 mg/L), calcium (23.07 mg/L), nickel (0.39 mg/L) and zinc (0.13 mg/L).

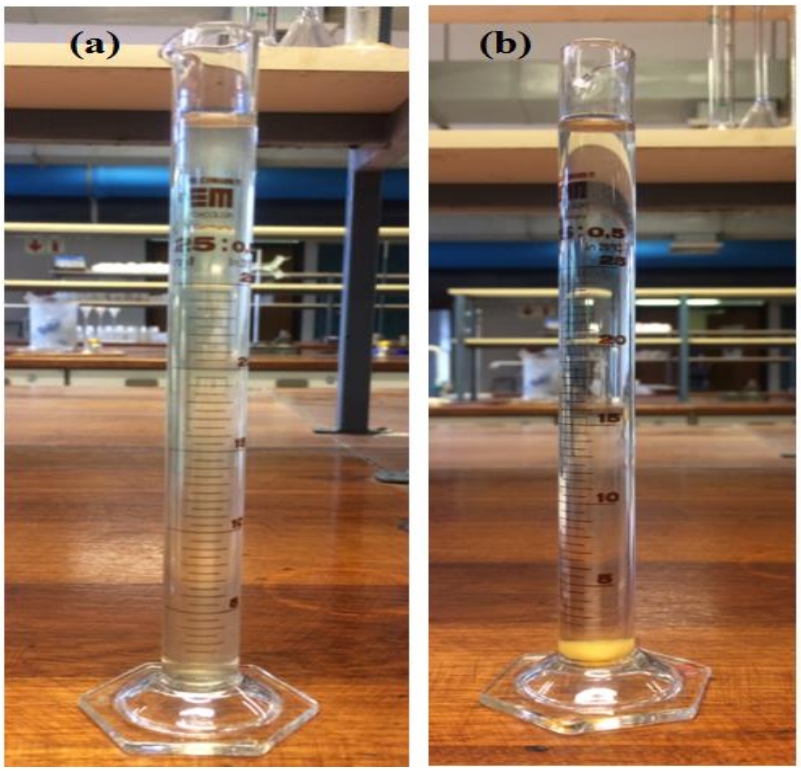

Figure 5. 17: Coal mine drainage. (a) Before and (b) after treatment (1 hour settling). Conditions: 50mL wastewater, adjusted the initial pH 7 by NaOH and H_2SO_4, produced coagulant dosage 20 mg/L, 20 minutes' treatment.

Table 5.2: Chemical analysis of the treated coal mine wastewater obtained from treatment of the acid coal mine drainage sample by the complex coagulant.

Parameter	Value
pH (value)	5.58
Colour	Absent
Turbidity (NTU)	0.00
Conductivity (µS/cm)	430
Total Dissolved Solids (TDS) (mg/L)	308.1
Fe (mg/L)	0.00
Al (mg/L)	0.19
Mn (mg/L)	7.25
Ca (mg/L)	23.07
Mg (mg/L)	19.42
Si (mg/L)	0.52
Ni (mg/L)	0.39
Zn (mg/L)	0.13
As (mg/L)	-0.02
Cr (mg/L)	-0.01
Cu (mg/L)	-0.00

5.4 Coagulation mechanism of the produced complex coagulant

The exact mechanism of colloid destabilization is a complex process in which several reactants and reactions can occur (Stumm and O'Melia, 1968). The coagulation (which is assumed to be time dependent) of coal mine wastewater included several reaction steps (Figures 5.18–5.21);

- Hydrolysis of Fe^{3+}, Al^{3+}, Mg^{2+}, Ca^{2+}, and Si^{4+} and following polymerization to polynuclear hydrolysis species,
- Adsorption of hydrolysis products at the solid-solution interface causing colloid destabilization,
- Agglomeration of destabilized colloid by interparticle bridging including particle transport and chemical interactions,

- Agglomeration of destabilized particles by particle transport and van der Waals forces.
- Growth of the flocs, accompanied by chemical modifications of the structure of the Metal-OH-Metal and/or Si-OH-Si bonds, as well as simultaneous changes in the stability of the flocs and the level of hydration of the flocs,
- Precipitation of the metal and/or silicon hydroxide.

Some of these steps are successive, some overlay, and some may occur simultaneously under certain conditions. Thus, coagulation in coal mine drainage treatment by hydrolyzable multivalent iron, aluminium, magnesium, calcium, and silicon salts involved the following mechanisms,

1. Electric double layer compression and electrostatic neutralization. The coagulant produced from CFA contains a large amount of Fe^{3+}, Al^{3+}, Mg^{2+}, Si^{4+}, and Ca^{2+} ions, which are multi-charged, and can efficiently reduce or remove the Zeta electric potential of negatively charged colloidal impurities suspended in wastewater, so that the repulsive force between the colloidal particles decreases and causes colloidal particles destabilization and coagulation (aggregation). In addition, the hydrolysis of these cations will result in several complicated polynuclear complexes containing bridging hydroxide ion. Since the attraction reaction continues constantly, the colloidal particles suspended in the wastewater coagulate easily.
2. Adsorption. The addition of complex coagulant, which contains cations, to wastewater results in precipitation of cation hydroxide (cationic hydrolysis species such as $Fe_2(OH)_2^{4+}$, $Fe_3(OH)_4^{5+}$, $Al_2(OH)_2^{4+}$, $Al_3(OH)_4^{5+}$, $Mg_4(OH)_4^{4+}$, and $Si_2O(OH)_6$), negatively charged colloidal particles (pollutants) can adsorb on these precipitates as they are produced and also collide with them subsequently. The hydroxide precipitates maintain open structure so that even a small mass may cause a large effective volume concentration and thus a high possibility of capturing dissolved impurities. This is according to the adsorption theory, on wastewater treatment, which says that the higher the surface area of the adsorbent, the better the adsorptive effect. Therefore, hydroxide precipitate adsorbs better dissolved substances.
3. Adsorption-bridging and network-capturing. Bridging of particles by hydroxide precipitates results in stronger aggregates. The complex coagulant contains

macromolecules of polysilicic acid, as well as Fe^{3+}, Al^{3+}, Mg^{2+}, and Ca^{2+} ions, which give high adsorption-bridging and network-capturing ability, with which the fine particles and poorly soluble compounds can be separated from the wastewater. This further increases the process of adsorption, coagulation and settling.

For all the impurities investigated, the removal efficiency of the synthesized complex coagulant (Figures 5.4–5.12), at pH at 20 mg/L coagulant dose and for 20 minutes' coagulation time, the hydroxide precipitates would be positively charged and thus able to neutralize the negative charge of particles in acid coal mine wastewater.

5.5 Flocs formation analysis using optical microscopy

From the coagulation by the complex coagulant under optimal conditions of the process, formed flocs were analysed using optical microscopy. Samples of treated AMD were collected at 10 minutes time interval (from 10 to 150minutes). This is in order to support the coagulation behaviour of coal mine drainage. The optical microscope images in Figures 5.18–5.21 show the obvious impact of the produced composite coagulant. Images in Figures 5.18–5.21 reveal that the size of the flocs was increasing as the time increased. These results confirm the fact that there was destabilisation by charge neutralisation and sweep flocculation. Specifically, formation of flocs is fast (may be after an initial delay) and flocs can become much bigger in the case of sweep flocculation, so that a high level of removal can be obtained. These effects may be due to the formation of a bulk cation (from the complex coagulant) hydroxide precipitates, originally in the form of very small particles (a few nm in size), which are positively charged at around neutral pH. Probably some of these hydroxide particles form a covering on the impurity particles, reversing their charge. Then, agglomeration of the hydroxide particles happens, either on the particle surfaces (a form of heterocoagulation) or in bulk solution (Figures 5.19). In addition, for details of this process, the microscopic images in Figures 5.18 of flocs formed under sweep conditions show the initial impurity particles surrounded by an amorphous precipitate. Images from Figures 5.19 to Figures 5.21 reveal that aggregations of particles were formed during the coagulation process.

Furthermore, the produced sludge samples were characterized using SEM/EDS technique in order to see the effect of the produced composite coagulant on the coagulation of iron,

aluminium, manganese, magnesium, calcium, silicon, nickel, and zinc; which provide a supplementary support to the coagulation behaviour of these elements.

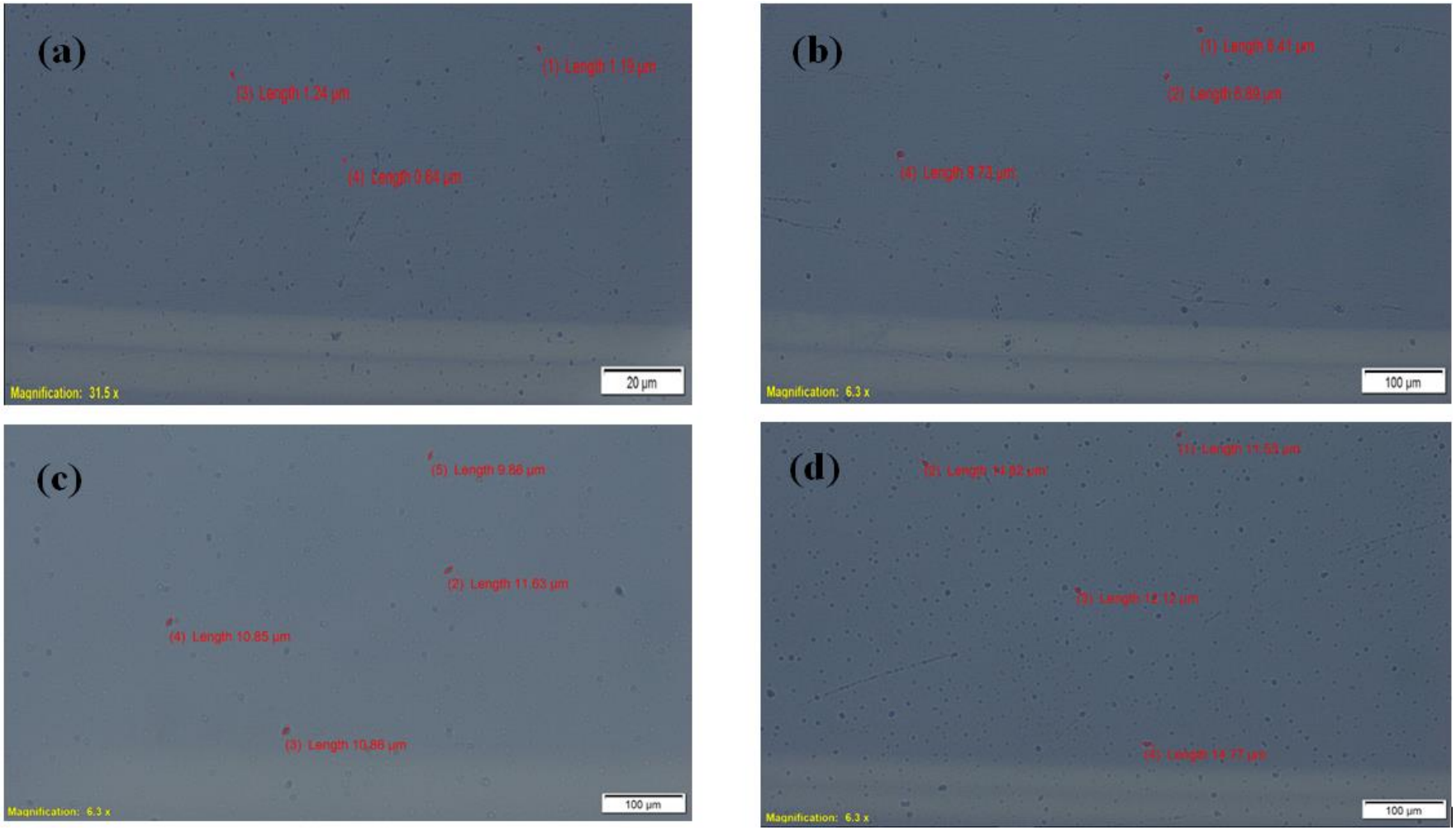

Figure 5.18: The optical microscope images showing flocs formation during coagulation using the composite coagulant under optimal experimental conditions at (a) 10, (b) 20, (c) 30, and (d) 40 minutes of settling time.

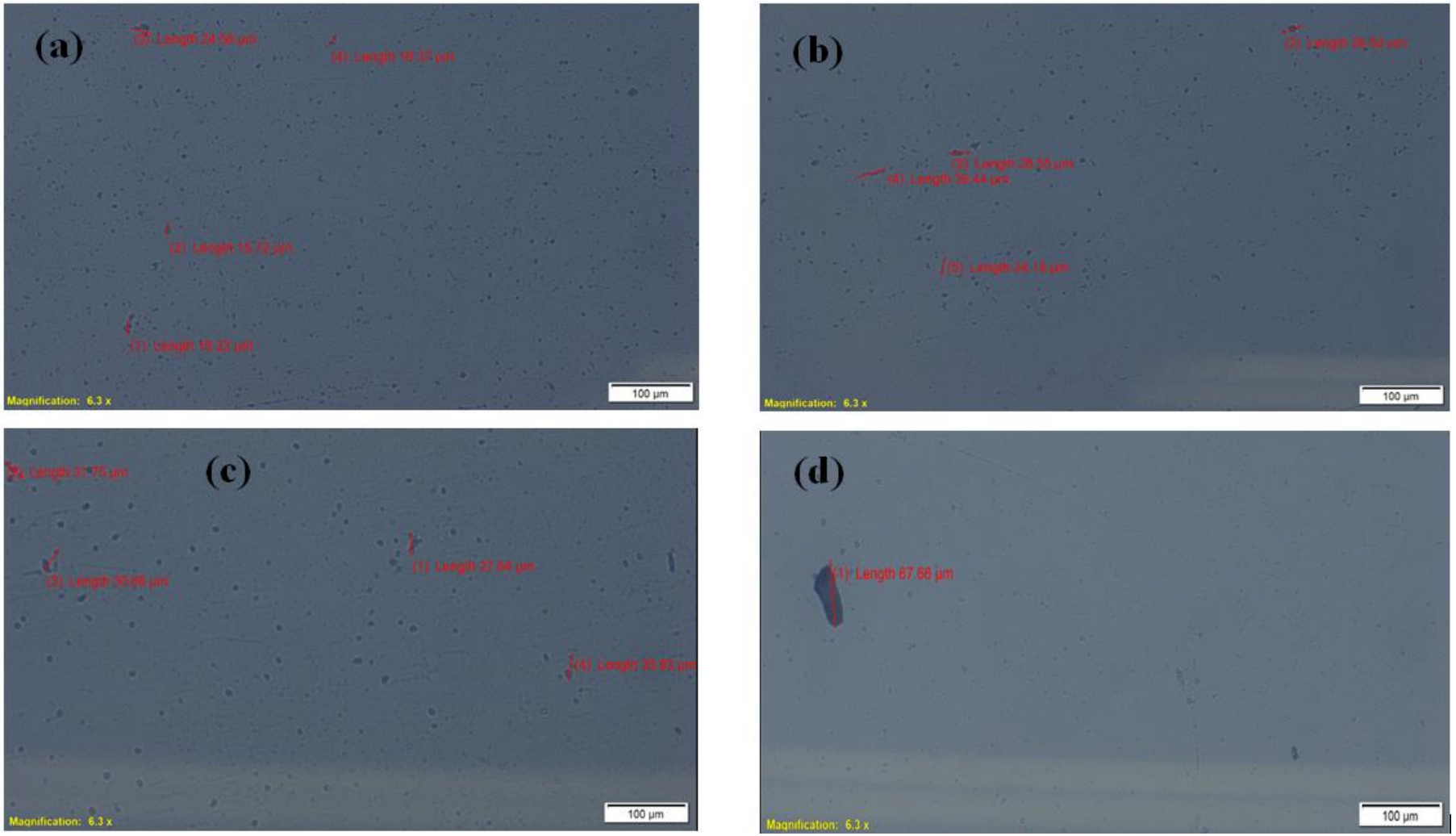

Figure 5.19: The optical microscope images showing flocs formation during coagulation using the composite coagulant under optimal experimental conditions at (a) 50, (b) 60, (c) 70, and (d) 80 minutes of settling time.

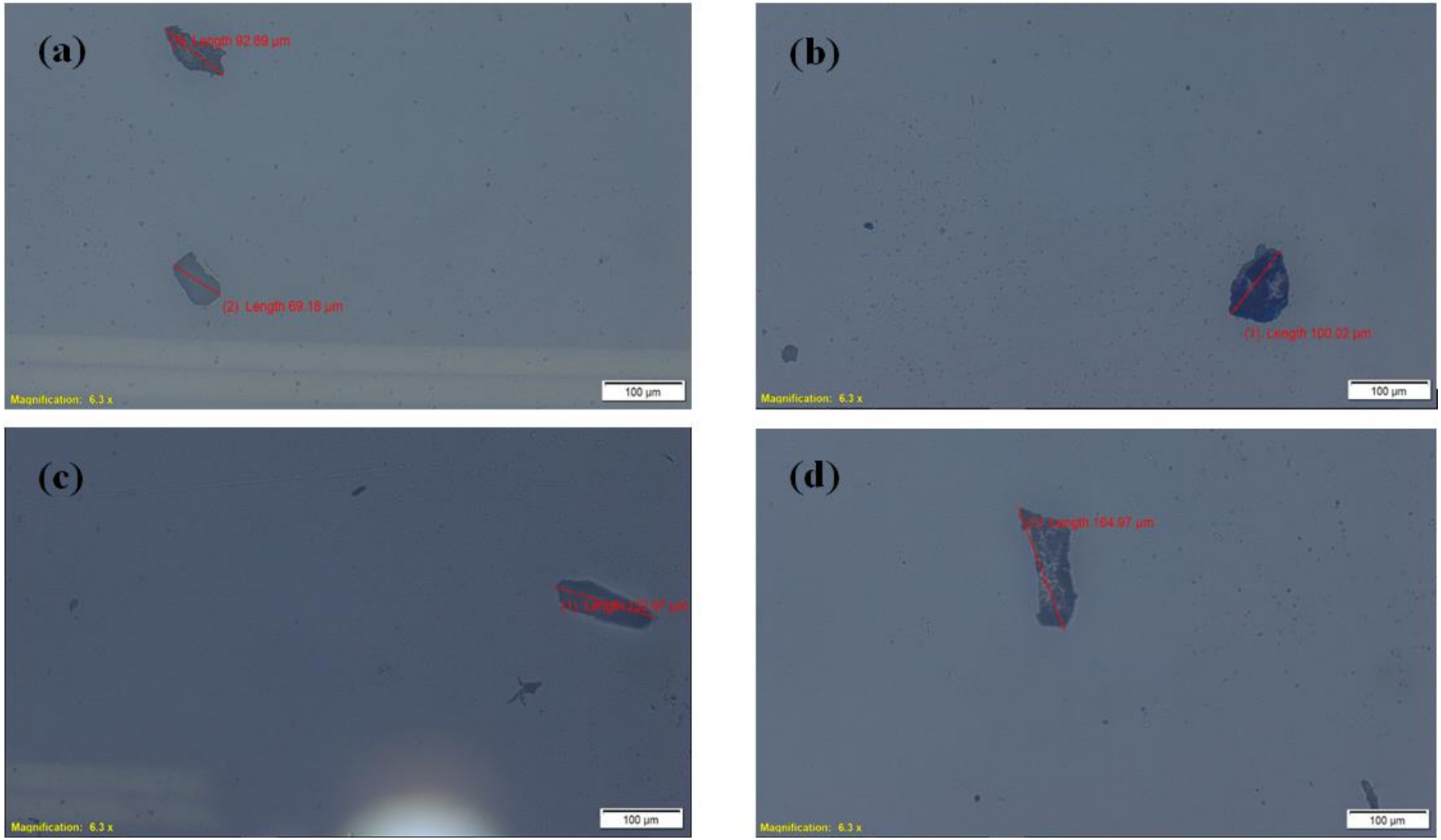

Figure 5.20: The optical microscope images showing flocs formation during coagulation using the composite coagulant under optimal experimental conditions at (a) 90, (b) 100, (c) 110, and (d) 120 minutes of settling time.

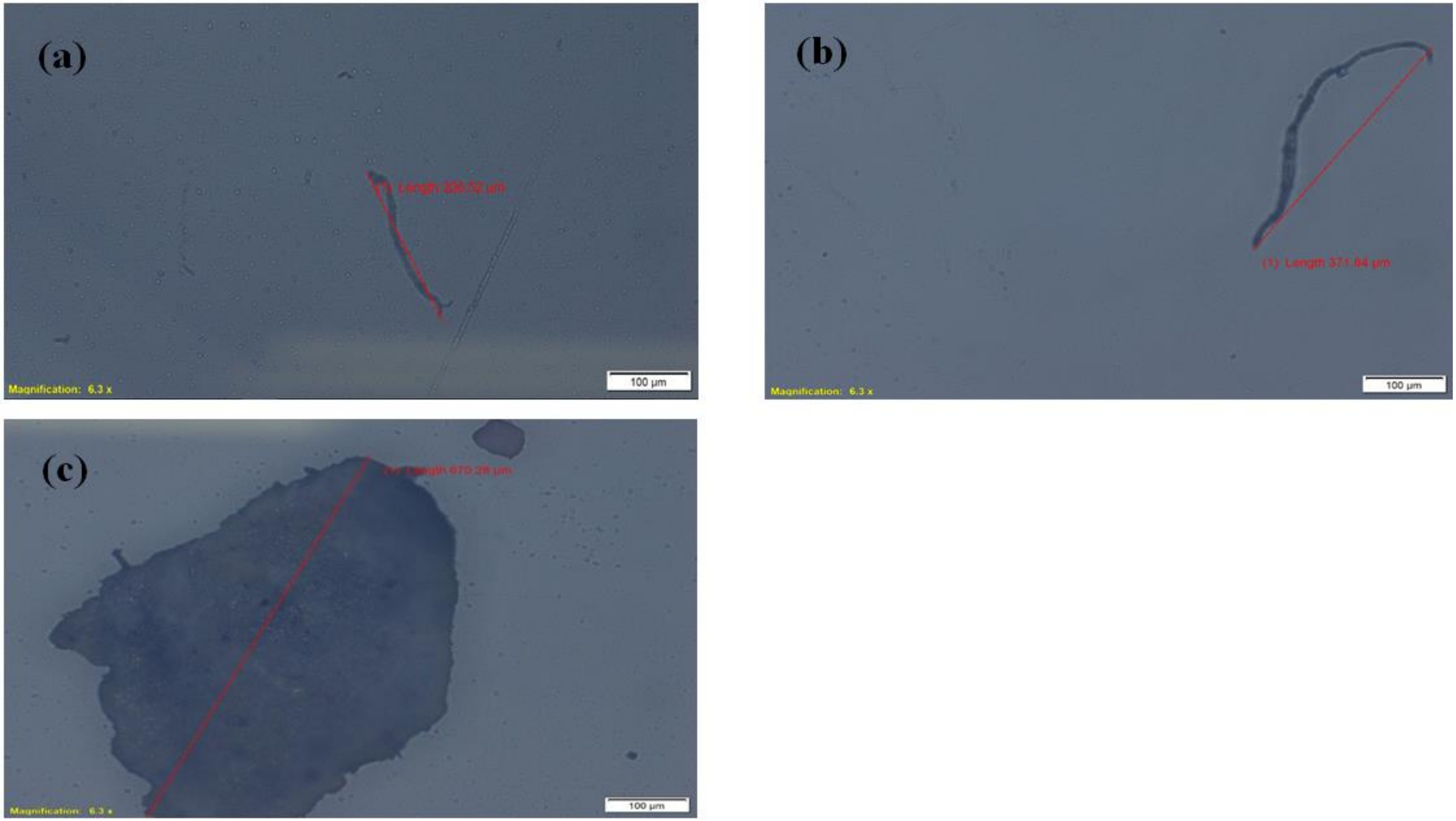

Figure 5.21: The optical microscope images showing flocs formation during coagulation using the composite coagulant under optimal experimental conditions at (a) 130, (b) 140, and (c) 150 minutes of settling time.

5.6 Scanning electron microscopy coupled with energy dispersive spectroscopy (SEM/EDS) of the dry sludge

In addition to studying the coagulation process of wastewater, the coagulated solid residue was characterized using scanning electron microscopy (SEM/EDS) to observe the impact of the composite coagulant on metals concentrations reduction. The residual sludge from selected experiments conducted at 20 mg/L (coagulant dosage) at pH 4, 7, 11, and 12 for TDS and toxic ions removal was taken, washed with deionized water (to less than 100 µS/cm) in order to remove any soluble elements, and air dried for SEM/EDS analysis. The SEM and EDS results of surface of the coagulated solid residue presented in Figure 5.22 and 5.23, and Table 5.3 show that the sludge mainly consists of Al, Fe, Mg, Ca, Si, Zn, Ni, and oxygen. This suggests that the mineral composition of the sludge is hydroxide precipitates of cation (from the coagulant) on which toxic elements (Al, Fe, Mn, Mg, Ca, Si, Zn, and Ni) from the effluent water were adsorbed. Further, these results are generally consistent with the experimental data since it can be seen from Table 5.3 that, for each impurity, the removal trend is similar to that of the experimental data previously discussed.

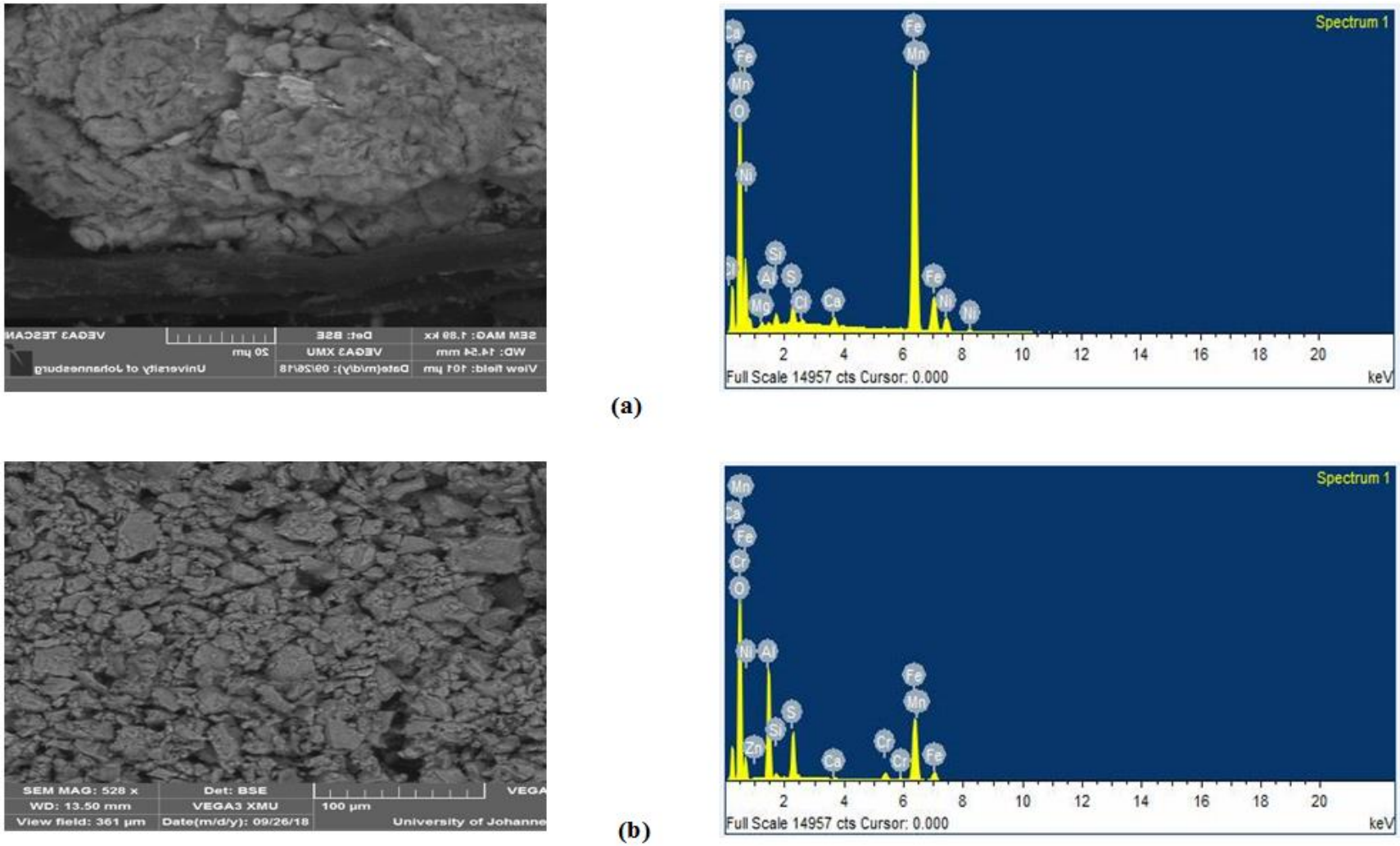

Figure 5.22: SEM images with elemental spectra of the sludge (a) pH 4 and (b) pH 7. Conditions: 20mg/L coagulant dosage, RT (23±2 °C); 5 minutes rapid mixing at 300 rpm; 20 minutes slow mixing at 30 rpm).

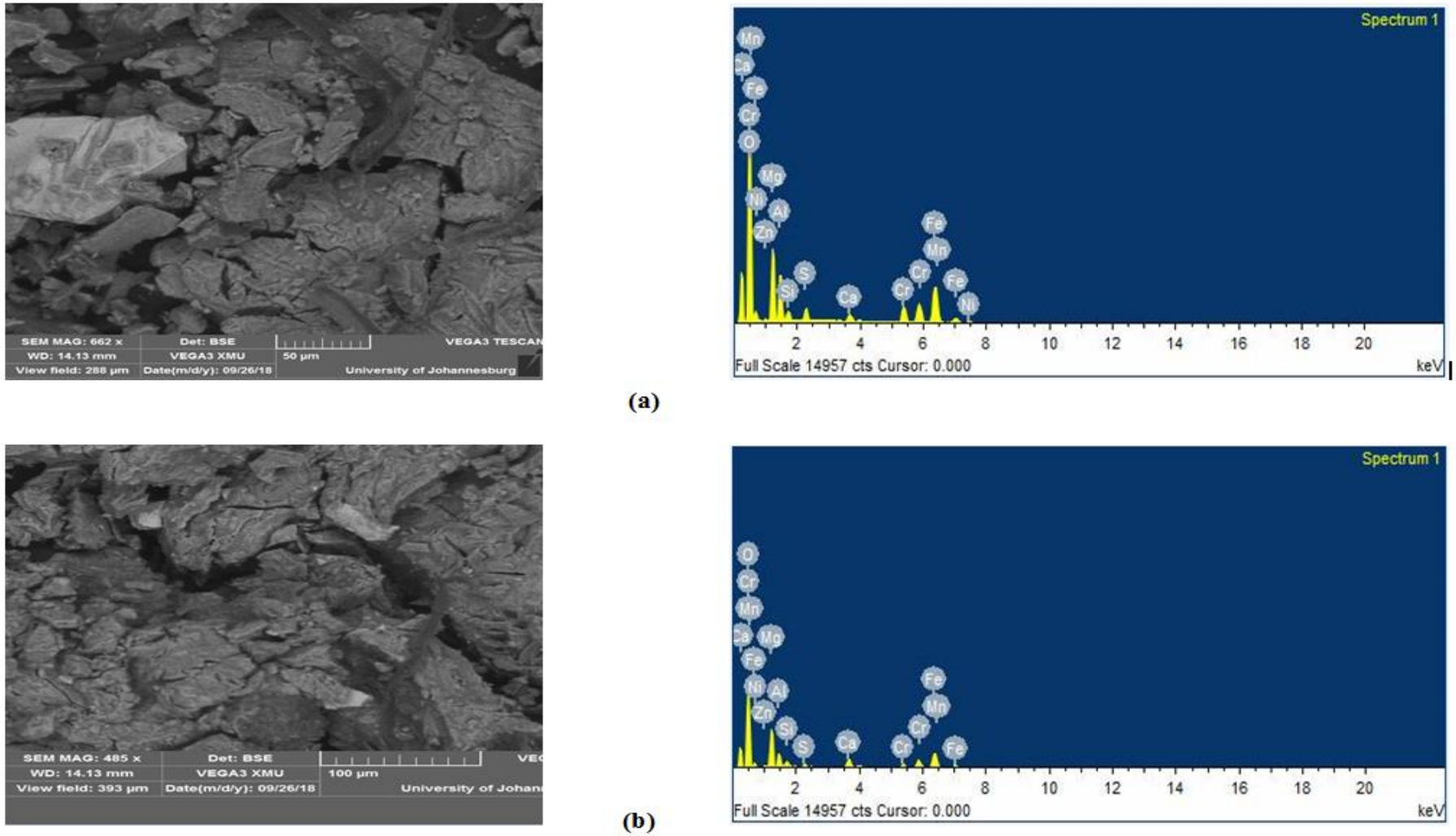

Figure 5.23: SEM images with elemental spectra of the sludge (a) pH 11 and (b) pH 12. Conditions: 20mg/L coagulant dosage, RT (23±2 °C); 5 minutes rapid mixing at 300 rpm; 20 minutes slow mixing at 30 rpm).

Table 5.3: Energy dispersive spectrometry (EDS) w% of elements in the sludge.

Elements	pH 4	pH 7	pH 11	pH 12
O	30.60	48.24	49.51	50.11
Mg	0.56	-	10.97	13.79
Al	0.25	12.80	6.42	4.48
Si	0.50	0.72	1.35	1.84
Ca	0.05	0.67	1.21	3.11
Mn	0.29	0.35	6.93	6.93
Fe	15.25	60.25	57.34	15.38
Ni	0.01	0.11	0.62	0.64
Zn	-	0.13	0.50	0.58

5.7 Comparative study of the performance of synthesized composite coagulant with conventional ferric sulphate and aluminium sulphate coagulants

In order to make comparison between the performance of the synthesized composite coagulant and available conventional coagulants (the monomeric aluminium and ferric sulphates) in treating coal mine wastewater, optimal process conditions found for the produced coagulant (i.e., 20 mg/L coagulant dose, pH 7, RT, and 20 minutes' coagulation period) were used for the conventional $Fe_2(SO_4)_3$ and $Al_2(SO_4)_3$. After treatment, pH, turbidity, TDS, Ca, Mg, Si, Zn, Al, Fe, Ni, and Mn of the wastewater sample were measured, and the results are presented in Table 5.4.

Table 5.4: Results of treating coal mine wastewater with different coagulants. Residual TDS and toxic elements (%) and turbidity (NTU).

Parameters	Composite coagulant (optimum)	$Fe_2(SO_4)_3$	$Al_2(SO_4)_3$
pH	5.58	6.78	7.24
TDS	60.83	89.70	63.22
Turbidity	0.00	0.88	1.19
Ca	74.13	81.48	85.02
Mg	64.35	69.19	67.09
Si	56.67	67.96	64.18
Zn	13.95	16.58	14.00
Al	1.36	0.11	0.11
Fe	0.23	0.07	0.20
Ni	65.30	50.34	45.96
Mn	53.61	56.46	51.47

Under the experimental conditions used in this study, it can be seen from Table 5.4 that the produced composite coagulant is much more effective, than aluminium and ferric sulphates coagulants, in removing TDS, Ca, Mg, Si, and Zn from AMD. This is due to the presence of different cation salts in the composite coagulant, moreover the complex coagulant is a pre-hydrolysed product of different cations (Fe^{3+}, Al^{3+}, Si^{4+}, Mg^{2+}, and Ca^{2+}) containing preformed polynuclear (polymeric) species of these cations. Furthermore, the high charge associated with species cause the effectiveness in neutralizing the negative charge of colloids in wastewater and large hydroxide precipitation giving sweep flocculation (Duan and Gregory, 2003; Yan et al., 2008 and 2009). In addition, the polysilicate species maintains a macromolecular structure, and a dominant function of adsorption bridging (Niu et al., 2011). Therefore, the composite coagulant produces important effect on colloids coagulation than the conventional non-pre-hydrolysed aluminium and iron sulphates coagulants used in this study. However, for the removal of Al, Fe, Ni, and Mn, it appears that the produced complex coagulant shows no significant benefit over traditional coagulants used in this study. Furthermore, the produced composite coagulant showed lower residual turbidity than ferric sulphate and aluminium sulphate coagulants.

In general, the composite coagulant which contains multinuclear hydroxyl complexes with different charges, showed higher coagulation efficiency than aluminium and ferric sulphates. This is consistent with the works by Cheng, 2002.

5.8 Adsorption isotherm study

Isotherm modeling is a mathematical method for describing adsorption mechanisms of coagulant–adsorbate aggregation. In order to optimize the design of an adsorption system for the adsorption of adsorbates, it is important to establish the most suitable correlation for the equilibrium curves (Namasivayam and Kavitha, 2002). Equilibrium isotherm equations such as Langmuir, Freundlich, Temkin, and BET isotherms are commonly used for modelling adsorption data. The adsorption experimental data of metals and silicon were analysed using linear forms of Langmuir, Freundlich, Temkin, and BET isotherm models. The adsorption capacity (q_e) of pollutant at time *t* was calculated using the following equation (Hussain et al., 2013):

$$q_e = \frac{(C_0 - C_t) \times V}{D} \quad (5.7)$$

where q_e (mg/mg) is the equilibrium (or saturation) adsorption capacity; C_0 and C_t (mg/L) represent the initial and final concentrations of impurity, respectively, *V* (mL) represents the volume of wastewater, and *D* (mg/L) is the coagulant dosage (as Fe + Al + Si + Mg + Ca). Values of q_e are presented in Table 5.5. It is shown from Table 5.5 that as the time increases, adsorption capacity (q_e, mg/mg) increases until 20 minutes. Thereafter with the increase of time, the slower adsorption was noticed.

Table 5.5: adsorption capacity (q_e) of pollutant at time *t*.

Time (minute)	q_e (mg pollutant/mg complex coagulant)							
	Al	Fe	Mn	Mg	Ca	Si	Ni	Zn
1	15.7	0.9	7.3	12.7	2.6	0.0	0.0	0.6
5	15.9	1.4	7.7	12.9	5.0	0.3	0.0	0.7
10	16.0	1.8	7.7	13.4	8.5	0.3	0.0	1.0
20	17.1	2.0	7.8	13.4	10.1	0.5	0.2	1.0
30	16.9	2.0	7.5	13.2	10.0	0.4	0.2	0.9
40	16.6	2.0	7.1	12.2	8.8	0.3	0.0	0.6
50	16.1	1.1	7.0	11.6	8.0	0.3	0.0	0.5

5.8.1 Langmuir model

The Langmuir isotherm assumes the formation of a monolayer of the adsorbate on the surface of the adsorbent. The Langmuir isotherm model is based on surface homogeneity having equal energy and assumes that all the adsorption sites obtain similarity of the adsorbate (Gode and Pehlivan, 2005). The Langmuir model was used to estimate the maximum adsorption capacity corresponding to complete monolayer coverage on the adsorbent surface. The Langmuir model is defined as follows (Maurya and Mittal, 2009):

$$q_e = \frac{q_m K_L C_e}{1+K_L C_e} \tag{5.8}$$

The inverse of the equation given in (5.8) is

$$\frac{1}{q_e} = \frac{1+K_L C_e}{q_m K_L C_e} \tag{5.9}$$

The equation (5.9) can be written as follows

$$\frac{C_e}{q_e} = \frac{1}{q_m K_L} + \frac{C_e}{q_m} \tag{5.10}$$

The linear form of Langmuir equation can be expressed as follow:

$$\frac{C_e}{q_e} = \frac{1}{q_m K_L} + \frac{1}{q_m} C_e \tag{5.11}$$

Where C_e represents the equilibrium concentration of the adsorbate in solution (mg/L), q_e is the amount (mg/L) of adsorbed pollutant per mg/L complex coagulant, q_m and K_L are the Langmuir constants related to monolayer capacity (maximum adsorption capacity) (mg/mg) and equilibrium constant related to bonding energy of the adsorption (L/mg), respectively. The constants q_m and K_L were determined from the slope and y-intercept of the Langmuir plot *of* C_e/q_e against the concentration of pollutant remaining in solution, C_e, as seen in Figure 5.24. The Langmuir constants, q_m, and K_L, are presented in Table 5.6. The calculated Langmuir constants were used to calculate a dimensionless constant R_L, which is an essential characteristic of the Langmuir isotherm (Namasivayam and Kavitha, 2002). R_L was calculated as follows

$$R_L = \frac{1}{1+ K_L C_0} \quad (5.12)$$

Where K_L is Langmuir constant (L/mg) and Co is initial concentration of adsorbate (mg/ L). R_L value indicates if Langmuir isotherm adsorption is favourable or not as per the following:

- $R_L > 1$: R_L values indicate the adsorption to be unfavourable
- $R_L = 1$: linear
- $0 < R_L < 1$: favourable
- $R_L = 0$: irreversible

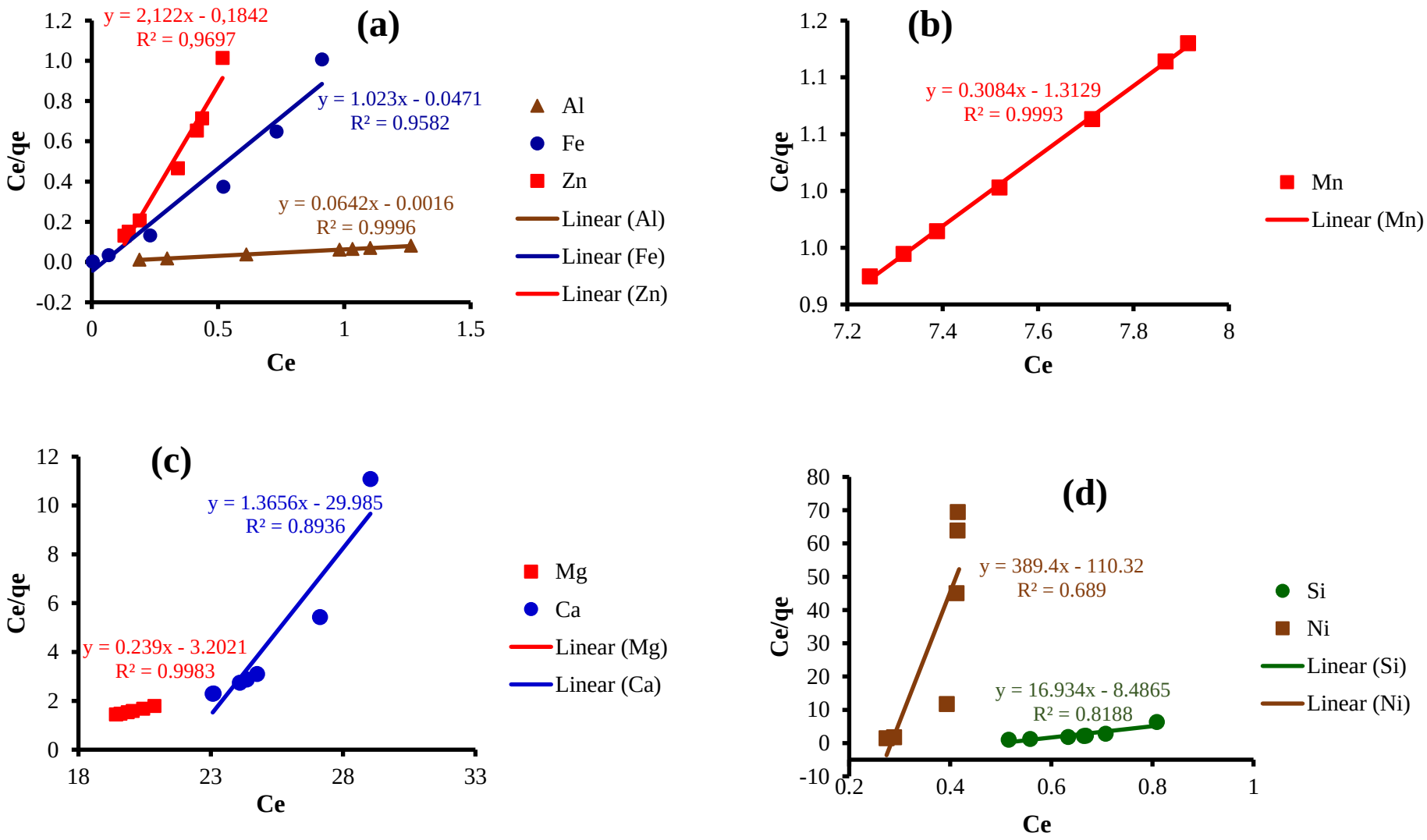

Figure 5.24: Langmuir adsorption isotherm model for the removal of (a) Al, Fe, Zn, (b) Mn, (c) Mg, Ca, and (d) Si, Ni onto hydroxide precipitates (pH: 7; coagulant dosage:20 mg/L; flash mixing time: 5 minutes; coagulation time (slow mixing time): 1–50 minutes).

Table 5.6: Langmuir isotherm parameters calculated for metals and silicon removal by the produced complex coagulant.

Pollutants	q_m (mg/mg)	K_L (L/mg)	R_L	Comment (R_L)
Al	15.58	-1 x 10^{-4}	1.00	> 1
Fe	0.98	-0.05	1.09	> 1
Mn	3.24	-0.41	-0.22	< 0
Ca	0.73	-40.95	-8 x 10^{-4}	< 0
Mg	4.18	-0.77	-0.05	< 0
Si	0.06	-143.71	-0.01	< 0
Zn	0.47	-0.39	1.57	> 1
Ni	3 x 10^{-3}	-42958.61	-6E-05	< 0

The adsorption capacity, q_m, which represents a measure of the maximum adsorption capacity corresponding to complete monolayer coverage showed that the complex coagulant had a mass capacity for Al (15.58 mg/mg) greater than Mg (4.18 mg/mg), Mn (3.24 mg/mg), Fe (0.98 mg/mg), Ca (0.73 mg/mg), Zn (0.47 mg/mg), Si (0.06 mg/mg), and Ni (3 x 10^{-3} mg/mg). A literature review on sorption using coagulants shows that there is limited or no information in the literature based on the removal of Al, Fe, Mn, Mg, Ca, Si, Zn, and Ni adsorption. According to Jnr and Spiff, 2005, fluted pumpkin waste biomass had a capacity of 1.40 x 10^{-3} mg/mg for Al. This value is considerably inferior to the capacity of hydroxide precipitates (coagulant) (15.58 mg/mg) towards Al. The adsorption coefficient, K_L, that is associated to the apparent energy of adsorption were negative values for Fe (-0.05 L/mg), Zn (-0.39 L/mg), Mn (-0.40 L/mg), Mg (-0.77 L/mg), Ca (-40.95 L/mg), Si (-143.71 L/mg), and Ni (-42958.61 L/mg). These negative values of K_L indicate that the adsorption mechanisms of Al, Fe, Mn, Ca, Mg, Si, Zn, and Ni were not based on monolayer formation with a homogeneous surface. The R_L values in general indicate that the adsorption in this case is unfavourable.

5.8.2 Freundlich model

The Freundlich isotherm model is based on surface heterogeneity describing the adsorption of toxic elements particles adsorbed in multilayer formation. The Freundlich isotherm model was used in order to estimate the adsorption intensity of the sorbate onto the surface of the sorbent. The Freundlich model equation is expressed as follows (Hussain et al., 2013):

$$q_e = K_f C_e^{1/n} \tag{5.13}$$

The Equation 5.13 may be linearised by taking logarithms:

$$\log q_e = \log\left(K_f C_e^{1/n}\right) \tag{5.14}$$

Equation (5.14) can be writen using logarithm properties as follows

$$\log q_e = \log K_f + \log C_e^{1/n} \tag{5.15}$$

The linear form of Freundlich equation can be expressed as follows:

$$\log q_e = \log K_f + \frac{1}{n}\log C_e \tag{5.16}$$

Where K_f represents the adsorption capacity (L/mg) and *n* (dimensionless) is the intensity. K_f is a constant used as relative measure for adsorption efficiency. The degree of the *n* gives an indication of the favorability (strength) of adsorption. Values of *n* greater than 1 show the favorability of adsorption (Daneshvar et al., 2002). The graph of $\log q_e$ plotted against $\log C_e$ will be a straight line from which the value of slope equal to 1/n and the value of intercept equal to $\log K_f$ can be obtained. The linear Freundlich isotherm equation was used to plot logarithmically the experimental data from the batch adsorption study of metals and Si onto hydroxide precipitates (Figure 5.25). The Freundlich isotherm constants for metals and Si onto the adsorbent are given in Table 5.7.

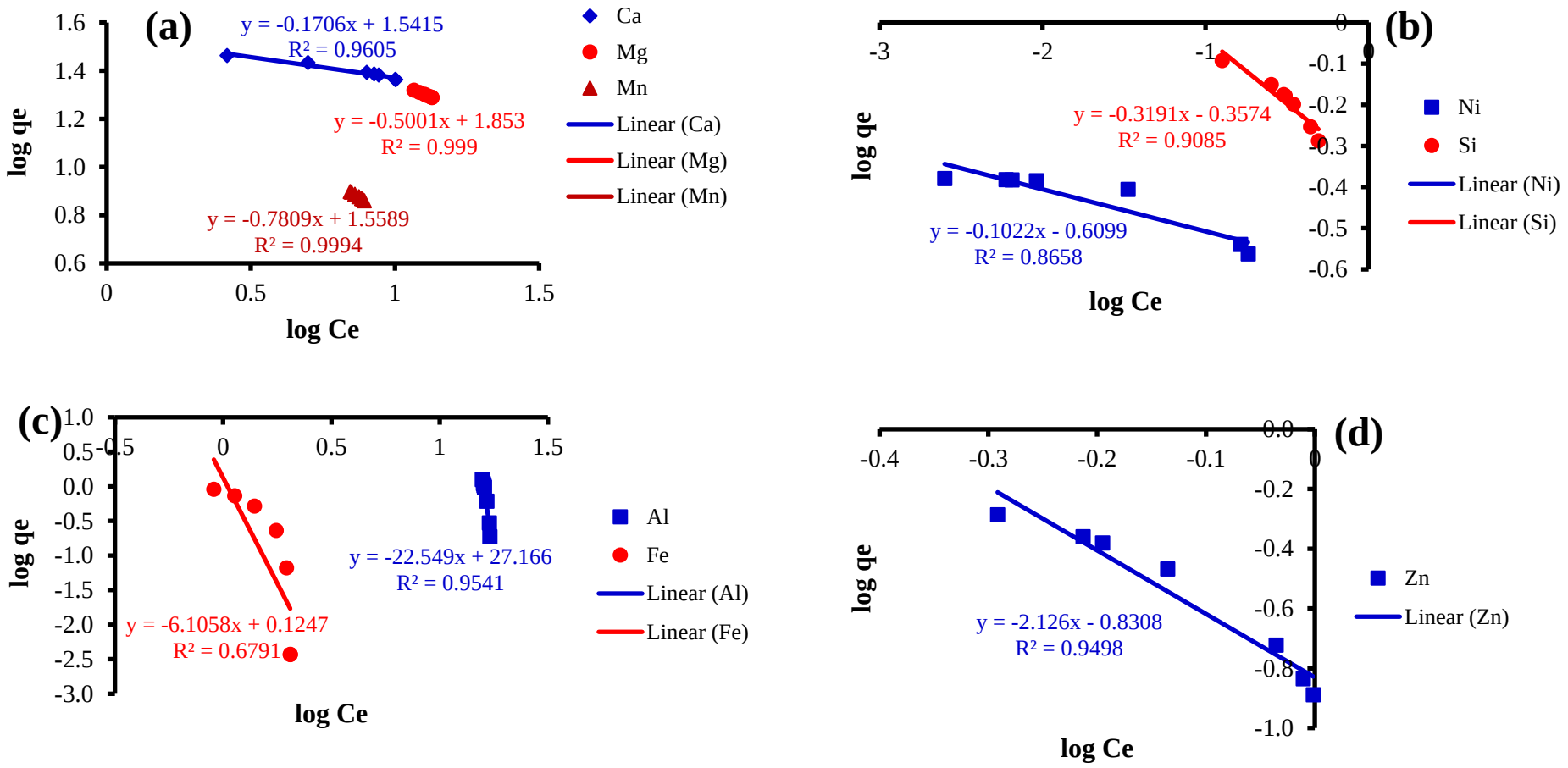

Figure 5.25: Freundlich equilibrium isotherms model for the sorption of (a) Ca, Mg, Mn, (b) Ni, Si, (c) Al, Fe, and (d) Zn on hydroxide precipitates (pH: 7; coagulant dosage:20 mg/L; flash mixing time: 5 minutes; coagulation time (slow mixing time): 1–50 minutes).

Table 5.7: Freundlich isotherm parameters.

Pollutants	*n*	K_f (L/mg)
Al	-0.04	1.47 x 10^{27}
Fe	-0.16	1.33
Mn	-1.28	36.22
Ca	-5.86	34.79
Mg	-1.99	71.29
Si	-3.13	0.44
Zn	-0.47	0.15
Ni	-9.78	0.25

The adsorption capacity, K_f, of the adsorbent was calculated from linear regression equation of the isotherm. The K_f value of Al (1.47 x 10^{27}) is greater than those of Mg (71.29), Mn (36.22), Ca (34.79), Fe (1.33), Si (0.44), Ni (0.25), and Zn (0.15), indicating that Al has greater adsorption tendency towards the adsorbent than the other all pollutants. The values of *n* are less than 1 indicating unfavorable adsorption. The experimental data of Freundlich isotherm adsorption parameters have negative slopes, which suggesting that the adsorption behaviour does not follow the assumption made for the Freundlich isotherm approach.

5.8.3 Temkin model

The Temkin model takes into account the effects of the adsorbate and adsorbent species interaction and assumes binding heterogeneity (Bolis et al., 1993). The Temkin isotherm also considers that the heat of adsorption (temperature function) of all the molecules in the layer would decrease linearly rather than logarithmically with coverage due to adsorbate–adsorbent interactions (Aljeboree et al., 2017). The Temkin isotherm model was used to estimate the adsorption potentials of the adsorbent for adsorbates. The Temkin isotherm equation is described as follows (Jnr and Spiff, 2005):

$$q_e = \frac{RT}{b_T} \ln K_T C_e \qquad (5.17)$$

The above equation may be linearized by rearanging the equation (5.17) through equations (5.18) and (5.19)

$$q_e = \frac{RT}{b_T}(\ln K_T + \ln C_e) \quad (5.18)$$

$$q_e = \frac{RT}{b_T}\ln K_T + \left(\frac{RT}{b_T}\right)\ln C_e \quad (5.19)$$

Where, R is the universal gas constant (8.314 J mol^{-1} K^{-1}), T is the absolute temperature (K), K_T (L/mg) is the Temkin constant representing the adsorbent–adsorbates interactions and b_T (kJ/mol) is another constant related to the adsorption heat. The isotherm constants, K_T and b_T, can be determined from a plot of q_e against $\ln C_e$. The Temkin isotherm plot for the metals and silicon are presented in Figure 5.26 and the isotherm parameters are presentated in Table 5.8.

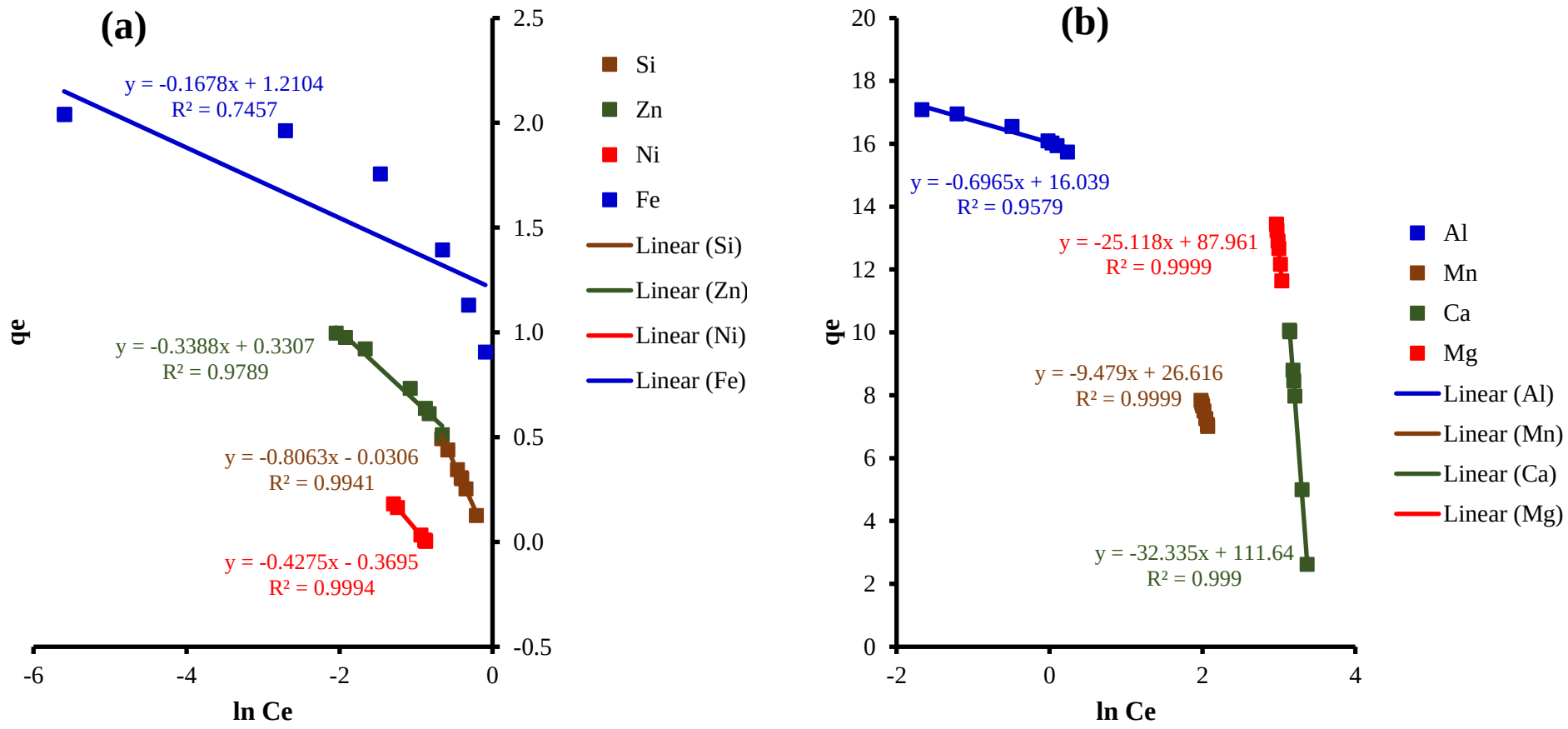

Figure 5.26: Temkin equilibrium isoterm model for the adsorption of (a) Si, Zn, Ni, Fe, and (b) Al, Mn, Ca, Mg onto hydroxide precipitates (pH: 7; coagulant dosage:20 mg/L; flash mixing time: 5 minutes; coagulation time (slow mixing time): 1–50 minutes).

Table 5.8: Temkin isotherm parameters.

Pollutants	b_T (J/mol)	K_T (L/mg)
Al	-3535.09	0.00
Fe	-14673.37	1.76E-275
Mn	-259.75	1.12E-107
Ca	-76.15	3.10E-132
Mg	-98.02	4.10E-134
Si	-3053.69	27.90
Zn	-7284.59	5.41E-38
Ni	-5759.51	8.36E+32

The ionic radius of the toxic elements trend is as follows:
Ca (0.231 nm) > Mn (0.205 nm) > Ni (0.163 nm) > Mg (0.160 nm) > Zn (0.139 nm) > Al (0.130 nm) > Fe (0.126 nm) > Si (0.118 nm).

The trend in Temkin adsorption potential, K_T, was inversely proportional to the ionic radius; exceptions were observed with Ni, Mn and Fe. The metal ionic potential affects the interaction between adsorbate and adsorbent. Higher atomic radius showed smaller potential as confirmed by the investigation of Jnr and Spiff (2005). The Temkin constant b_T indicates the energy involved during the adsorption process. Calcium with the highest ionic radii, showed less energy release, while iron had the highest heat of sorption. These values showed also the relationship between the sorption energy and the ionic size. The heat of sorption should be between 8–16 kJ/mol and a value lower than 8 indicates a weak interaction between sorbate and sorbent (Ho et al., 1995; Jnr and Spiff, 2005). As seen in Table 5.8, the adsorption process was exothermic. Aljeboree et al. (2017) in their investigation also confirmed that the adsorption process was exothermic. Further investigation should be carried out in order to understand the miss behaviour of some elements.

5.8.4 BET model

The BET model is a perfection of the Langmuir model based on the principle that adsorbate can be adsorbed onto the surface of the adsorbent forming more than one layer or multilayer

formation in a random distribution of adsorbed particles and assumes that a Langmuir equation applies to each layer (de Rome and Gadd, 1987; Hussain et al., 2013). A further assumption is that adsorption energy and condensation energy are responsible for the first monolayer and for the adsorption of consecutive layers, respectively. The BET equation can be expressed as follows (Hussain et al., 2013; Brunauer et al., 1938):

$$q_e = \frac{AC_e x_m}{(C_s - C_e)\left[1+(A-1)\frac{C_e}{C_s}\right]} \tag{5.20}$$

Equation 5.20 can be rearranged to facilitate its use to experimental data, giving the linear form (Equation 5.23) through the following steps given in (5.21) and (5.22)

$$q_e \left[1 + (A-1)\frac{C_e}{C_s}\right] = \frac{AC_e x_m}{(C_s - C_e)} \tag{5.21}$$

$$1 + (A-1)\frac{C_e}{C_s} = Ax_m \frac{C_e}{q_e(C_s - C_e)} \tag{5.22}$$

$$\frac{C_e}{(C_s - C_e)q_e} = \frac{A-1}{Ax_m}\left(\frac{C_e}{C_s}\right) + \frac{1}{A(x_m)} \tag{5.23}$$

Where C_e represents the final concentration of adsorbate in solution at equilibrium (mg/L); C_s is the initial or saturation concentration of adsorbate in solution (mg/L); q_e is the amount (mg/L) of adsorbate adsorbed per mg/L of complex coagulant (mg/mg); x_m is the amount of adsorbate adsorbed to form a complete monolayer (mg/mg); and *A* is a constant to describe the energy of interaction between the adsorbate (metal and silicon) and coagulant (solid precipitate of metal and silicon hydroxides) surface. The BET isotherm plots of $\frac{C_e}{q_e(C_s - C_e)}$ against $\frac{C_e}{C_s}$ for the metals and silicon are presented in Figure 5.27. The isotherm parameters (x_m and *A*) were determined from these plots and are presented in Table 5.9.

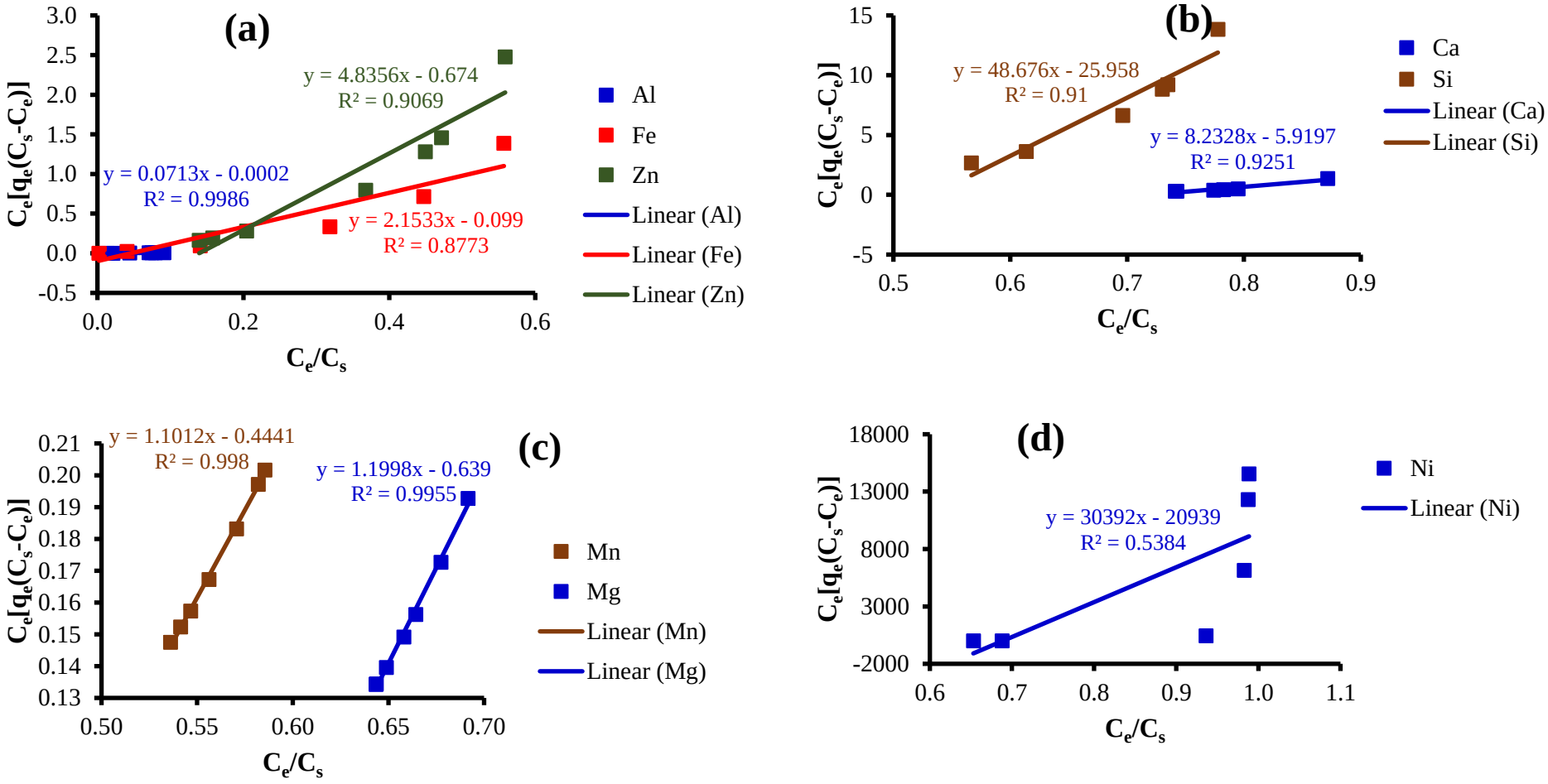

Figure 5.27: BET equilibrium isoterm model for the adsorption of (a) Al, Fe, Zn, (b) Ca, Si, and (c) Mn, Mg, Ni onto hydroxide precipitates (pH: 7; coagulant dosage:20 mg/L; flash mixing time: 5 minutes; coagulation time (slow mixing time): 1–50 minutes).

Table 5.9: BET isotherm parameters.

Pollutants	A	x_m (mg/mg)
Al	-355.5	5.63 x10^{-7}
Fe	-20.75	47 x10^{-4}
Mn	-1.48	0.3
Ca	-0.39	15.15
Mg	-0.88	0.73
Si	-0.88	29.66
Zn	-6.17	0.11
Ni	2.45	8541.46

Table 5.9 shows that Ni (X_m = 8541.46 mg/mg) required more amount for complete monolayer coverage compare to others, and aluminium (X_m = 5.63 x10^{-7}mg/mg) a smaller amount. The heats of adsorption in general have a negative value, which indicates the exothermic behaviour of the adsorption process as confirmed by Aljeboree et al. (2017). Aluminium showed a greater energy released with the smaller amount required for complete monolayer coverage. There is no strong observed relationship between the adsorption energy and monolayer coverage as per the experimental values of A and x_m. This could be due to the competition in the interaction between adsorbent–adsorbate and between adsorbates and adsorption environment.

5.8.5 Coefficients of determination

The regression coefficients of determination, R^2, from the linearization of the four isotherm models are presented in Table 5.10. For Al, the R^2 values of the Langmuir, BET, Temkin, and Freundlich models were highest, $R^2 > 0.90$. Furthermore, for Al, the values of R^2 of the Langmuir, BET, Temkin, and Freundlich models were 0.99, 0.99, 0.96, and 0.95, respectively. The higher coefficient of determination values shows that for aluminium, the best fitted model among the four investigated could be the Langmuir adsorption model. But from the previous discussion based on the Langmuir adsorption parameters, the adsorption behaviour was not based on the monolayer theory assumption made by Langmuir. And also, the adsorption in this case was unfavourable. This indicates that an R-squared value, which

provides the accuracy of the variability of the response data around the mean, is not the only factor that can confirm the adsorption behaviour or model of aluminium.

For Fe, the R^2 value of the Langmuir model was 0.96 which was highest compared with the R^2 values of the BET (0.88), Temkin (0.75), and Freundlich (0.68) models. This shows that the good fit was obtained with the Langmuir adsorption model due to the highest coefficient of determination values. Thus, the adsorption of Fe on the surface of hydroxide precipitates could be assumed to be monolayer formation based on R-squared value. As per the above discussion on the aluminium behaviour, Langmuir is not the best isotherm model for Fe and R-squared value cannot be used in this case.

For Mn, Mg, and Zn, the R^2 values of the BET, Langmuir, Freundlich, and Temkin models were all >0.90 which could indicate that the four investigated isotherm models fit the adsorption experimental data of Mn, Mg, and Zn.

For Ni, the R^2 value of the Temkin model (0.99) was higher than those of the Freundlich (0.87), BET (0.54), and Langmuir (0.69) models, implying that the Temkin isotherm model was the best fitting model for the adsorption of Ni. This will be discussed later. For Si, the R^2 values of the Temkin, BET and Freundlich models were higher, $R^2 > 0.90$, than that of the Langmuir model ($R^2 < 0.90$). In addition, for Si, the obtained values of R^2 of the Temkin, BET and Freundlich isotherm models were 0.99, 0.91, and 0.91, respectively, which were higher compared to the R^2 value of the Langmuir model (0.82). Similarly, the Temkin, Freundlich, and BET adsorption isotherm models well describe the adsorption of Ca ($R^2 >$ 0.90) based on R-squared value. The values of R^2 indicate the following order to fit the isotherms: Temkin model (0.99) > Freundlich model (0.96) > BET model (0.93) > Langmuir (0.89) for Ca.

In conclusion, the adsorption isotherm model should consider the isotherm parameters (based on the isotherm assumptions model) and the R-squared value (which provides an indication on the fitting of the model). The R-squared values for Temkin and BET were in the acceptable range. Both indicate that the adsorption energy was less than zero (exothermic behaviour), and seem to be the adsorption models for this investigation in general. The BET parameters could not provide, from the experimental data, a relationship between adsorption energy and monolayer coverage. As known, BET is an extension of Langmuir's monolayer

theory to multi-layer adsorption (Cerofolini et al., 1999). Temkin's theory also supports this case by describing the induced heterogeneity among the adsorbed particles (Bolis et al., 1993). Temkin model was able to confirm in general, the relationship between the adsorption model and the ionic size of the species involved in the process.

Table 5.10: Linear isotherm coefficients of determination (R^2).

Impurities	Linear isotherm			
	Langmuir	**Freundlich**	**Temkin**	**BET**
Al	0.9996	0.9541	0.9579	0.9986
Fe	0.9582	0.6791	0.7457	0.8773
Mn	0.9993	0.9994	0.9999	0.998
Ca	0.8936	0.9605	0.999	0.9251
Mg	0.9983	0.9990	0.9999	0.9955
Si	0.8188	0.9085	0.9941	0.9100
Zn	0.9697	0.9498	0.9789	0.9069
Ni	0.6890	0.8658	0.9994	0.5384

5.9 Coagulation kinetics of the synthesized composite coagulant

To design and scale up the coagulation process, investigation of kinetic behaviour or models is essential since they describe the rate of impurity removal by the coagulant which is associated with the coagulation time. The analysis of the kinetic behaviour can provide the understanding of mechanism and the rate determining step of the process. The experimental data were used to fit the exiting kinetic models in order to determine the suitable model for the coagulation process and diffusion behaviour of elements involved in the process. Two types of kinetic models were investigated, namely the adsorption reaction kinetic models and the kinetic diffusion models. Four reaction kinetic models, namely, the pseudo-first-order, the pseudo-second-order, the elovich model, and the second-order model equations were used to investigate the suitability of these reaction kinetic models to the experimental data. Furthermore, three diffusion kinetic models namely Weber-Morris (intra-particle diffusion), Boyd's, and Bangham's model equations were investigated in order to explore the diffusion in the adsorption process.

The kinetic studies for various metals and silicon were carried out by using the proposed coagulation optimum conditions found in previous section (complex coagulant dosage: 20 mg/L, pH: 7). The treated wastewater samples were withdrawn at pre-set time intervals ranging from 1 to 50 minutes, and the concentrations of the impurities were in the same way determined. Plots of residual metals and silicon concentration against time are previously presented in Figure 5.16. The amount of impurity removed at time *t*, q_t (mg/mg), was calculated using Equation 5.24 (Hussain et al., 2013):

$$q_t = \frac{(C_0 - C_t) \times V}{D} \quad (5.24)$$

where C_0 (mg/L) represents the initial concentration and C_t (mg/L) represents the concentration of the pollutant at time *t* in the wastewater, *V* (mL) is the volume of the wastewater, and *D* (mg/L) is the coagulant dosage (as Fe + Al + Si + Mg + Ca). The amount of impurity removed at saturation (or equilibrium), q_e (mg/mg), were determined by Equation 5.24 with q_e= maximum value of q_t for each pollutant.

5.9.1 Adsorption reaction models

Pseudo-first-order rate equation

The most primitive first-order rate equation relating to the adsorption rate based on the adsorption was established by Lagergren (1898) and was used to describe the kinetic process of liquid-solid phase adsorption of oxalic acid and malonic acid on charcoal. It can be expressed as

$$\frac{dq_t}{dt} = k_\rho (q_e - q_t) \quad (5.25)$$

where q_t and q_e (mg/mg) represent the adsorption capacities at time *t* (minute) and equilibrium, respectively. k_ρ (min^{-1}) represents the pseudo-first-order rate constant for the kinetic model. Integrating Equation 5.25 with the boundary conditions of $q_t = 0$ at $t = 0$ and $q_t = q_t$ at $t = t$, yields (Ho, 2004)

$$\ln\left(\frac{q_e}{q_e - q_t}\right) = k_\rho t \quad (5.26)$$

which can be rearranged to:

$$\ln(q_e - q_t) = \ln q_e - k_\rho t \quad (5.27)$$

Lagergren's first order equation has been called pseudo-first-order in order to differentiate the kinetic equations based on the adsorption capacity from the concentration of the solution (Ho and McKay, 1998a). Recently, it has been successfully applied to describe the adsorption of impurities from aqueous solutions in various fields, such as the adsorption of nickel and zinc from aqueous solutions by ion exchange resins and the removal of textile dyes using coconut shell activated carbon (Alyüz and Veli, 2009; Aljeboree et al., 2017). The rate constant k_ρ and q_e for Al, Fe, Mn, Mg, Ca, Si, Zn, and Ni were calculated by plotting $\ln(q_e - q_t)$ against *t*. Figures 5.28–5.35 show the plots of $\ln(q_e - q_t)$ versus *t* for Al, Fe, Mn, Mg, Ca, Si, Zn, and Ni, respectively, and Table 5.11 shows the kinetic parameters of the pseudo-first-order kinetic model for Al, Fe, Mn, Mg, Ca, Si, Zn, and Ni.

.

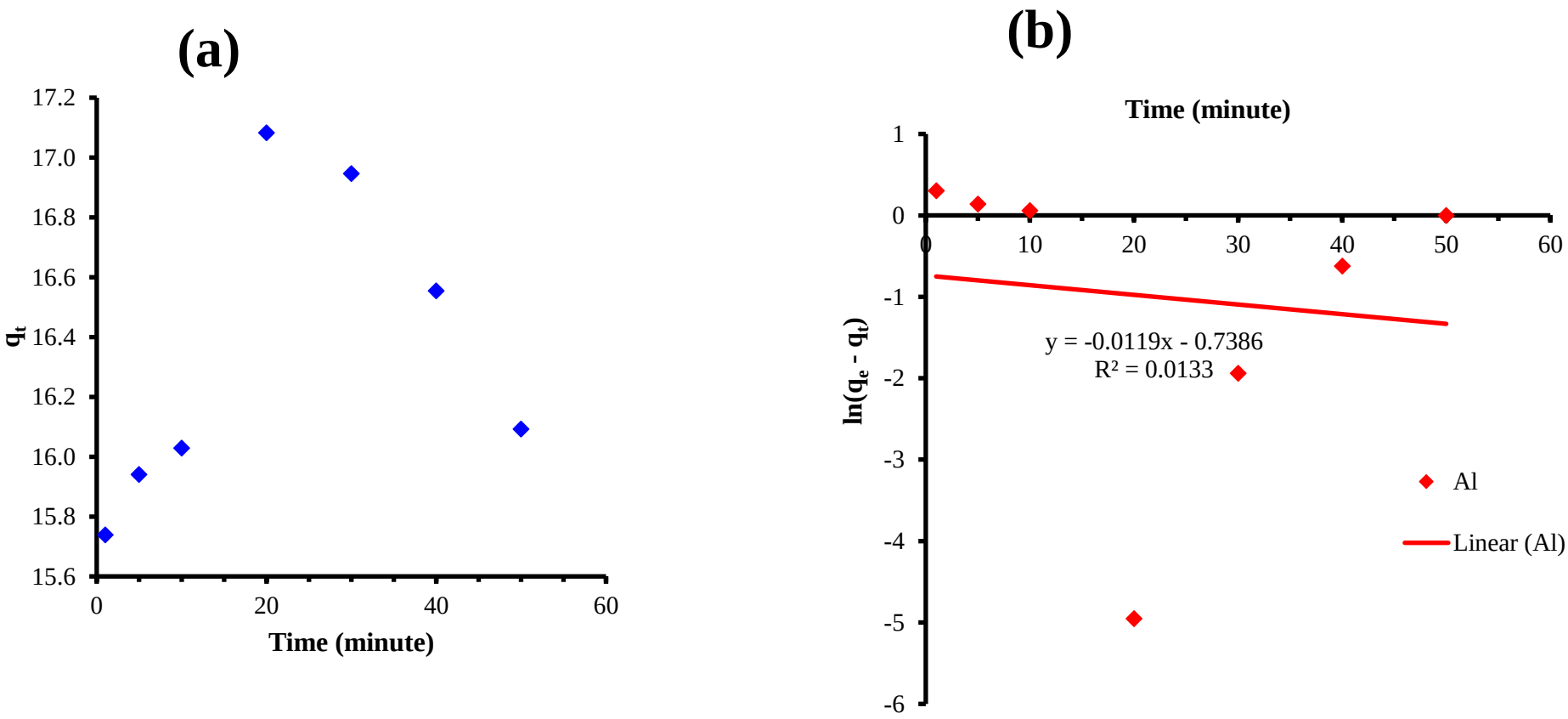

Figure 5.28: (a) Adsorption rate curves of Al and (b) Pseudo-first-order reaction kinetics for the adsorption of Al onto hydroxide precipitate (pH: 7, coagulant dosage 20 mg/L, and RT 23 ±2 ºC).

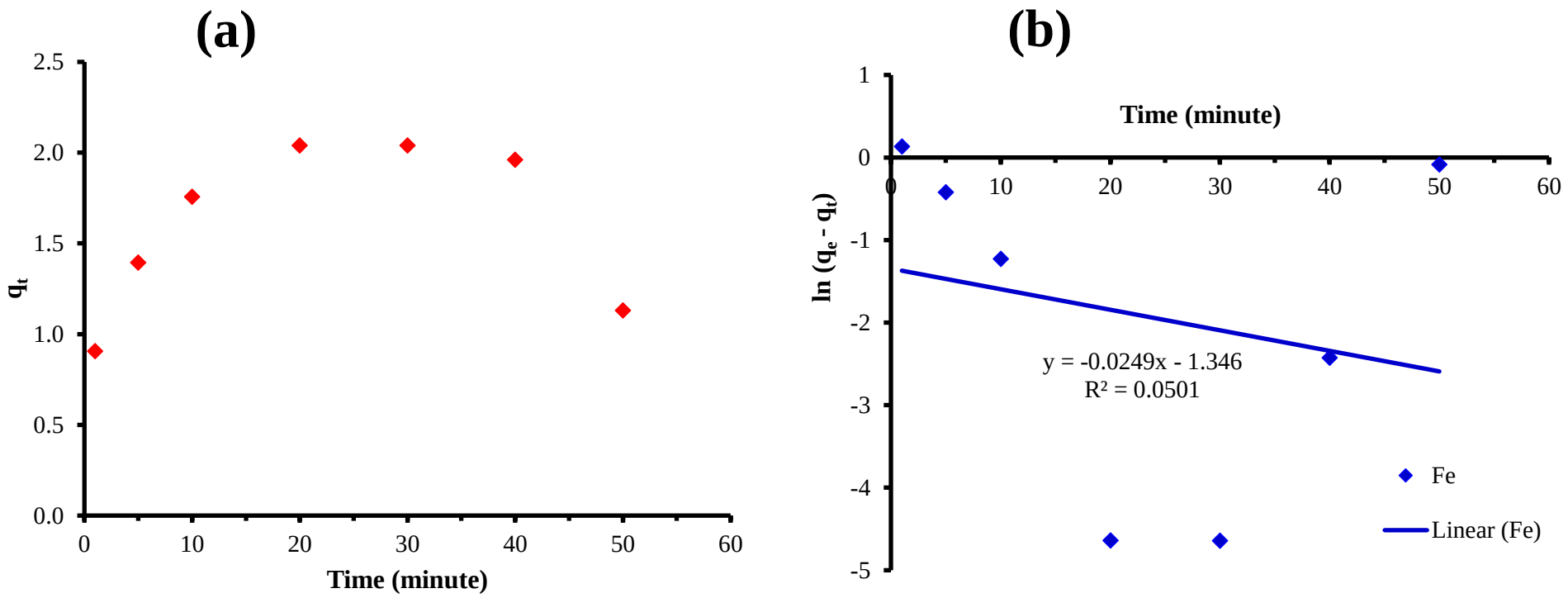

Figure 5.29: (a) Adsorption rate curves of Fe and (b) Pseudo-first-order reaction kinetics for the adsorption of Fe onto hydroxide precipitate (pH: 7, coagulant dosage 20 mg/L, and RT 23 ±2 ºC).

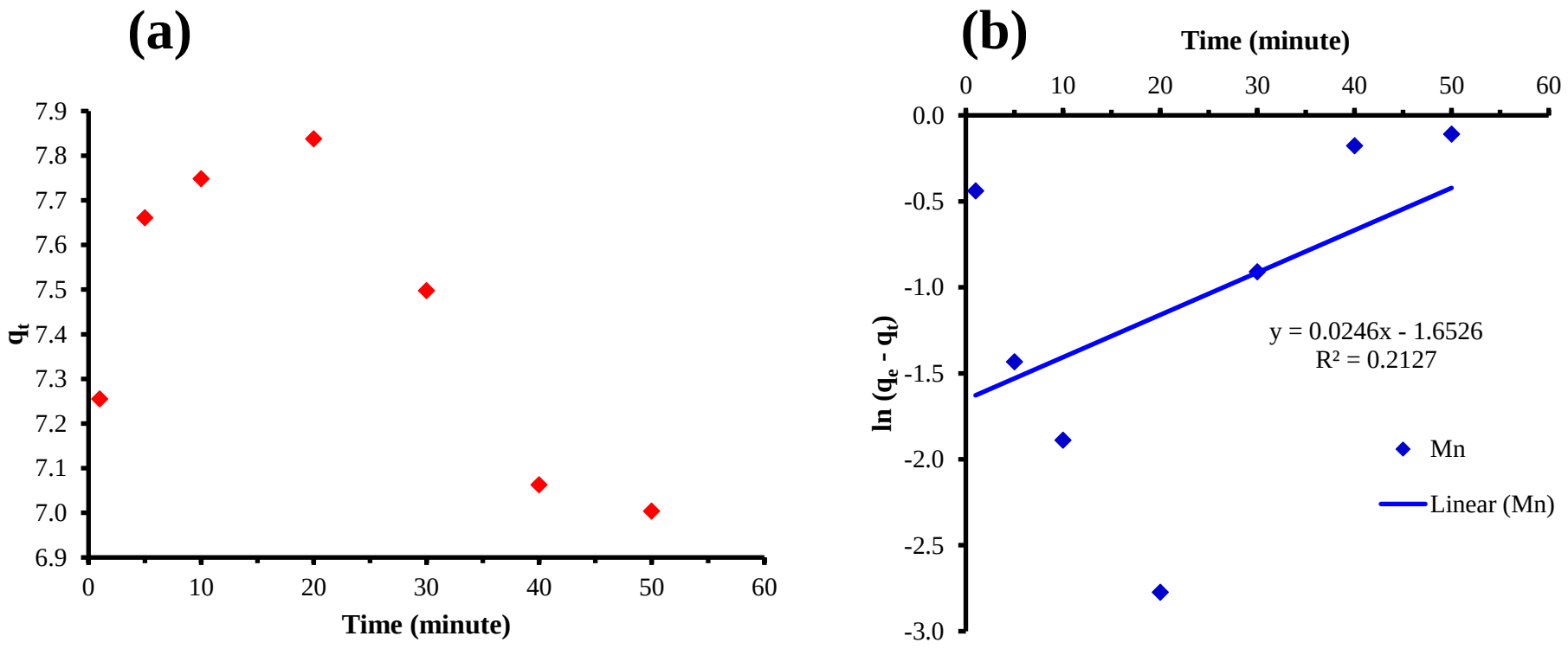

Figure 5.30: (a) Adsorption rate curves of Mn and (b) Pseudo-first-order reaction kinetics for the adsorption of Mn onto hydroxide precipitate (pH: 7, coagulant dosage 20 mg/L, and RT 23 ±2 ºC).

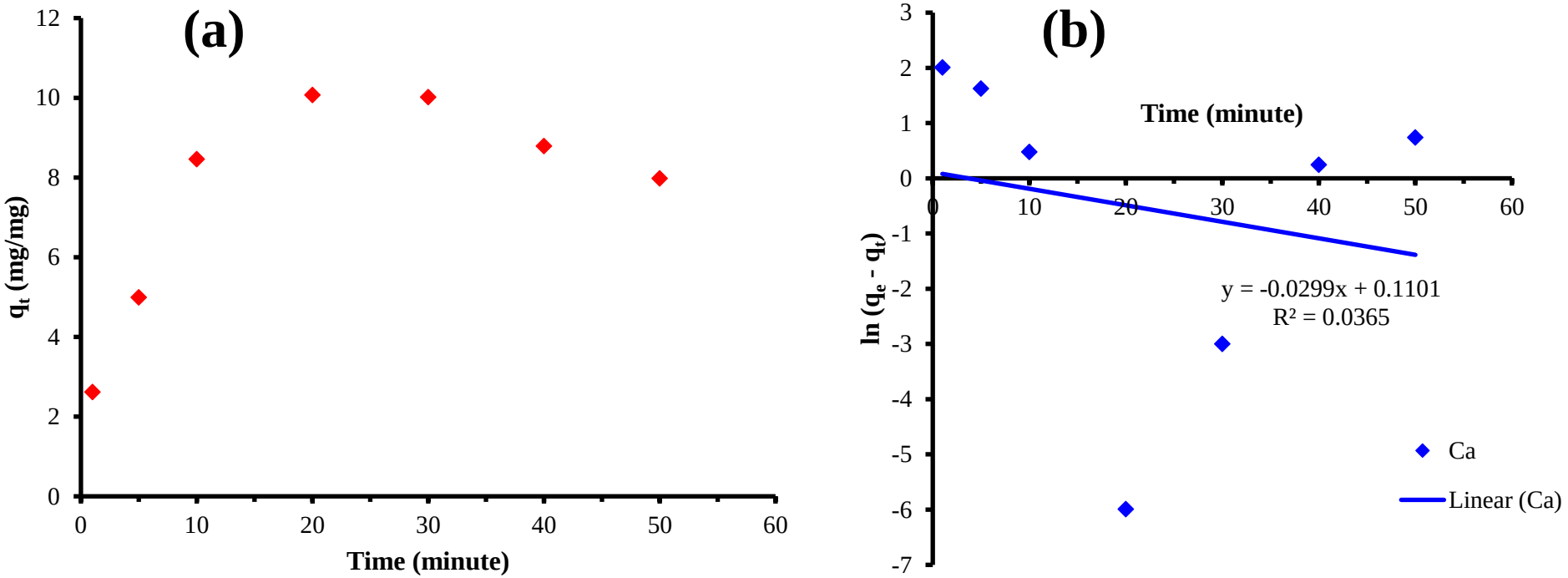

Figure 5.31: (a) Adsorption rate curves of Ca and (b) Pseudo-first-order reaction kinetics for the adsorption of Ca onto hydroxide precipitate (pH: 7, coagulant dosage 20 mg/L, and RT 23 ±2 ^{o}C).

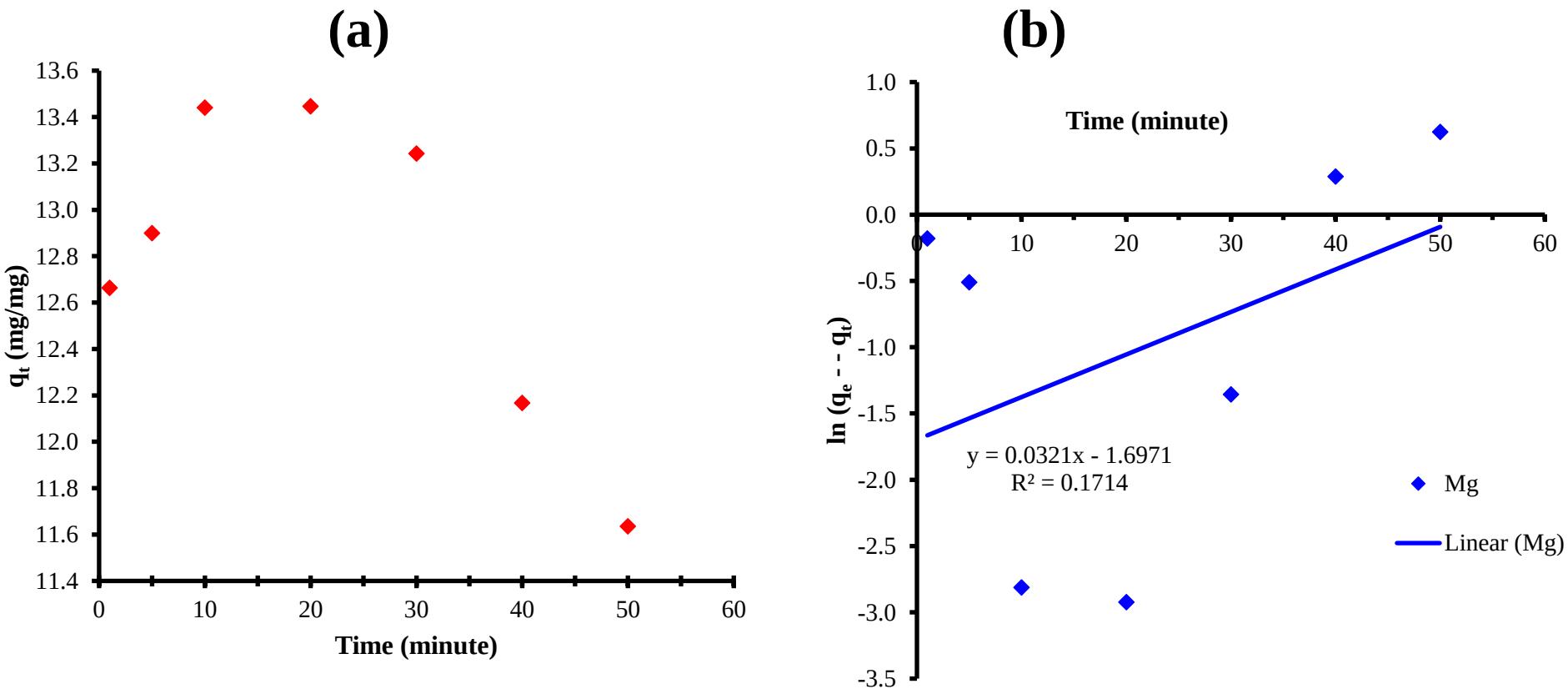

Figure 5.32: (a) Adsorption rate curves of Mg and (b) Pseudo-first-order reaction kinetics for the adsorption of Mg onto hydroxide precipitate (pH: 7, coagulant dosage 20 mg/L, and RT 23 ±2 ºC).

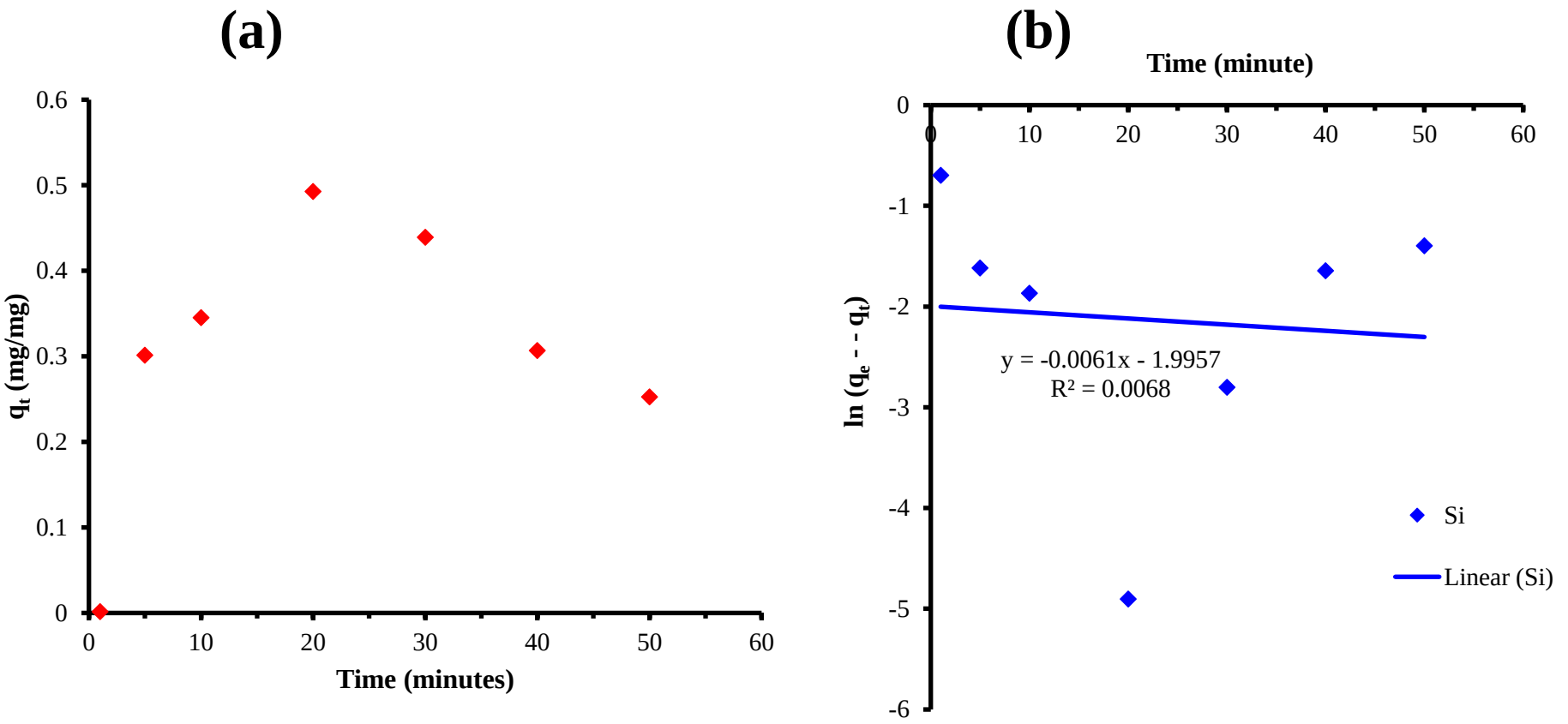

Figure 5.33: (a) Adsorption rate curves of Si and (b) Pseudo-first-order reaction kinetics for the adsorption of Si onto hydroxide precipitate (pH: 7, coagulant dosage 20 mg/L, and RT 23 ±2 ^{o}C).

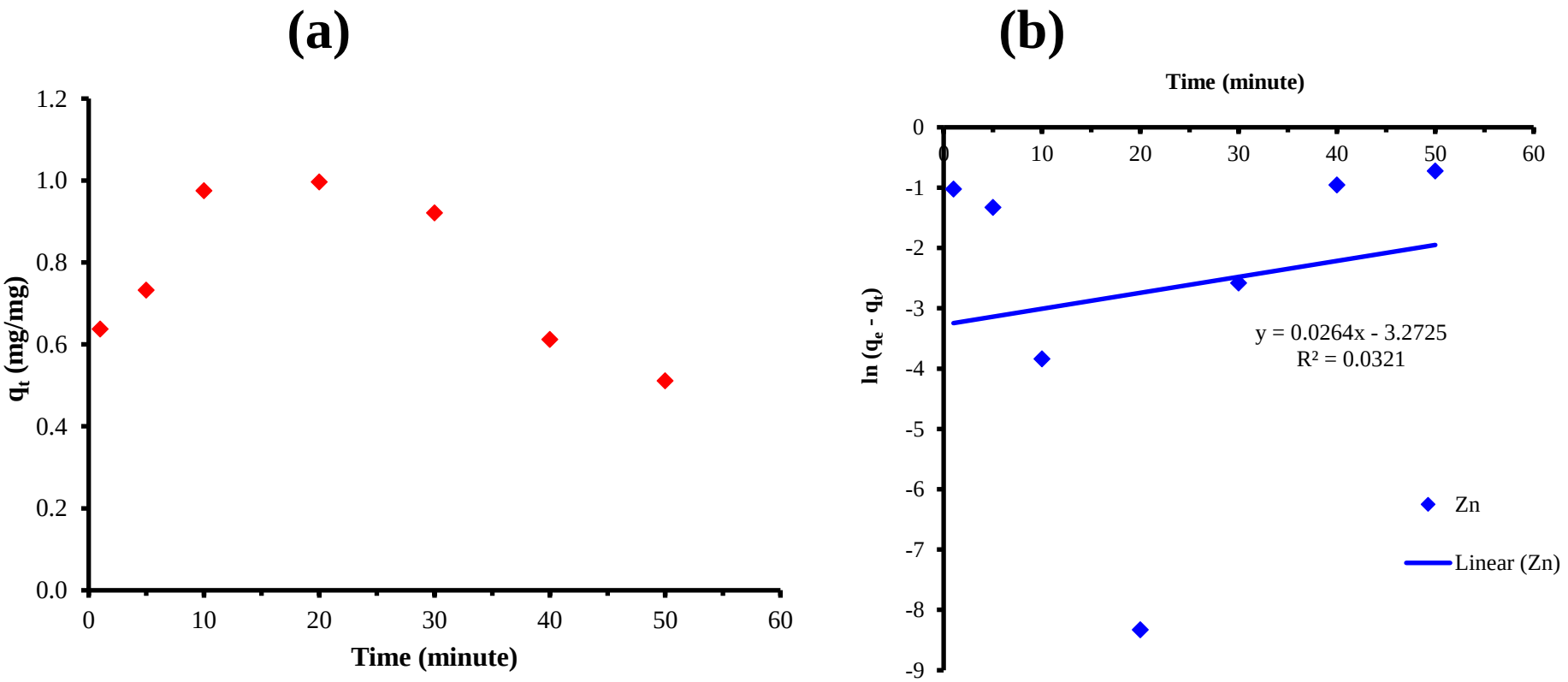

Figure 5.34: (a) Adsorption rate curves of Zn and (b) Pseudo-first-order reaction kinetics for the adsorption of Zn onto hydroxide precipitate (pH: 7, coagulant dosage 20 mg/L, and RT 23 ±2 ºC).

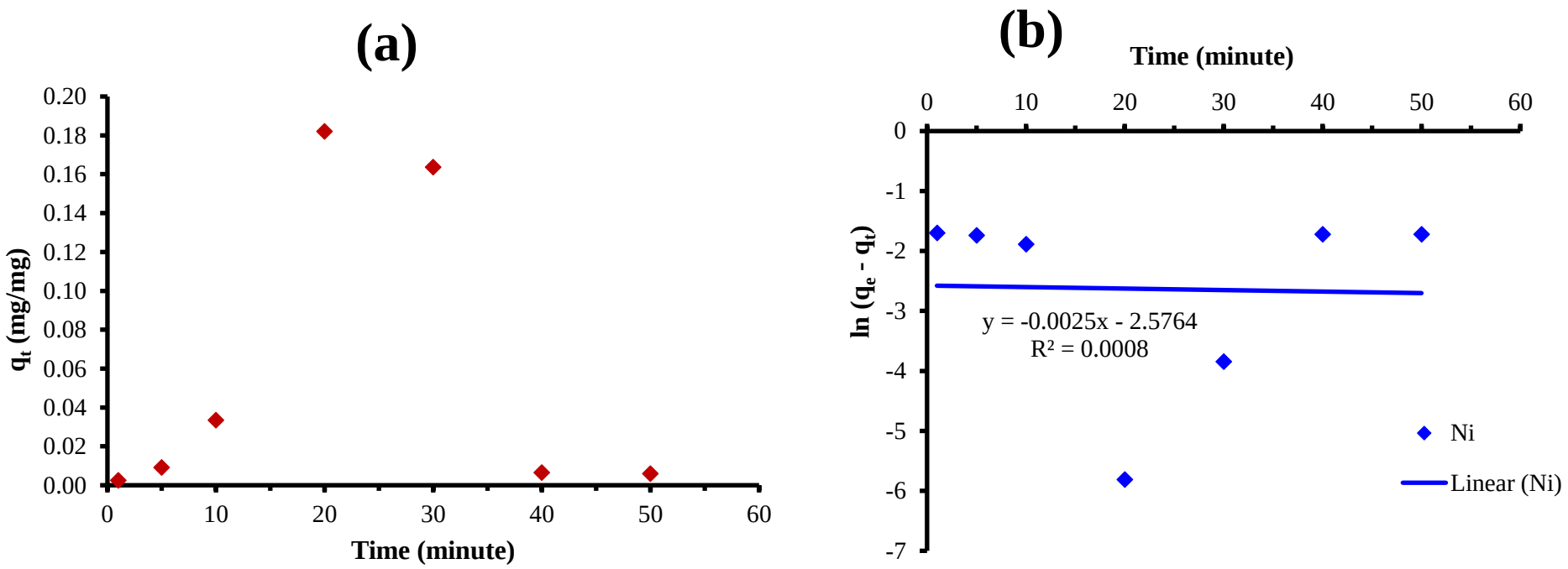

Figure 5.35: (a) Adsorption rate curves of Ni and (b) Pseudo-first-order reaction kinetics for the adsorption of Ni onto hydroxide precipitate (pH: 7, coagulant dosage 20 mg/L, and RT 23 ±2 ºC).

The slopes and intercepts of the curves in Figures 5.28-5.35 were used for determining the pseudo-first-order constants, k_ρ, and the saturation (equilibrium) capacity, q_e. The data presented in Table 5.11 show that the values of the rate constant (k_ρ) are negative for Al (-0.0119), Fe (-0.0249), Ca (-0.0299), Si (-0.0061), and Ni (-0.0025). However, k_ρ values are positive for Mn (0.0246), Mg (0.0321), and Zn (0.0264). Furthermore, it can be seen from Table 5.11 that the values of the maximum sorption capacity, q_e, calculated by the Lagergren pseudo-first-order are not in agreement with q_e experimental for all investigated adsorption processes. This could suggest that the sorption of Al, Fe, Mn, Mg, Ca, Si, Zn, and Ni onto hydroxide precipitate (coagulant) is not a pseudo-first-order reaction.

Table 5.11: kinetic parameters of the pseudo-first-order kinetic model for Al, Fe, Mn, Mg, Ca, Si, Zn, and Ni.

Pollutants	**q_e, experimental (mg/mg)**	**q_e calculated (mg/mg)**	**k_ρ (min^{-1})**
Al	17.090	0.478	-0.0119
Fe	2.050	0.260	-0.0249
Mn	7.900	0.192	0.0246
Ca	10.070	1.116	-0.0299
Mg	13.500	0.183	0.0321
Si	0.500	0.136	-0.0061
Zn	0.997	0.038	0.0264
Ni	0.185	0.076	-0.0025

Pseudo-second-order rate equation

Ho and McKay (1998b) described a kinetic process of the adsorption of divalent metal ions onto peat, in which the chemical bonding between divalent metal ions and polar functional groups on peat are responsible for the cation-exchange capacity of the peat. Thus, the reaction between peat and metal can be presented as follows, which may be dominant in the adsorption of M^{n+} (metal) ions on peat (Coleman et al., 1956):

$$SO_4^{2-} + M^{n+} \leftrightarrow M_2(SO_4)_n \quad (5.28)$$

if n = 2

$$SO_4^{2-} + M^{2+} \leftrightarrow MSO_4 \quad (5.29)$$

and $$H_2SO_4 + M^{n+} \leftrightarrow M_2(SO_4)_n + 2H^+ \quad (5.30)$$

where SO_4^{2-} and H_2SO_4 are active sites on the sorbent surface. The main assumptions for the above three equations were that the adsorption may be second order and the rate limiting step may be chemical adsorption involving valence forces by sharing or electrons exchange between the adsorbent and metal ions. Furthermore, the adsorption conforms to the Langmuir equation (Ho and McKay, 2000). The adsorption rate described by Equations 5.28 and 5.30 is function of the amount of metal ions on the surface of the adsorbent at time *t* and that adsorbed at equilibrium. Therefore, the rate expression may be presented as

$$\frac{dP_t}{dt} = k_\rho (P_0 - P_t)^2 \quad (5.31)$$

$$\frac{d[H_2SO_4]_t}{dt} = k_\rho ([H_2SO_4]_0 - [H_2SO_4]_t)^2 \quad (5.32)$$

where P_0 and $(H_2SO_4)_0$ are the amount of equilibrium sites available on the adsorbent, P_t and $(H_2SO_4)_t$ represent the amount of active sites occupied on the adsorbent at time *t*, and k_ρ (mg/(mg·min) is the pseudo-second-order rate constant of adsorption (Ho and McKay, 1998b). The driving force, $(q_e - q_t)$, is proportional to the available fraction of active sites (Ho, 2006). Then, it can be expressed as

$$\frac{dq_t}{dt} = k_\rho (q_e - q_t)^2 \quad (5.33)$$

Eq. (5.33) can be rearranged as follows:

$$\frac{dq_t}{(q_e - q_t)^2} = k_\rho \, dt \quad (5.34)$$

Integrating Eq. (5.34) with the boundary conditions of of $q_t = 0$ at t= 0 and $q_t = q_t$ at t= t, yields

$$\frac{1}{(q_e - q_t)} = \frac{1}{q_e} + k_\rho \, t \quad (5.35)$$

which can be rearranged as follows:

$$q_e - q_t = \frac{q_e}{1 + q_e \, k_\rho \, t} \quad (5.36)$$

$$\frac{q_e - q_t}{q_e} = \frac{1}{1 + q_e\, k_\rho\, t} \tag{5.37}$$

$$\frac{t}{q_t} = \frac{1}{q_e} t + \frac{1}{{q_e}^2\, k_\rho} \tag{5.38}$$

The constants $\frac{1}{q_e}$ and $\frac{1}{{q_e}^2\, k_\rho}$ were determined experimentally by plotting of t/q_t versus *t*.

Similarly, to differentiate the kinetic equations based on the adsorption capacity of the solution concentration, the second-order rate equation of Ho has been called the pseudo-second-order rate equation (Ho, 2006). This equation has been extensively used to describe the adsorption of organic matters, dyes, heavy metal ions, herbicides, oils from aqueous solutions (Hussain et al., 2013; Cheng et al., 2008; Arami et al., 2005; Hui et al., 2005; Yan and Viraraghavan, 2003; Hameed, 2008; Achak et al., 2009). Figures 5.36–5.39 show plots of t/q_t versus *t* for each impurity from which the maximum adsorption capacity, q_e, and the rate constant of the pseudo second order kinetic model, k_ρ, can be determined. The kinetic parameters of the pseudo-second-order kinetic are presented in Table 5.12.

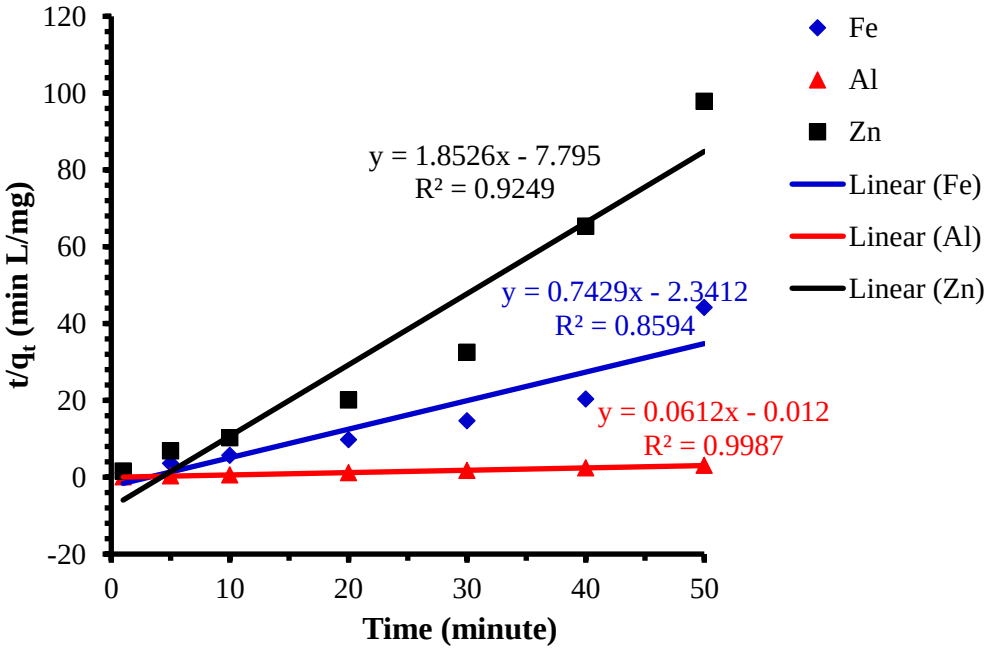

Figure 5.36: Pseudo-second-order reaction kinetics for the adsorption of Fe, Al, and Zn onto hydroxide precipitate (pH: 7, coagulant dosage 20 mg/L, and RT 23 ±2 ^{o}C).

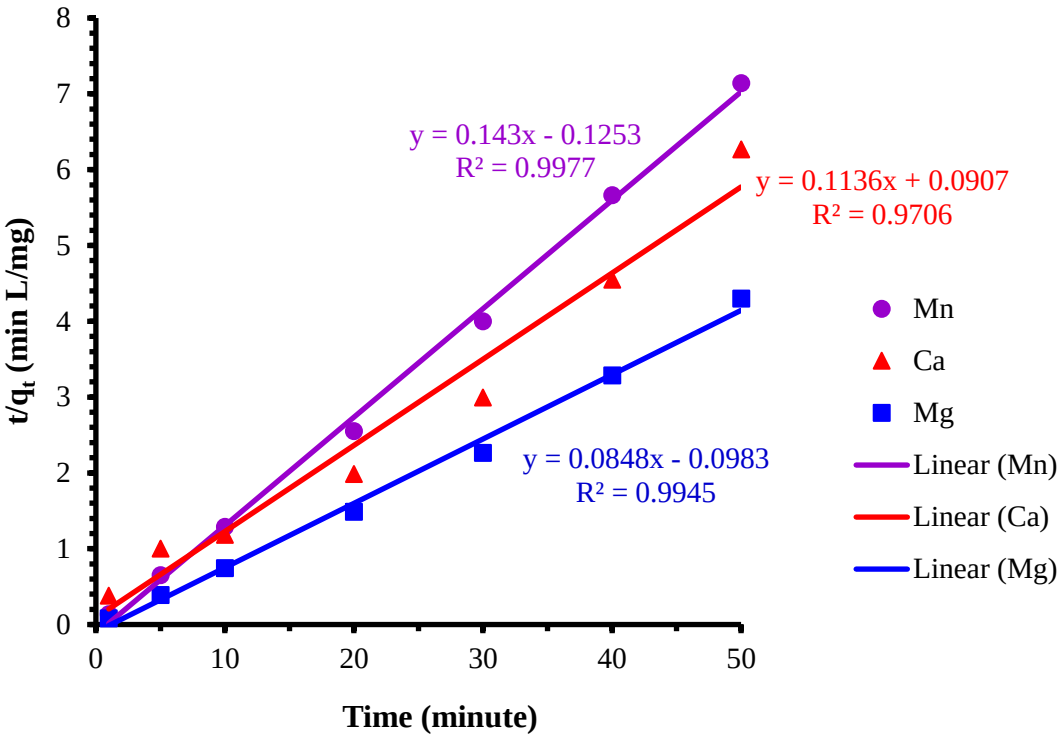

Figure 5.37: Pseudo-second-order reaction kinetics for the adsorption of Mn, Ca, and Mg onto hydroxide precipitate (pH: 7, coagulant dosage 20 mg/L, and RT 23 ±2 ^{o}C).

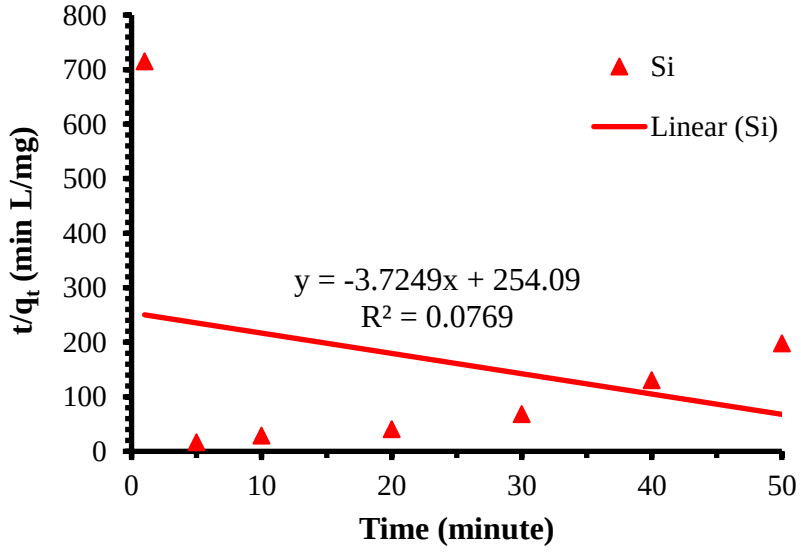

Figure 5.38: Pseudo-second-order reaction kinetics for the adsorption of Si onto hydroxide precipitate (pH: 7, coagulant dosage 20 mg/L, and RT 23 ±2 ^{o}C).

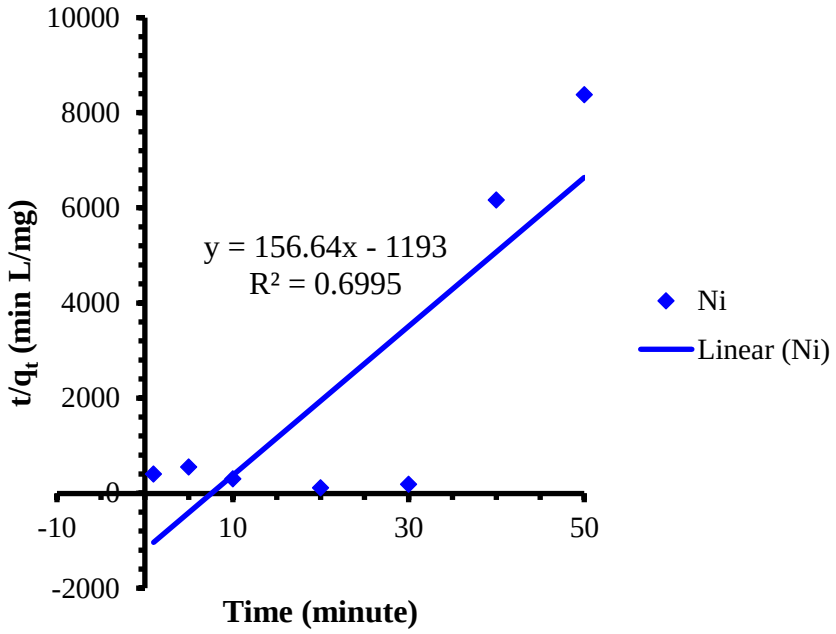

Figure 5.39: Pseudo-second-order reaction kinetics for the adsorption of Ni onto hydroxide precipitate (pH: 7, coagulant dosage 20 mg/L, and RT 23 ±2 ^{o}C).

Table 5.12: kinetic parameters of the pseudo-second-order kinetic model for Al, Fe, Mn, Mg, Ca, Si, Zn, and Ni.

Pollutants	q_e, **experimental (mg/mg)**	q_e, **calculated (mg/mg)**	k_ρ
Al	17.09	16.3399	-0.3121
Fe	2.05	1.3461	-0.2357
Mn	7.90	6.9930	-0.1632
Ca	10.07	8.8028	0.14228
Mg	13.50	11.7925	-0.0732
Si	0.5	-0.2685	0.05461
Zn	0.997	0.5398	-0.4403
Ni	0.185	0.0064	-20.567

As for the pseudo-first-order, negative values of the rate constant were observed for Al (-0.3121), Fe (-0.2357), Mn (-0.1632), Mg (-0.0732), Zn (-0.4403), and Ni (-20.567), while positive values were obtained for Ca (0.14228) and Si (0.05461). But the theoretical q_e values from the pseudo-second-order were more consistent with the experimental q_e values than

those calculated from the pseudo-first-order model. These results suggest that the sorption of Al, Fe, Mn, Mg, Ca, Si, Zn, and Ni onto hydroxide precipitate (coagulant) follows to the pseudo-second-order kinetic model which further indicates that chemical adsorption is the rate-controlling step (Ho and McKay, 2000).

Elovich's equation

Zeldowitsch (1934) presented a kinetic equation of chemisorption which describe the rate of adsorption of carbon monoxide on manganese dioxide that decreases exponentially with an increase in the amount of gas adsorbed (Ho, 2006). This model is called Elovich equation and can be presented as follows (Low, 1960):

$$\frac{dq_t}{dt} = \beta\, e^{-\alpha\, q_t} \tag{5.39}$$

where q_t (mg/mg) is the amount of gas adsorbed at time *t*, β (mg/mg) is the desorption constant, and α (mg/mg min) the initial adsorption rate (Ho and McKay, 1998a). Equation 5.39 can be rearranged to a linear form:

$$q_t = \left(\frac{2.3}{\alpha}\right)\log(t + t_0) - \left(\frac{2.3}{\alpha}\right) log\, t_0 \tag{5.40}$$

With $$t_0 = \frac{1}{\alpha\,\beta} \tag{5.41}$$

The plot of q_t versus $\log(t + t_0)$ should produce a straight line with an appropriate value of t_0. The Elovich equation is used to determine the kinetics of gases chemisorption on heterogeneous solids (Rudzinski and Panczyk, 2000). Assuming $\beta\alpha t \gg 1$ (Chien and Clayton, 1980), Equation 5.40 was integrated using the boundary conditions of $q_t = 0$ at $t = 0$ and $q_t = q_t$ at $t = t$ to give (Ho, 2006):

$$q_t = \alpha \ln t + \alpha \ln(\beta\, \alpha) \tag{5.42}$$

Elovich's equation has been satisfactorily used to describe the adsorption of gases onto solid systems (Rudzinski and Panczyk, 2000). In recent years, it has also been used to describe the adsorption process of contaminants from wastewater, such as dyes adsorption on coconut shell activated carbon (Aljeboree et al., 2017), silver and copper adsorption by vermiculite (Długosz and Banach, 2018), and Fe(III), Co(II), Ni(II), Cu(II), and Zn(II) removal from

sulphate solutions with macroporous resins (Juang and Chen, 1997). Figures 5.40 and 5.41 show the plots of q_t versus $\ln t$ for different impurities. The calculated parameters (α and a) of the Elovich model for Al, Fe, Mn, Mg, Ca, Si, Zn, and Ni are presented in Table 5.13.

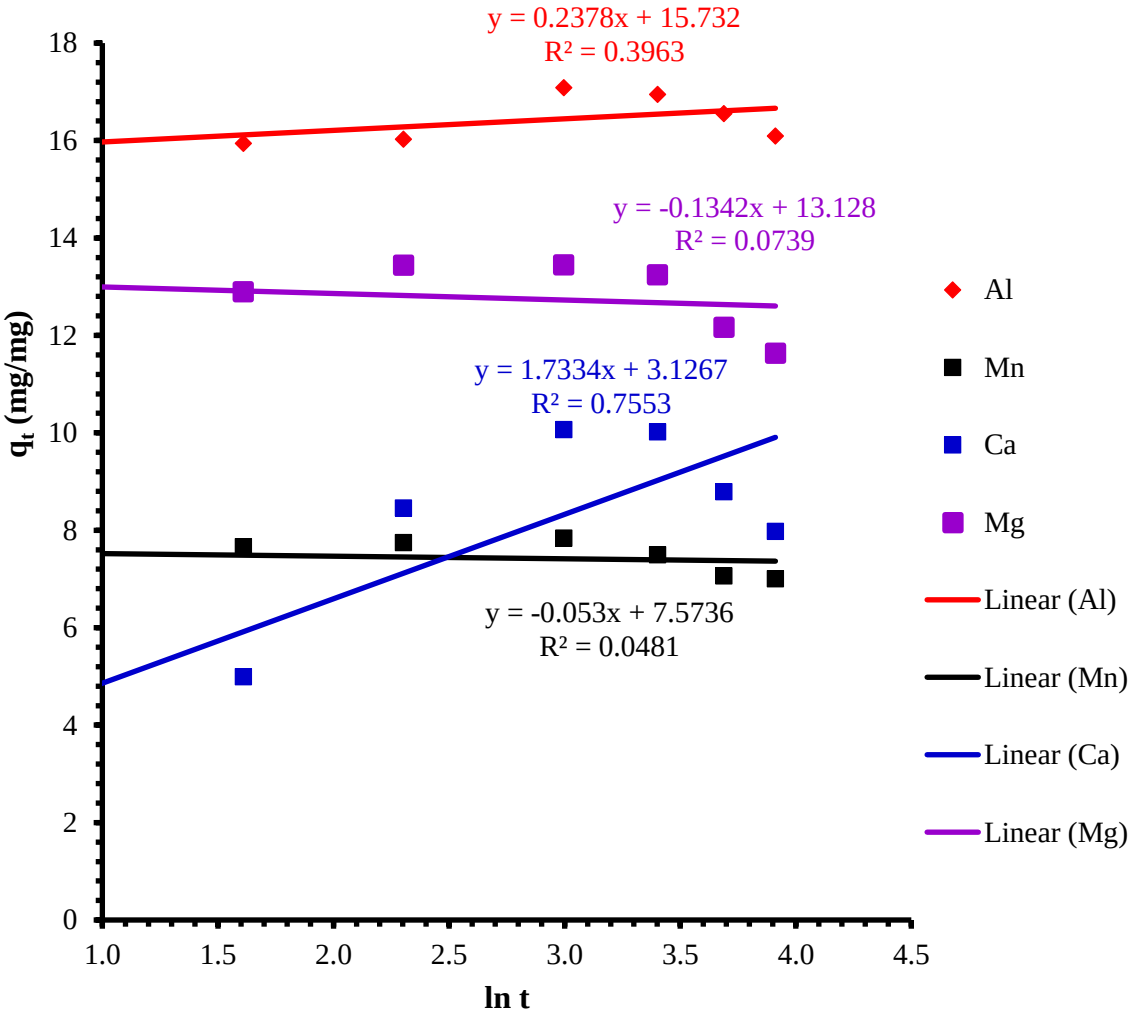

Figure 5.40: Elovich reaction kinetics for the adsorption of Al, Mn, Ca, and Mg onto hydroxide precipitate (pH: 7, coagulant dosage 20 mg/L, and RT 23 ±2 ^{o}C).

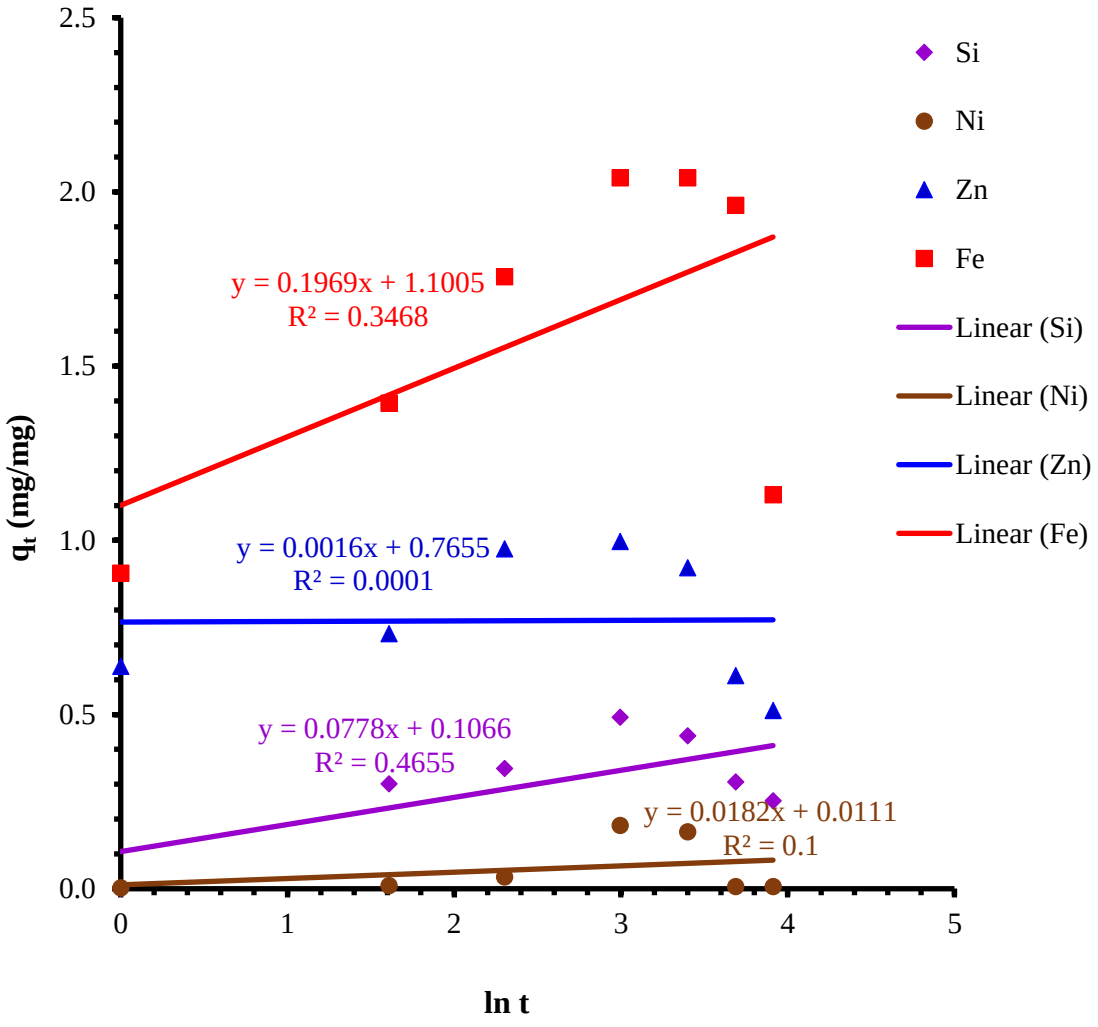

Figure 5.41: Elovich reaction kinetics for the adsorption of Si, Ni, Zn, and Fe onto hydroxide precipitate (pH: 7, coagulant dosage 20 mg/L, and RT 23 ±2 ^{o}C).

Table 5.13: kinetic parameters of the Elovich kinetic model for Al, Fe, Mn, Mg, Ca, Si, Zn, and Ni.

Pollutants	α (mg/mg min)	β (mg/mg)
Al	0.2378	2.26549E+29
Fe	0.1969	1358.573909
Mn	-0.0553	-6.0057E-59
Ca	1.7334	3.5033
Mg	-0.1342	-2.4421E-42
Si	0.0778	50.5920
Zn	0.0016	1.3229E+211
Ni	0.0182	101.1115

The Elovich constants, α, for Al, Fe, Mn, Ca, Mg, Si, Zn, and Ni have values of 0.2378, 0.1969, -0.553, 1.7334, -0.1342, 0.0778, 0.0016, and 0.0182 mg/mg min, respectively. Whereas, the constant β values were obtained to be 2.26549E+29, 1358.573909, -6.0057E-59, 3.50332042, -2.4421E-42, 50.59201697, 1.3229E+211, and 101.1114926 mg/mg for Al, Fe, Mn, Ca, Mg, Si, Zn, and Ni, respectively. Thus, it was observed in Table 5.13 that the value of the rate of chemisorption, α, for Ca (1.7334 mg/mg min) is higher than those of Al (0.2378 mg/mg min), Fe (0.1969 mg/mg min), Si (0.0778 mg/mg min), Ni (0.0182 mg/mg min), Zn (0.0016 mg/mg min), Mn (-0.0553 mg/mg min), and Mg (-0.1342 mg/mg min).

For all the investigated elements, the plotted graphs showed a non - linear behaviour. This confirmed that the experimental data do not fit the Elovich model, even if the assumption made ($\beta\alpha t \gg 1$) for all elements investigated stand. Therefore, the assumption of exponential covering of adsorption sites, which suggests multilayer adsorption, is not in agreement with the experimental data for all the studied impurities.

Second-order rate equation

The typical second-order rate equations in solution systems can be expressed as follows (Ho, 2006):

$$\frac{dC}{dt} = -k_2 C_t^2 \qquad (5.43)$$

By integrating Equation 5.43 with the boundary conditions of $C_t = 0$ at $t = 0$ and $C_t = C_t$ at $t = t$ to give the linear form

$$\frac{1}{C_t} = k_2 t + \frac{1}{C_0} \tag{5.44}$$

where C_0 (mg/L) is the initial concentration of solute, C_t (mg/L) the concentration of solute at time *t*, k_2 (L/mg·min) the rate constant, and *t* the time (min). In previous years, the second-order rate equation has been used to describe the adsorption reactions between soil and soil minerals (Kuo and Lotse, 1972; Griffin and Jurinak, 1974). Lately, the equation was also used to describe the removal of fluoride using acid-treated spent bleaching earth (Mahramanlioglu et al., 2002) and the adsorption of phosphamidon onto an antimony (V) phosphate cation exchanger (Varshney et al., 1996). The plots of $1/C_t$ versus *t* for different impurities are shown in Figures 5.42–5.44. The calculated parameters of second-order model for Al, Fe, Mn, Mg, Ca, Si, Zn, and Ni are presented in Table 5.14.

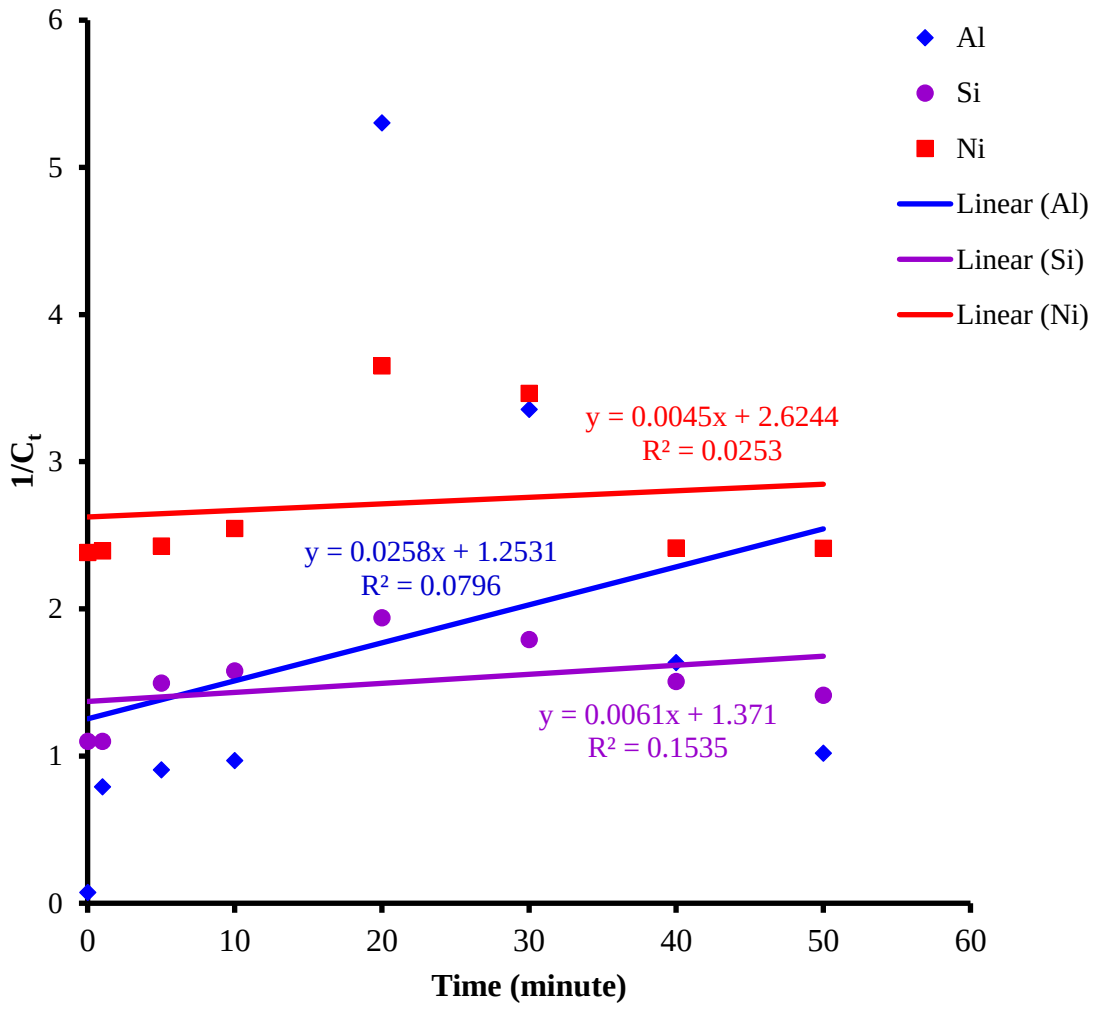

Figure 5.42: Second-order reaction kinetics for the adsorption of Al, Si, and Ni onto hydroxide precipitate (pH: 7, coagulant dosage 20 mg/L, and RT 23 ±2 ^{o}C).

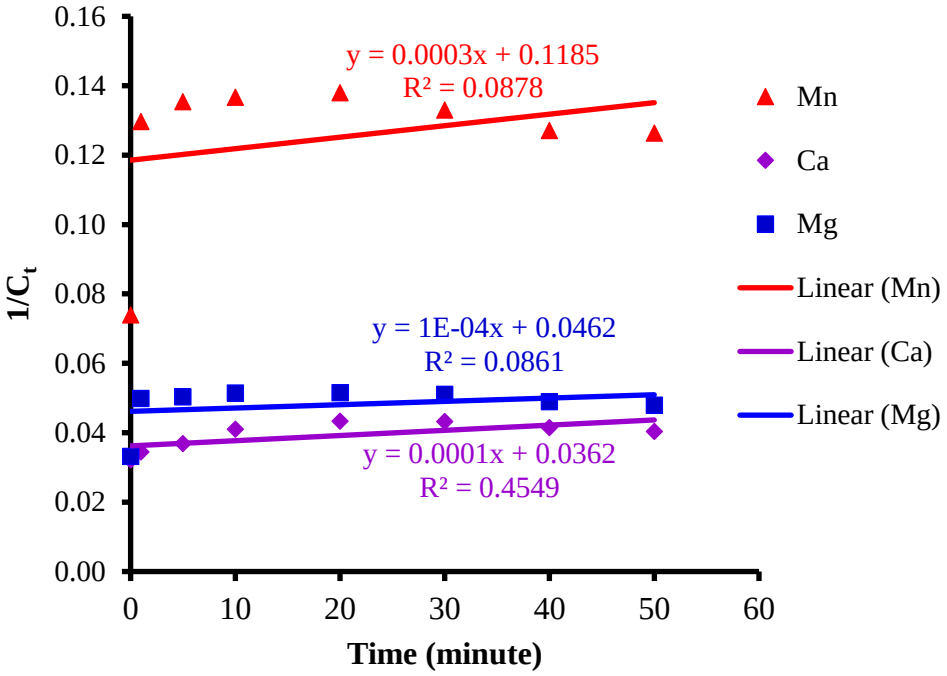

Figure 5.43: Second-order reaction kinetics for the adsorption of Mn, Ca, and Mg onto hydroxide precipitate (pH: 7, coagulant dosage 20 mg/L, and RT 23 ±2 ^{o}C).

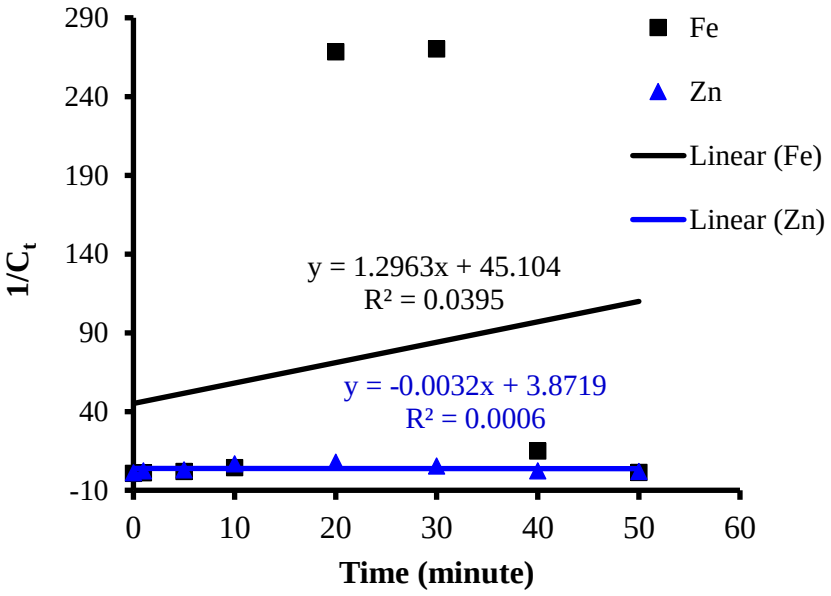

Figure 5.44: Second-order reaction kinetics for the adsorption of Fe and Zn onto hydroxide precipitate (pH: 7, coagulant dosage 20 mg/L, and RT 23 ±2 ^{o}C).

Table 5.14: kinetic parameters of the second-order kinetic model for Al, Fe, Mn, Mg, Ca, Si, Zn, and Ni.

Pollutants	k_2 (L/mg min)	C_0 (mg/L) calculated	C_0 (mg/L) experimental
Al	0.0258	0.79802091	13.850
Fe	1.2963	0.02217098	1.636
Mn	0.0003	8.43881857	13.517
Ca	0.0001	27.6243094	31.128
Mg	1.00E-04	21.6450216	30.177
Si	0.0061	0.7293946	0.910
Zn	-0.0032	0.25827113	0.930
Ni	0.0045	0.38103948	0.420

The second-order rate constants are determined to be 1.2963 > 0.0258 > 0.0061 > 0.0045 > 0.0003 > 0.0001 > 1 x 10^{-6} > -0.0032 Lmg^{-1} min^{-1} for the adsorption of Fe, Al, Si, Ni, Mn, Ca, Mg, and Zn, respectively. Furthermore, it can be seen from Table 5.14 that the values of the initial concentration calculated from the graph are not in agreement with experimental initial concentration for all investigated impurities. This could suggest that the sorption of Al, Fe, Mn, Mg, Ca, Si, Zn, and Ni onto hydroxide precipitate (coagulant) is not a second-order reaction. Therefore, the rate constants from the model equation are not significant.

5.9.2 Adsorption diffusion models

Usually, a typical liquid/solid adsorption involves film diffusion, intraparticle diffusion, and mass action. In the case of physical adsorption, mass action is a very fast process and can be negligible for kinetic study. So, the kinetic process of adsorption is always controlled by intraparticle diffusion or liquid film diffusion, that is to say that one of the processes should be the limiting step of the flow (Meng, 2005). Therefore, adsorption diffusion models are generally used to describe the process of intraparticle diffusion and/or film diffusion.

In this section, the adsorption mechanism models were analysed in order to predict and understand the rate-limiting step in the process. There are three basics mechanisms that

characterise the adsorption process such as film diffusion, particle diffusion, and pore diffusion, which was included in the discussion. The discussion of the models includes the kinetics behaviour up to the saturation of the adsorption process, thereafter the kinetics graph shows a decrease in adsorption capacity.

Weber–Morris model or intraparticle diffusion model

The application of the Weber–Morris model or intraparticle diffusion model is important because the internal diffusion determines the adsorption rate in most of the liquid systems. A general illustration of kinetics is given by Equation 5.45, where the intercept is related to the mass transfer through the boundary layer and the estimated value of the exponent is 0.5 (for Fickian diffusion and plate geometry).

$$q = k_{in}\, t^{n} + C \tag{5.45}$$

According to the Weber–Morris model, Equation 5.46, solute uptake varies almost proportionally with $t^{0.5}$ rather than with the contact time *t* (Alkan et al., 2007). The rate constant, $k_{in,}$ was calculated from the plot of q_t versus $t^{0.5}$ and is related to the respective intraparticle diffusion coefficient (*D*) according to Equation 5.47.

$$q_t = k_{in}\, t^{0.5} + C \tag{5.46}$$

$$k_{in} = 6\,\frac{q_0}{r}\,\sqrt{\frac{D}{\pi}} \tag{5.47}$$

where k_{in} (mg $L^{-1}min^{-1/2}$) is the intraparticle diffusion rate constant and r is the radius of the adsorbent particle (hydroxide precipitate = 5.11667 x 10^{-5} cm). The different mass-transfer mechanisms occur in the form of different slopes in the linear plot of q_t against $t^{0.5}$, obtained by piecewise linear regression. These mechanisms correspond to different successive steps of mass transfer with diminishing rate: external mass transfer and intraparticle diffusion in the macro-, meso- and microporous structure of the adsorbent (Aroua et al., 2008).

The Weber–Morris model equation was applied to the experimental data for initial concentration of each impurity investigated (Al, Fe, Mn, Mg, Ca, Si, Zn, and Ni) and plots are given in Figure 5.45 and 5.46. The values of the rate constant for Weber-Morris were obtained from the slopes of the linear plots of q_t versus $t^{0.5}$ for different pollutants. The

obtained rate constants k_{in} and the intraparticle diffusion coefficients D calculated by Equation 5.47 are presented in Table 5.15.

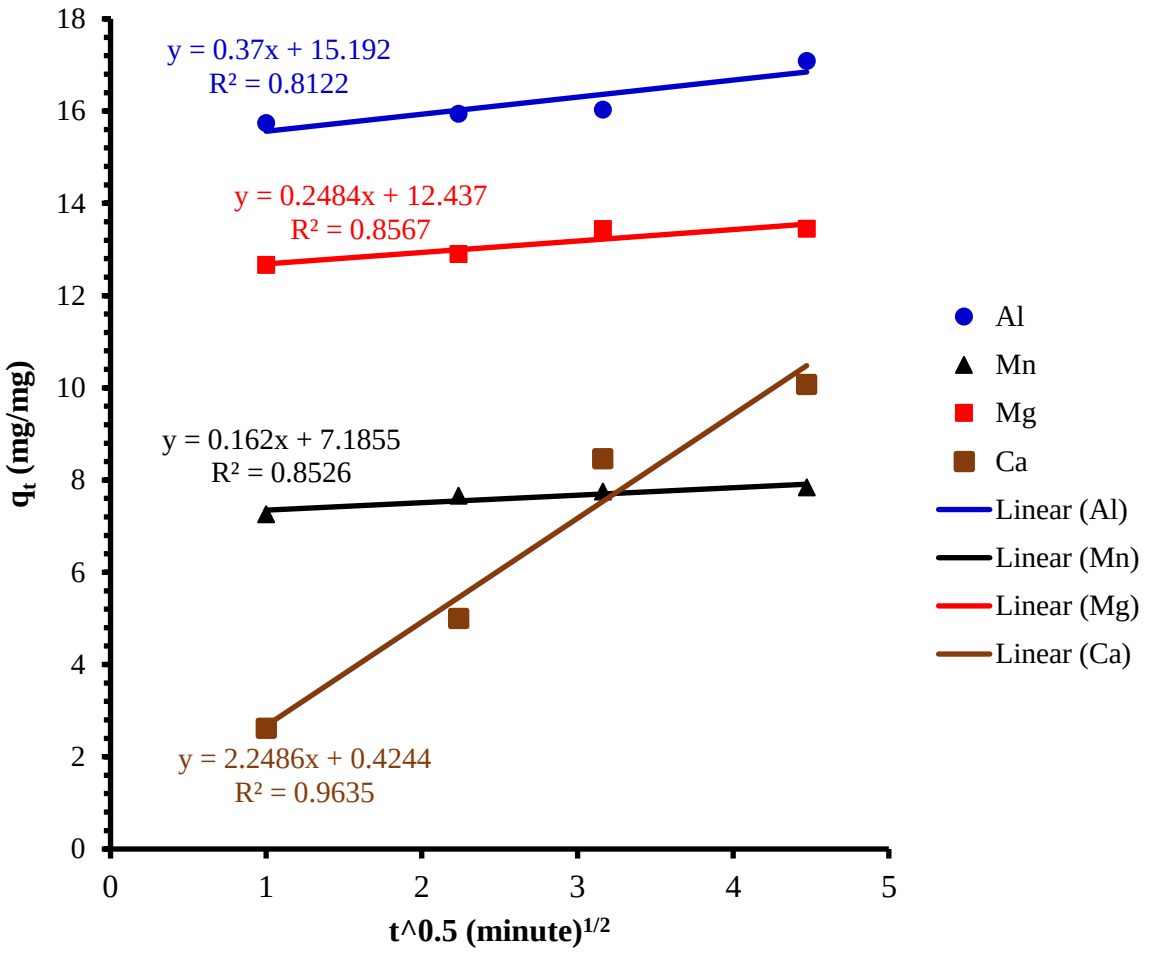

Figure 5.45: Weber-Morris diffusion kinetics for the adsorption of Al, Mn, Mg, and Ca onto hydroxide precipitate (pH: 7, coagulant dosage 20 mg/L, and RT 23 ±2 ^{o}C).

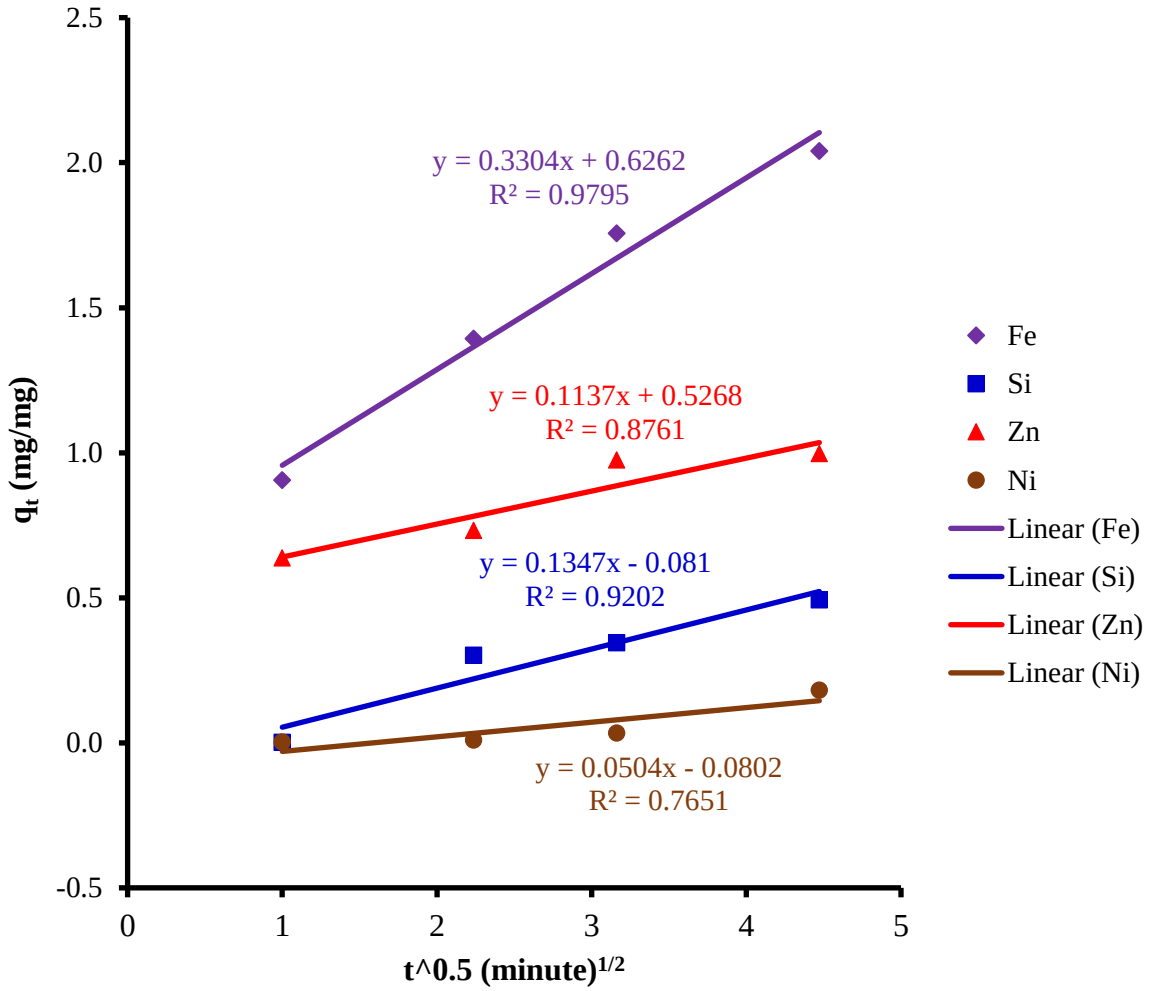

Figure 5.46: Weber-Morris diffusion kinetics for the adsorption of Fe, Si, Zn, and Ni onto hydroxide precipitate (pH: 7, coagulant dosage 20 mg/L, and RT 23 ±2 ^{o}C).

Table 5.15: kinetic parameters of the Weber-Morris kinetic model for Al, Fe, Mn, Mg, Ca, Si, Zn, and Ni.

Pollutants	k_{in} (mg $L^{-1}min^{-1/2}$)	D (cm^2/min)	D (cm^2/sec)
Al	0.3700	6.00093×10^{-9}	10.00×10^{-11}
Fe	0.3304	6.67189×10^{-11}	1.112×10^{-12}
Mn	0.1620	1.09495×10^{-9}	1.820×10^{-11}
Ca	2.2486	1.11874×10^{-6}	1.865×10^{-8}
Mg	0.2484	1.28309×10^{-8}	19.72×10^{-11}
Si	0.1347	3.42737×10^{-12}	0.57×10^{-13}
Zn	0.1137	2.53521×10^{-12}	0.42×10^{-13}
Ni	0.0504	1.02095×10^{-13}	1.702×10^{-15}

The calculated intraparticle diffusion coefficients of Al, Fe, Mn, Mg, Si, and Zn are in the range of $1.8\ 10^{-11}$ to $0.57\ 10^{-13}$ cm^2/sec, which is physically suitable for intraparticle or pore diffusion as proposed by Karthikeyan et al. (2010). However, the obtained intraparticle diffusion coefficients of Ni and Ca are not in the range as per Karthikeyan et al. (2010) investigation and it can be concluded that they do not follow the intraparticle diffusion model. The diffusion coefficient calculated for Ca ranges in the film diffusion as rate determining step (Karthikeyan et al., 2010). Furthermore, the values of intercept which provide an indication about the thickness of boundary layer (i.e., the higher the intercept the greater is the boundary layer effect) (Kavitha and Namasivayam, 2008; Kannan and Sundaram, 2001) show that the boundary layer effect is greater for Al (15.192) than for Mg (12.437), Mn (7.1855), Fe (0.6262), Zn (0.5268), Ca (0.4244), Ni (-0.0802), and Si (-0.081).

Boyd's model

The Boyd's particle diffusion model (Boyd et al. 1947) is presently one of the most intensively used models to investigate the adsorption kinetics mechanism (Malash and El-Khaiary 2010). This model is applied to kinetic data to determine the rate limiting step, particle diffusion or film diffusion. It is also used to establish the effective intraparticle diffusion coefficient (D_{eff}). The Boyd's film-diffusion model was originally proposed for intraparticle diffusion in a spherical particle. When used to external mass transfer, it assumes

a linear dependence through the origin between $F = \frac{q}{q_e}$ (the fractional approach to equilibrium) and *t* (time) (Boyd et al. 1947):

$$\ln(1 - F) = kt \tag{5.48}$$

Where, *k* is the external mass transfer coefficient. The general solution of the model, used to solid phase control, is:

$$F = \frac{q}{q_t} = 1 - \frac{6}{\pi^2} \sum_{n=1}^{\infty} \frac{1}{n^2} e^{-n^2 \beta_t} \tag{5.49}$$

For n= 1 $$F = 1 - \frac{6}{\pi^2} e^{-\beta_t} \tag{5.50}$$

where the rate coefficient β (min^{-1}) is related to the effective diffusion coefficient (D_{eff}) and the adsorbent (hydroxide precipitate) particle radius (r = 5.11667 x 10^{-5} cm) as $\beta = \pi^2 \frac{D_{eff}}{r^2}$. By applying Fourier transform, the relation between the fractional approach to equilibrium *F* and the rate coefficient β is written as

$$\beta_t = \left(\sqrt{\pi} - \sqrt{\pi - \frac{\pi^2 F(t)}{3}} \right)^2 \quad \text{for } F(t) \leq 0.85 \tag{5.51}$$

and $$\beta_t = -0.498 - \ln(1 - F(t)) \quad \text{for } F(t) > 0.85 \tag{5.52}$$

The linear plot of β_t (calculated by Equations 5.51 or 5.52) against time (Boyd plot), f (*F*), is used to evaluate the rate parameter β (by the slope of β_t vs. t). The presence of an intercept (i.e., intercept value ≠ 0) indicates the effect of a second mass transfer mechanism (external mass transfer). For each kinetic data, *F(t)* was calculated as $\frac{q_t}{q_e}$ (Equation 5.49) and β_t was determined using Equation 5.51 if $F(t) \leq 0.85$ or Equation 5.52 if $F(t) > 0.85$. A linear representation of β_t vs *t* was applied to obtain the kinetic parameter β and the respective effective diffusion coefficient (D_{eff}). Results of the Boyd's model for the studied impurities (Al, Fe, Mn, Mg, Ca, Si, Zn, and Ni) are presented in Table 5.16 and Figures 5.47 and 5.48.

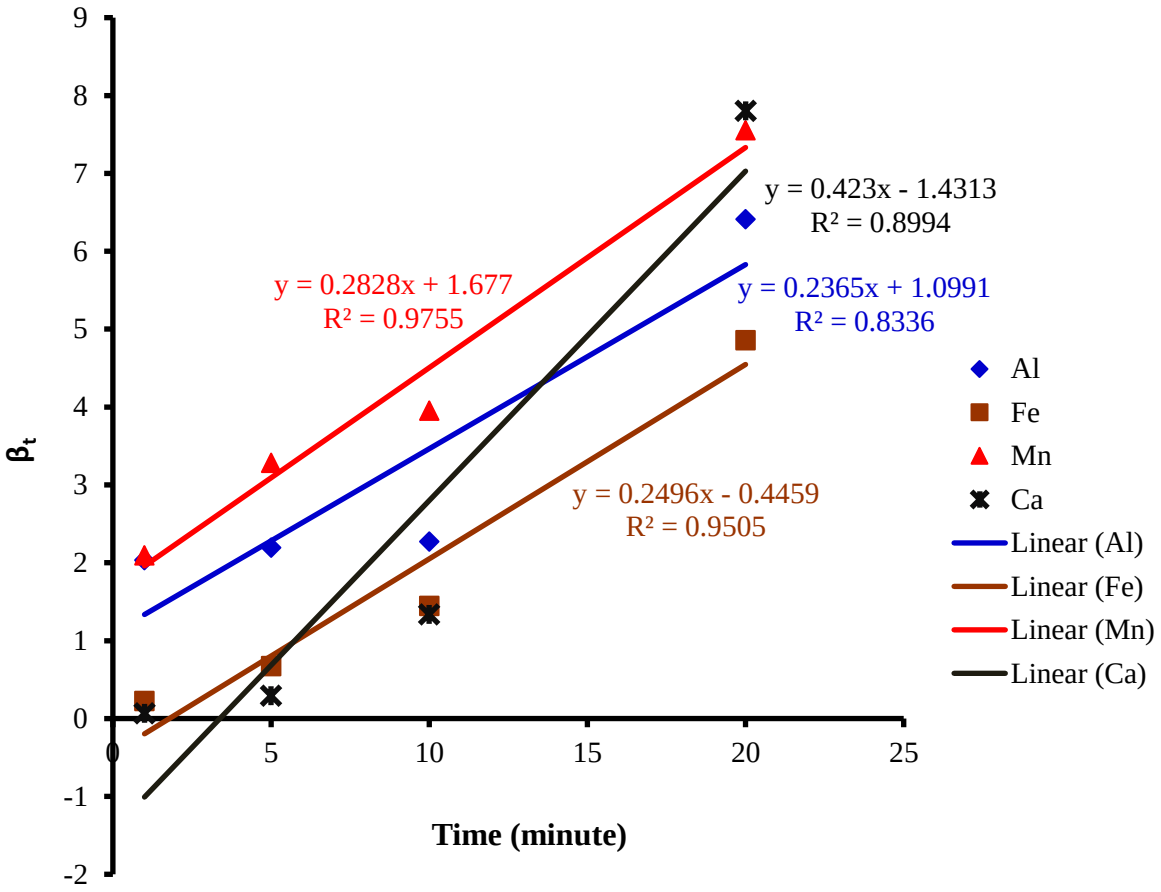

Figure 5.47: Boyd's diffusion kinetics for the adsorption of Al, Fe, Mn, and Ca onto hydroxide precipitate (pH: 7, coagulant dosage 20 mg/L, and RT 23 ±2 ^{o}C).

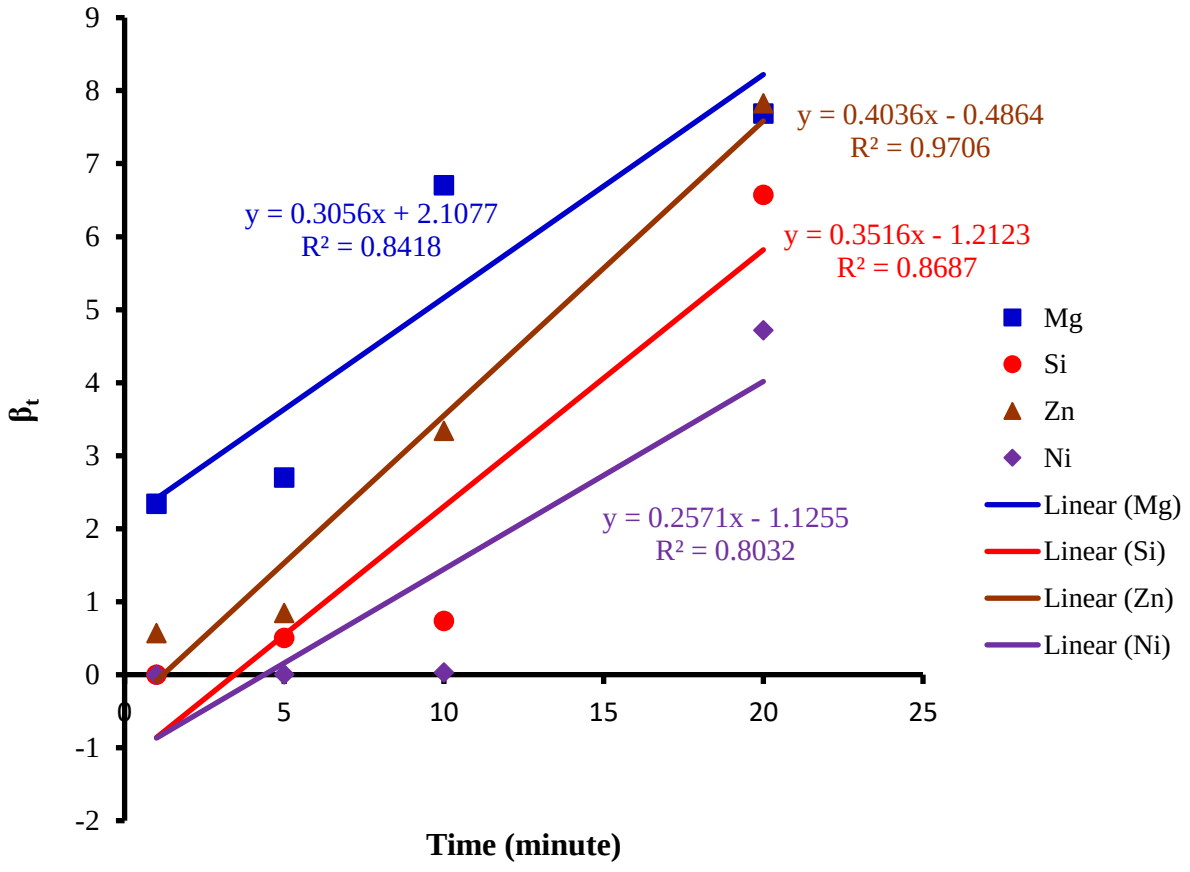

Figure 5.48: Boyd's diffusion kinetics for the adsorption of Mg, Si, Zn, and Ni onto hydroxide precipitate (pH: 7, coagulant dosage 20 mg/L, and RT 23 ±2 ^{o}C).

Table 5.16: Rate parameters of the Boyd's kinetic model for Al, Fe, Mn, Mg, Ca, Si, Zn, and Ni.

Pollutants	**β (min^{-1})**	**D_{eff} x 10^{+11} (cm^2/min)**	**D_{eff} x 10^{+12} (cm^2/sec)**
Al	0.2365	6.2798	1.050
Fe	0.2496	6.6277	1.100
Mn	0.2828	7.5092	1.250
Ca	0.4230	0.1123	1.87
Mg	0.3056	8.1146	1.350
Si	0.3516	9.3361	1.560
Zn	0.4036	0.1072	1.79
Ni	0.2571	6.8268	1.140

It can be seen from Table 5.16 that the D_{eff} values of Al, Fe, Ca, and Ni (6.2798 x 10^{-11}, 6.6277 x 10^{-11}, 1.1232 x 10^{-11}, and 1.0717 x 10^{-}11 cm^2/min, respectively) are almost the same

than those from the Morris and Weber model (6.0009 x 10^{-11}, 6.6719 x 10^{-11}, 1.1187 x 10^{-11}, and 2.5352 x 10^{-11} cm^2/min, respectively). While values of D_{eff} of Mn, Mg, Si, and Ni (7.5092 x 10^{-11}, 8.1146 x 10^{-11}, 9.3361 x 10^{-11}, and 6.8268 x 10^{-11} cm^2/min, respectively) are higher than those obtained with the Morris and Weber model (1.0949 x 10^{-11}, 1.2831 x 10^{-11}, 3.4274 x 10^{-11}, and 1.0210 x 10^{-11} cm^2/min, respectively). Such comparison has been made even if several of the impurities studied based on a survey of sorption shows that there is very little or no information in the literature based on Al, Fe, Mn, Mg, Ca, Si, Zn, and Ni removal by adsorption. Furthermore, the observation of an intercept, for all the pollutants investigated (Al, Fe, Mn, Mg, Ca, Si, Zn, and Ni), suggests that diffusion is not the only observed mechanism of transfer. Hence, there is of a second mass transfer mechanism (external mass transfer).

The calculated diffusion coefficients range from 1.05 10^{-12} to 1.87 10^{-12} cm^2/sec, which is physically suitable for intraparticle or pore diffusion as per the investigation of Karthikeyan et al. (2010); therefore, based on the diffusion coefficient the film diffusion model is not suitable for these processes.

Bangham's model (pore diffusion model)

The next method to explain the rate-determining step of the biosorption of Zn (II) ion on the surface of CDS resulted to implementation of Bangham's model. Equation 5.53 (Abdelwahab, 2007) represents the linearized form of Bangham's equation.

$$log\left[log\left(\frac{C_0}{C_0 - q_t m}\right)\right] = log\left(\frac{K_0\, m}{2.303\, V}\right) + \alpha \log t \qquad (5.53)$$

where C_0 (mg/L) denotes the initial concentration of adsorbate in solution, V (mL) represents the volume of wastewater used, m (g/L) is the amount of adsorbent (coagulant), q_t is the amount of impurity in solution at time t and α (< 1) and K_0 are constants which can be obtained from slope and intercept, respectively. The pore diffusion is the rate-controlling step if the experimental data suits well into Equation 5.53. The experimental data of Al, Fe, Mn, Mg, Ca, Si, Zn, and Ni were further used to investigate whether pore diffusion is the only rate-controlling step or not in the present adsorption system using Bangham's equation given in Equation 5.53. The plots of $log\left[log\left(\frac{C_0}{C_0 - q_t m}\right)\right]$ versus $\log t$ for different impurities are

shown in Figures 5.49 and 5.50. The calculated parameters of the Bangham's model for Al, Fe, Mn, Mg, Ca, Si, Zn, and Ni are presented in Table 5.17.

The constant α is less than 1 except for Si and Ni, which was determined as the slope of the straight line. These results confirm that pore diffusion is the rate-determining factor for these processes.

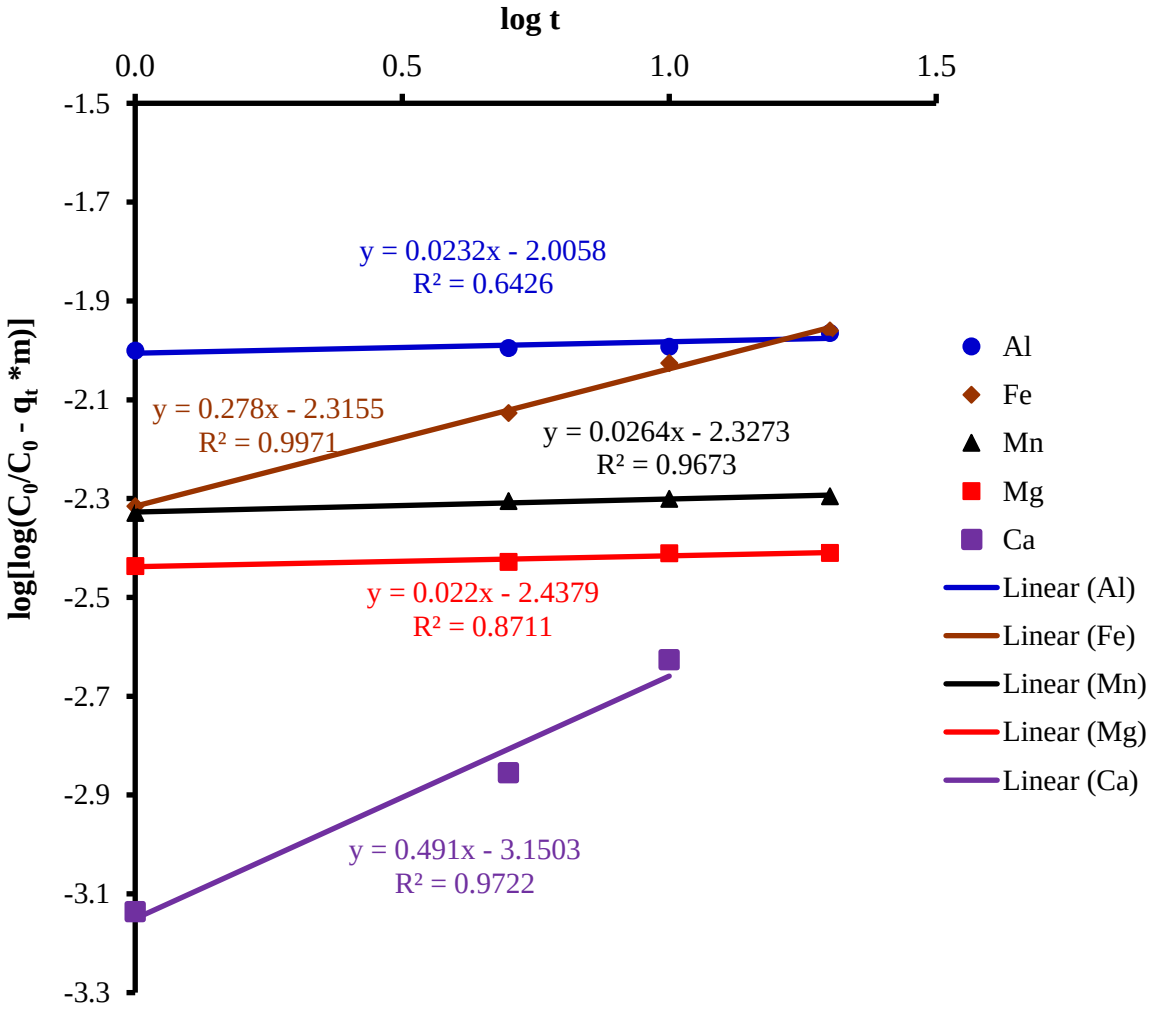

Figure 5.49: Bangham's diffusion kinetics for the adsorption of Al, Fe, Mn, Mg, and Ca onto hydroxide precipitate (pH: 7, coagulant dosage 20 mg/L, and RT 23 ±2 ^{o}C).

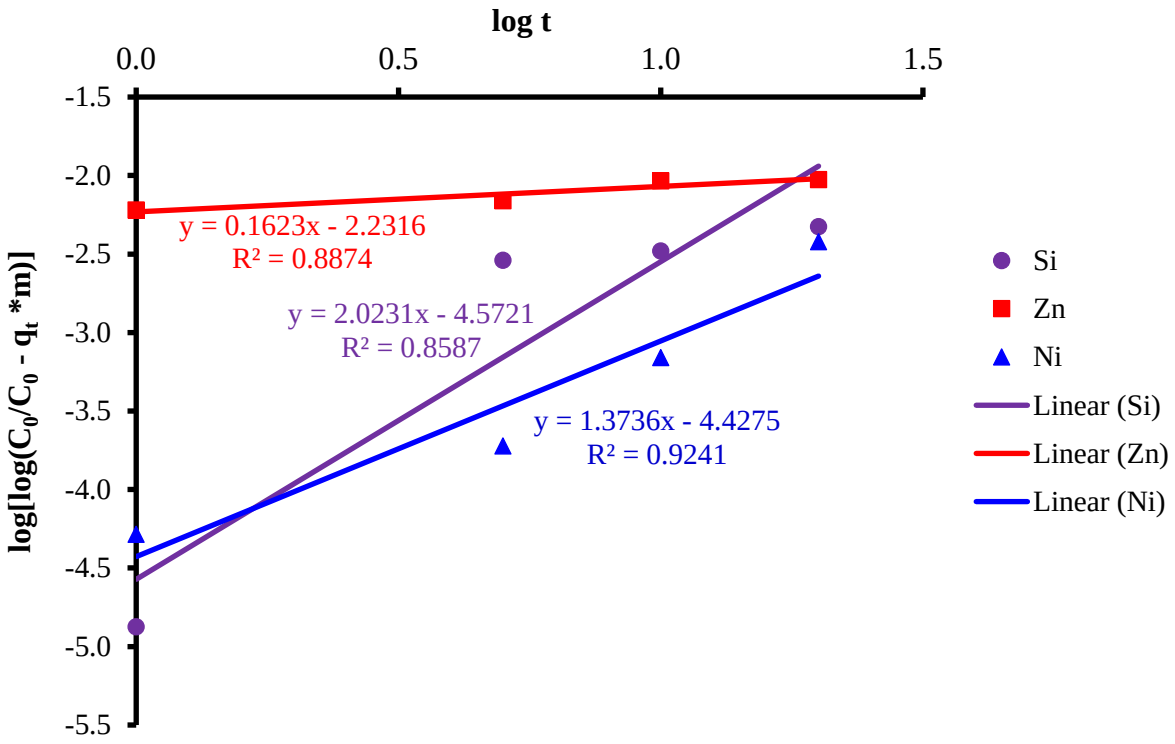

Figure 5.50: Bangham's diffusion kinetics for the adsorption of Ni, Si, and Zn onto hydroxide precipitate (pH: 7, coagulant dosage 20 mg/L, and RT 23 ±2 ^{o}C).

Table 5.17: kinetic parameters of the Bangham's kinetic model for Al, Fe, Mn, Mg, Ca, Si, Zn, and Ni.

Pollutants	α	K_0
Al	0.0232	28.40559894
Fe	0.2780	13.92207442
Mn	0.0264	13.54889730
Ca	0.4910	2.03659161
Mg	0.0220	10.50277232
Si	2.0231	0.07710880
Zn	0.1623	16.88900059
Ni	1.3736	0.10757317

5.9.3 Coefficient of determination

Adsorption reaction models

The comparison of all chemisorption models, as sshown in Table 5.18, indicates that the correlation coefficients are higher for second order kinetic studies. Contrary it was observed in Figure 5.38 that the pseudo-second-order model did not fit well for Si (R^2 = 0.0769). However, after 1 minute coagulation's time, this model fitted well silicon experimental data, providing an R^2 value of 0.9164 (Appendix Figure B.1). Therefore, all the experimental data showed better compliance with pseudo-second-order chemisorption kinetic model for the hydroxide precipitates in terms of higher correlation coefficient values. It may be concluded that the pseudo-second-order kinetic model well describe the experimental data, which indicates the chemical sorption nature of the coagulation process. Zewail and Yousef (2015), and Alyüz and Veli (2009) have found that the removal of Ni and Zn ions were well fitted by second order model.

Adsorption diffusion models

The correlation coefficient obtained from the diffusion models (Weber–Morris, Boyd, and Bangham) (Table 5.18) ranged between 0.6426 and 0.997 suggesting that multiple adsorption stages occurred and not only intraparticle or pore diffusion were involved in the diffusion mechanism. Also, the linearity of the models' plot suggests that adsorbate pore diffusion is not the only rate controlling step. Multilinear profiles were obtained for intraparticle diffusion model plot if we account for the entire range of time investigated, and this plot does not pass through the origin, which suggests that boundary layer diffusion also occurred in the adsorption mechanism.

Table 5.18: Linear kinetic coefficients of determination (R^2)

Impurities	Reaction kinetic models				Diffusion kinetic models		
	Pseudo-first-order	**Pseudo-second-order**	**Elovich**	**Second-order**	**Weber-Morris**	**Boyd**	**Bangham**
Al	0.0133	0.9987	0.3963	0.0796	0.8122	0.8336	0.6426
Fe	0.0501	0.8594	0.3468	0.0395	0.9795	0.9505	0.9971
Mn	0.2127	0.9977	0.0481	0.0878	0.8526	0.9755	0.9673
Ca	0.0365	0.9706	0.7553	0.4549	0.9635	0.8994	0.9722
Mg	0.1714	0.9945	0.0739	0.0861	0.8567	0.8418	0.8711
Si	0.0068	0.0769	0.4655	0.1535	0.9202	0.8687	0.8587
Zn	0.0321	0.9249	0.0001	0.0006	0.8761	0.9706	0.8874
Ni	0.0008	0.6995	0.1000	0.0253	0.7651	0.8032	0.9241

5.10 Conclusion

The research on the coagulation in removing Al, Fe, Mn, Mg, Ca, Si, Zn, Ni, TDS, and turbidity during wastewater treatment has been conducted. The application of the control of the pH of the raw acid mine drainage by the addition of NaOH and H_2SO_4 and varying doses of coagulant, time, and temperature were important to increase the removal of these impurities by coagulation. In the optimal range of pH values, coagulant dosages, and coagulation time, the synthesized complex coagulant has remarkable effect on coagulation and impurity removal. The colloid materials in the coal mine wastewater generally carry negative electrical charges, while the coagulant contains a large quantity of Fe^{3+}, Al^{3+}, Si^{4+}, Mg^{2+}, and Ca^{2+} ions. At the optimal pH value and coagulant dosage, Fe^{3+}, Al^{3+}, Si^{4+}, Mg^{2+}, and Ca^{2+} are hydrolysed into monomeric and polymeric hydroxy complex ions, which have the ability to compress the electric double layer of the particles, to electrically neutralize and are capable of adsorbing particles. The optimum coagulation effect was achieved when the coagulant dose was 20 mg/L, the pH value 7.0 and the coagulation time 20 minutes. In these conditions, the residual rate was 60.83, 1.36, 0.23, 53.61, 74.13, 64.35, 56.57, 13.95, and 65.29% for TDS, Al, Fe, Mn, Ca, Mg, Si, Zn, and Ni, respectively. The temperature did not show any effect on the removal of impurities. In addition, the comparison between the produced complex coagulant and conventional ones demonstrated that the former produced remarkable coagulation effect in removing TDS, Ca, Mg, Si, and Zn. However, no significant benefit compared to traditional coagulants was observed for the removal of Al, Fe, Mn and Ni. Furthermore, the optimization of the design of the adsorption system for the adsorption of adsorbates was studied and modeled using four adsorption isotherm models, namely, Langmiur, Freundlich, Temkin, and BET equations. The results established that the adsorptions are, in general, exothermic processes as indicated by Temkin and BET isotherm models. The assessment of the regression coefficients of determination from the four isotherm equations for the fit of the analytical data showed that the R^2 values for Temkin and BET were in the suitable range and they could be considered as the adsorption models for this investigation in general.

The comparison of different adsorption reaction models showed that the experimental data of all the impurities studied are well described by the pseudo-second-order kinetic model, which suggests that the chemical sorption is the rate-controlling step of the coagulation process. Besides, the equilibrium data, from the pseudo-second-order equation, agrees well

with the experimental one. For the adsorption of all the investigated impurities onto hydroxide precipitates, the pseudo-second-order chemical reaction kinetics gives the best correlation of the experimental data.

For the adsorption diffusion kinetic study, the intraparticle diffusion coefficients calculated from the Weber–Morris and boyd's models are in the range of 1.8 10^{-11} to 0.57 10^{-13} cm^2/sec and 1.05 10^{-12} to 1.87 10^{-12} cm^2/sec, respectively, (except for Ni and Ca for the Weber–Morris model). This is suitable for the case of internal diffusion control. Further, the presence of an intercept from the Boyd's model, for all the impurities investigated indicates that diffusion is not the only observed mechanism of transfer. In addition, in terms of correlation coefficient, the adsorption kinetics of all the studied pollutants in coal mine wastewater with hydroxide precipitates was well described by the Weber-Morris, Boyd, and bangham models. Multiple adsorption stages occurred during the diffusion mechanism, namely, intraparticle or pore diffusion, and film diffusion (boundary diffusion).

References

Abdelwahab, O., 2007. Kinetic and isotherm studies of copper (II) removal from wastewater using various adsorbents. *Egyptian journal of aquatic research*, 33 (1), 125–143.

Abdullah, S.R.S., Rahman, R.A., Mohamad, A.B., Mustafa, M.M., Khadum, A.A.H. 1999. Removal of Mixed Heavy Metals by Hydroxide Precipitation. *Jurnal Kejuruteraan* 11 (2), 85–101.

Achak, M., Hafidi, A., Ouazzani, N., Sayadi, S. and Mandi, L., 2009. Low cost biosorbent "banana peel" for the removal of phenolic compounds from olive mill wastewater: Kinetic and equilibrium studies. *Journal of hazardous materials*, 166 (1), 117–125.

Aljeboree, A.M., Alshirifi, A.N. and Alkaim, A.F., 2017. Kinetics and equilibrium study for the adsorption of textile dyes on coconut shell activated carbon. *Arabian journal of chemistry*, 10, S3381–S3393.

Alkan, M., Demirbaş, Ö. and Doğan, M., 2007. Adsorption kinetics and thermodynamics of an anionic dye onto sepiolite. *Microporous and Mesoporous Materials*, 101(3), 388–396.

Alyüz, B., Veli, S. 2009. Kinetics and equilibrium studies for the removal of nickel and zinc from aqueous solutions by ion exchange resins. *Journal of Hazardous Materials* 167, 482–488.

Arami, M., Limaee, N.Y., Mahmoodi, N.M. and Tabrizi, N.S., 2005. Removal of dyes from colored textile wastewater by orange peel adsorbent: equilibrium and kinetic studies. *Journal of Colloid and interface Science*, 288 (2), .371–376.

Aroua, M.K., Leong, S.P.P., Teo, L.Y., Yin, C.Y. and Daud, W.M.A.W., 2008. Real-time determination of kinetics of adsorption of lead (II) onto palm shell-based activated carbon using ion selective electrode. *Bioresource Technology*, 99 (13), 5786–5792.

Aziz, H.A., Alias, S., Assari, F., Adlan, M.N., 2007. The use of alum, ferric chloride and ferrous sulphate as coagulants in removing suspended solids, colour and COD from semi-aerobic landfill leachate at controlled pH. *Waste Manage Ressources* 25, 556–565.

Baes Jr, C.F. and Mesmer, R.E., 1981. Thermodynamics of cation hydrolysis. *American Journal of Science. 281* (7), 935–962.

Barnum, D.W., 1983. Hydrolysis of cations. Formation constants and standard free energies of formation of hydroxy complexes. *Inorganic Chemistry*, *22* (16), 2297–2305.

Bolis, V., Morterra, C., Fubini, B., Ugliengo, P. and Garrone, E., 1993. Temkin-type model for the description of induced heterogeneity: CO adsorption on group 4 transition metal dioxides. Langmuir, 9(6), pp.1521–1528.

Boyd, G.E., Adamson, A.W. and Myers Jr, L.S., 1947. The exchange adsorption of ions from aqueous solutions by organic zeolites. II. Kinetics1. *Journal of the American Chemical Society*, 69 (11), 2836–2848.

Brunauer, S., Emmett, P.H. and Teller, E., 1938. Adsorption of gases in multimolecular layers. *Journal of the American chemical society 60* (2), 309–319.

Cerofolini, G.F., Meda, L. and Bandosz, T.J., 1999. Adsorption with soft adsorbents or adsorbates. Theory and practice. In *Studies in Surface Science and Catalysis* 120, 227–272.

Cheng, W.P. and Chi, F.H., 2002. A study of coagulation mechanisms of polyferric sulfate reacting with humic acid using a fluorescence-quenching method. *Water research, 36* (18), .4583–4591.

Cheng, W.P., 2002. Comparison of hydrolysis/coagulation behavior of polymeric and monomeric iron coagulants in humic acid solution. *Chemosphere*, 47(9), 963–969.

Cheng, W., Wang, S.G., Lu, L., Gong, W.X., Liu, X.W., Gao, B.Y. and Zhang, H.Y., 2008. Removal of malachite green (MG) from aqueous solutions by native and heat-treated anaerobic granular sludge. *Biochemical engineering journal*, 39 (3), 538–546.

Chien, S.H. and Clayton, W.R., 1980. Application of Elovich equation to the kinetics of phosphate release and sorption in soils 1. *Soil Science Society of America Journal*, 44 (2), 265–268.

Coleman, N.T., McClung, A.C. and Moore, D.P., 1956. Formation constants for Cu (II)-peat complexes. *Science*, 123 (3191), 330–331.

Daneshvar, N., Salari, D., Aber, S., 2002. Chromium adsorption and Cr(VI) reduction to trivalent chromium in aqueous solutions by soya cake. *Journal of hazardous materials* 94 (1), 49-61.

De Abreu, H.A., Guimaraes, L. and Duarte, H.A., 2006. Density-functional theory study of iron (III) hydrolysis in aqueous solution. *The Journal of Physical Chemistry A*, *110* (24), 7713–7718.

de Rome, L., Gadd, G.M., 1987. Copper adsorption by Rhizopus arrhizus, Cladosporium resinae and Penicillium italicum. *Applied microbiology and biotechnology 26* (1), 84–90.

Długosz, O. and Banach, M., 2018. Kinetic, isotherm and thermodynamic investigations of the adsorption of Ag+ and Cu2+ on vermiculite. *Journal of Molecular Liquids*, 258, 295–309.

Duan, J., Gregory, J., 2003. Coagulation by hydrolysing metal salts. *Advances in Colloid and Interface Science* 100–102, 475–502.

Eigen, M., 1964. Proton Transfer, Acid-Base Catalysis, and Enzymatic Hydrolysis. Part I: Elementary processes. *Angewandte Chemie International Edition in English 3* (1), 1–19.
Fan, M., Brown, R.C., Wheelock, T.D., Cooper, A.T., Nomura, M., Zhuang, Y., 2005. Production of a complex coagulant from fly ash. *Chemical Engineering Journal* 106, 269–277.

Fu, F., Wang, Q., 2011. Removal of heavy metal ions from wastewaters: A review. *Journal of Environmental Management* 92, 407–418.

Gao, B.Y., Yue, Q.Y., 2005. Natural organic matter (NOM) removal from surface water by coagulation. *Journal of Environmental Sciences*, *17* (1), 119–122.

Griffin, R.A., Jurinak, J.J., 1974. Kinetics of the Phosphate Interaction with Calcite 1. *Soil Science Society of America Journal*, 38 (1), 75–79.

Gode, F. and Pehlivan, E., 2005. Adsorption of Cr (III) ions by Turkish brown coals. *Fuel Processing Technology*, *86* (8), 875–884.

Gregor, J.E., Nokes, C.J. and Fenton, E., 1997. Optimising natural organic matter removal from low turbidity waters by controlled pH adjustment of aluminium coagulation. *Water Research*, *31*(12), 2949–2958.

Hameed, B.H., 2008. Equilibrium and kinetic studies of methyl violet sorption by agricultural waste. Journal of hazardous materials, 154 (1-3), 204–212.

Henry, M., Jolivet, J.P., and Livage, J., 1992. Aqueous chemistry of metal cations: hydrolysis, condensation and complexation. In *Chemistry*, *Spectroscopy and Applications of Sol-Gel Glasses*. Springer, Berlin, Heidelberg.

Ho, Y.S., Wase, D.J. and Forster, C.F., 1995. Batch nickel removal from aqueous solution by sphagnum moss peat. *Water Research*, 29 (5), 1327–1332.

Ho, Y.S., McKay, G., 1998a. A comparison of chemisorption kinetic models applied to pollutant removal on various sorbents. *Process safety and environmental protection*, 76 (4), 332–340.

Ho, Y.S. and McKay, G., 1998b. Sorption of dye from aqueous solution by peat. *Chemical engineering journal*, 70 (2), 115–124.

Ho, Y.S. and McKay, G., 2000. The kinetics of sorption of divalent metal ions onto sphagnum moss peat. *Water research*, 34 (3), 735–742.

Ho, Y.S., 2004. Citation review of Lagergren kinetic rate equation on adsorption reactions. *Scientometrics*, *59* (1), 171–177.

Ho, Y.S., 2006. Review of second-order models for adsorption systems. *Journal of hazardous materials*, 136 (3), 681–689.

Hui, K.S., Chao, C.Y.H. and Kot, S.C., 2005. Removal of mixed heavy metal ions in wastewater by zeolite 4A and residual products from recycled coal fly ash. *Journal of Hazardous Materials*, 127 (1–3), 89–101.

Hussain, S., van Leeuwen, J., Chow, C., Beecham, S., Kamruzzaman, M., Wang, D., Drikas, M., Aryal, R., 2013. Removal of organic contaminants from river and reservoir waters by three different aluminum-based metal salts: Coagulation adsorption and kinetics studies. *Chemical Engineering Journal* 225, 394–405.

Ikeda, T., Boero, M., Terakura, K., 2007. Hydration properties of magnesium and calcium ions from constrained first principles molecular dynamics. *The Journal of Chemical Physics*, 127, 1–8.

Jnr, M.H. and Spiff, A.I., 2005. Equilibrium sorption study of Al^{3+}, Co^{2+} and Ag^{+} in aqueous solutions by fluted pumpkin (Telfairia occidentalis HOOK f) waste biomass. *Acta Chim. Slov*, 52, 174–181.

Juang, R.S. and Chen, M.L., 1997. Application of the Elovich equation to the kinetics of metal sorption with solvent-impregnated resins. *Industrial & Engineering Chemistry Research*, 36 (3), 813–820.

Kannan, N. and Sundaram, M.M., 2001. Kinetics and mechanism of removal of methylene blue by adsorption on various carbons—a comparative study. *Dyes and pigments*, 51 (1), 25–40.

Karthikeyan, S., Sivakumar, B. and Sivakumar, N., 2010. Film and pore diffusion modeling for adsorption of reactive red 2 from aqueous solution on to activated carbon prepared from bio-diesel industrial waste. *Journal of Chemistry*, 7 (S1), S175–S184.

Kavitha, D. and Namasivayam, C., 2008. Capacity of activated carbon in the removal of acid brilliant blue: Determination of equilibrium and kinetic model parameters. *Chemical Engineering Journal*, 139 (3), 453–461.

Kuo, S. and Lotse, E.G., 1972. Kinetics of Phosphate Adsorption by Calcium Carbonate and Ca-Kaolinite 1. *Soil Science Society of America Journal*, 36 (5), 725–729.

Lagergren, S.K., 1898. About the theory of so-called adsorption of soluble substances. *Svenska Vetenskapsakademiens. Handlingar*, 24, 1–39.

Li, L., Fan, M., Brown, R.C., Koziel, J.A., Leeuwen, J. H., 2009. Production of a new wastewater treatment coagulant from fly ash with concomitant flue gas scrubbing. *Journal of harzardous Materials* 162, 1430–1437.

Low, M.J.D., 1960. Kinetics of chemisorption of gases on solids. *Chemical Reviews*, 60 (3), 267–312.

Mahramanlioglu, M., Kizilcikli, I. and Bicer, I.O., 2002. Adsorption of fluoride from aqueous solution by acid treated spent bleaching earth. *Journal of Fluorine Chemistry*, 115 (1), 41–47.

Malash, G.F. and El-Khaiary, M.I., 2010. Piecewise linear regression: A statistical method for the analysis of experimental adsorption data by the intraparticle-diffusion models. *Chemical Engineering Journal*, 163 (3), 256–263.

Maurya, N.S., Mittal, A.K., 2009. Biosorptive color removal: Applicability of equilibrium isotherm model. *Practice periodical of hazardous, toxic, and radioactive waste management* 14 (1), 25–36.

Meng, X., Bang, S., Korfiatis, G.P., 2000. Effects of silicate, sulfate, and carbonate on arsenic removal by ferric chloride. *Water Research 34*(4), 1255–1261.

Meng, F.W., 2005. *Study on a mathematical model in predicting breakthrough curves of fixed-bed adsorption onto resin adsorbent* (Doctoral dissertation, MS Thesis, Nanjing University, China).

Mercer, K.L. and Tobiason, J.E., 2008. Removal of arsenic from high ionic strength solutions: effects of ionic strength, pH, and preformed versus in situ formed HFO. *Environmental science & technology 42*(10), 3797–3802.

Mirsal, I., 2008. *Soil pollution: origin, monitoring & remediation*. Springer Science & Business Media.

Monhemius, A.J., 1977. Precipitation diagrams for metal-hydroxides, sulfides, arsenates and phosphates. *Transactions of the institution of mining and metallurgy section c-mineral processing and extractive metallurgy*, *86* (DEC), C202–C206.

Namasivayam C., Kavitha, D., 2002. Removal of Congo Red from water by adsorption onto activated carbon prepared from coir pith, an agricultural solid waste. *Dyes and Pigment*s 54, 47–58.

Niu, X., Li, X., Zhao, J., Ren, Y. and Yang, Y., 2011. Preparation and coagulation efficiency of polyaluminium ferric silicate chloride composite coagulant from wastewater of high-purity graphite production. *Journal of Environmental Sciences*, *23* (7), 1122–1128.

Pálinkás, G., Heinzinger, K., 1986. Hydration shell structure of the calcium ion. *Chemical Physics Letters*, 126 (3–4), 251–254.

Rebhun, M. and Lurie, M., 1993. Control of organic matter by coagulation and floc separation. *Water Science and Technology, 27*(11), 1–20.

Richens, D.T., 1997. The Chemistry of Aqua Ions, Wiley, Chichester.

Rose, A.L. and Waite, T.D., 2003. Kinetics of hydrolysis and precipitation of ferric iron in seawater. *Environmental science & technology*, 37 (17), 3897–3903.

Rudzinski, W. and Panczyk, T., 2000. Kinetics of isothermal adsorption on energetically heterogeneous solid surfaces: a new theoretical description based on the statistical rate theory of interfacial transport. *The Journal of Physical Chemistry B*, 104 (39), 9149–9162.

Stephenson, R.J. and Duff, S.J., 1996. Coagulation and precipitation of a mechanical pulping effluent—I. Removal of carbon, colour and turbidity. *Water research*, 30 (4), 781–792.

Stumm, W. and Morgan, J.J., 1962. Chemical aspects of coagulation. *Journal-American Water Works Association*, *54* (8), 971–994.

Stumm, W. and O'Melia, C.R., 1968. Stoichiometry of coagulation. *Journal-American Water Works Association*, 60 (5), 514–539.

Sui, Z., Qiao, C., Zhao, X., Qiang, X., 2009. Application of Fly ash-based coagulant in tanning wastewater treatment. Available at http://www.aaqtic.org.ar/congresos/china2009/download/2-5/2-196.pdf. Accessed Jun 2017.

Varshney, K.G., Khan, A.A., Gupta, U. and Maheshwari, S.M., 1996. Kinetics of adsorption of phosphamidon on antimony (V) phosphate cation exchanger: evaluation of

the order of reaction and some physical parameters. *Colloids and Surfaces A: Physicochemical and Engineering Aspects*, 113 (1–2), 19–23.

Yan, G. and Viraraghavan, T., 2003. Heavy-metal removal from aqueous solution by fungus Mucor rouxii. *Water research*, 37(18), 4486–4496.

Yan, M., Wang, D., Ni, J., Qu, J., Chow, C.W. and Liu, H., 2008. Mechanism of natural organic matter removal by polyaluminum chloride: effect of coagulant particle size and hydrolysis kinetics. *Water research*, *42* (13), 3361–3370.

Yan, M., Wang, D., Ni, J., Qu, J., Ni, W. and Van Leeuwen, J., 2009. Natural organic matter (NOM) removal in a typical North-China water plant by enhanced coagulation: Targets and techniques. *Separation and Purification Technology*, *68* (3), 320–327.

Zeldowitsch, J., 1934. Über den mechanismus der katalytischen oxydation von CO an MnO2. *Acta Physicochim. URSS*, 1, 364–449.

Zewail, T.M., Yousef, N.S., 2015. Kinetic study of heavy metal ions removal by ion exchange in batch conical air spouted bed. *Alexandria Engineering Journal*, *54* (1), 83–90

.

CHAPTER 6
MODELLING BEHAVIOURS OF THE PROCESSES OF SYNTHESIS OF COMPLEX COAGULANT AND ACID MINE DRAINAGE TREATMENT USING THE PRODUCED COAGULANT

6.1 Introduction

This chapter presents the development of models for the leaching process of Fe, Al, Si, Mg, and Ca from coal fly ash (CFA) using sulphuric acid, with a new approach based on the Eureqa Newtonian method. The development of mathematical model based on the first principle of material balance to predict the dissolution of CFA with time is presented and discussed in this chapter. The leaching model of a partial differential equation was applied to describe the mass transfer of element as it moves through the CFA particle towards the solution. In addition, this chapter also discusses the development of models for the coagulation process of Al, Fe, Zn, Si, Mn, Mg, Ca, and Ni from acid mine drainage (AMD) using a synthesized CFA-based coagulant, with a new approach based on the Eureqa Newtonian technique.

6.2 Synthesis of the complex coagulant by leaching process

6.2.1 Fitting models analysis

Dissolution of iron

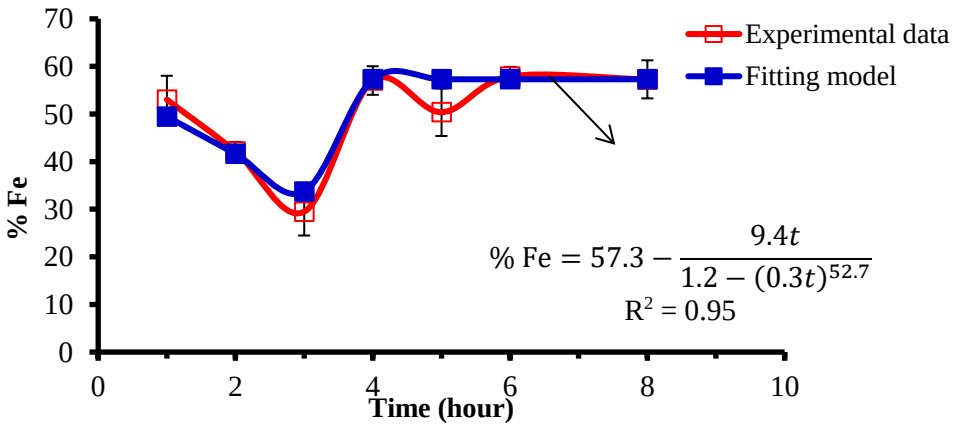

Figure 6.1: Iron recovery from CFA with time.

The behaviour of leaching process of iron followed a damping model. This behaviour can be explained by the dissolution and precipitation of iron, which can be attributed to many factors such as the presence of some ions in the environment, solution concentration, and temperature. This behaviour can be expressed by the following Equation (6.1) with an R^2 value of 0.95:

$$\% \text{ Fe} = 57.3 - \frac{9.4\,t}{1.2-(0.3\,t)^{52.7}} \tag{6.1}$$

As observed from the iron leaching behaviour, below 3 hours the iron concentration decreased significantly in the produced complex coagulant solution. This could be due to the affinity of iron with some ions which may be found in the prepared CFA coagulant solution, such as OH^-, and produce insoluble compounds (precipitates of low permeability) that could coat the iron metal and inhibits mass transfer, and consequently reduce the iron leaching. After 3 hours, the self- inhibition effect of iron to the mass transfer is affected by the dissolution of other ions from the solid site. The leaching kinetics of iron is then modified and enhanced the dissolution of iron from the CFA. As observed, the leaching of both iron and aluminium are affected by the dissolution of calcium, which reduced the self-inhibition process after three and two hours of the leaching process, respectively for iron and aluminium (Figures 6.1 and 6.2). The concentration of calcium ion in solution was not affected by the presence of sulphate ions, and no precipitation of $CaSO_4$ was observed in this investigation. Seidel and Zimmels (1998) observed the precipitation of $CaSO_4$, which enhanced self-inhibition effect to mass transfer at the leaching sites. This effect was not observed in this investigation due to the low content of calcium in the used CFA sample. The dissolution and precipitation reactions during the leaching process of CFA can be described as follows:

a. Metals dissolution

$$M_aO_b + 2bH^+ \leftrightarrow aM^{b+} + bH_2O \tag{6.2}$$

$$Fe_2O_3 + 6H^+ \leftrightarrow 2{F_e}^{3+} + 3H_2O \tag{6.3}$$

$$Al_2O_3 + 6H^+ \leftrightarrow 2Al^{+3} + 3H_2O \tag{6.4}$$

$$CaO + 2H^+ \leftrightarrow Ca^{2+} + H_2O \tag{6.5}$$

b. Metals precipitation

$$M^{b+} + bH_2O \leftrightarrow M(OH)_b \downarrow + bH^+ \quad (6.6)$$

$$F_e{}^{3+} + 3H_2O \leftrightarrow F_e(OH)_3 \downarrow + 3H^+ \quad (6.7)$$

$$Al^{3+} + 3H_2O \leftrightarrow Al(OH)_3 \downarrow + 3H^+ \quad (6.8)$$

The reactivity of calcium and magnesium assist in the breakage of Si–O bond, and then modifies the pore structure of the solid phase (Seidel and Zimmels, 1998). The breakage of Si–O bond in the presence of the H_2SO_4 favours the dissolution of silicon as seen in Figure 6.3. The structure modification allows further chemical attack and enhances the leaching process of aluminium and iron. The acid regenerated by the precipitation reaction favours the reverse reaction; therefore, the dissolution process of metals is improved.

Dissolution of aluminium

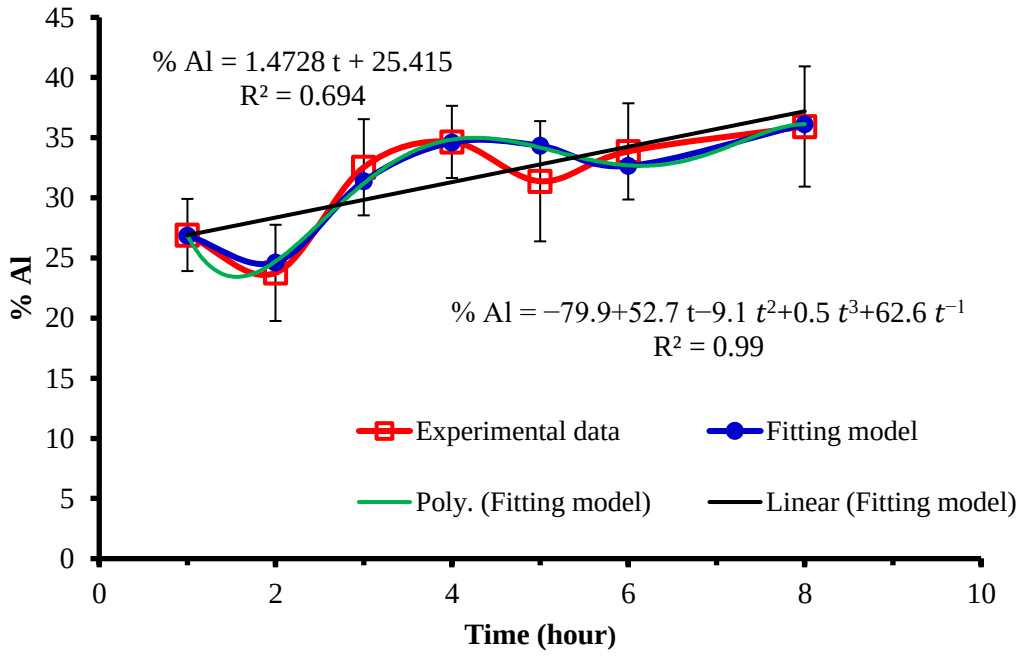

Figure 6.2: Aluminium recovery from CFA with time.

The dissolution of aluminium increases with the leaching time as seen in Figure 6.2. The linear behaviour of the leaching of aluminium is given by % Al = 1.47 t + 25.42 (with a

lower R^2 value) which cannot explain the dumping behaviour of Al. The upper and lower values of aluminium concentration can be attributed to the reversal process (dissolution–precipitation) as discussed above. However, the dissolution behaviour of aluminium can be described by Equation 6.9 using "Eureqa Newtonian" software (with an R^2 value of 0.99).

$$\% \text{ Al } = -79.9 + 52.7\,\text{t} - 9.1\,t^2 + 0.5\,t^3 + 62.6\,t^{-1} \qquad (6.9)$$

Dissolution of silicon

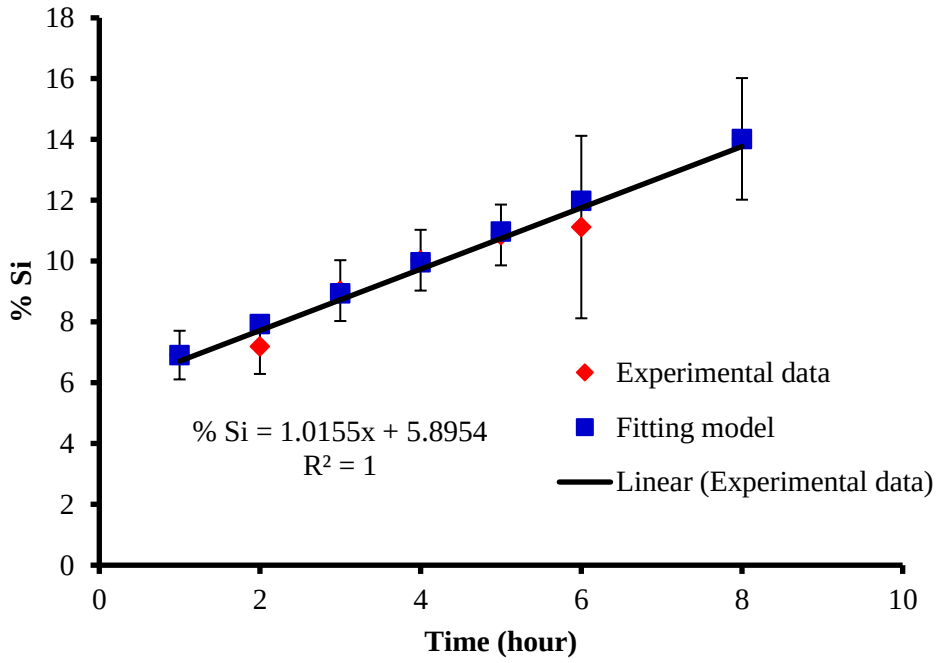

Figure 6.3: Silicon recovery from CFA with time.

The dissolution of silicon increases linearly with the leaching time as discussed above, and is not affected like aluminium and iron. The leaching environment has less effect on the dissolution process of silicon, and this can be attributed to higher concentration of silicon in the used CFA sample. The leaching behaviour of silicon can be expressed by the following Equation (6.10) with an R^2 value of 1.

$$\% \text{ Si } = 1.01\,\text{t} + 5.9 \qquad (6.10)$$

Dissolution of magnesium

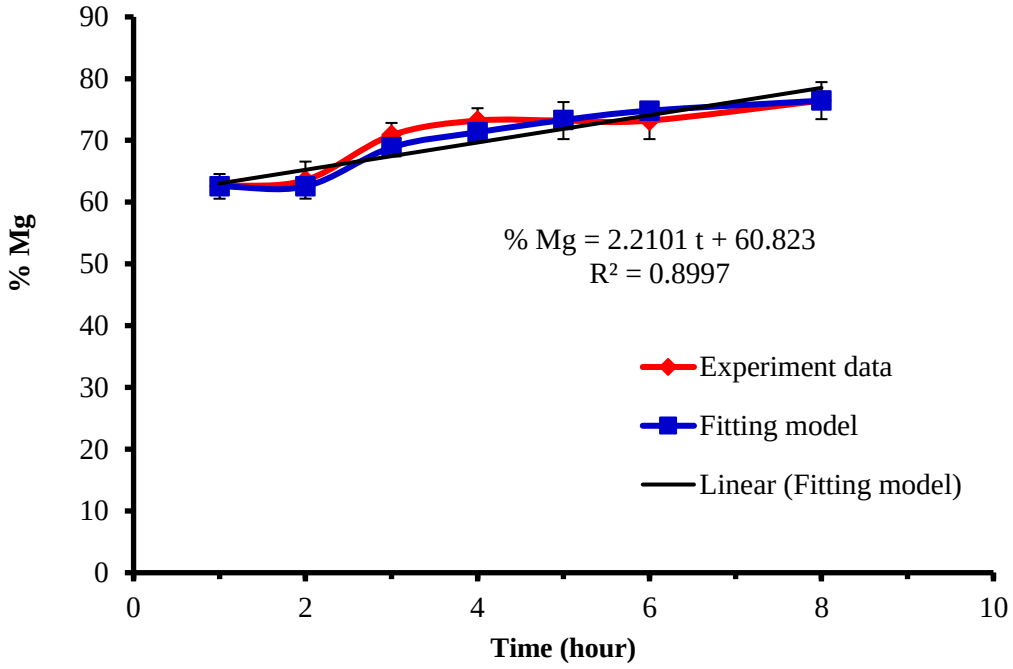

Figure 6.4: Magnesium recovery from CFA with time.

The leaching of magnesium increases with the leaching time up to 4 hours, thereafter no variation of magnesium concentration was observed. The linear behaviour of magnesium dissolution is given by % Mg = 2.2 t + 60.8 with an R^2 value of 0.8997. However, the fitting behaviour software "Eureqa Newtonian" gave gentle curve given by the Equation (6.11) with an R^2 value of 0.91. The linear fitting model can be used to describe the dissolution behaviour of magnesium in acidic solution as the R^2 values for both equations are closer.

$$\% \text{ Mg } = \text{ } 58.7 + 4.1 \text{ t} - 0.2 \, t^2 \qquad (6.11)$$

Dissolution of calcium

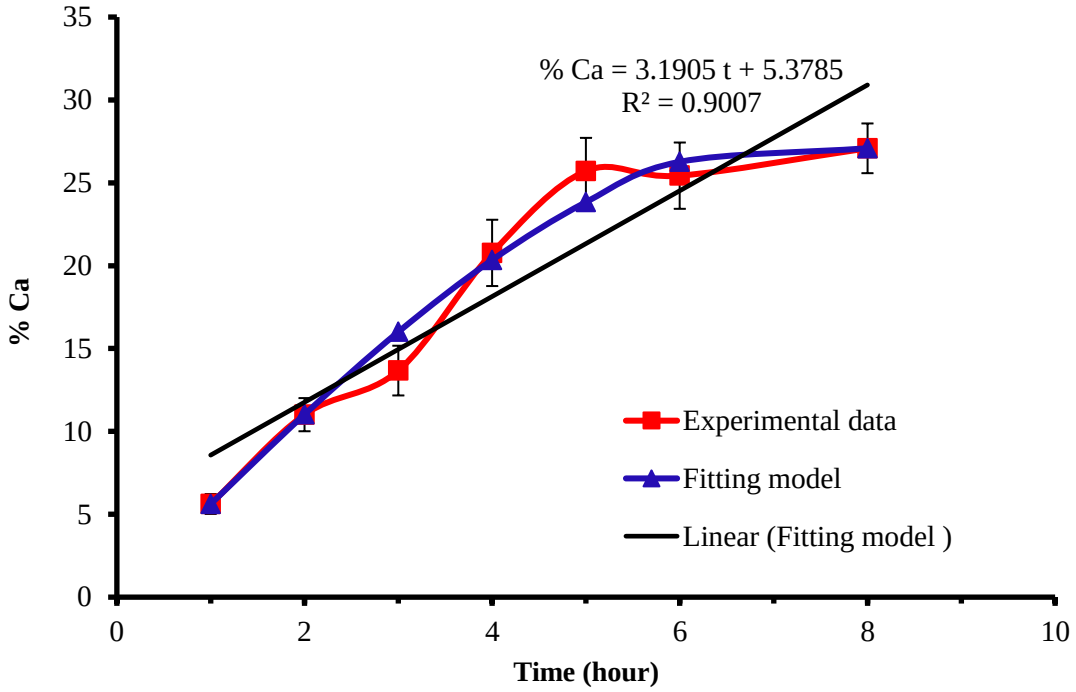

Figure 6.5: Calcium recovery from CFA with time.

Figure 6.5 shows that the leaching of calcium increases with the leaching time up to 5 hours, afterward no variation of calcium concentration was observed. The plateau was reached when no more calcium was extracted from the solid. The linear behaviour of calcium before reaching a plateau is given by % Ca = 0.6 + 5 t with an R^2 value of 0.98. However, the software "Eureqa Newtonian" gave a curve that includes the maximum calcium concentration, and is given by the Equation (6.12) with an R^2 value of 0.98. This third order polynomial equation can be used to predict the dissolution behaviour of calcium. The linear behaviour in Figure 6.5 (% Ca = 3.1905 t + 5.3785, with $R^2 = 0.90$) does not account for the maximum concentration of Ca and therefore cannot be used to describe the dissolution of Ca.

$$\%\,\mathrm{Ca} = 5.6\,\mathrm{t} - 0.04\,t^3 \qquad (6.12)$$

6.2.2 Mathematical modelling development of leaching of coal fly ash

Dissolution model based on the rate of reaction

The models are based on the general dissolution equation given by the following equation discussed above (Equation 6.2):

$$M_aO_b + 2bH^+ \leftrightarrow aM^{b+} + bH_2O$$

The dissolution rate is given by

$$Rate = K_M(C)^m \tag{6.13}$$

where K_M is the dissolution rate constant of the metal and *m* the order of reaction.

$$Rate = -\frac{d}{dt}(C) \tag{6.14}$$

The two above equations give the following

$$-\frac{d}{dt}(C) = K_M(C)^m \tag{6.15}$$

$$-\frac{dC}{C^m} = K_M dt \tag{6.16}$$

By integrating the above equation, the dissolution time can be expressed by the following

$$t = -\frac{1}{K_M}\int_{C_0}^{C_t}\frac{d\,C}{C^m} \tag{6.17}$$

$$t = -\frac{1}{K_M}\int_{C_0}^{C_t} C^{-m}\,dC \tag{6.18}$$

$$t = -\frac{1}{K_M}\left(\frac{C^{-m+1}}{-m+1}\right)\Big|_{C_0}^{C_t} \tag{6.19}$$

Dissolution model from mass balance equation

The dissolution model is based on the conservation of mass by considering below leaching system (Figure 6.6), which comprised the solid CFA and aqueous phase.

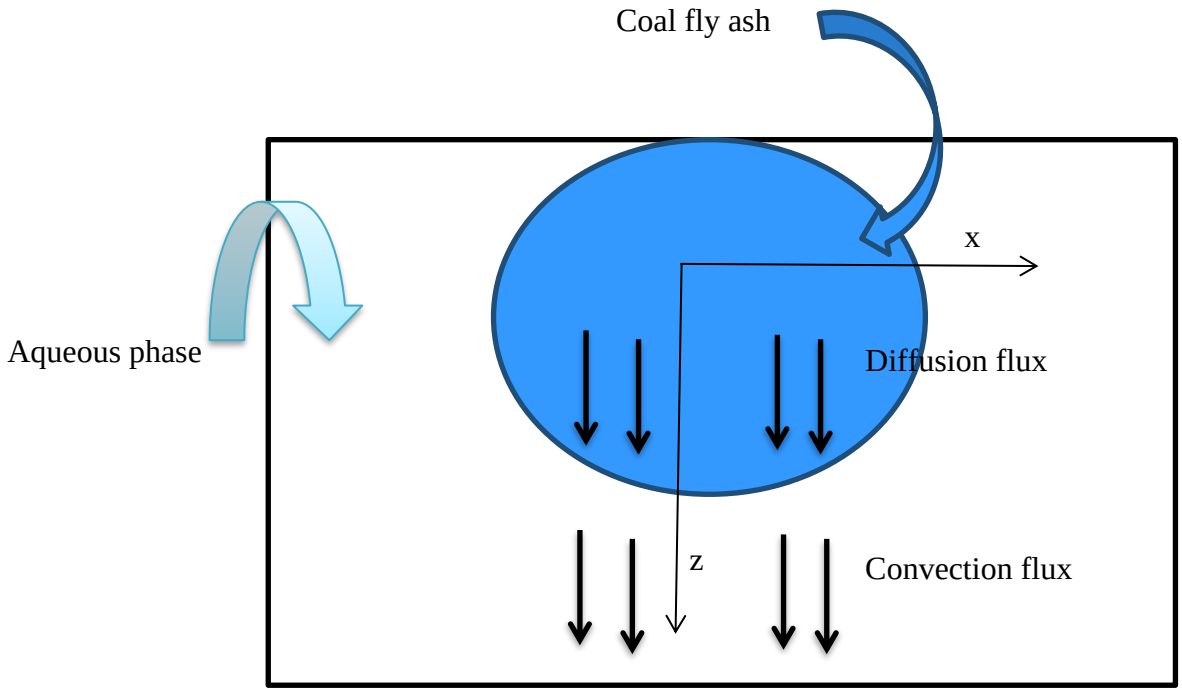

Figure 6.6: Convection and diffusion fluxes during dissolution process of coal fly ash.

Model assumptions: The model assumptions are defined as follows

- The effect of gravity is neglected
- Interaction between particles is neglected
- Precipitation reactions are neglected

Mass balance: The mass balance equation can be written as follows

Diffusive flux of element within the coal fly ash particle into the solid–liquid interface	=	*Dissolution rate of element*	+	*Convective flux of element from solid–fluid interface to the fluid phase*	(6.20)

In a differential form:

$$\frac{\partial}{\partial z}\left(D_{eff}\,\frac{\partial C_M}{\partial z}\right) = \frac{\partial C_M}{\partial t} + K_M(C_{M_t} - C_{M_0})^m \qquad (6.21)$$

where K_M and m are the rate constant and the order of reaction, respectively.

Aluminium:

D = 28 exp [- (114000 + 15000) / RT], T = 150 °C (Paladino and Kingery, 1962)

$D_{eff} = 3.2948 \times 10^{-15}$, $C_{M_0} = 17.01$ and $K = 1.4635$

Assuming a first-order reaction ($m = 1$)

$$3.2948 \text{ x } 10^{-15} \frac{\partial^2 C_M}{\partial z^2} = v \frac{\partial C_M}{\partial z} + 1.4635 \left(C_{M_t} - 17.01 \right)$$

$$3.2948 \text{ x } 10^{-15}\, y'' = v\, y' + 1.4635 \left(\text{y} - 17.01 \right)$$

$$3.2948 \text{ x } 10^{-15}\, y'' = v\, y' + 1.4635 \text{ y} - 1.4635 \text{ x } 17.01)$$

$$y'' = v\, y' + 0.444 \text{ x } 10^{15} \text{ y} - 7.55 \text{ x } 10^{15}$$

$$y'' - v\, y' - 0.444 \text{ x } 10^{15} \text{ y} + 7.55 \text{ x } 10^{15} = 0$$

Given a function E: $y'' - 42.1 \times 10^{-2} y' - 0.444 \times 10^{15} y + 7.55 \times 10^{15} = 0$ and

Let assume a function E(0) given by $y'' - 42.1 \times 10^{-2} y' - 0.444 \times 10^{15} y = 0$

The general solution of E is given by $y = y_H + y_P$ where y_H and y_P are general solution of E(0) and particular solution of E.

If *y* is a solution of E, then the differential equation can be written

$$y'' - 42.1 \times 10^{-2} y' - 0.444 \times 10^{15} y + 7.55 \times 10^{15} = 0 \quad (6.22)$$

And if y_P is a solution of E, the following can be written

$$y_P'' - 42.1 \times 10^{-2} y_P' - 0.444 \times 10^{15} y_P + 7.55 \times 10^{15} = 0 \quad (6.23)$$

Subtracting both Equations 6.22 and 6.23

$$\left(y'' - y_p''\right) - 42.1 \times 10^{-2} (y' - y_P') - 0.444 \times 10^{15} (y - y_P) = 0$$

Based on the derivation rules

$$(y - y_P)'' - 42.1 \times 10^{-2} (y - y_P)' - 0.444 \times 10^{15} (y - y_P) = 0$$

By assuming $y_H = y - y_P$, the solution verified the homogenous equation E(0) and therefore

$$y = y_H + y_P$$

- Let find the expression of y_H solution of E(0)

As the roots of the characteristic polynomial of $Ar^2 + Br + C = 0$ gives delta = 0

$y_H = e^{rz}(k_1 + k_2)$ with $y_1(z) = e^{rz}$ and $y_2(z) = ze^{rz}$

a. $y_1(x) = e^{rz}$ therefore $y_1'(z) = re^{rz}$ and $y_1''(z) = r^2e^{rz}$

$y_1'' - 42.1 \times 10^{-2}y_1' - 0.444 \times 10^{15}y_1 = 0$

$[r^2 - 42.1 \times 10^{-2}r - 0.444 \times 10^{15}]e^{rz} = 0$

As the discriminant is Zero ($b^2 - 4ac = 0$), there is one real solution given by

$2r + 42.1 \times 10^{-2} = 0$ that $r = -21.05 \times 10^{-2}$

$y_1 = e^{(-21.05\times10^{-2z})}$ is a solution of E(0)

b. $y_2(z) = ze^{rz}$ therefore $y_2'(z) = (zr + z')e^{rz}$ and $y_2''(z) = (z'' + 2z'r + zr^2)e^{rz}$

$y_2'' - 42.1 \times 10^{-2}y_2' - o.444 \times 10^{15}y_2 = 0$

$[(z'' + 2z'r + zr^2) - 42.1 \times 10^{-2}(zr + z') - 0.444 \times 10^{15}(z)]e^{rx} = 0$

$z'' + z'(2r - 42.1 \times 10^{-2}) + z(r^2 - 42.1 \times 10^{-2}r - 0.444 \times 10^{15}) = 0$

- Let find the expression of y_P solution of E

Let assume K_1 and K_2 unknown function of x and $y_P = K_1(x)y_1(x) + K_2(x)y_2(x)$

$y_P = K_1e^{(-21.05\times10^{-2}\times z)} + K_2 \times 4.43 \times 10^{14} \times e^{(-21.05\times10^{-2}\times z)}$

The first derivation of y_P is given by

$y_P' = K_1'(x)y_1(x) + K_2'(x)y_2(x) + K_1(x)y_1'(x) + K_2(x)y_2'(x)$

$y_P' = K_1'e^{(-21.05\times10^{-2}\times z)} + K_2' \times 4.43 \times 10^{14} \times e^{(-21.05\times10^{-2}\times z)}$

$- 21.05 \times 10^{6}K_1e^{(-21.05\times10^{-2}\times z)} - 9.32 \times 10^{21}K_2e^{(-21.05\times10^{-2}\times z)}$

Let assume that $K_1'(x)y_1(x) + K_2'(x)y_2(x) = 0$ in order to find a particular solution of E

Then

$K_1'e^{(-21.05\times10^{-2}\times z)} + K_2' \times 4.43 \times 10^{14} \times e^{(-21.05\times10^{-2}\times z)}$=0 (6.24)

Therefore, $y_P' = K_1(x)y_1'(x) + k_2(x)y_2'(x)$

$$= -21.05 \times 10^{-2} K_1 e^{(-21.05\times10^{-2}\times z)} - 9.32 \times 10^{21} K_2 e^{(-21.05\times10^{-2}\times z)}$$

The second derivation of y_P is

$$y_P'' = k_1 4.43 \times 10^{14} e^{(-21.05\times10^{-2}\times z)} + K_2 1.96 \times 10^{29} e^{(-21.05\times10^{-2}\times z)} - K_1' 21.05 \times 10^{-2} e^{(-21.05\times10^{-2}\times z)} - K_2'(x) 9.32 \times 10^{21} e^{(-21.05\times10^{-2}\times z)}$$

Substituting y_P'', y_P', and y_P into E, the equation of E becomes

$$\begin{aligned} & k_1 4.43 \times 10^{14} e^{(-21.05\times10^{-2}\times z)} + K_2 1.96 \times 10^{29} e^{(-21.05\times10^{-2}\times z)} \\ & - K_1' 21.05 \times 10^{-2} e^{(-21.05\times10^{-2}\times z)} - K_2'(x) 9.32 \times 10^{21} e^{(-21.05\times10^{-2}\times z)} \\ & - 42.1 \\ & \times 10^{-2}\left[-21.05 \times 10^{-2} K_1 e^{(-21.05\times10^{-2}\times z)}\right. \\ & \left. - 9.32 \times 10^{21} K_2 e^{(-21.05\times10^{-2}\times z)}\right] \\ & - 0.444 \times 10^{15}\left[K_1 e^{(-21.05\times10^{-2}\times z)} + K_2 4.43 \times 10^{14} e^{(-21.05\times10^{-2}\times z)}\right] \\ & + 7.55 \times 10^{15} = 0 \end{aligned}$$

$$\begin{aligned} & K_1 e^{(-21.05\times10^{-2}\times z)}[4.43 \times 10^{14} + 8.86 \times 10^{14} - 0.444 \times 10^{15}] \\ & + K_2 e^{(-21.05\times10^{-2}\times z)}[1.96 \times 10^{29} + 3.92 \times 10^{29} - 1.97 \times 10^{29}] \\ & + 7.55 \times 10^{15} \\ & - K_1' 21.05 \times 10^{-2} e^{(-21.05\times10^{-2}\times z)} - K_2'(x) 9.32 \times 10^{21} e^{(-21.05\times10^{-2}\times z)} \\ & = 0 \end{aligned}$$

And knowing that

$$K_1'(x) y_1(x) + K_2'(x) y_2(x) = 0$$

$$K_1'(x) y_1'(x) + K_2'(x) y_2'(x) = F(x)$$

$$K_1' e^{(-21.05\times10^{-2}\times z)} + K_2' 4.43 \times 10^{14} e^{(-21.05\times10^{-2}\times z)} = 0$$

$$-K_1' 21.05 \times 10^{-2} e^{(-21.05\times10^{-2}\times z)} - K_2' 9.32 \times 10^{21} e^{(-21.05\times10^{-2}\times z)} = 7.55 \times 10^{15}$$

The solution of the above linear system determined the values of K_1' and K_2' where the determinant of $y_1(x) y_2'(x) - y_1'(x) y_2(x) = 0$ is not zero ($\frac{y_2(x)}{y_1(x)}$ is not constant). Below are the values of K_1' and K_2' from the above linear system.

$$K_1' = -K_2' \times 4.43 \times 10^{14}$$

$$K_2' e^{(-21.05\times10^{-2}\times z)}(4.43\times10^{14}\times21.05\times10^{-2}-9.32\times10^{21})=7.55\times10^{15}$$

$$K_2' = \frac{7.55 \text{ x } 10^{15}}{4.43 \text{ x } 10^{14} \text{ x } 21.05 \text{ x } 10^{-2} - 9.32 \text{ x } 10^{21}} e^{21.05 \text{ x } 10^{-2} z} = 0.00147\, e^{21.05 \text{ x } 10^{-2} z}$$

$$K_1' = 4.43 \text{ x } 10^{14} \text{x } 0.00147\, e^{21.05 \text{ x } 10^{6} z} = 6.5 \text{ x } 10^{11}\, e^{21.05 \text{ x } 10^{6} z}$$

$$K_2' = 0.00147\, e^{21.05 \text{ x } 10^{-2} z} \text{ and } K_2 = \frac{\delta K_2'}{\delta z} = 6.98 \text{ x } 10^{-11}\, e^{21.05 \text{ x } 10^{-2} z}$$

$$K_1' = 6.5 \text{ x } 10^{11}\, e^{21.05 \text{ x } 10^{-2} z} \text{ and } K_1 = \frac{\delta K_1'}{\delta z} = 3.09 \text{ x } 10^{4}\, e^{21.05 \text{ x } 10^{-2} z}$$

Therefore, the general solution for E become

$$y(z) = K_1 y_1(x) + K_2 y_2(x) = 6.98 \text{ x } 10^{-11}\, e^{z\times42.10 \text{ x } 10^{-2}} + 3.09 \text{ x } 10^{4} \times z \times e^{z\times42.10 \text{ x } 10^{-2}} \quad (6.25)$$

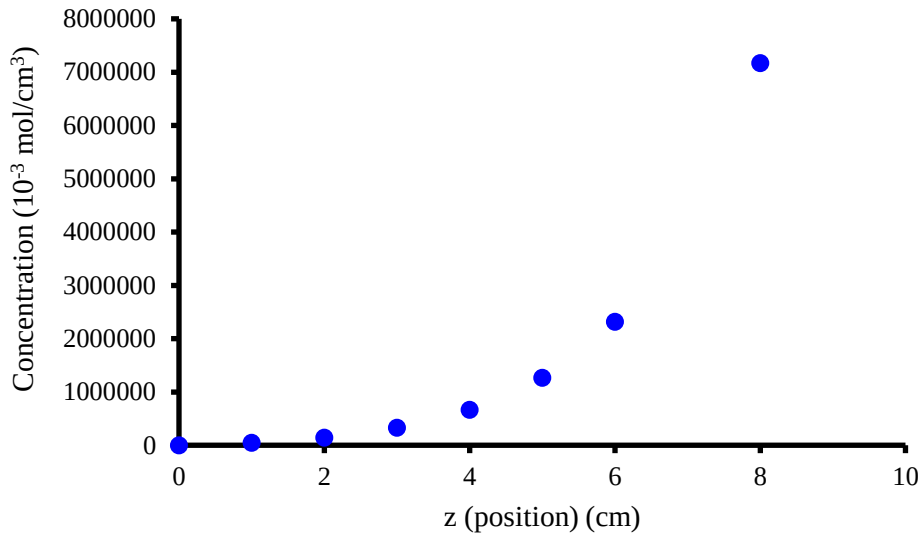

Figure 6.7: Aluminium concentration with position during the leaching process.

Figure 6.7 shown above describes the exponential leaching behaviour of aluminium, which match the behaviour as per the findings of Ghorbani et al. (2013) in leaching Zn.

All other minerals can be modelled using the first principle knowing the diffusion coefficient of the mineral involved, leaching temperature and the speed of the mineral in the reactor. The concentration will have polynomial or exponential behaviour as seen in the work done by Ghorbani et al. (2013).

6.3 Acid mine drainage treatment by coagulation process

6.3.1 Fitting model analysis

In order to understand the coagulation behaviour, Eureqa Newtonian software was used to develop fitting model. The general equation behaviour of the coagulation from Eureqa Newtonian software had polynomial form given by Equation 6.26. The model equation showed two regions with an optimum point (minimum value for % residual adsorbate or maximum value for the coagulation process) that depends on the chemical species involved in the process. The first region of the % residual behaviour had an exponential trend, which confirms the behaviour found by Banihashemi et al. (2008). Banihashemi et al. (2008) obtained an exponential model for iron and aluminium coagulants for predicting the coagulant dose. The second region showed the reverse process with an increase in % residual. More investigation should be done in order to understand the reversal process, which at this stage can be understood as results of concentration gradient. The general equation of the coagulation process model as per Equation 6.26 was confirmed by the work done by Smoczyński et al. (2012) and Smoczyński et al. (2014).

$$Ax^n + Bx^{n-1} + \cdots + Fx + G = 0 \tag{6.26}$$

Coagulation of aluminium

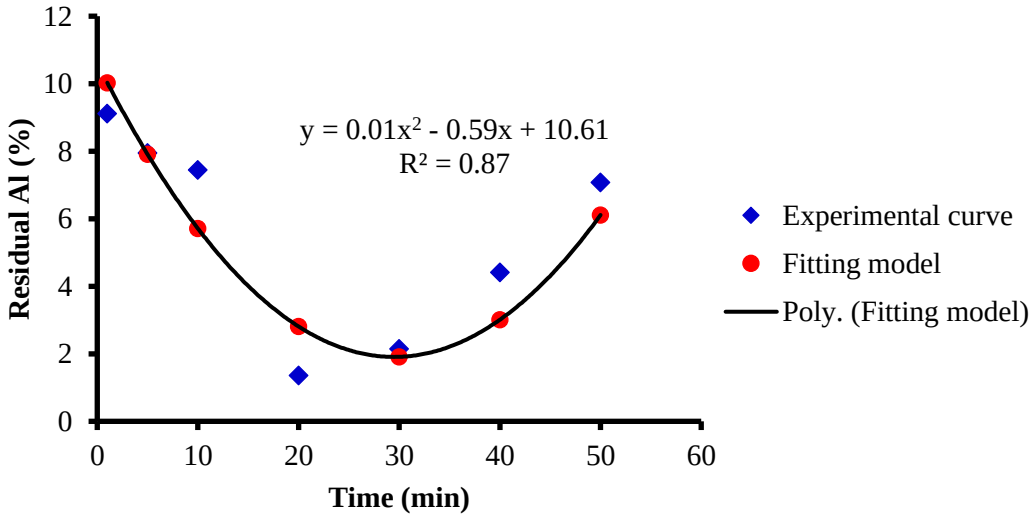

Figure 6.8: Residual aluminium in coal mine wastewater with time.

Figure 6.8 shows that the % residual aluminium decreased up to a minimum value of 1.9 (almost same values for both fitting model and experimental), and then increased. The decrease in % residual alumimium showed that the coagulation process was favoured at the operating conditions of pH and temperature. It can be seen that after 30 minutes, the process efficiency decreases, and the reverse process takes place. The model behaviour of % residual for Al is given by Equation 6.27 with $R^2 = 0.87$.

$$\% \, Al = 0.01x^2 - 0.59x + 10.61 \tag{6.27}$$

Coagulation of iron

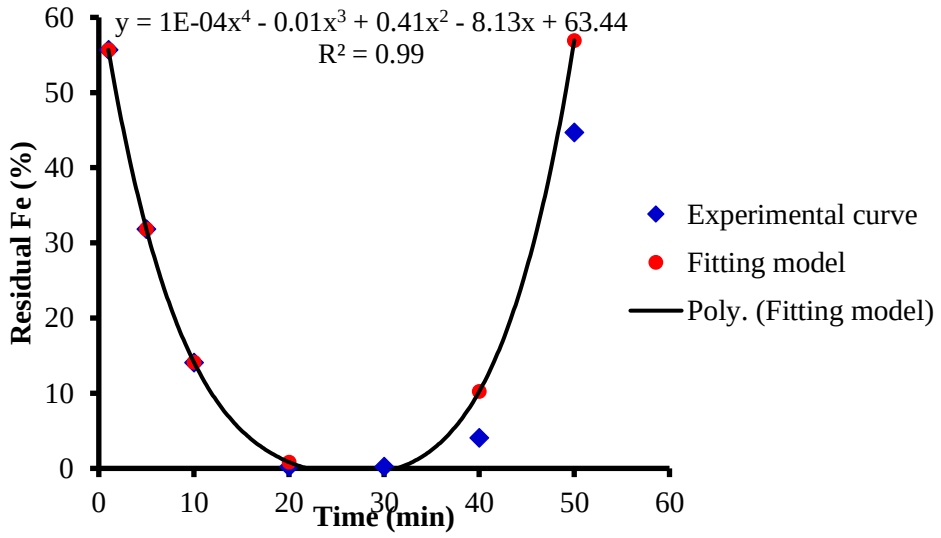

Figure 6.9: Residual iron in coal mine wastewater with time.

As seen in Figure 6.9, the % residual iron decreased with the coagulation time up to a minimum value of -0.46 after that increased. The % residual showed similar polynomial behaviour as aluminium with less deviation 30 minutes seem to be the optimum period for the coagulation process, thereafter an increase in time affected negatively the coagulation process. The behaviour of % residual for Fe is described by a fourth-degree polynomial equation (Equation 6.28) with $R^2 = 0.99$.

$$\% \, Fe = 0.0001x^4 - 0.01x^3 + 0.41x^2 - 8.13x + 63.44 \tag{6.28}$$

Coagulation of zinc

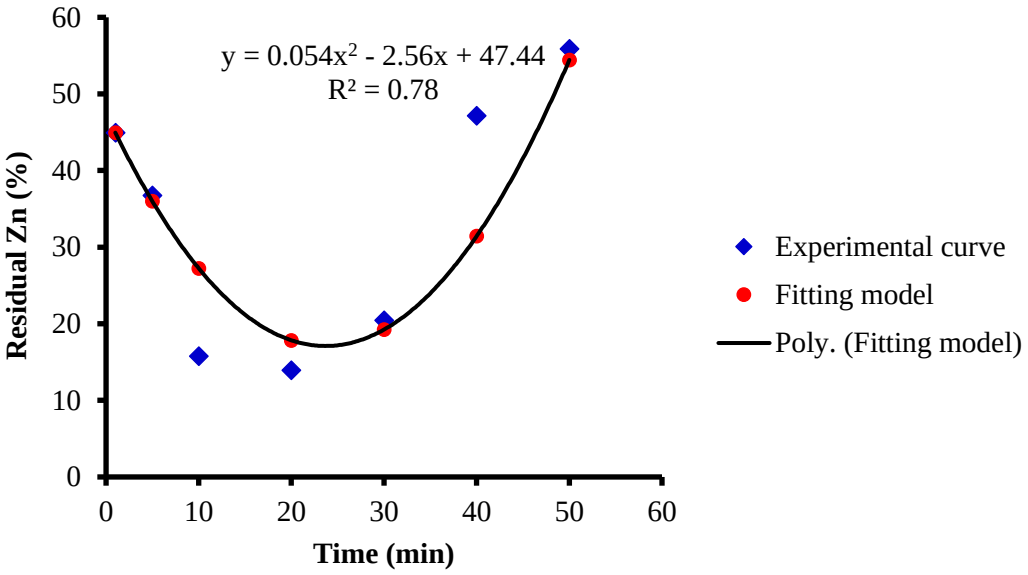

Figure 6.10: Residual zinc in coal mine wastewater with time.

For the coagulation of Zn as seen in Figure 6.10, the % residual zinc decreased up to a minimum value of 17.84 (both fitting model and Experimental gave almost same values), and then increased. When the minimum % residual zinc had been reached, a further increase in time negatively affected the parameters of the AMD treatment process, which was also observed for aluminium and iron. The deviation between the model behaviour and the experimental curve can be attributed to the competition with the reverse process and experimental errors. The polynomial equation model ($R^2 = 0.78$) describing the behaviour of % residual for Zn in coagulated AMD is given below:

$$\% \, Zn = 0.054x^2 - 2.56x + 47.44 \qquad (6.29)$$

Coagulation of silicon

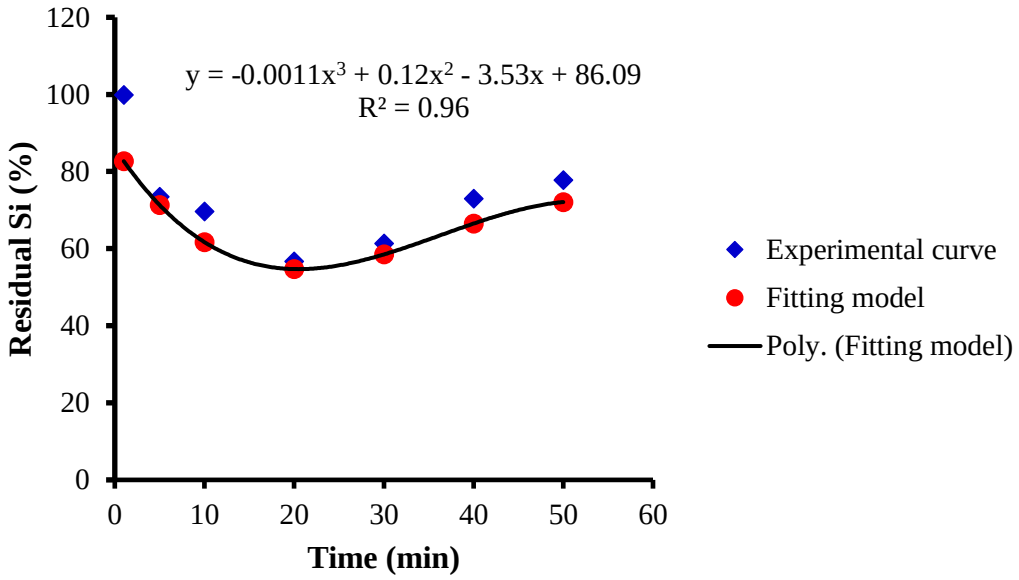

Figure 6.11: Residual silicon in coal mine wastewater with time.

Change in % residual Si in coagulated acid mine effluent is presented in Figure 6.10. An increase in coagulation time increased the effectiveness of Si removal, similarly as in the case of aluminium, iron, and zinc (Figures 6.8–6.10). The minimum value of 54.69 % residual Si was obtained after 20 minutes coagulation time, a further increase in time influenced negatively the process efficiency, which was also observed for aluminium, iron, and zinc (Figures 6.8–6.10). The polynomial equation model, with $R^2 = 0.96$, describing the % residual for Si in coagulated AMD can be expressed as follows:

$$\%\, Si = -0.0011x^3 + 0.12x^2 - 3.53x + 86.09 \qquad (6.30)$$

Coagulation of manganese

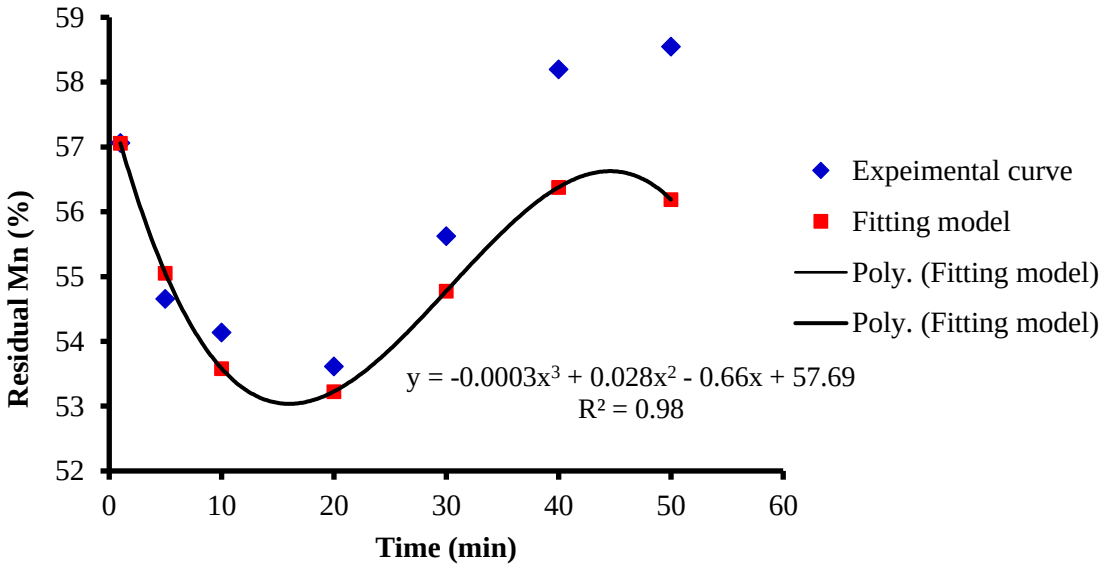

Figure 6.12: Residual manganese in coal mine wastewater with time.

For the coagulation of manganese (Figure 6.12), it was noticed that before 20 minutes, the % residual Mn diminished until a minimum value of 53.23. So, 20 minutes were adopted as the optimum time for manganese coagulation in the model systems. A significant increase in % remaining of manganese was observed after the minimum coagulation time. The behaviour of the % remaining for manganese in AMD coagulation can be described by a third-degree polynomial equation model given below with $R^2 = 0.98$:

$$\%\, Mn = -0.0003x^3 + 0.028x^2 - 0.66x + 57.69 \qquad (6.31)$$

Coagulation of magnesium

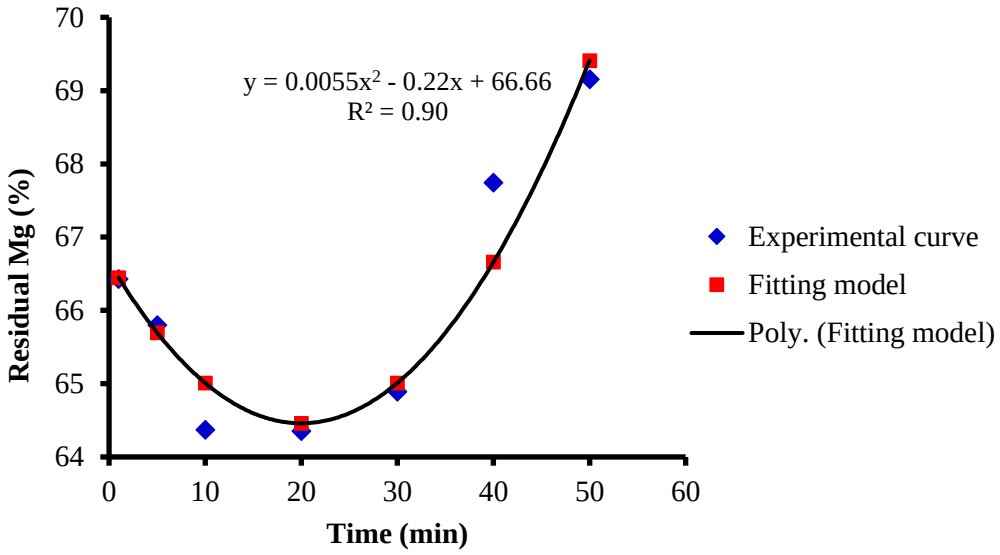

Figure 6.13: Residual magnesium in coal mine wastewater with time.

The remaining percentage of magnesium in coagulated acid mine wastewater is shown in Figure 6.13. The most effective time that gave the lowest value, 64.46 % residual Mg (almost identical value for fitting model and experimental data) was found to be 30 minutes. An increase in the coagulation period increased the percentage of magnesium in the treated AMD. A coagulation period of 30 minutes was sufficient for the adsorption of magnesium on the hydroxide precipitates (coagulant). Beyond 30 minutes, magnesium is no longer destabilized by coagulant (cations and polycations). The equation model (Equation 6.32) for magnesium gave high value of the coefficient of determination, $R^2 = 0.90$. The dependency behaviour is shown in Figure 6.13 and the value of R^2 indicates that the AMD used is susceptible to coagulation treatment.

$$\% Mg = 0.0055x^2 - 0.22x + 66.66 \quad (6.32)$$

Coagulation of calcium

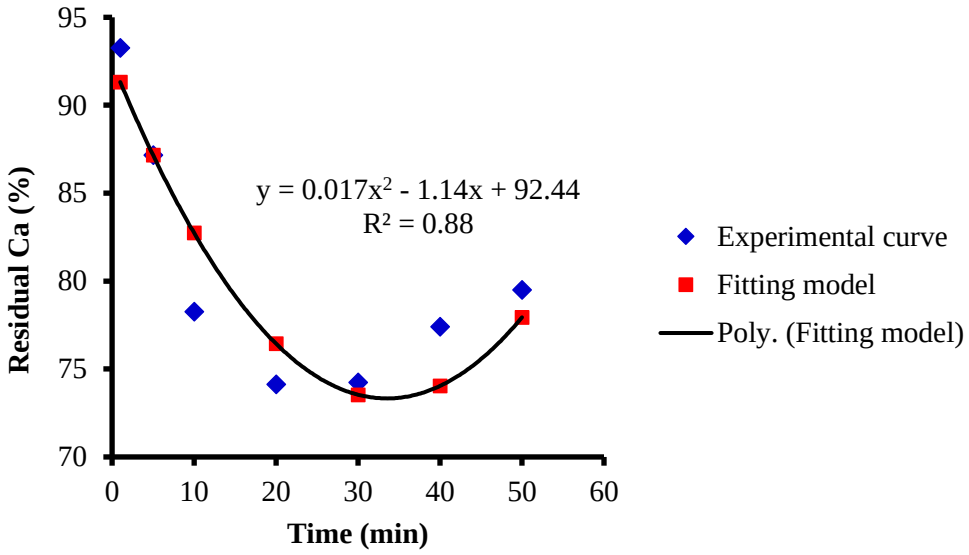

Figure 6.14: Residual calcium in coal mine wastewater with time.

The remaining percentage of calcium in the coagulated acid mine wastewater is presented in Figure 6.14. The effectiveness of the applied model is demonstrated by high value of the coefficient of determination $R^2 = 0.88$. As per above coagulation behaviour, Ca % residual behaviour presented in Figure 6.13 showed a small deviation compared to the proposed model, which could be due to experimental errors and the interaction between chemical species in the coagulation reactor. The optimum time for the process was found at 30 minutes. The proposed model is given by Equation 6.33.

$$\% \, Ca = 0.017x^2 - 1.14x + 92.44 \tag{6.33}$$

Coagulation of nickel

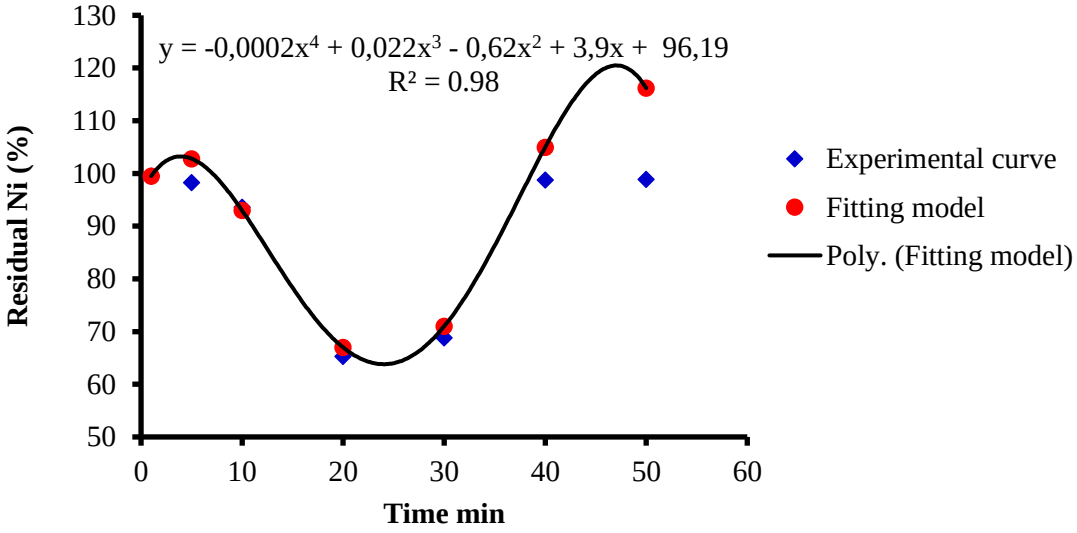

Figure 6.15: Residual nickel in coal mine wastewater with time.

Fitting model and experimental data overlap except for reversal process after 30 minutes. Figure 6.15 suggested that the optimum time for the coagulation process should be 25 minutes. The accuracy of the model can be seen through the R^2 value that is 0.98. Figure 6.15 suggested that the process can be again efficient after 50 minutes; therefore, more investigation should be carried out in order to propose a better polynomial equation. The proposed model is given by the Equation 6.34.

$$\%\, Ni = -0.0002x^4 + 0.022x^3 - 0.62x^2 + 3.9x + 96.19 \qquad (6.34)$$

6.4 Conclusion

It can be concluded from the fitting model studies of the coagulant production that the trend of the dissolution of iron and aluminium was characterized by a damping model due to precipitation and dissolution of iron and aluminium. The precipitation reaction may be related to the presence of OH^- ions in solution which lead to the formation of insoluble compounds. On the other hand, the leaching of other ions, such as calcium, from the solid site favoured the dissolution of both iron and aluminium. Using "Eureqa Newtonian" software, the leaching behaviour of iron can be described by equation

$y = 57.3 - \frac{9.4\,t}{1.2-(0.3\,t)^{52.7}}$ with an R^2 value of 0.95. While the dissolution behaviour of aluminium can be expressed by equation $y = -79.9 + 52.7\,t - 9.1\,t^2 + 0.5\,t^3 + 62.6\,t^{-1}$ with an R^2 value of 0.99. Unlike iron and aluminium, the dissolution of silicon is not influenced by the leaching medium. This is due to silicon high content in the used CFA. The equation $y = 1.01\,t + 5.9$ with an R^2 value of 1 can describe the dissolution behaviour of silicon. For magnesium, the linear fit model that describes the leaching behaviour of magnesium is given by equation: $y = 58.7 + 4.1\,t - 0.2\,t^2$ with a R^2 value of 0.91. The third order polynomial equation (that includes the maximum concentration of calcium), $y = 5.6\,t - 0.04\,t^3$ with a value of R^2 of 0.98, given by the software "Eureqa Newtonian" can be used to predict the dissolution behaviour of calcium.

The mathematical model developed from the first principle of material balance for the CFA dissolution as function of time was

$$y(z) = 6.98 \times 10^{-11}\, e^{42.10 \times 10^{6} z} + 3.09 \times 10^{4} z\, e^{42.10 \times 10^{6} z}$$

For the AMD coagulation process, experimental data were modelled and showed a polynomial equation form as $Ax^n + Bx^{n-1} + \cdots + Fx + G = 0$. The model equations can be summarized as follows where the output and input variables are concentration and time, respectively: the equation obtained for aluminium was $y = 0.01x^2 - 0.59x + 10.61$ with $R^2 = 0.87$, for iron as $y = 0.0001x^4 - 0.01x^3 + 0.41x^2 - 8.13x + 63.44$ with $R^2 = 0.99$, for zinc as $y = 0.054x^2 - 2.56x + 47.44$ with $R^2 = 0.78$, for silicon as $y = -0.0011x^3 + 0.12x^2 - 3.53x + 86.09$ with $R^2 = 0.96$, for manganese as $y = -0.0003x^3 + 0.028x^2 - 0.66x + 57.69$ with $R^2 = 0.98$, for magnesium as $y = 0.0055x^2 - 0.22x + 66.66$ with $R^2 = 0.90$, for calcium as $y = 0.017x^2 - 1.14x + 92.44$ with $R^2 = 0.88$, and for nickel as $y = -0.0002x^4 + 0.022x^3 - 0.62x^2 + 3.9x + 96.19$ with $R^2 = 0.98$.

The above polynomial equations can be used to predict the coagulation behaviour of aluminium, iron, zinc, silicon, manganese, magnesium, calcium, and nickel for AMD treatment plants.

References

Banihashemi, A., Moghadam, M.R.A., Maknoon, R. and Nikazar, M., 2008. Development of a coagulation/flocculation predictive model for turbidity removal from tehran water treatment plants. *Environmental Engineering & Management Journal (EEMJ), 7* (1), 13–16.

Ghorbani, Y., Petersen, J., Becker, M., Mainza, A.N. and Franzidis, J.P., 2013. Investigation and modelling of the progression of zinc leaching from large sphalerite ore particles. *Hydrometallurgy*, *131*, 8-23.

Paladino, A.E. and Kingery, W.D., 1962. Aluminum ion diffusion in aluminum oxide. *The Journal of Chemical Physics*, 37(5), 957−962.

Seidel, A., Zimmels, Y., 1998. Mechanism and kinetics of aluminum and iron leaching from coal fly ash by sulfuric acid. *Chemical Engineering Science* 53 (22), 3835–3852.

Smoczyński, L., Muńska, K.T., Pierożyński, B. and Kosobucka, M., 2012. Electrocoagulation of model wastewater using aluminum electrodes. *Polish Journal of Chemical Technology*, *14* (3), 66–70.

Smoczyński, L., Muńska, K.T., Kosobucka, M., Pierożyński, B., Wardzyńska, R. and Załęska-Chróst, B., 2014. Destabilization of model wastewater in the chemical coagulation process. *Ecological Chemistry and Engineering S*, *21* (2), 269–279.

CHAPTER 7
CONCLUSION AND RECOMMANDETIONS

7.1 Conclusion

7.1.1 Introduction

The coal fly ash (CFA), power plant solid waste abundantly available, can be used as low-cost alternative raw material for the production of coagulant for acid mine drainage (AMD) treatment. Sulphuric acids can be used to leach CFA. The CFA contains valuable elements that can be extracted and used as coagulant in AMD treatment. The main aim of this study was to synthesize a composite coagulant from CFA and subsequently use it to treat AMD through the coagulation process.

In order to achieve the main aim, the objectives of the present study were defined as:

1) To characterize the CFA.
2) To produce a complex coagulant by sulphuric acid leaching of iron, aluminium, silicon, magnesium, and calcium from CFA.
3) To characterize and upgrade the complex coagulant to reach commercial standard as chemicals and substitute source of AMD treatment coagulant.
4) To optimize the coagulant production process parameters.
5) To determine the quality of AMD.
6) To study the coagulation performance of the produced coagulant in treating AMD.
7) To optimize the coagulation process parameters.
8) To model the processes of synthesis of complex coagulant and AMD treatment using the produced coagulant.

7.1.2 Production of coagulant by leaching process

Physicochemical characteristic studies of CFA using XRD pattern, XRF, FTIR, and SEM/EDS graphs confirmed the presence of different minerals in CFA, which may act as

potential inorganic wastewater treatment coagulants. Quartz, mullite and hematite were identified by XRD. The low CaO content as determined by XRF analysis has confirmed that this is a Class F coal fly ash. The FTIR bands in CFA provided evidence for important peaks in the spectrum originating from Si–O and Al–O bending and stretching vibrations. This indicates that CFA has a good potential and could be utilized in coagulant synthesis for the treatment of wastewater.

The pressure leaching process and reaction kinetics of synthesizing a composite coagulant from CFA was studied. Temperature, S/L, H_2SO_4 concentration, and dissolution time play an important role in the characteristics of the composite coagulant. Iron, aluminium, silicon, magnesium, and calcium can be extracted from CFA using H_2SO_4 medium. Optimum conditions are pH 0.3–3.9, 1.5 M H_2SO_4 concentration, temperature = 150 °C, S/L ratio = 0.20, and time = 6 h while stirring speed at 300 rpm using −49 μm particle size. Aluminium, silicon, and calcium dissolve poorly from CFA. This may be attributed to the presence of an unfavourable structure aluminium, silicon, and calcium oxides, resulting from burning coal at high temperatures. The dissolutions of iron and magnesium increase with an increase in temperature, S/L, H_2SO_4 concentration, and dissolution time. The composite coagulant containing polymeric ferric sulphate, polymeric aluminium sulphate, polymeric magnesium sulphate, polymeric silicon sulphate, and polymeric calcium sulphate has been successfully produced by the reaction of CFA with H_2SO_4. The dissolution process involves change in the particle size distribution of the CFA residues. The initial average diameter of 49 μm changed to 47 μm throughout the complete leaching phase. After the leaching process, mineral phases in the untreated CFA sample along with new phases were identified in the treated CFA. H_2SO_4 leaching has affected the morphology of CFA particles. Porous and stem-like structures were formed after the dissolution.

The kinetic investigation of the leaching behaviour of iron, aluminium, silicon, magnesium, and calcium in CFA based on the shrinking core model shows that the rate of the reaction is controlled by mixed controlled mechanism (diffusion and chemical reaction). Investigation of the Arrhenius expression for iron, aluminium, and silicon found that iron required more activation energy for its acid dissolution, followed by aluminium and silicon. The kinetic model investigation revealed that zero-order kinetic model fitted mostly the investigated elements (Al: R^2 = 0.63; Si: R^2 = 0.9733; Ca: R^2 = 0.877 and Mg: R^2 = 0.8180). For Si and magnesium, the half-order kinetic R^2 values were closer to those

of the zero order (0.9704 and 0.8112, respectively). The rate constants of reactions were determined using the rates of the dissolution from the zero-order kinetic model.

7.1.3 Acid mine drainage treatment by coagulation process

The performance of the synthesized composite coagulant is largely understood, in terms of toxic ions, total dissolved solids (TDS), and turbidity removal. The reasons for the effectiveness of the composite coagulant have not been sufficiently explored. A more detailed understanding of the behaviour of these materials is expected to further improve the treatment of water and wastewater. The coagulation process has been studied under different experimental conditions such as pH, coagulant dosage, temperature, and coagulation time. The synthesized composite coagulant was effective in removing Al, Fe, Mn, Mg, Ca, Si, Zn, Ni, TDS, and turbidity in coal mine wastewater. The efficiency of the complex coagulant in coagulating coal mine wastewater is mainly dependent on time, coagulant dosage, and pH value. At a coagulation time of 20 minutes, the complex coagulant was effective in waste effluent treatment. The removal of turbidity has an optimal dosage of 20 mg/L and pH range 6–8. For TDS removal, the composite coagulant favours pH 7 at 20 mg/l coagulant dosage. While the removal of Mn and Mg has an optimal dosage of 20 mg/L at pH 10. For Si and Zn removal, the produced complex coagulant favours 20 mg/L coagulant dosage at pH 9 and 10. An optimal coagulant dosage of 20 mg/L at pH in the range 7–10 was found for the removal of Al. The best coagulation effect for Fe removal was achieved at 2–20 mg/L coagulant dosage at pH values ranging from 6 to 10. For the removal of Ni and Ca, the best results were obtained at coagulant dosages of 10–20 mg/L at pH 10 and 20 mg/L at pH 12, respectively. However, in general due to the multi-component nature of the coal mine wastewater used, optimal process conditions were found to be coagulant dosage = 20 mg/L, pH = 7, and coagulation time = 20 minutes.

The optical microscopy images confirmed the adsorption of impurities (Al, Fe, Mn, Mg, Ca, Zn, Ni, Si, TDS, and turbidity) onto hydroxide precipitates. The SEM/EDS study also made a support to this hypothesis by observing the difference in the concentrations of metal and silicon adsorbed as the pH value increased.

The synthesized composite coagulant was found more efficient than conventional iron and aluminium sulphate coagulants in removing TDS, Ca, Mg, Si, and Zn. while no important

benefit, compared to traditional coagulants, was observed for the removal of Al, Fe, Mn and Ni.

A comprehensive isotherm analysis of the experimental data was performed to determine the best adsorption isotherm models for equilibrium data sets for impurities: Al, Fe, Mn, Mg, Ca, Zn, and Ni on hydroxide precipitates (complex coagulant). The experimental results were analysed using four adsorption isotherm models, viz the Langmuir, Freundlich, Temkin, and BET isotherms. Temkin and BET isotherm models indicated that the adsorptions are, in general, exothermic processes. The Temkin and BET isotherm equations could be considered as the adsorption models for this investigation since their R^2 values were in the appropriate range for all the studied impurities.

Besides, a study on the kinetic model for the description of the present data was performed using adsorption reaction kinetic models such as pseudo-first-order, pseudo-second-order, Elovich, and second-order equations; and adsorption diffusion kinetic models such as Weber-Morris, Boyd, and Bangham‘s equations. Among the different adsorption reaction models studied, the pseudo-second-order model is the best to describe the experimental data. It is therefore proposed that chemisorption was the rate-controlling step for the sorption of pollutants onto hydroxide precipitate. The adsorption diffusion models revealed that both intraparticle diffusion and film diffusion contribute to the coagulation processes. This is based on the intraparticle diffusion coefficients, of the specific pollutants, calculated from the Weber–Morris and boyd’s models which are in the range of $1.8\ 10^{-11}$ to $0.57\ 10^{-13}$ cm^2/sec and $1.05\ 10^{-12}$ to $1.87\ 10^{-12}$ cm^2/sec, respectively, (except for Ni and Ca for the Weber–Morris model). These ranges are appropriate for the case of intraparticle diffusion control. Also, the Bangham model demonstrated that the pore diffusion is the rate-determining factor for these processes (except for Ni and Si). The existence of an intercept from the Boyd’s model, for all the impurities investigated indicates that there is an external diffusion mechanism. In addition, in terms of correlation coefficient, the adsorption kinetics of all the studied pollutants in coal mine wastewater with hydroxide precipitates was well described by the Weber-Morris, Boyd, and bangham models. This indicates that the diffusion mechanism occurred in multiple adsorption stages, namely, film diffusion and intraparticle or pore diffusion.

7.1.4 Modelling behaviours of the processes of synthesis of complex coagulant and acid mine drainage treatment using the produced coagulant

The fitting model investigation using the "Eureqa Newtonian" software for the prediction of the dissolution of iron, aluminium, silicon, magnesium, and calcium from CFA in acidic solution gave the following equations (y is the concentration and *t* the time), respectively: $y = 57.3 - \frac{9.4\,t}{1.2-(0.3\,t)^{52.7}}$ (R^2 value of 0.95); $y = -79.9 + 52.7\,t - 9.1\,t^2 + 0.5\,t^3 + 62.6\,t^{-1}$ (R^2 value of 0.99); $y = 1.01\,t + 5.9$ (R^2 value of 1); $y = 58.7 + 4.1\,t - 0.2\,t^2$ (R^2 value of 0.91); and $y = 5.6\,t - 0.04\,t^3$ (R^2 value of 0.98).

A mathematical model from the first principle of material balance to predict the leaching of CFA with time was developed. The general model equation was

$$y(z) = 6.98 \times 10^{-11}\, e^{42.10 \times 10^6 z} + 3.09 \times 10^4 z\, e^{42.10 \times 10^6 z}$$

The fitting model investigation using the "Eureqa Newtonian" software for the prediction of the coagulation of aluminium, iron, zinc, silicon, manganese, magnesium, calcium, and nickel from AMD by a CFA-based complex coagulant showed a polynomial equation form as $Ax^n + Bx^{n-1} + \cdots + Fx + G = 0$. The model equations can be summarized as follows where the output and input variables are concentration and time, respectively: the equation obtained for aluminium was $y = 0.01x^2 - 0.59x + 10.61$ with $R^2 = 0.87$, for iron as $y = 0.0001x^4 - 0.01x^3 + 0.41x^2 - 8.13x + 63.44$ with $R^2 = 0.99$, for zinc as $y = 0.054x^2 - 2.56x + 47.44$ with $R^2 = 0.78$, for silicon as $y = -0.0011x^3 + 0.12x^2 - 3.53x + 86.09$ with $R^2 = 0.96$, for manganese as $y = -0.0003x^3 + 0.028x^2 - 0.66x + 57.69$ with $R^2 = 0.98$, for magnesium as $y = 0.0055x^2 - 0.22x + 66.66$ with $R^2 = 0.90$, for calcium as $y = 0.017x^2 - 1.14x + 92.44$ with $R^2 = 0.88$, and for nickel as $y = -0.0002x^4 + 0.022x^3 - 0.62x^2 + 3.9x + 96.19$ with $R^2 = 0.98$.

7.1.5 Potential application in industry

In conclusion, the produced complex coagulant based on CFA could be used for the removal of Al, Fe, Mn, Mg, Zn, Ca, Si, Ni, TDS, and turbidity from acid mine wastewater. The CFA is abundantly available but is not quite useful. For this reason, CFA could be considered as economic raw material for the production of coagulant for removal of toxic metals and elements from acid mine wastewater. The coagulant based on CFA may be an

alternative material to more costly coagulants such as commercial poly ferric sulphate for the treatment of AMD containing mixed metal ions and silicon.

7.2 Recommendations

Based on challenges encountered during the course of this study and the need to investigate beyond the set aim of this research, the following recommendations are made.

7.2.1 Production of coagulant by leaching process

- The design of experiments using design expert tools should be conducted prior experimental method in order to optimize the dissolution process.

7.2.2 Acid mine drainage treatment by coagulation process

- Performance investigation of the produced complex coagulant on the removal of other impurities such as dissolved organic matters, sulphide (S) from acid mine wastewater. This will assist in determining the further benefits of CFA–based coagulant compared to that already studied.
- Although an amount of 0.19 mg/L of aluminium can be remained in the treated AMD, if this is consistently discharged into water bodies, it will increase the amount of aluminium over time up to toxic levels. Therefore, future research on removing the remaining aluminium is necessary.
- Investigation of the floc strength and breakage during the coagulation process can be performed.
- Study of the dynamic continuous flow can be performed to get information on the hydrodynamic parameters to use together with the information on the rate of adsorption uptake of pollutants (provided by the kinetics studies in Section 5.7) for design of the adsorption process.
- Safety study for solid residue can be performed to see the remobilization of the adsorbed metals on solid residue which is crucial concern for final landfill disposal and groundwater treatment systems. Toxicity characteristic leaching procedure (TCLP) and synthetic precipitation leaching procedure (SPLP) can be used as leaching methods.

- Study on how the sludge from the coagulation-flocculation process could be effectively managed in an environmentally friendly manner.

APPENDIX A: CHAPTER 4

Table A.1: Data from the effect of time on the dissolution experiments of iron, aluminium, silicon, magnesium, and calcium.

Time (hour)	Recovery (%)				Standard deviation			
	Fe	Al	Si	Mg	Fe	Al	Si	Mg
1	7.97	13.23	10.21	60.15	1.00	1.00	0.20	1.20
2	7.99	13.9	10.4	60.15	2.00	1.60	0.10	1.00
3	8.01	15.17	10.66	59.4	1.00	1.60	0.15	1.00
4	8.04	15.28	10.24	59.72	1.00	2.00	0.25	1.50
5	8.08	15.59	10.37	59.29	2.00	2.20	0.30	1.20
6	8.13	17.66	9.89	59.77	2.50	2.25	0.40	1.60

Table A.2: Data from the effect of sulphuric acid concentration on the dissolution experiments of iron, aluminium, silicon, magnesium, and calcium.

H_2SO_4 concentration (M)	Recovery (%)				Standard deviation			
	Fe	Al	Si	Mg	Fe	Al	Si	Mg
0.5	10.83	14.08	9.06	42.32	0.86	1.20	0.60	1.00
1.0	11.92	14.70	10.65	42.32	0.80	1.20	0.80	1.24
1.5	14.96	16.00	11.59	42.32	0.86	1.40	0.85	1.40
2.0	15.04	16.17	12.63	42.32	1.20	0.90	0.80	1.25
3.0	15.35	16.24	13.01	42.32	1.20	1.66	0.68	1.20
4.0	15.47	16.46	14.11	42.32	1.65	1.90	0.80	1.40
5.0	15.6	16.47	14.5	42.32	1.80	1.66	0.70	1.40
6.0	16.51	17.04	15.37	42.32	1.98	1.64	0.60	1.46

Table A.3: Data from the effect of temperature on the dissolution experiments of iron, aluminium, silicon, magnesium, and calcium.

Temperature (°C)	Recovery (%)					Standard deviation				
	Fe	Al	Si	Mg	Ca	Fe	Al	Si	Mg	Ca
25	7.04	24.23	21.57	60.15	0.00	1.10	2.30	1.00	1.97	1.60
80	7.37	25.42	21.57	62.56	17.67	1.12	2.40	1.10	1.33	1.85
90	8.54	30.91	22.07	65.44	19.98	1.00	2.20	1.10	1.50	2.04
100	9.28	31.57	21.68	68.57	26.09	0.80	2.10	0.90	1.52	2.56
110	12.43	31.76	21.2	69.43	26.31	1.12	1.90	0.85	1.59	1.98
120	14.58	32.21	20.66	71.01	25.95	1.42	1.80	0.90	1.74	1.67
130	30.17	32.62	18.00	72.76	25.86	1.48	1.90	1.10	1.96	1.35
140	35.78	32.84	17.72	73.32	25.45	1.60	1.86	0.80	2.03	1.40
150	39.15	33.7	17.36	75.83	25.34	1.86	1.80	0.85	2.21	2.01
160	45.21	26.74	16.76	75.93	25.02	1.86	1.80	0.90	1.43	1.92
170	71.36	27.23	16.72	76.00	24.95	1.90	1.90	1.00	2.03	1.83
180	85.69	27.27	16.68	76.21	24.90	2.20	1.80	1.10	1.89	1.71
190	98.38	27.25	16.64	76.32	24.58	2.80	2.00	1.20	1.57	1.64

Table A.4: Data from the effect of solid-liquid ratio on the dissolution experiments of iron, aluminium, silicon, magnesium, and calcium.

S/L	Recovery (%)					Standard deviation				
	Fe	Al	Si	Mg	Ca	Fe	Al	Si	Mg	Ca
0.17	96.59	25.51	7.7	75.3	27.02	2.20	2.00	0.60	1.58	1.30
0.2	98.37	28.88	7.81	78.67	27.11	2.00	2.10	0.80	1.64	1.46
0.22	41.01	27.40	7.56	76.73	25.78	2.20	2.00	1.00	1.56	1.38
0.25	40.28	26.30	7.38	76.02	25.48	2.50	2.20	1.10	1.61	1.51
0.33	37.24	24.73	7.30	75.83	25.34	2.20	2.20	0.80	1.73	2.42
0.40	25.23	21.90	7.29	74.42	24.93	2.20	2.00	0.80	1.85	2.02

Table A.5: Data from the effect of time on optimal experimental conditions on the dissolution experiments of iron, aluminium, silicon, magnesium, and calcium.

Time (hour)	Recovery (%)					Standard deviation				
	Fe	Al	Si	Ca	Mg	Fe	Al	Si	Mg	Ca
1	53.04	26.91	6.91	5.62	62.56	5.0	3.0	0.8	2.0	0.6
2	42.15	23.76	7.19	11.01	63.57	2.0	4.0	0.9	3.0	1.0
3	29.48	32.54	9.03	13.67	70.83	5.0	4.0	1.0	2.0	1.5
4	57.04	34.65	10.03	20.77	73.21	3.0	3.0	1.0	2.0	2.0
5	50.39	31.38	10.86	25.71	73.21	5.0	5.0	1.0	3.0	2.0
6	57.9	33.86	11.12	25.43	73.21	2.0	4.0	3.0	3.0	2.0
8	57.29	35.93	14.02	27.08	76.44	4.0	5.0	2.0	3.0	1.5

Table A.6: Data from the Kinetic of dissolution of iron.

Time (hour)	Out	Reacted	X = Conversion	(1- (1-x)^1/3)	1-3(1-x)^2/3 + 2(1-x)	[(1 - x)^(-1/3) -1] + (1/3)ln(1 - x)
0	2.91	0.00	0.000000000	0.666666667	2.000000000	0.000000000
1	1.64	1.27	0.436426117	0.812142039	1.809532245	0,019491515
2	1.82	1.09	0.374570447	0.791523482	1.859696980	0,012900407
3	2.28	0.63	0.216494845	0.738831615	1.953129982	0,003398449
4	1.5	1.41	0.484536082	0.828178694	1.765224785	0,026297713
5	1.65	1.26	0.432989691	0.810996564	1.812519928	0,019067161
6	1.47	1.44	0.494845361	0.831615120	1.755128069	0,027990718
8	1.57	1.34	0.460481100	0.820160367	1.787957157	0,022682918

$$Conversion = \frac{(in - out)}{in} = \frac{(C_0 - C_{sol})}{C_0}$$

Table A.7: Data from the Kinetic dissolution of aluminium.

Time (hour)	Out	Reacted	X = Conversion	(1- (1-x)^1/3)	1-3(1-x)^2/3 + 2(1-x)	[(1 - x)^(-1/3) -1] + (1/3)ln(1 - x)
0	17.01	0.00	0.000000000	0.666666667	2.000000000	0.000000000
1	14.92	2.09	0.122868901	0.707622967	1.984903233	0.000968890
2	14.02	2.99	0.175778954	0.725259651	1.969101759	0.002121506
3	12.75	4.26	0.250440917	0.750146972	1.937279347	0.004768141
4	13.34	3.67	0.215755438	0.738585146	1.953449591	0.003371863
5	13.34	3.67	0.215755438	0.738585146	1.953449591	0.003371863
6	13.55	3.46	0.203409759	0.734469920	1.958624470	0.002947193
8	13.74	3.27	0.192239859	0.730746620	1.963043837	0.002593261

Table A.8: Data from the Kinetic of dissolution of silicon.

Time (hour)	Out	Reacted	X = Conversion	(1- (1-x)^1/3)	1-3(1-x)^2/3 + 2(1-x)	[(1 - x)^(-1/3) -1] + (1/3)ln(1 - x)
0	23.34	0.0	0.000000000	0.666666667	2.000000000	0.00000
1	23.14	0.20	0.00856898	0.669522993	1.999926573	4.11847E-06
2	23.1	0.24	0.010282776	0.670094259	1.999894265	5.94199E-06
3	23.05	0.29	0.012425021	0.67080834	1.999845619	8.69660E-06
4	23.06	0.28	0.011996572	0.670665524	1.999856082	8.10328E-06
5	22.96	0.38	0.016281063	0.672093688	1.999734927	1.49970E-05
6	23.14	0.2	0.00856898	0.669522993	1.999926573	4.11847E-06
8	23.01	0.33	0.014138817	0.671379606	1.999800094	1.12828E-05

Table A.9: Data from the Kinetic dissolution of calcium.

Time (hour)	Out	Reacted	X = Conversion	(1- (1-x)^1/3)	1-3(1-x)^2/3 + 2(1-x)	[(1 - x)^(-1/3) -1] + (1/3)ln(1 - x)
0	4.47	0.00	0.000000000	0.666666667	2.000000000	0.000000000
1	3.99	0.48	0.107382550	0.70246085	1.988468988	0.000726042
2	3.59	0.88	0.196868009	0.732289336	1.961242987	0.002736503
3	4.42	0.05	0.011185682	0.670395227	1.999874881	7.03844E-06
4	4.25	0.22	0.049217002	0.683072334	1.997577687	0.000142306
5	4.41	0.06	0.013422819	0.671140940	1.999819828	1.01608E-05
6	4.00	0.47	0.105145414	0.701715138	1.988944442	0.000694203
8	3.44	1.03	0.230425056	0.743475019	1.946904294	0.003924513

Table A.10: Data from the Kinetic dissolution of magnesium.

Time (hour)	Out	Reacted	X = Conversion	(1- (1-x)^1/3)	1-3(1-x)^2/3 + 2(1-x)	[(1 - x)^(-1/3) -1] + (1/3)ln(1 - x)
0	0.84	0.00	0.000000000	0.666666667	2.000000000	0.000000000
1	0.27	0.57	0.678571429	0.892857143	1.539540816	0.081513069
2	0.34	0.5	0.595238095	0.865079365	1.645691610	0.050379986
3	0.34	0.5	0.595238095	0.865079365	1.645691610	0.050379986
4	0.27	0.57	0.678571429	0.892857143	1.539540816	0.081513069
5	0.28	0.56	0.666666667	0.888888889	1.555555556	0.076045474
6	0.27	0.57	0.678571429	0.892857143	1.539540816	0.081513069
8	0.25	0.59	0.702380952	0.900793651	1.506660998	0.093794153

Aluminium kinetic analysis:

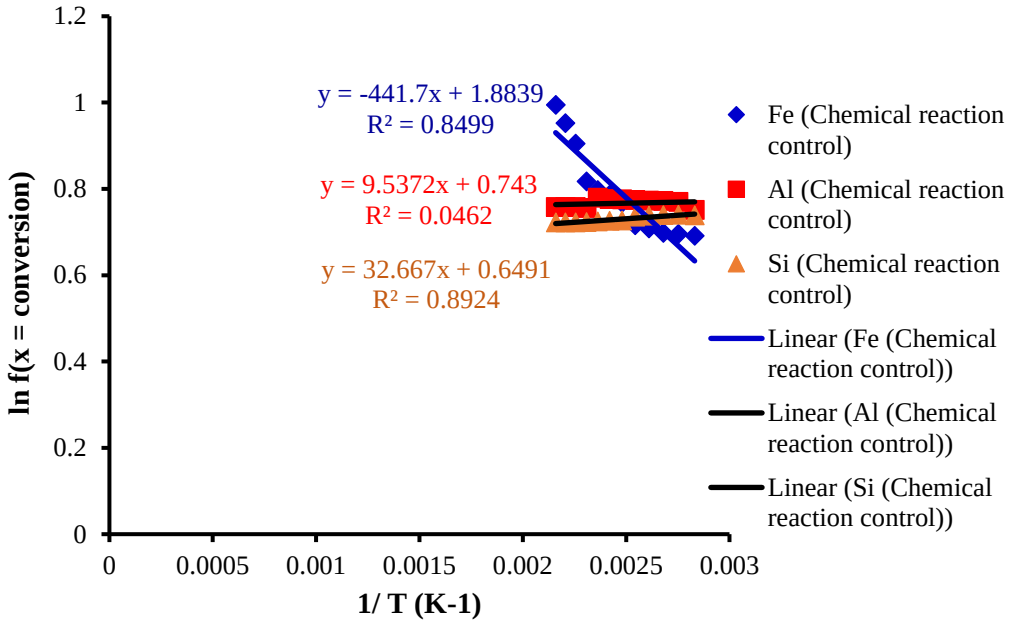

Figure A.1: Determination of Ea using chemical reaction kinetic model

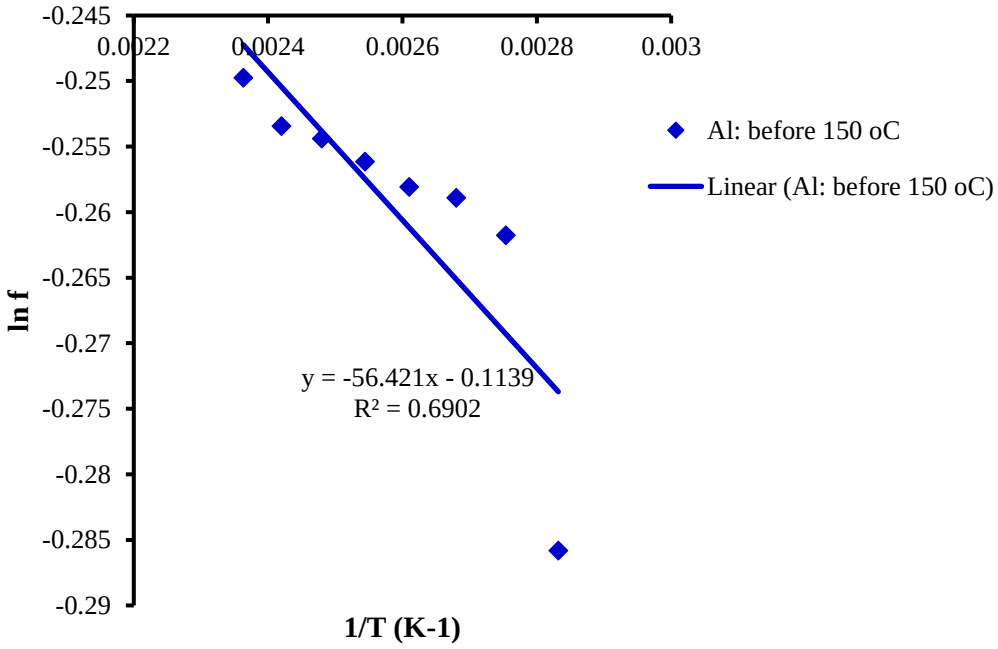

Figure A.2: Determination of Ea using chemical reaction kinetic model for Al before 150 ^{0}C.

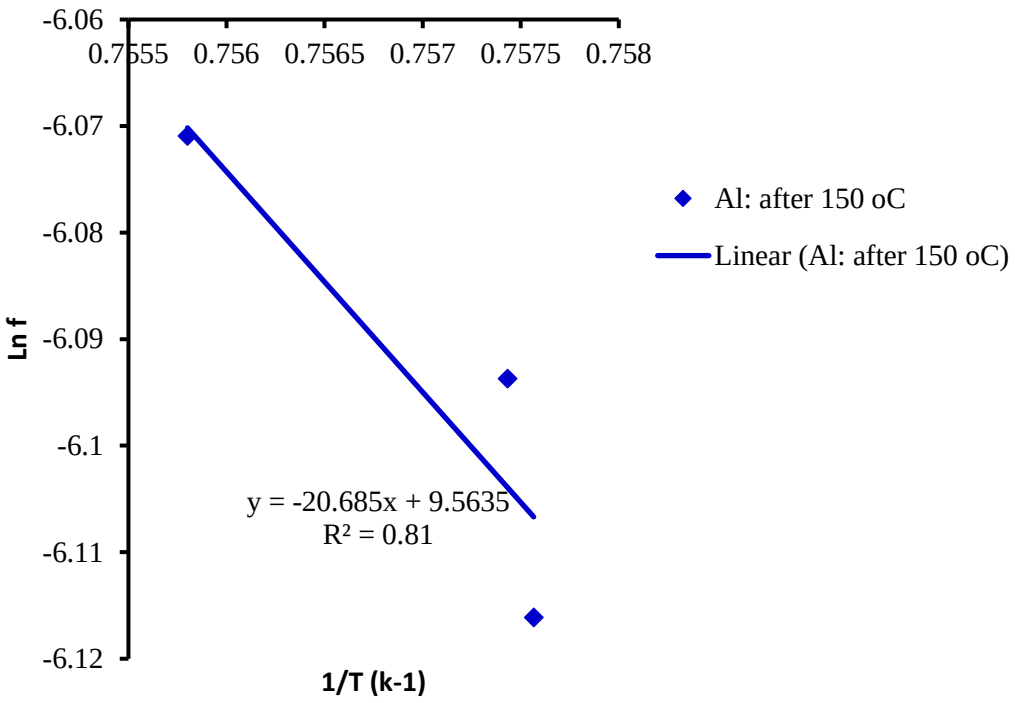

Figure A.3: Determination of Ea using chemical reaction kinetic model for Al after 150 ^{0}C

Table A.11: Data from the zero-order kinetic model.

Time (h)	C_t				
	Fe	**Al**	**Si**	**Ca**	**Mg**
1	53.04	26.91	6.91	5.62	62.56
2	42.15	23.76	7.19	11.01	63.57
3	29.48	32.54	9.03	13.67	70.83
4	57.04	34.65	10.03	20.77	73.21
5	50.39	31.38	10.86	25.71	73.21
6	57.90	33.86	11.12	25.43	73.21
8	57.29	35.93	14.02	27.08	76.44

Table A.12: Data from the half-order kinetic model.

Time (h)	$C_s^{1/2}$				
	Fe	**Al**	**Si**	**Ca**	**Mg**
1	7.28	5.19	2.63	2.37	7.91
2	6.49	4.87	2.68	3.32	7.97
3	5.43	5.70	3.00	3.70	8.42
4	7.55	5.89	3.17	4.56	8.56
5	7.10	5.60	3.30	5.07	8.56
6	7.61	5.82	3.33	5.04	8.56
8	7.57	5.99	3.74	5.20	8.74

Table A.13: Data from the first-order kinetic model.

Time (h)	$\ln C_t$				
	Fe	**Al**	**Si**	**Ca**	**Mg**
1	3.97	3.29	1.93	1.73	4.14
2	3.74	3.17	1.97	2.40	4.15
3	3.38	3.48	2.20	2.62	4.26
4	4.04	3.55	2.31	3.03	4.29
5	3.92	3.45	2.39	3.25	4.29
6	4.06	3.52	2.41	3.24	4.29
8	4.05	3.58	2.64	3.30	4.34

Table A.14: Data from the second-order kinetic model.

Time (h)	$1/C_t$				
	Fe	**Al**	**Si**	**Ca**	**Mg**
1	0.019	0.037	0.145	0.178	0.016
2	0.024	0.042	0.139	0.091	0.016
3	0.034	0.031	0.111	0.073	0.014
4	0.018	0.029	0.100	0.048	0.014
5	0.020	0.032	0.092	0.039	0.014
6	0.017	0.030	0.090	0.039	0.014
8	0.017	0.028	0.071	0.037	0.013

Table A.15: Data from the Hixson-Crowell kinetic model.

Time (h)	$C_t^{1/3}$				
	Fe	**Al**	**Si**	**Ca**	**Mg**
1	3.71	2.96	1.89	1.77	3.92
2	3.44	2.84	1.92	2.21	3.94
3	3.05	3.16	2.07	2.37	4.08
4	3.80	3.22	2.14	2.72	4.12
5	3.65	3.12	2.20	2.92	4.12
6	3.82	3.20	2.21	2.91	4.12
8	3.80	3.26	2.39	2.97	4.18

Table A.16: Data from the Gompertz kinetic model.

log time	$\ln\left[-\ln\left(\frac{C_t}{C_{max}}\right)\right]$				
	Fe	**Al**	**Si**	**Ca**	**Mg**
0,00	-2.41	-1.23	-0.34	0.45	-1.61
0,30	-1.14	-0.88	-0.40	-0.10	-1.69
0,48	-0.39	-2.29	-0.82	-0.38	-2.57
0,60	-4.09	-3.26	-1.09	-1.32	-3.14
0,70	-1.96	-1.99	-1.36	-2.94	-3.14
0,78	-6.36	-2.79	-1.46	-2.76	-3.14
0,90	-4.40	-6.24	-7.25	-7.21	-8.94

APPENDIX B: CHAPTER 5

Table B.1: Data from the effect of the volume of the composite coagulant on the coagulation experiments of TDS.

Coagulant volume (mL)	Residual TDS (%)	standard deviation
0.5	100.00	0.13
1	100.00	0.05
1.5	100.00	0.84
2.5	100.00	0.02
4	100.00	0.61
5	97.86	1.02
6	96.10	1.04
7	92.23	0.76
8	90.79	1.02
9	88.17	0.55
10	86.92	0.09

Table B.2: Data from the effect of the initial concentration of wastewater on the coagulation experiments of TDS.

Residual TDS concentration (%)			
Initial TDS concentration of wastewater (mg/L)	Time (min)		Standard deviation
	0	20	
5276	100.00	74.33	0.23
1902	100.00	120.00	0.19
1206	100.00	108.33	0.24
720.2	100.00	53.21	0.16
578.8	100.00	104.12	0.20

Table B.3: Data from the effect of composite coagulant dosage and pH on the coagulation experiments of TDS.

Residual TDS (%)								Standard deviation						
Coagulant dosage (mg/L)	**pH 4**	**pH 5**	**pH 6**	**pH 7**	**pH 8**	**pH 9**	**pH 10**	**pH 4**	**pH 5**	**pH 6**	**pH 7**	**pH 8**	**pH 9**	**pH 10**
0	100.00	100.00	100.00	100.00	100.00	100.00	100.00	0.00	0.00	0.00	0.00	0.00	0.00	0.00
2	65.65	64.46	77.87	71.15	78.23	88.75	95.07	1.00	0.90	1.40	0.40	1.00	0.53	0.06
5	62.14	57.36	69.81	61.11	64.94	81.63	88.14	1.20	1.50	1.30	1.31	1.40	1.80	0.48
10	60.54	55.44	62.36	53.21	58.91	67.16	79.58	1.03	1.80	1.40	1.92	1.00	1.40	1.34
20	60.33	53.55	53.47	42.78	50.58	62.02	67.18	1.30	1.22	1.23	1.28	1.27	2.00	1.43
30	71.05	68.77	71.09	72.63	73.26	79.98	87.57	1.90	1.40	1.27	1.23	0.01	1.60	1.64
40	76.40	72.05	74.62	85.82	79.45	93.22	98.13	1.50	1.27	1.00	1.03	1.60	1.25	1.08
50	83.00	74.56	78.12	96.51	87.21	100.00	100.00	1.49	1.60	1.50	1.24	1.30	1.47	1.39

Table B.4: Data from the effect of composite coagulant dosage and pH on the coagulation experiments of iron.

	Residual Fe (%)							Standard deviation						
Coagulant dosage (mg/L)	**pH 4**	**pH 5**	**pH 6**	**pH 7**	**pH 8**	**pH 9**	**pH 10**	**pH 4**	**pH 5**	**pH 6**	**pH 7**	**pH 8**	**pH 9**	**pH 10**
2	99.71	98.45	0.52	0.27	0.69	0.82	0.22	0.02	0.02	0.06	0.00	0.00	0.03	0.00
5	99.70	88.75	0.45	0.14	0.64	0.66	0.29	0.02	0.01	0.00	0.00	0.05	0.02	0.00
10	98.92	71.23	0.35	0.07	0.12	0.20	0.27	0.02	0.01	0.00	0.00	0.00	0.00	0.00
20	96.82	49.01	6.04	0.23	0.26	0.01	0.28	0.00	0.02	0.00	0.00	0.00	0.00	0.00
30	414.79	364.12	326.16	4.86	56.55	0.25	0.04	0.02	0.13	0.09	0.04	0.01	0.00	0.00
40	489.55	472.80	474.69	265.28	187.59	0.15	0.25	0.01	0.14	0.02	0.02	0.04	0.00	0.00
50	605.38	550.98	542.97	402.26	323.17	0.58	0.12	0.12	0.04	0.07	0.05	0.03	0.00	0.00

Table B.5: Data from the effect of composite coagulant dosage and pH on the coagulation experiments of aluminium.

	Residual Al (%)							Standard deviation						
Coagulant dosage (mg/L)	**pH 4**	**pH 5**	**pH 6**	**pH 7**	**pH 8**	**pH 9**	**pH 10**	**pH 4**	**pH 5**	**pH 6**	**pH 7**	**pH 8**	**pH 9**	**pH 10**
2	55.94	27.86	1.01	0.43	0.36	1.23	4.70	0.14	0.54	0.05	0.03	0.02	0	0.04
5	52.85	23.73	0.05	0.02	0.26	0.96	3.53	0.10	0.05	0.00	0.00	0.04	0.03	0.08
10	53.63	22.74	1.40	0.03	0.21	0.12	0.64	0.06	0.07	0.02	0.00	0.00	0.00	0.01
20	54.21	20.82	1.74	1.36	0.14	0.92	0.40	0.14	0.07	0.01	0.00	0.00	0.01	0.00
30	77.71	47.47	25.97	7.59	0.49	0.02	0.52	0.54	0.34	0.47	0.12	0.01	0.00	0.00
40	86.47	64.38	41.08	14.45	1.38	0.06	0.35	0.47	0.27	0.23	0.01	0.04	0.00	0.00
50	94.22	74.36	59.26	24.34	10.22	0.05	0.24	0.62	0.23	0.13	0.15	0.01	0.00	0.01

Table B.6: Data from the effect of composite coagulant dosage and pH on the coagulation experiments of manganese.

	Residual Mn (%)							Standard deviation						
Coagulant dosage (mg/L)	**pH 4**	**pH 5**	**pH 6**	**pH 7**	**pH 8**	**pH 9**	**pH 10**	**pH 4**	**pH 5**	**pH 6**	**pH 7**	**pH 8**	**pH 9**	**pH 10**
2	66.91	64.66	59.50	58.16	55.32	29.98	2.76	0.03	0.04	0.03	0.05	0.04	0.04	0.03
5	66.41	61.12	57.71	57.38	53.04	25.32	2.12	0.07	0.04	0.03	0.03	0.03	0.03	0.01
10	61.73	59.98	54.01	51.73	35.50	13.52	1.28	0.03	0.04	0.05	0.05	0.03	0.02	0.00
20	66.66	66.28	56.61	53.61	42.43	28.40	0.57	0.03	0.11	0.14	0.03	0.04	0.02	0.00
30	70.21	66.10	63.40	58.90	58.24	50.47	13.46	0.05	0.15	0.07	0.07	0.04	0.05	0.04
40	72.65	66.28	64.25	60.80	64.09	40.12	34.13	0.04	0.09	0.06	0.03	0.03	0.02	0.04
50	69.10	66.75	69.37	62.91	64.80	56.36	53.93	0.05	0.05	0.04	0.03	0.03	0.06	0.05

Table B.7: Data from the effect of composite coagulant dosage and pH on the coagulation experiments of silicon.

Residual Si (%)								Standard deviation						
Coagulant dosage (mg/L)	**pH 4**	**pH 5**	**pH 6**	pH 7	**pH 8**	**pH 9**	**pH 10**	**pH 4**	**pH 5**	**pH 6**	pH 7	**pH 8**	**pH 9**	**pH 10**
2	83.37	82.57	71.95	58.98	51.55	46.14	32.77	0.00	0.00	0.00	0.00	0.00	0.00	0.00
5	82.02	81.32	70.08	58.49	49.57	37.94	32.90	0.01	0.00	0.00	0.00	0.00	0.00	0.00
10	83.33	81.66	70.01	57.37	48.91	33.69	29.79	0.01	0.01	0.00	0.00	0.00	0.00	0.01
20	83.90	83.49	71.99	56.64	41.91	30.61	28.62	0.01	0.01	0.01	0.00	0.00	0.00	0.00
30	83.50	82.27	80.29	68.71	61.76	40.39	33.16	0.01	0.01	0.01	0.01	0.00	0.00	0.00
40	83.97	82.26	79.74	72.66	63.80	46.56	46.39	0.00	0.00	0.01	0.00	0.00	0.00	0.00
50	83.77	82.05	83.10	75.79	70.53	54.10	45.81	0.00	0.01	0.01	0.01	0.01	0.00	0.00

Table B.8: Data from the effect of composite coagulant dosage and pH on the coagulation experiments of magnesium.

Residual Mg (%)										Standard deviation								
Coagulant dosage (mg/L)	**pH 4**	**pH 5**	**pH 6**	**pH 7**	**pH 8**	**pH 9**	**pH 10**	**pH 11**	**pH 12**	**pH 4**	**pH 5**	**pH 6**	**pH 7**	**pH 8**	**pH 9**	**pH 10**	**pH 11**	**pH 12**
2	70.06	69.84	68.81	68.00	67.74	61.38	44.97	12.69	1.36	0.25	0.17	0.35	0.18	0.26	0.13	0.16	0.00	0.00
5	69.89	68.54	65.49	66.89	67.03	58.52	34.08	10.61	0.03	0.12	0.05	0.20	0.23	0.14	0.16	0.15	0.02	0.00
10	69.60	67.15	65.23	66.01	65.78	57.52	20.89	10.44	1.15	0.20	0.25	0.28	0.20	0.27	0.36	0.08	0.00	0.00
20	68.29	66.56	65.34	64.35	63.37	57.79	14.79	8.33	0.66	0.24	0.28	0.41	0.17	0.21	0.17	0.01	0.00	0.00
30	74.31	72.03	68.17	69.21	67.04	63.22	38.64	22.39	12.91	0.17	0.43	0.19	0.53	0.10	0.20	0.10	0.00	0.00
40	74.83	72.48	70.21	69.53	70.15	63.67	55.11	27.49	17.55	0.26	0.28	0.64	0.04	0.16	0.14	0.12	0.00	0.00
50	75.88	73.23	75.33	69.84	70.93	64.68	63.85	33.81	26.91	0.11	0.52	0.31	0.33	0.22	0.27	0.13	0.03	0.00

Table B.9: Data from the effect of composite coagulant dosage and pH on the coagulation experiments of calcium.

Residual Ca (%)										Standard deviation								
Coagulant dosage (mg/L)	**pH 4**	**pH 5**	**pH 6**	**pH 7**	**pH 8**	**pH 9**	**pH 10**	**pH 11**	**pH 12**	**pH 4**	**pH 5**	**pH 6**	**pH 7**	**pH 8**	**pH 9**	**pH 10**	**pH 11**	**pH 12**
2	86.55	81.69	74.08	73.47	69.79	65.87	61.39	56.94	20.44	0.25	0.18	0.38	0.27	0.31	0.25	0.23	0.01	0.01
5	84.68	80.75	73.37	72.95	68.76	65.20	58.84	53.92	17.03	0.34	0.06	0.37	0.30	0.32	0.30	0.22	0.00	0.00
10	86.26	82.18	75.30	71.95	68.75	64.93	55.21	43.04	13.15	0.36	0.33	0.41	0.32	0.38	0.35	0.17	0.01	0.00
20	87.80	85.39	75.98	74.13	68.67	64.55	54.20	34.36	6.88	0.38	0.22	0.49	0.12	0.31	0.26	0.19	0.01	0.00
30	89.00	86.71	79.35	76.16	70.49	66.26	64.59	47.25	13.97	0.28	0.63	0.14	0.13	0.15	0.22	0.24	0.00	0.01
40	88.86	85.90	83.67	80.11	74.58	72.53	73.88	55.50	23.76	0.32	0.23	0.92	0.05	0.08	0.13	0.19	0.01	0.00
50	88.72	85.82	84.48	79.61	75.83	74.69	74.43	57.12	24.87	0.22	0.71	0.45	0.41	0.19	0.32	0.08	0.00	0.00

Table B.10: Data from the effect of composite coagulant dosage and pH on the coagulation experiments of zinc.

Residual Zn (%)								Standard deviation						
Coagulant dosage (mg/L)	**pH 4**	**pH 5**	**pH 6**	**pH 7**	**pH 8**	**pH 9**	**pH 10**	**pH 4**	**pH 5**	**pH 6**	**pH 7**	**pH 8**	**pH 9**	**pH 10**
2	68.80	66.43	52.25	13.95	9.22	1.55	0.97	0.00	0.00	0.01	0.01	0.01	0.00	0.00
5	66.90	66.15	48.22	5.36	4.80	0.91	1.21	0.00	0.00	0.01	0.01	0.00	0.00	0.00
10	66.07	66.14	44.33	9.05	2.37	0.69	1.26	0.00	0.00	0.01	0.00	0.00	0.00	0.00
20	65.68	65.86	42.79	13.95	0.61	0.36	1.13	0.00	0.01	0.01	0.00	0.00	0.00	0.00
30	71.05	66.41	61.01	47.53	32.57	0.67	1.14	0.01	0.01	0.01	0.02	0.00	0.00	0.00
40	72.60	67.91	60.78	50.69	37.67	1.43	0.26	0.01	0.00	0.00	0.00	0.00	0.00	0.00
50	72.65	68.55	65.74	56.97	54.16	15.07	1.33	0.00	0.01	0.00	0.00	0.00	0.00	0.00

Table B.11: Data from the effect of composite coagulant dosage and pH on the coagulation experiments of nickel.

	Residual Ni (%)							Standard deviation						
Coagulant dosage (mg/L)	**pH 4**	**pH 5**	**pH 6**	**pH 7**	**pH 8**	**pH 9**	**pH 10**	**pH 4**	**pH 5**	**pH 6**	**pH 7**	**pH 8**	**pH 9**	**pH 10**
2	140.71	136.33	128.47	83.49	78.24	36.74	4.74	0.01	0.01	0.02	0.01	0.01	0.00	0.02
5	125.89	122.27	92.25	72.89	49.15	8.76	1.34	0.01	0.01	0.00	0.00	0.01	0.01	0.00
10	100.31	101.43	68.51	51.34	21.37	2.17	1.02	0.01	0.02	0.01	0.01	0.01	0.00	0.00
20	118.19	104.97	86.47	93.52	31.92	10.20	0.86	0.00	0.01	0.01	0.00	0.00	0.01	0.00
30	310.00	295.00	282.86	276.67	229.34	62.91	1.87	0.01	0.01	0.02	0.05	0.01	0.01	0.00
40	367.67	341.90	322.24	280.00	327.38	68.69	66.52	0.02	0.00	0.03	0.02	0.01	0.00	0.02
50	413.33	402.62	364.52	355.71	338.81	260.00	181.95	0.01	0.02	0.01	0.00	0.01	0.01	0.01

Table B.12: Data from the effect of composite coagulant dosage and pH on the coagulation experiments of turbidity.

Residual turbidity (%)								Standard deviation						
Coagulant dosage (mg/L)	**pH 4**	**pH 5**	**pH 6**	**pH 7**	**pH 8**	**pH 9**	**pH 10**	**pH 4**	**pH 5**	**pH 6**	**pH 7**	**pH 8**	**pH 9**	**pH 10**
2	0.84	0.71	0.60	0.38	0.24	0.63	0.76	0.35	1.00	1.00	0.03	978.00	0.11	0.26
5	0.69	0.53	0.41	0.25	0.14	0.50	0.68	0.48	0.20	0.40	0.35	0.15	0.31	0.31
10	0.62	0.39	0.22	0.20	0.11	0.39	0.64	0.34	0.03	0.00	0.44	0.09	0.42	0, 291
20	0.56	0.34	0.00	0.00	0.00	0.36	0.50	0.00	0.30	0.45	0.35	0.32	0.13	0.28
30	0.72	0.26	0.17	0.17	0.18	0.46	0.57	0.60	0.90	0.00	0.36	0.24	0.73	0.12
40	0.88	0.27	0.22	0.19	0.23	0.72	0.60	0.25	0.50	0.60	0.65	0.73	0.01	0.10
50	0.97	0.38	0.24	0.29	1.03	1.17	1.15	0.47	0.49	0.93	0.89	0.36	0.51	0.33

Table B.13: Data from the effect of composite coagulant dosage on the final pH of wastewater experiments.

Coagulant dosage (mg/L)	pH 4	pH 5	pH 6	pH 7	pH 8	pH 9	pH 10	pH 11	pH 12
0	4.00	5.00	6.00	7.00	8.00	9.00	10.00	11.00	12.00
2	4.41	4.54	5.32	6.35	6.20	6.76	8.11	8.77	11.08
5	4.46	4.84	5.95	6.26	6.28	7.38	8.25	8.91	11.22
10	4.10	5.37	5.60	6.02	6.20	6.63	7.28	7.93	11.05
20	4.32	4.97	5.56	5.58	6.29	6.60	7.39	8.04	11.14
30	3.96	4.65	4.70	5.15	5.92	6.29	7.01	7.66	10.67
40	3.63	4.41	4.74	6.14	5.05	6.80	6.64	7.39	10.29
50	3.73	4.40	4.61	4.88	4.55	6.29	7.74	8.48	11.47

Table B.14: Data from the effect of temperature on the coagulation experiments.

Temperature (ºC)	Residual metal, silicon, and TDS concentrations (%)									Standard deviation								
	Fe	Al	Ni	Mn	Si	Zn	Mg	Ca	TDS	Fe	Al	Ni	Mn	Si	Zn	Mg	Ca	TDS
20	0.23	1.36	93.52	53.60	56.64	13.90	64.35	74.12	42.78	0.00	0.00	0.00	0.00	0.00	0.00	0.17	0.12	0.04
25	0.23	2.27	92.67	54.41	57.82	13.23	64.72	74.41	43.29	0.22	0.63	0.06	0.31	0.00	0.00	0.02	0.15	0.12
30	0.20	1.94	94.33	53.55	56.18	14.76	65.52	74.13	44.64	0.23	0.20	0.28	0.00	0.00	0.01	0.02	0.01	0.02
40	0.22	2.19	93.98	54.32	57.46	14.63	64.94	74.17	43.75	0.33	0.41	0.64	0.19	0.01	0.01	0.01	0.03	0.01
50	0.23	3.44	94.43	53.21	57.27	14.89	65.56	74.58	44.95	0.71	0.18	0.35	0.01	0.01	0.00	0.01	0.01	0.04

Table B.15: Data from the effect of time on the coagulation experiments.

Time (min)	Residual metal, silicon, and TDS concentrations (%)									Standard deviation								
	Al	Fe	Mn	Ca	Mg	Si	Zn	Ni	TDS	Al	Fe	Mn	Ca	Mg	Si	Zn	Ni	TDS
1	9.12	55.71	57.06	93.27	66.43	99.88	44.93	99.52	117.95	0.05	0.00	0.01	0.46	0.18	0.28	0.00	0.01	0.09
5	7.96	31.85	54.66	87.16	65.80	73.48	36.77	98.26	129.17	0.01	0.00	0.02	0.31	0.36	0.02	0.00	0.00	0.17
10	7.45	14.10	54.14	78.26	64.37	69.63	15.79	93.63	98.72	0.00	0.09	0.03	0.37	0.28	0.00	0.00	0.00	0.00
20	1.36	0.23	53.61	74.13	64.35	56.67	13.95	65.29	60.83	0.00	0.00	0.03	0.12	0.17	0.00	0.00	0.00	0.37
30	2.15	0.23	55.63	74.25	64.89	61.36	20.46	68.80	97.22	0.00	0.01	0.04	0.03	0.05	0.00	0.00	0.00	0.02
40	4.41	4.08	58.20	77.40	67.74	73.01	47.16	98.76	98.68	0.02	0.00	0.02	0.66	0.41	0.00	0.01	0.00	0.00
50	7.08	44.72	58.55	79.50	69.16	77.77	55.88	98.86	119.19	0.02	0.00	0.04	0.42	0.25	0.01	0.01	0.02	0.28

Adsorption isotherm study

$V = 25$ mL

$D = 20$ mg/L

Table B.16: Data from the Langmiur adsorption isotherm model for the removal of Al, Fe, Zn, and Mn.

Time (min)	Al		Fe		Zn		Mn	
	C_e (mg/L)	C_e/q_e	C_e (mg/L)	C_e/q_e	C_e (mg/L)	C_e/q_e	C_e (mg/L)	C_e/q_e
1	1.264	0.080	0.911	1.006	0.416	0.653	7.713	1.063
5	1.102	0.069	0.521	0.374	0.341	0.465	7.388	0.964
10	1.032	0.064	0.231	0.131	0.146	0.150	7.318	0.944
20	0.189	0.011	0.004	0.002	0.129	0.130	7.247	0.925
30	0.298	0.018	0.004	0.002	0.190	0.206	7.519	1.003
40	0.611	0.037	0.067	0.034	0.437	0.714	7.867	1.114
50	0.981	0.061	0.732	0.647	0.518	1.013	7.914	1.130

Table B.17: Data from the Langmiur adsorption isotherm model for the removal of Mg, Ca, Si, and Ni.

Time (min)	Mg		Ca		Si		Ni	
	C_e (mg/L)	C_e/q_e	C_e (mg/L)	C_e/q_e	C_e (mg/L)	C_e/q_e	C_e (mg/L)	C_e/q_e
1	20.046	1.583	29.033	11.087	0.808	6.396	0.418	
5	19.857	1.539	27.132	5.432	0.668	2.217	0.412	45.070
10	19.425	1.445	24.360	2.879	0.633	1.834	0.393	11.751
20	19.420	1.444	23.074	2.292	0.515	1.046	0.274	1.505
30	19.583	1.479	23.112	2.307	0.558	1.270	0.289	1.764
40	20.443	1.680	24.094	2.740	0.664	2.164	0.414	63.894
50	20.869	1.794	24.746	3.102	0.707	2.799	0.415	69.504

Table B.18: Data from the Freundlich adsorption isotherm model for the removal of Mn, Ca, Mg, Si, and Ni.

Time (min)	Mn		Ca		Mg		Si		Ni	
	$\log C_e$	$\log q_e$	$\log C_e$	$\log q_e$	$\log C_e$	$\log q_e$	$\log C_e$	$\log q_e$	$\log C_e$	$\log q_e$
1.00000	0.88722	0.86064	1.46289	0.41809	1.30203	1.10256	-0.09237	-0.89826	-0.37931	-2.60098
5.00000	0.86853	0.88430	1.43348	0.69854	1.29791	1.11059	-0.17499	-0.52077	-0.38487	-2.03876
10.00000	0.86439	0.88923	1.38668	0.92737	1.28836	1.12840	-0.19842	-0.46178	-0.40583	-1.47590
20.00000	0.86016	0.89418	1.36312	1.00292	1.28825	1.12860	-0.28781	-0.30752	-0.56236	-0.73991
30.00000	0.87616	0.87492	1.36384	1.00087	1.29188	1.12197	-0.25330	-0.35725	-0.53964	-0.78615
40.00000	0.89581	0.84896	1.38191	0.94411	1.31054	1.08520	-0.17780	-0.51309	-0.38263	-2.18809
50.00000	0.89840	0.84533	1.39351	0.90187	1.31950	1.06577	-0.15038	-0.59734	-0.38220	-2.22421

Table B.19: Data from the Freundlich adsorption isotherm model for the removal of Al, Fe, and Zn.

Time (min)	Al		Fe		Zn	
	$\log C_e$	$\log q_e$	$\log C_e$	$\log q_e$	$\log C_e$	$\log q_e$
1	0.10175	1.19697	-0.04032	-0.04296	-0.38054	-0.19521
5	0.04227	1.20251	-0.28316	0.14419	-0.46758	-0.13521
10	0.01381	1.20489	-0.63700	0.24469	-0.83478	-0.01076
20	-0.72436	1.23256	-2.42887	0.30970	-0.88838	-0.00141
30	-0.52587	1.22908	-2.43180	0.30971	-0.72217	-0.03555
40	-0.21364	1.21891	-1.17591	0.29262	-0.35949	-0.21317
50	-0.00846	1.20663	-0.13569	0.05324	-0.28581	-0.29149

Table B.20: Data from the Temkin adsorption isotherm model for the removal of Si, Zn, Ni, and Fe.

Time (min)	Si		Fe		Zn		Ni	
	q_e (mg/mg)	$\ln C_e$	q_e (mg/mg)	$\ln C_e$	q_e (mg/mg)	$\ln C_e$	q_e (mg/mg)	$\ln C_e$
1	0.1264	-0.2127	0.9058	-0.0928	0.6380	-0.8762	0.0025	-0.8734
5	0.3015	-0.4029	1.3938	-0.6520	0.7325	-1.0766	0.0091	-0.8862
10	0.3453	-0.4569	1.7567	-1.4667	0.9755	-1.9221	0.0334	-0.9345
20	0.4926	-0.6627	2.0403	-5.5927	0.9968	-2.0456	0.1820	-1.2949
30	0.4393	-0.5832	2.0404	-5.5994	0.9214	-1.6628	0.1636	-1.2426
40	0.3068	-0.4094	1.9616	-2.7076	0.6121	-0.8278	0.0065	-0.8810
50	0.2527	-0.3463	1.1304	-0.3124	0.5111	-0.6581	0.0060	-0.8800

Table B.21: Data from the Temkin adsorption isotherm model for the removal of Al, Mn, Ca, and Mg.

Time (min)	Al		Mn		Ca		Mg	
	q_e (mg/mg)	$\ln C_e$	q_e (mg/mg)	$\ln C_e$	q_e (mg/mg)	$\ln C_e$	q_e (mg/mg)	$\ln C_e$
1	15.7388	0.2343	7.2550	2.0429	2.6188	3.3684	12.6638	2.9980
5	15.9410	0.0973	7.6613	1.9999	4.9950	3.3007	12.9000	2.9886
10	16.0284	0.0318	7.7488	1.9903	8.4600	3.1929	13.4400	2.9666
20	17.0829	-1.6679	7.8375	1.9806	10.0675	3.1387	13.4463	2.9663
30	16.9463	-1.2109	7.4975	2.0174	10.0200	3.1404	13.2425	2.9747
40	16.5544	-0.4919	7.0625	2.0627	8.7925	3.1820	12.1675	3.0176
50	16.0929	-0.0195	7.0038	2.0686	7.9775	3.2087	11.6350	3.0383

Table B.22: Data from the BET adsorption isotherm model for the removal of Al, Fe, Zn, Ca, and Si.

Time (min)	Al		Fe		Zn		Ca		Si	
	C_e/C_s	$\frac{C_e}{q_e(C_s - C_e)}$	C_e/C_s	$\frac{C_e}{q_e(C_s - C_e)}$	C_e/C_s	$\frac{C_e}{q_e(C_s - C_e)}$	C_e/C_s	$\frac{C_e}{q_e(C_s - C_e)}$	C_e/C_s	$\frac{C_e}{q_e(C_s - C_e)}$
1	0.09123	0.00638	0.55705	1.38836	0.44928	1.27877	0.9327	5.29193	0.88882	63.2486
5	0.07956	0.00542	0.31846	0.33526	0.36769	0.79389	0.87163	1.35932	0.73484	9.19314
10	0.07451	0.00502	0.141	0.09344	0.15786	0.19216	0.78258	0.42545	0.69626	6.63821
20	0.01362	0.00081	0.00228	0.00112	0.13953	0.16269	0.74126	0.28457	0.56673	2.65549
30	0.0215	0.0013	0.00226	0.00111	0.20459	0.27916	0.74248	0.28775	0.61361	3.61509
40	0.04413	0.00279	0.04077	0.02167	0.47159	1.45801	0.77403	0.38958	0.73011	8.81653
50	0.07078	0.00473	0.44723	0.71571	0.55878	2.47791	0.79498	0.48605	0.7777	13.84241

Table B.23: Data from the BET adsorption isotherm model for the removal of Mn, Mg, and Ni.

Time (min)	Mn		Mg		Ni	
	C_e/C_s	$\frac{C_e}{q_e(C_s - C_e)}$	C_e/C_s	$\frac{C_e}{q_e(C_s - C_e)}$	C_e/C_s	$\frac{C_e}{q_e(C_s - C_e)}$
1	0.57061	0.18317	0.66428	0.15625	0.99522	83090.62755
5	0.54657	0.15734	0.65802	0.14916	0.98256	6159.62098
10	0.54139	0.15235	0.6437	0.13442	0.93626	439.40933
20	0.53614	0.14747	0.64354	0.13426	0.65294	10.33652
30	0.55626	0.1672	0.64894	0.13959	0.68799	13.47635
40	0.58201	0.19715	0.67744	0.1726	0.98763	12315.65162
50	0.58548	0.20167	0.69155	0.1927	0.98862	14558.82118

Coagulation kinetics of the synthesized composite coagulant:

Adsorption reaction models

Table B.24: Data from the adsorption rate and the pseudo-first-order reaction kinetics for the adsorption of Al.

Time (min)	C_t (mg/L)	q_t (mg/mg)	$\ln(q_e - q_t)$
0	13.85500		
1	1.26400	15.73875	0.30103
5	1.10224	15.94096	0.13893
10	1.03231	16.02836	0.05981
20	0.18864	17.08295	-4.95455
30	0.29794	16.94632	-1.94018
40	0.61145	16.55444	-0.62444
50	0.98071	16.09286	-0.00287

Table B.25: Data from the adsorption rate and the pseudo-first-order reaction kinetics for the adsorption of Fe.

Time (min)	C_t (mg/L)	q_t (mg/mg)	$\ln(q_e - q_t)$
0	1.63600		
1	0.91134	0.90583	0.13468
5	0.52100	1.39375	-0.42122
10	0.23068	1.75666	-1.22641
20	0.00373	2.04034	-4.64015
30	0.00370	2.04038	-4.64339
40	0.06669	1.96163	-2.42625
50	0.73166	1.13042	-0.08384

Table B.26: Data from the adsorption rate and the pseudo-first-order reaction kinetics for the adsorption of Mn.

Time (min)	C_t (mg/L)	q_t (mg/mg)	$\ln(q_e - q_t)$
0	13.5170		
1	7.7130	7.2550	-0.4385
5	7.3880	7.6613	-1.4323
10	7.3180	7.7488	-1.8888
20	7.2470	7.8375	-2.7726
30	7.5190	7.4975	-0.9101
40	7.8670	7.0625	-0.1773
50	7.9140	7.0038	-0.1095

Table B.27: Data from the adsorption rate and the pseudo-first-order reaction kinetics for the adsorption of Ca.

Time (min)	C_t (mg/L)	q_t (mg/mg)	$\ln(q_e - q_t)$
0	31.128		
1	29.033	2.619	2.008
5	27.132	4.995	1.624
10	24.360	8.460	0.476
20	23.074	10.068	-5.991
30	23.112	10.020	-2.996
40	24.094	8.793	0.245
50	24.746	7.978	0.738

Table B.28: Data from the adsorption rate and the pseudo-first-order reaction kinetics for the adsorption of Mg.

Time (min)	C_t (mg/L)	q_t (mg/mg)	$\ln(q_e - q_t)$
0	30.177		
1	20.046	12.664	-0.179
5	19.857	12.900	-0.511
10	19.425	13.440	-2.813
20	19.420	13.446	-2.923
30	19.583	13.243	-1.357
40	20.443	12.168	0.287
50	20.869	11.635	0.623

Table B.29: Data from the adsorption rate and the pseudo-first-order reaction kinetics for the adsorption of Si.

Time (min)	C_t (mg/L)	q_t (mg/mg)	$\ln(q_e - q_t)$
0	0.910		
1	0.908	0.001	-0.696
5	0.668	0.301	-1.617
10	0.633	0.345	-1.866
20	0.515	0.493	-4.904
30	0.558	0.439	-2.802
40	0.664	0.307	-1.644
50	0.707	0.253	-1.397

Table B.30: Data from the adsorption rate and the pseudo-first-order reaction kinetics for the adsorption of Zn.

Time (min)	C_t (mg/L)	q_t (mg/mg)	$\ln(q_e - q_t)$
0	0.927		
1	0.416	0.638	-1.024
5	0.341	0.732	-1.330
10	0.146	0.976	-3.841
20	0.129	0.997	-8.330
30	0.190	0.921	-2.582
40	0.437	0.612	-0.955
50	0.518	0.511	-0.722

Table B.31: Data from the adsorption rate and the pseudo-first-order reaction kinetics for the adsorption of Ni.

Time (min)	C_t (mg/L)	q_t (mg/mg)	$\ln(q_e - q_t)$
0	0.927		
1	0.416	0.638	-1.024
5	0.341	0.732	-1.330
10	0.146	0.976	-3.841
20	0.129	0.997	-8.330
30	0.190	0.921	-2.582
40	0.437	0.612	-0.955
50	0.518	0.511	-0.722

Table B.32: Data from pseudo-second-order reaction kinetics for the adsorption of Fe, Al, and Zn.

Time (min)	Al	Fe	Zn
1	0.06354	1.10397	1.56751
5	0.31366	3.58744	6.82626
10	0.62389	5.69264	10.25089
20	1.17076	9.80227	20.06504
30	1.77030	14.70318	32.55937
40	2.41627	20.39118	65.34787
50	3.10697	44.23120	97.82797

Table B.33: Data from pseudo-second-order reaction kinetics for the adsorption of Mn, Ca, and Mg.

Time (min)	Mn	Ca	Mg
1	0.13784	0.38186	0.07897
5	0.65264	1.00100	0.38760
10	1.29053	1.18203	0.74405
20	2.55183	1.98659	1.48740
30	4.00133	2.99401	2.26543
40	5.66372	4.54933	3.28745
50	7.13903	6.26763	4.29738

Table B.34: Data from pseudo-second-order reaction kinetics for the adsorption of Si.

Time (min)	Si
1	714.9240
5	16.5861
10	28.9586
20	40.6024
30	68.2926
40	130.3626
50	197.8376

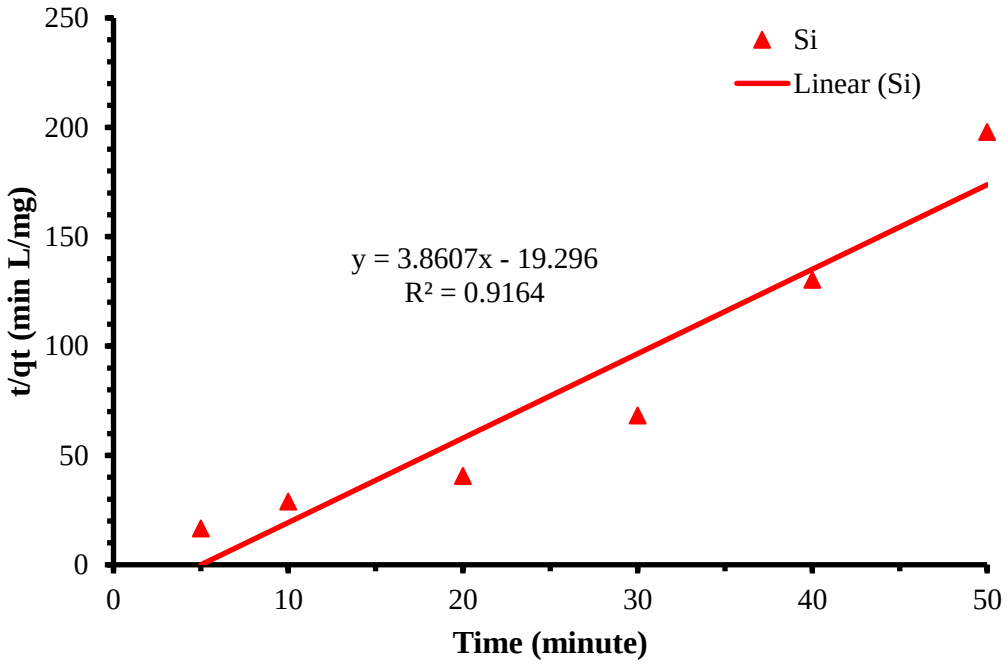

Figure B.1: Pseudo-second-order for the adsorption of silicon after 1 min coagulation's time.

Table B.35: Data from pseudo-second-order reaction kinetics for the adsorption of Ni.

Time (min)	Ni
1	399.002
5	546.672
10	299.155
20	109.886
30	183.347
40	6168.080
50	8378.718

Table B.36: Data from the Elovich reaction kinetics for the adsorption of Al, Mn, Ca, and Mg.

$\ln t$	q_t (mg/mg)			
	Al	Mn	Ca	Mg
0.00000	15.73875	7.25500	2.61875	12.66375
1.60944	15.94096	7.66125	4.99500	12.90000
2.30259	16.02836	7.74875	8.46000	13.44000
2.99573	17.08295	7.83750	10.06750	13.44625
3.40120	16.94632	7.49750	10.02000	13.24250
3.68888	16.55444	7.06250	8.79250	12.16750
3.91202	16.09286	7.00375	7.97750	11.63500

Table B.37: Data from the Elovich reaction kinetics for the adsorption of Si, Ni, Zn, and Fe.

$\ln t$	q_t (mg/mg)			
	Si	Zn	Ni	Fe
0.00000	0.00140	0.63795	0.00251	0.90583
1.60944	0.30146	0.73247	0.00915	1.39375
2.30259	0.34532	0.97553	0.03343	1.75666
2.99573	0.49258	0.99676	0.18201	2.04034
3.40120	0.43929	0.92139	0.16362	2.04038
3.68888	0.30684	0.61211	0.00649	1.96163
3.91202	0.25273	0.51110	0.00597	1.13042

Table B.38: Data from the second-order reaction kinetics for the adsorption of Al, Si, and Ni.

Time (min)	$1/C_t$		
	Al	Si	Ni
0	0.07218	1.09948	2.38357
1	0.79114	1.10084	2.39502
5	0.90725	1.49622	2.42588
10	0.96870	1.57912	2.54585
20	5.30107	1.94004	3.65054
30	3.35635	1.79183	3.46454
40	1.63546	1.50591	2.41342
50	1.01967	1.41376	2.41101

Table B.39: Data from the second-order reaction kinetics for the adsorption of Mn, Ca, and Mg.

Time (min)	$1/C_t$		
	Mn	Ca	Mg
0	0.07398	0.03213	0.03314
1	0.12965	0.03444	0.04989
5	0.13535	0.03686	0.05036
10	0.13665	0.04105	0.05148
20	0.13799	0.04334	0.05149
30	0.13300	0.04327	0.05106
40	0.12711	0.04150	0.04892
50	0.12636	0.04041	0.04792

Table B.40: Data from the second-order reaction kinetics for the adsorption of Fe and Zn.

Time (min)	$1/C_t$	
	Fe	Zn
0	0.61125	1.07908
1	1.09729	2.40182
5	1.91939	2.93478
10	4.33508	6.83560
20	268.45638	7.73359
30	270.27027	5.27432
40	14.99385	2.28819
50	1.36675	1.93113

Adsorption diffusion models

$r = 5.11667 \times 10^{-5}$ cm

$\pi = 3.14$

Table B.41: Data from the Weber-Morris diffusion kinetics for the adsorption of Al, Mn, Mg, and Ca.

Time (min)	$t^{1/2}$	q_t (mg/mg)			
		Al	Mn	Mg	Ca
1	1.0000	15.7388	7.2550	12.6638	2.6188
5	2.2361	15.9410	7.6613	12.9000	4.9950
10	3.1623	16.0284	7.7488	13.4400	8.4600
20	4.4721	17.0829	7.8375	13.4463	10.0675

Table B.42: Data from the Weber-Morris diffusion kinetics for the adsorption of Fe, Si, Zn, and Ni.

Time (min)	$t^{1/2}$	q_t (mg/mg)			
		Fe	Si	Zn	Ni
1	1.0000	0.9058	0.0014	0.6380	0.0025
5	2.2361	1.3938	0.3015	0.7325	0.0091
10	3.1623	1.7567	0.3453	0.9755	0.0334
20	4.4721	2.0403	0.4926	0.9968	0.1820

Table B.43: Data from the Boyd's diffusion kinetics for the adsorption of Al, Fe, Mn, and Ca.

Time (min)	β_t (min^{-1})			
	Al	**Fe**	**Mn**	**Ca**
1	2.03268	0.22359	2.09738	0.06774
5	2.19348	0.67305	3.28301	0.29514
10	2.27189	1.44625	3.95539	1.33735
20	6.41261	4.85999	7.55270	7.80303

Table B.44: Data from the Boyd's diffusion kinetics for the adsorption of Mg, Si, Zn, and Ni.

Time (min)	β_t (min^{-1})			
	Mg	**Si**	**Zn**	**Ni**
1	2.34146	0.00001	0.56799	0.00016
5	2.69882	0.50242	0.84686	0.00221
10	6.70615	0.73377	3.33986	0.03182
20	7.68698	6.57299	7.82867	4.71901

Table B.45: Data from the Banbham's diffusion kinetics for the adsorption of Al, Fe, Mn, Ca, and Mg.

Time (min)	$\log t$	$log\left[log\left(\frac{C_0}{C_0 - q_t m}\right)\right]$				
		Al	**Fe**	**Mn**	**Ca**	**Mg**
1	0.0000	-2.0008	-2.3155	-2.3291	-3.1359	-2.4365
5	0.6990	-1.9952	-2.1271	-2.3053	-2.8551	-2.4284
10	1.0000	-1.9928	-2.0256	-2.3003	-2.6258	-2.4105
20	1.3010	-1.9648	-1.9598	-2.2954	-2.5500	-2.4103

Table B.46: Data from the Banbham's diffusion kinetics for the adsorption of Ni, Si, and Zn.

Time (min)	$\log t$	$log\left[log\left(\frac{C_0}{C_0 - q_t m}\right)\right]$		
		Si	**Zn**	**Ni**
1	0.0000	-4.8743	-2.2203	-4.2849
5	0.6990	-2.5393	-2.1599	-3.7226
10	1.0000	-2.4801	-2.0343	-3.1595
20	1.3010	-2.3252	-2.0248	-2.4220

APPENDIX C: CHAPTER 6

Fitting models analysis: coagulant synthesis by coal fly ash leaching process.

Table C.1: Data from the dissolution of iron.

Time (hour)	Experimental data	Fitting model	Standard deviation
1	53.04	49.4667	5
2	42.15	41.6333	2
3	29.48	33.7238	5
4	57.04	57.3025	3
5	50.39	57.3	5
6	57.90	57.3	2
8	57.29	57.3	4

Table C.2: Data from the dissolution of aluminium.

Time (hour)	Experimental data	Fitting model	Standard deviation
1	26.91	26.8733	3
2	23.76	24.6357	4
3	32.54	31.3849	4
4	34.65	34.6117	3
5	31.38	34.3331	5
6	33.86	32.6538	4
8	35.93	36.1221	5

Table C.3: Data from the dissolution of silicon.

Time (hour)	Experimental data	Fitting model	Standard deviation
1	6.91	6.91089	0.8
2	7.19	7.92643	0.9
3	9.03	8.94196	1
4	10.03	9.9575	1
5	10.86	10.973	1
6	11.12	11.9886	3
8	14.02	14.0196	2

Table C.4: Data from the dissolution of magnesium.

Time (hour)	Experimental data	Fitting model	Standard deviation
1	62.56	62.5598	2
2	63.57	62.5598	3
3	70.83	68.8657	2
4	73.21	71.3165	2
5	73.21	73.2992	3
6	73.21	74.8139	3
8	76.44	76.4388	3

Table C.5: Data from the dissolution of calcium.

Time (hour)	Experimental data	Fitting model	Standard deviation
1	5.62	5.617525374	0.6
2	11.01	11.02248981	1
3	13.67	16.00233237	1.5
4	20.77	20.34449211	2
5	25.71	23.83640809	2
6	25.43	26.26551938	2
8	27.08	27.08508412	1.5

Fitting models analysis: AMD treatment by coagulation process using the produced coagulant.

Table C.6: Data from the coagulation of aluminium.

Time (min)	Experimental data	Fitting model	Standard deviation
1	9.12	10.03	2
5	7.96	7.91	4
10	7.45	5.71	3
20	1.36	2.81	4
30	2.15	1.91	4
40	4.41	3.01	2
50	7.08	6.11	3

Table C.7: Data from the coagulation of iron.

Time (min)	Experimental data	Fitting model	Standards deviation
1	55.71	55.71	2
5	31.85	31.85	1.5
10	14.10	14.14	2
20	0.23	0.84	3
30	0.23	-0.46	2
40	4.08	10.24	1
50	44.72	56.94	3

Table C.8: Data from the coagulation of manganese.

Time (min)	Experimental data	Fitting model	Standard deviation
1	57.06	57.06	3
5	54.66	55.05	2
10	54.14	53.58	1
20	53.61	53.23	1
30	55.63	54.77	2
40	58.20	56.38	4
50	58.55	56.19	3

Table C.9: Data from the coagulation of magnesium.

Time (min)	Experimental data	Fitting model	Standard deviation
1	66.43	66.45	2
5	65.80	65.70	1.5
10	64.37	65.01	1
20	64.35	64.46	3
30	64.89	65.01	2
40	67.74	66.66	2
50	69.16	69.41	1

Table C.10: Data from the coagulation of calcium.

Time (min)	Experimental data	Fitting model	Standard deviation
1	93.27	91.32	2
5	87.16	87.17	3
10	78.26	82.74	2
20	74.13	76.44	1
30	74.25	73.54	4
40	77.40	74.04	4
50	79.50	77.94	2

Table C.11: Data from the coagulation of silicon.

Time (min)	Experimental data	Fitting model	Standard deviation
1	99.88	82.6789	3
5	73.48	71.3025	5
10	69.63	61.69	2
20	56.67	54.69	2
30	61.36	58.49	3
40	73.01	66.49	4
50	77.77	72.09	4

Table C.12: Data from the coagulation of zinc.

Time (min)	Experimental data	Fitting model	Standard deviation
1	44.93	44.93	4
5	36.77	35.99	2
10	15.79	27.24	2
20	13.95	17.84	5
30	20.46	19.24	3
40	47.16	31.44	3
50	55.88	54.44	2

Table C.13: Data from the coagulation of nickel.

Time (min)	Experimental data	Fitting model	Standard deviation
1	99.52	99.49	2
5	98.26	102.80	1
10	93.63	92.99	3
20	65.29	66.99	2
30	68.80	70.99	3
40	98.76	104.99	1
50	98.86	116.19	4

APPENDIX D

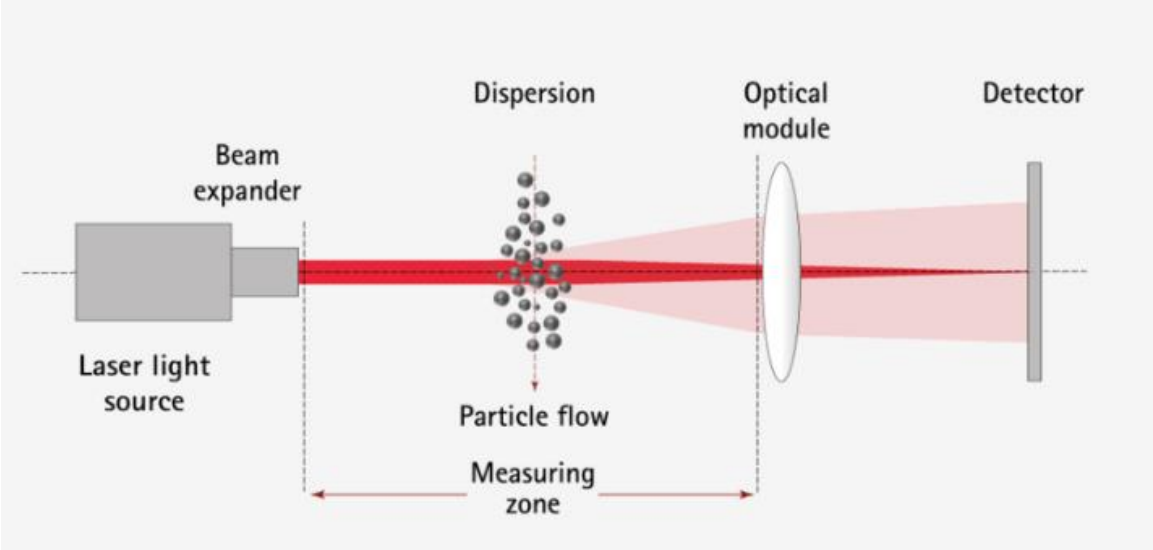

Figure D.1: Basic optical system of a laser diffraction particle size analyser (Laser Diffraction. Available at https://www.sympatec.com/en/particle-measurement/sensors/laser-diffraction/. Accessed 15 August 2019)

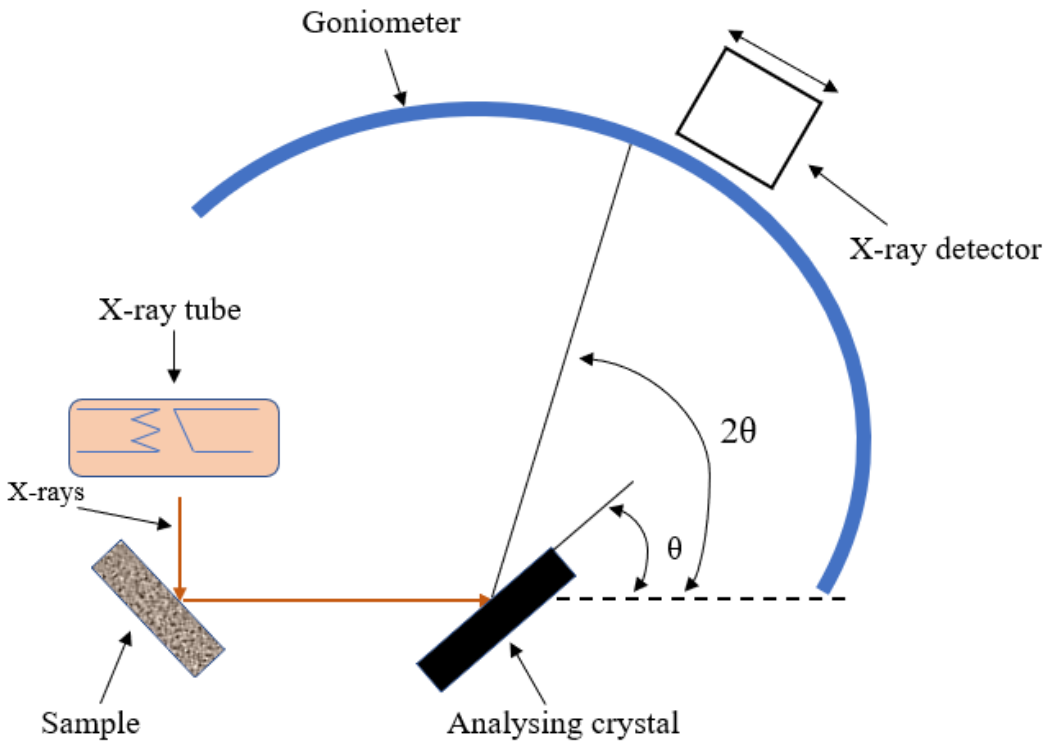

Figure D.2: Basic system of an x-ray diffraction spectrometer

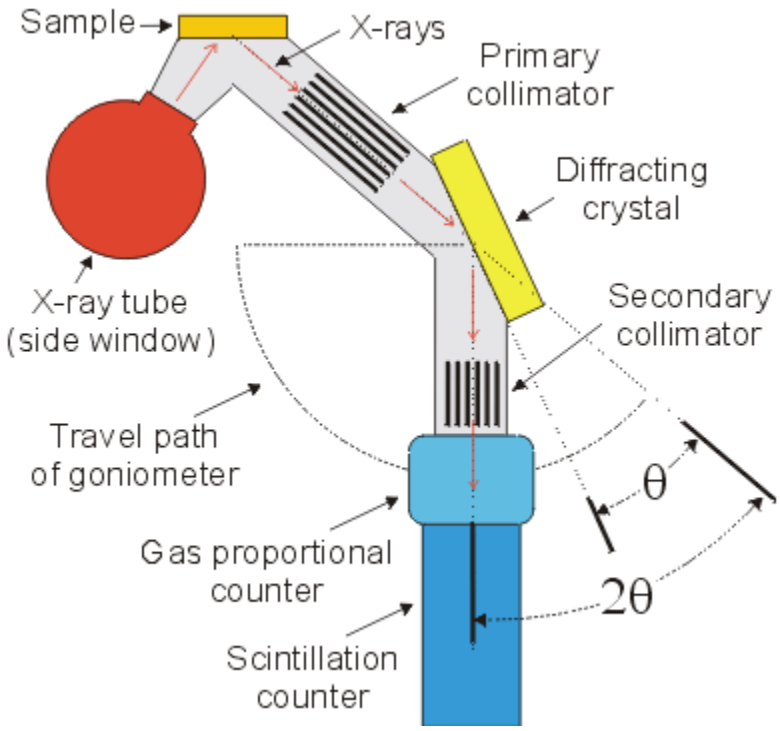

Figure D.3: Basic system of an x-ray fluorescence spectrometer (x-ray fluorescence (XRF). Available at https://projects.exeter.ac.uk/geomincentre/estuary/Main/xrf.htm. Accessed 15 August 2019).

REFERRED PUBLICATION

CHARACTERIZATION OF COAL FLY ASH FOR THE PRODUCTION OF COAGULANT FOR USAGE IN WASTEWATER TREATMENT

M. Clotilde Apua[a,*], Geoffrey S. Simate[a,b,c,*]

[a]School of Chemical and Metallurgical Engineering, University of the Witwatersrand, Johannesburg, P/Bag 3, Wits 2050, South Africa

[b]Industrial and Mining Water Research Unit, University of the Witwatersrand, Johannesburg, P/Bag 3, Wits 2050, South Africa

[c]Centre in Water Research and Development, University of the Witwatersrand, Johannesburg, P/Bag 3, Wits 2050, South Africa

* Corresponding author.

Email addresses: clotildeapua@gmail.com (M.C. Apua); simateg@gmail.com (G.S. Simate)

Keywords: characterization; coal fly ash; coagulant.

Abstract

In this study, the physicochemical characterization of coal fly ash sample (CFA) were investigated using a combination of complementary characterization techniques, and the findings are discussed with reference to its use in the synthesis of coagulants for wastewater treatment. The XRF results showed that the sample belongs to Class F fly ash. Quartz, mullite, and hematite were the major crystalline phases identified by the XRD, XRF, SEM/EDS, and FTIR. Surface morphology of individual CFA ash particles was characterized by SEM/EDS as spherical particles with smooth surfaces and PSD with a P80 particle diameter of 49 µm was determined.

---

1 Introduction

Coal fly ash (CFA) is an abundant waste residue from the combustion of coal in coal-fired power plants [1]. It is estimated that more than 750 million tons of CFA is produced all over the world annually. However, only a small fraction (20–30%) is used in cement manufacture, metals recovery, agriculture, zeolite production, and many other applications [2, 3]. In South Africa, almost 25 million tons of CFA is produced per annum by Eskom, the main country's electricity producer, but only 5% is used for cement and brick making while the rest is disposed of on a landfill adjacent to the power stations [4].

Ideally, CFA is rich in iron and aluminium oxides which are essential raw materials for the production of coagulants for water and wastewater treatment. In fact, the weight ratio of iron to aluminium oxides in CFA is suitable for producing complex coagulants [5, 6]. Use of CFA to manufacture complex coagulants can, therefore, result in significant cost savings, since CFA cost much less than industrial-grade iron or aluminium ores which are traditionally used as raw materials for the synthesis of coagulants. In addition, such a concept of using these by-products would help in lessening the environmental degradation resulting from the storage and disposal techniques presently used in several countries [2]. Mineralogical study and determination of the elemental composition of CFA and how it affects the physico-chemical characteristics of wastewater after treatment is important. The purpose of the present investigation was to use X-ray diffraction (XRD), X-ray fluorescence (XRF), scanning electron microscopy combined with energy dispersive X-ray spectrometry (SEM/EDS), Fourier transform infrared spectroscopy (FTIR), and particle size distribution analysis (PSD) to characterize a CFA sample and thus ascertain its suitability in the synthesis of coagulant for wastewater treatment.

2 Material and Methods

2.1 Material Preparation

The CFA used in this study was supplied by the Eskom Kendal power station in South Africa. The surface area of the interface is an important factor in the rate of electrons transfer during the leaching process; the rate of leaching is fast with finely ground particles than with coarse particles due to large surface area in the fine particles. In order to liberate the minerals so that they are accessible to the lixiviant, the CFA was milled to fine particles. The sample was then split using a spinning riffler, and was further re-split in order to obtain a

representative sample. The representative sample was utilized in analytical techniques discussed in this paper and will be used later for leaching experiments in the production of the coagulant.

2.2 Characterization of Coal Fly Ash

The mineralogical studies were conducted using XRD and XRF. Surface morphology study of CFA was carried out using SEM and elemental composition was determined using EDS. Functional groups were identified using FTIR. Particle size distribution study was done using PSD analysis. The sample characterisation procedures of various techniques are outlined in the subsections below.

2.2.1 Particle Size Distribution: A Microtrac S3500 particle size analyser used in this study is a laser-based system which processes particle-laser interactions in the size range of 0.02 to 2800 μm. In this study, a sample was placed in the laser diffraction instrument where it was dispersed in distilled water and particle size distribution was then measured. Subsequently, the PSD was reported in a graph of % passing vs particle diameter.

2.2.2 X-ray Diffraction Spectroscopy: The diffractometer used in this study is a Rigaku Ultima IV model. The fine powder sample was pressed in a sample holder with a smooth plane surface, and mounted onto the sample chamber.

2.2.3 X-ray Fluorescence Spectroscopy: A Rigaku ZSX Primus II model X-ray fluorescence spectrometer was used in this study to perform a dispersive wavelength analysis. The standard diffraction crystal used was lithium fluoride LiF (220). The sample was first ground to fine powder. After that, 10 g was weighed and filled into an aluminium cap and pressed by applying 15 MPa of pressure, using a hydraulic press for a 1 min. This procedure was aimed at producing a smooth flat surface. Thereafter, the sample was oven dried at 80ºC for 30 min to remove all moisture and, lastly, the sample was mounted onto the sample chamber. The x-ray tube that provided primary radiation was operated at a high voltage of about 60 kV. The high voltage helped to obtain a continuous spectrum that allowed excitation of a large range of atoms.

In the XRF analysis of the ground sample used in this study (sample type: pressed pellet), only transitions Kα were considered. Quantification (%) of different elements present in the minerals sample was given.

2.2.4 Fourier-transform Infrared Spectroscopy: In this analytical technique, CFA sample was used and subjected to infrared radiation. The FTIR spectrum was obtained using a Thermo Scientific Nicolet iS10 spectrometer in the wavenumber region of 500–4000 cm^{-1}. The vertical axis obtained from the spectrometer indicates the percentage of transmitted light while the horizontal axis shows wavenumbers of the infrared wavelength at which the sample has absorbed infrared. The resulting spectrum represents the molecular absorption and transmission, which is a molecular fingerprint of the sample.

2.2.5 Scanning Electron Microscopy Coupled with Energy Dispersive Spectroscopy: The SEM/EDS gives detailed imaging information about the morphology and surface texture of individual particles, as well as elemental composition of the sample. In this work, a Vega3 Tescan model XMU Scanning Electron Microscope equipped with secondary electron (SE) and backscattered electron (BSE) detectors combined with EDS was used to study the microstructure of the sample.

For the SEM sample preparation and analysis, a small portion of the CFA sample was dispersed onto double-sided carbon tape. It was then coated with a thin layer of carbon to provide surface conductivity. The coating technique was done under vacuum. The coated piece was then placed in a SEM microscope to determine the particle morphology and external surface structure, and external elemental composition of individual CFA particles using EDS. The elemental analysis using EDS was carried out in a ‘‘spot mode” by randomly selecting 4 spots or areas of view and examining all the CFA particles observed within the selected areas. The morphology and elemental composition were noted for each particle and compiled.

3 Results and Discussion

3.1 Particle Size Distribution

The PSD of the CFA sample in Figure 1 shows that the sample has a P80 particle diameter of 49 μm (i.e., 80% of the volume distribution of the sample having particle sizes smaller than 49 μm). In the coagulant production, which is the leaching process of iron and aluminium in CFA, inclusions of the iron and aluminium bearing minerals are to be dissolved from the CFA particles. Since the smaller the particle size, the better the recovery effectiveness (due to the exposure of the iron and aluminium mineral grains), particle size less than 49 μm is suitable for the leaching of iron and aluminium in CFA.

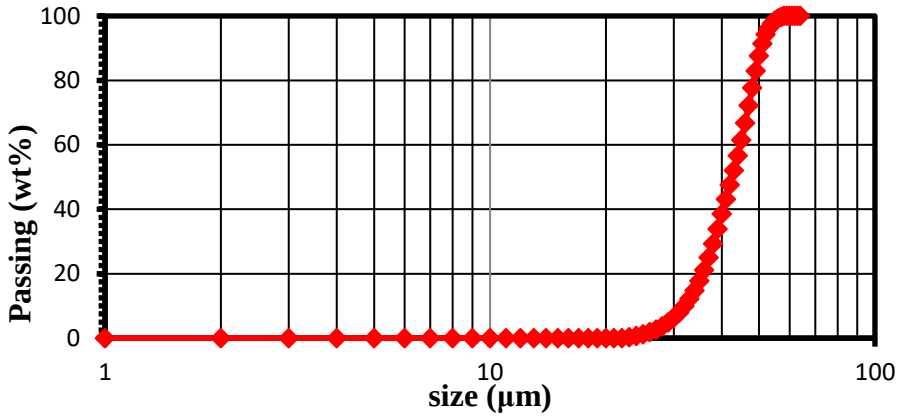

Figure 1. Curve of particle size distribution (PSD) of CFA sample shows that the sample has a P80 particle diameter of 49 µm.

3.2 Mineralogical Study

The CFA is the residue produced by the inorganic and organic matter during combustion of coal. Its chemical composition is influenced by the geographical and geological factors of the coal deposit, coal rank, boiler operation conditions, and fuel gas pollution control technology applied [7, 8]. Minerals in CFA belong to different classes and generally consist of silicates and oxyhydroxides, lower amount of sulphates and carbonates, and more rarely phosphates and other mineral species [9].

In this work, the mineralogical composition of CFA was determined by XRD, XRF, FTIR, SEM/EDS. Whilst the XRD was used in order to find out the different mineral phases present in the CFA sample, the XRF was used for the quantification of various elements present in the sample, the FTIR was used to determine the chemical functional bonds in the material, and the SEM/EDS for the microstructural study and the elemental composition determination of the sample. The results of various techniques are outlined in the subsections below.

3.2.1 XRD and XRF Analyses: Major crystalline phases in CFA found by XRD were quartz (SiO_2), mullite ($Al_{5.65}Si_{0.35}O_{9.175}$), and hematite ($Fe_2O_3$) (Figure 2). The XRF results summarised in Table 1 shows that the as-received CFA sample contains mainly 32.15% alumina (Al_2O_3), 4.16% hematite (Fe_2O_3), 6.25% lime (CaO), 49.92% silica (SiO_2), and 2.15% titanium dioxide (TiO_2). Elements found by XRF agree well with phases found by XRD analysis especially with the predominance of silicon compound (quartz) and aluminium compound (mullite). In addition, the XRF results showed that the sample belongs to class F

CFA due to the low content of CaO. Ideally, the XRD and XRF results show that the following were the main elements: Al, Fe, Ca, Si, and Ti. These results are supported by the findings of Authier-Martin et al. [10].

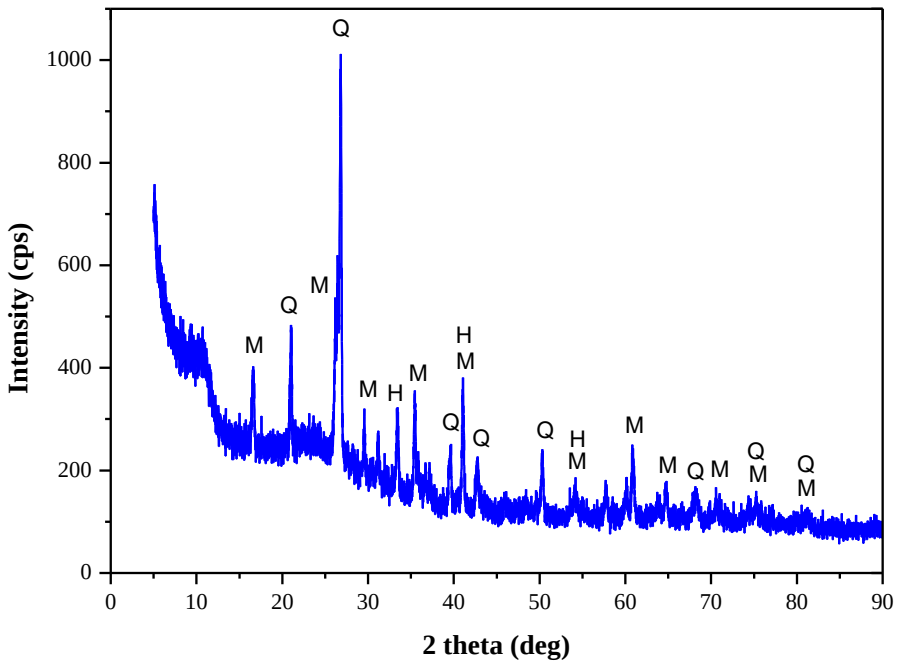

Figure 2. XRD pattern of CFA. Q, M, and H indicate quartz (SiO_2), mullite ($Al_{5.65}Si_{0.35}O_{9.175}$), and hematite ($Fe_2O_3$), respectively.

Table I. Chemical Composition of CFA Sample (Only Major Elements are presented)

Chemical composition	Content (wt%)
Al_2O_3	32.15
Fe_2O_3	4.16
SiO_2	49.92
CaO	6.25
TiO_2	2.15
MgO	1.40
K_2O	1.00
P_2O_5	1.04

Mineralogical study confirmed that CFA contains essential mineral elements (Fe and Al) in oxide form, which can be used to produce coagulants. Due to the presence of Fe_2O_3 (4.16%) and Al_2O_3 (32.15%) in CFA, the pulverized CFA has a huge potential for use in the synthesis of coagulant for wastewater treatment [5, 6].

3.2.2 FTIR Analysis: The FTIR spectrum of the CFA sample is displayed in Figure 3. Characterization of the chemical functional bonds as shown in FTIR spectrum was done by comparing peak frequencies with the typical infrared absorption frequencies of functional groups (Table 2).

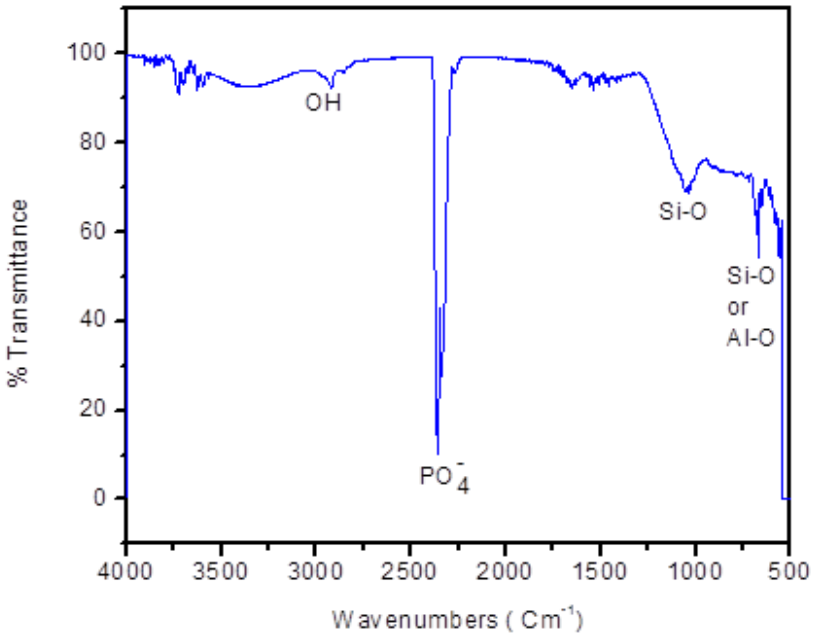

Figure 3. FTIR spectrum for CFA

The peak at 669.14 cm^{-1}, in Figure 3, was associated to Si-O or Al-O bending vibrations and has contributions from quartz (SiO_2) and mullite ($Al_{5.65}Si_{0.35}O_{9.175}$). This agrees well with the findings of the studies by van der Merwe et al. [4] and Mackenzie [11]. The broad band observed at around 1032.97 cm^{-1} originates from Si-O stretching vibrations. This is also in agreement with the findings of the investigations by van der Merwe et al. [4], Vempati et al. [12], Fernandez and Palomo [13], and Voll et al. [14]. This broad band indicates the presence of high percentage of quartz as shown by XRD and XRF. The bands appearing in the wavenumber range of 2400–2200 cm^{-1} may be associated with the P=O bonds of the phosphate PO_4^- group. The OH stretching vibrations of Si–OH group occured at the

wavenumber values from 2900 to 3400 cm^{-1}. This is consistent with the works by Kaur and Goyal [15], Andini et al. [16], Thonsang and Sombatsompop [17], and Vempati et al. [12].

Table II. Band Assignment for Coal Fly Ash Compounds Related to the Band Positions in cm^{-1}

Wavenumber range (cm^{-1})	Band assignment for coal fly ash
450–520	Si–O
550–920	Si–O, Al–O
950–1168	Si–O
2200–2400	P=O
2500–3400	O–H

From the FTIR results, major components of CFA were found to be quartz and mullite. The later can be used for the production of aluminium type coagulants that may help in wastewater treatment.

3.2.3 SEM/EDS Analysis: Morphology study using SEM shows that particles in CFA have smooth spherical surfaces; (Figure 4). Ideally, the single CFA particles were found to be hollow, empty spheres (cenospheres) or filled with smaller amorphous particles and crystals (plerospheres) [18]. The EDS results of surface of CFA were in agreement with XRD and XRF data, i.e., the CFA sample has high mineralogical content rich in Al, Si, Fe, and Ca and minor amounts of the elements: Ti, Mg, K, Na, and S (Figure 5 and Table 3). The SEM and EDS results show that CFA sample contains essential mineral oxides like Fe_2O_3 and Al_2O_3 that are essential in the production of coagulants for the treatment of water and wastewater effluents.

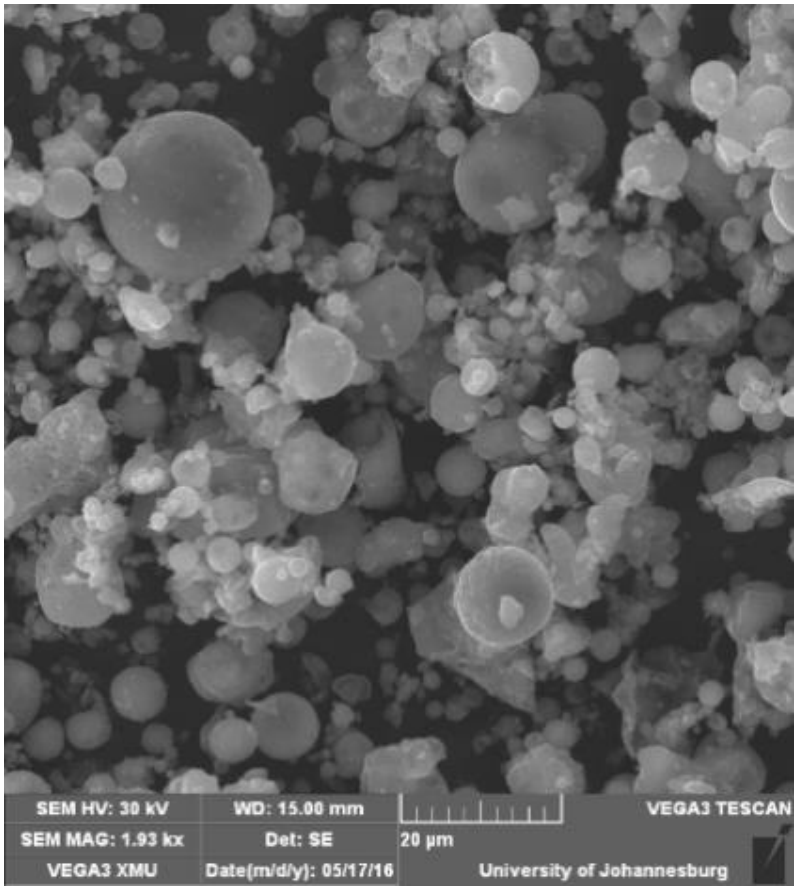

Figure 4. Scanning electron micrograph (SEM) of the coal fly ash showing smooth spheres.

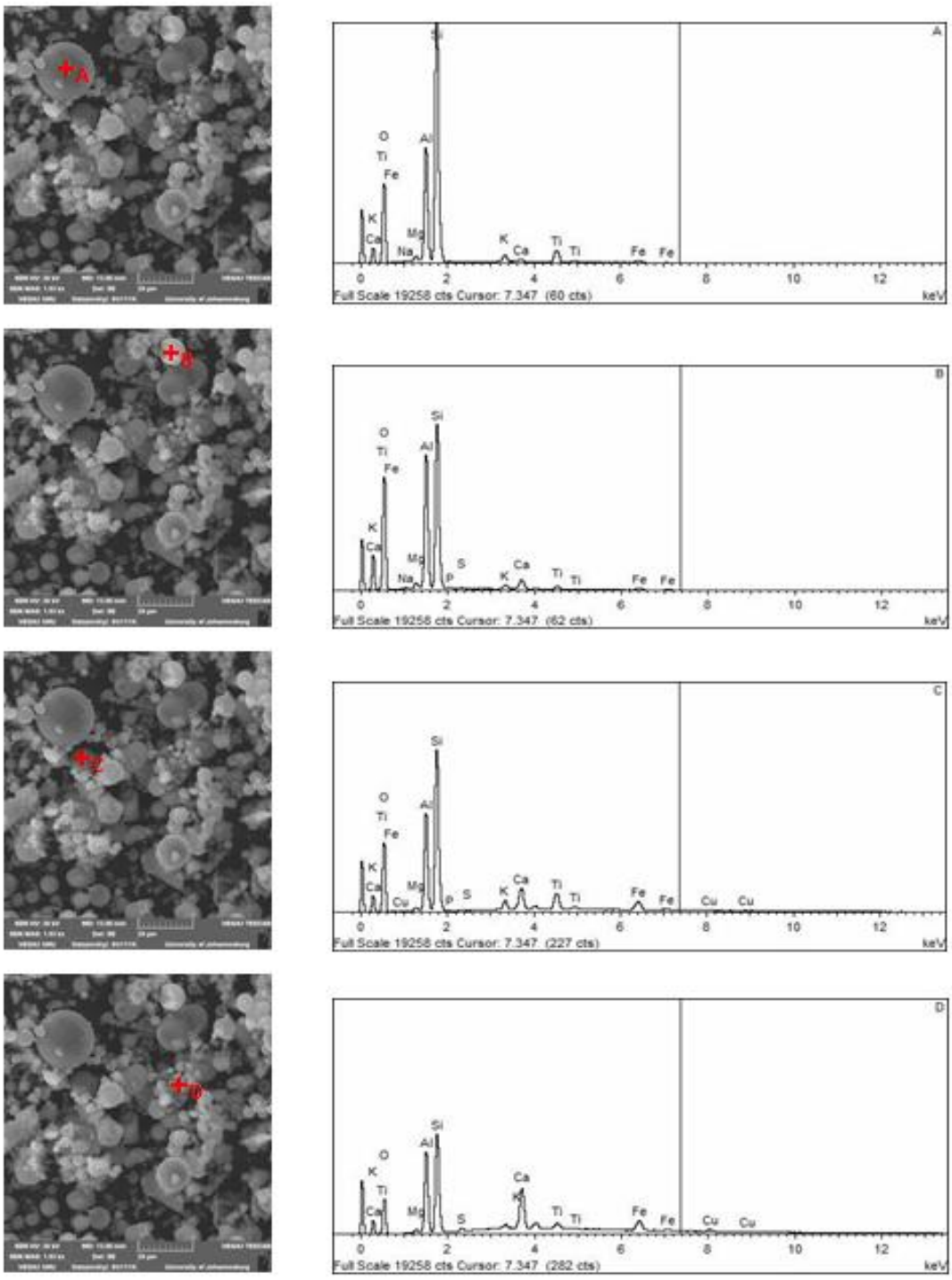

Figure 5. SE images with elemental spectra of the coal fly ash spheres (spots A, B, C, and D). These coal fly ash particles have small variations in proportions of Al, Si and Fe.

Table III. Energy Dispersive Spectrometry (EDS) w% of Elements in Coal Fly Ash

Spectrum	Na	Mg	Al	Si	P	S	K	Ca	Ti	Fe	Cu	O	Total
A	0.28	0.55	12.42	32.28			1	0.34	2.17	0.69		50.27	100
B	0.24	0.69	16.92	28.08	0.34	0.24	0.67	1.62	0.67	0.71		49.81	100
C		0.61	13.27	26.36	0.21	0.2	1.44	3.55	3.4	2.86	0.4	47.71	100
D		0.65	14.93	21.91		0.78	0.83	8.59	1.57	4.02	0.86	45.85	100
Max.	0.28	0.69	16.92	32.28	0.34	0.78	1.44	8.59	3.4	4.02	0.86	50.27	
Min.	0.24	0.55	12.42	21.91	0.21	0.2	0.67	0.34	0.67	0.69	0.4	45.85	

4 Conclusion

Physicochemical characteristic studies of CFA using XRD pattern, XRF, and SEM/EDS graphs confirmed the presence of different minerals in CFA, which may act as potential inorganic wastewater treatment coagulants. Quartz, mullite and hematite were identified by XRD. The low CaO content as determined by XRF analysis has confirmed that this is a Class F CFA. The FTIR bands in CFA provided evidence for important peaks in the spectrum originating from Si–O and Al–O bending and stretching vibrations. This indicates that CFA has a good potential and could be utilized in coagulant synthesis for the treatment of wastewater.

Disclaimer

The contents of this paper reflect the views of the authors who are responsible for the facts and accuracy of the data presented herein and do not necessarily reflect the official views or policies of any agency or institute. This paper does not constitute a standard, specification, nor is it intended for design, construction, bidding, or permit purposes. Trade names were used solely for information and not for product endorsement.

Acknowledgements

The authors are thankful to the technicians in the extraction metallurgy laboratories of the University of Johannesburg.

References

1. Z.T. Yao, M.S. Xia, P.K. Sarker, T. Chen, T., "A review of the alumina recovery from coal fly ash, with a focus in China," *Fuel*, 120 (2014), 74–85.
2. M. Fan, R.C. Brown, J.H.V. Leeuwen, M. Nomura, Y. Zhuang, "The kinetics of producing sulfate-based complex coagulant from fly ash," *Chemical Engineering and Processing*, 42 (2003), 1019–1025.
3. L. Yan, Y. Wang, H. Ma, Z. Han, Q. Zhang, Y. Chen, "Feasibility of fly ash-based composite coagulant for coal washing wastewater treatment," *Journal of Hazardous Materials*, 203–204 (2012), 221–228.
4. E.M. van der Merwe, L.C. Prinsloo, C.L. Mathebula, H.C. Swart, E. Coetsee, F.J. Doucet, "Surface and bulk characterization of an ultrafine South African coal fly ash with reference to polymer applications," *Applied Surface Science*, 317 (2014), 73–83.
5. J.Y. Bottero, M. Axelos, D. Tchoubar, J.M. Cases, J.J. Fripiat, F. Fiessinger, "Mechanism of formation of aluminum trihydroxide from keggin Al13 polymers," *Journal of Colloid Interface Science*, 117 (1) (1987), 47–57.
6. A. Seidel, Y. Zimmels, "Mechanism and kinetics of aluminum and iron leaching from coal fly ash by sulfuric acid," *Chemical Engineering Science*, 53 (22) (1998), 3835–3852.
7. L. Li, M. Fan, R.C. Brown, J.A. Koziel, J.H. Leeuwen, "Production of a new wastewater treatment coagulant from fly ash with concomitant flue gas scrubbing," *Journal of harzardous Materials*, 162 (2009), 1430–1437.
8. M. Fan, R.C. Brown, T.D. Wheelock, A.T. Cooper, M. Nomura, Y. Zhuang, "Production of a complex coagulant from fly ash," *Chemical Engineering Journal*, 106 (2005), 269–277.
9. S.V. Vassilev, C.G. Vassileva, "Occurrence, abundance and origin of minerals in coals and coal ashes," *Fuel Processing Technology*, 48 (1996), 85–106.
10. M. Authier-Martin, G. Forte, S. Ostap, J. See, "The Mineralogy of Bauxite for Producing Smelter Grade Alumina," *Journal of the Minerals, Metals and Materials Society*,53 (2001), 36–40.
11. K.J.D. MacKenzie, "Infrared Frequency Calculations for Ideal Mullite ($3Al_2O_3.2SiO_2$)," *Journal of the American Ceramic Society*, 55 (1972), 68–71.

12. R.K. Vempati, R. Ajoy, T.R. Hess, D.L. Cocke, H.V. Lauer, Jr, “Fractionation and characterization of texas lignite class F fly ash by XRD, TGA, FTIR and SEM,” *Cement and Concrete Research*, 24 (6) (1994), 1153–116.
13. A. Fernandez-Jimenez, A. Palomo, “Mid-infrared spectroscopic studies of alkali-activated fly ash structure,” *Microporous and Mesoporous Materials*, 86 (2005), 207–214.
14. D. Voll, P. Angerer, A. Beran, H. Schneider, “A new assignment of IR vibrational modes in mullite,” *Vibrational Spectroscopy*, 30 (2002), 237–243.

15. R. Kaur, D. Goyal, “Mineralogical comparison of coal fly ash with soil for use in agriculture,” *Journal of Mater Cycles Waste Management*, 18 (2016), 186–200.
16. S. Andini, R. Cioffi, F. Colangelo, T. Grieco, F. Montagnaro, L. Santoro, “Coal fly ash as raw material for the manufacture of geopolymer-based products,” *Waste Management*, 28 (2008), 416–423.
17. S. Thongsang, N. Sombatsompop, “Effect of NaOH and Si69 treatments on the properties of fly ash/natural rubber composites,” *Polymer Composites*, 27 (1) (2006), 30–40.
18. R. Giere, L.E. Carleton, G.R. Lumpkin, “Micro and nanochemistry of fly ash from a coal fired power plant,” *American Mineralogist*, 88 (2003), 1853–1865.